Over-The-Air Design Methodology for Wearable Antennas under the Influence of Human-Multipath Mutual Interactions

PhD Dissertation

Kun Li

March 2017

人体・多重波相互作用影響下におけるウェアラブルアンテナの Over-The-Air 設計方法論

博士論文

李 鯤

2017 年 3 月

Contents

APPENDIX A. MATLAB PROGRAM FOR RICE CHANNEL BAN-OTA TESTING

1. Preface

1.1 Background

1.1.1 Prospect of Mobile Communication Technology

Owing to the rapid development of mobile Internet technologies in recent 20 years, innovation of mobile communication industry are leading human society to enter the era of big data. With an increasing demand of information exchange, ultra-high-speed and large-capacity mobile communications will be realized as a result of the development of LTE-Advanced, Beyond 4G, and 5G in future, using such as MIMO (multiple-input multiple-output) technique [1].

Fig. 1.1 shows a development history of mobile communication technology. The evolution process of mobile phone can be characterized form the user perspective. As a continuation of a trend spearheaded by the mobile phone, wireless device will become smaller and more convenient for personalized operation. Alongside the trend, wireless intelligent devices can autonomously respond to diverse environments in which they operate. This indicates that future human society will be constantly more interconnected through the power of wireless network, as the concept of Internet of Things (IoT) [2].

Fig. 1.2 shows global units shipments of electrical device from 2010s to 2020s [3]. It can be predicted that wearable applications will lead the next generation of mobile communication technology instead of smartphone in future 20 years. This is because wearable device is more convenient to realize abundance applications through wireless interconnections, such as healthcare, smart home, personal entertainment and identification systems. Especially in medical-healthcare system, wearable applications has a wide prospect in future human society.

On the basis of recent data published by WHO (World Health Organization) [4], health expenditure is rapidly increased in many countries due to a large healthcare cost caused by upcoming aging society. Especially in the countries with large population, owing to the extension of life expectancy, health expenditure has already accounted for a significant portion of GDP (Gross Domestic Product). UNFPA (United Nations Population Fund) statistics indicate that the population over the age of 60 years will reach 2.03 billion in 2050, accounting for 22% of the world's total population [5]. In Japan, the document published by MHLW (Ministry of Health, Labour and Welfare) declares that national health expenditure will reach 50 trillion yen in 2025 [6]. Main reason of this fact is that the population over 65 years old in Japan has more than 33 million, while 23% of them are one-person household. These surveys indicate that medical-healthcare management of elderly population and prevention of life-threatening diseases are common subjects for most countries in the world.

The general requirement of intelligent medical service published by Economics Think Tanks shows that users mostly expect an overall management of health, medical information and recommendation. With the health problem getting more and more attention in future, the demand of health management from aged people, patients, and even healthy people in daily life will increase. This social requirement also indicates that the medical-healthcare monitoring system that realizes the personalized life management of human society, is anticipated to be established through the mobile communication technology.

Fig. 1.3 a typical application mode of medical-healthcare system using Body Area Network (BAN) technology. The concept of BAN was firstly proposed by Zimmermann in 1995 [7]. IEEE 802.15.6 standard Task Group 6 (TG6) has provided the definition of BAN: A wireless communication network comprised of wearable and implantable sensor devices that operates in the area of human vicinity based on RF (radio frequency) technology [8]. In Fig. 1.3, the biotelemetry information of human such as EEG (Electroencephalogram) and ECG (Electrocardiogram) can be detected using body-attached vital sensor nodes or implantable medical devices. These medical information will be collected and delivered from access point to external terminals such as hospital or medical service center, using the cellular system. This mode reduces the work of medical staff, and improves the efficiency of healthcare management for the patients or aged people at home through the air.

Since the implantable medical application are related to some issues on security or moral principle in many countries, it still remains at a research level due to some legal limitations. On the contrary, wearable devices are always the most popular topic owing to various available applications based on the mature communication technologies of mobile terminals, such as handset and tablet.

So far, preliminary research of medical-healthcare system have been conducted in various fields, including medicine, biology, engineering, pharmacy, and even law. Such research data indicate that the medical-healthcare service system using mobile communication technology can reduce considerable medical expenses and labor costs. It also has a great potential to improve social medical insurance institution. The advanced core techniques in this system will lead an innovation of industrialization and commercialization of wearable medical applications that can support the development of industry standards and increase employment opportunities, simultaneously, and finally construct a social network comprised of numerous healthcare infrastructures.

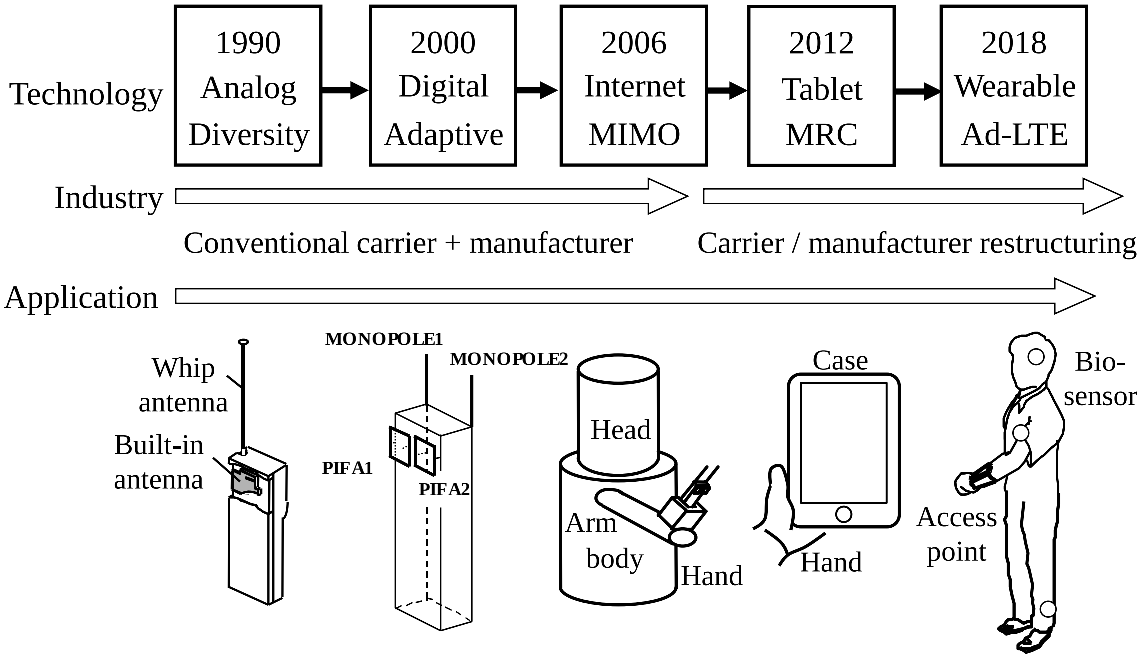

Fig. 1.1 History of mobile communication technology development

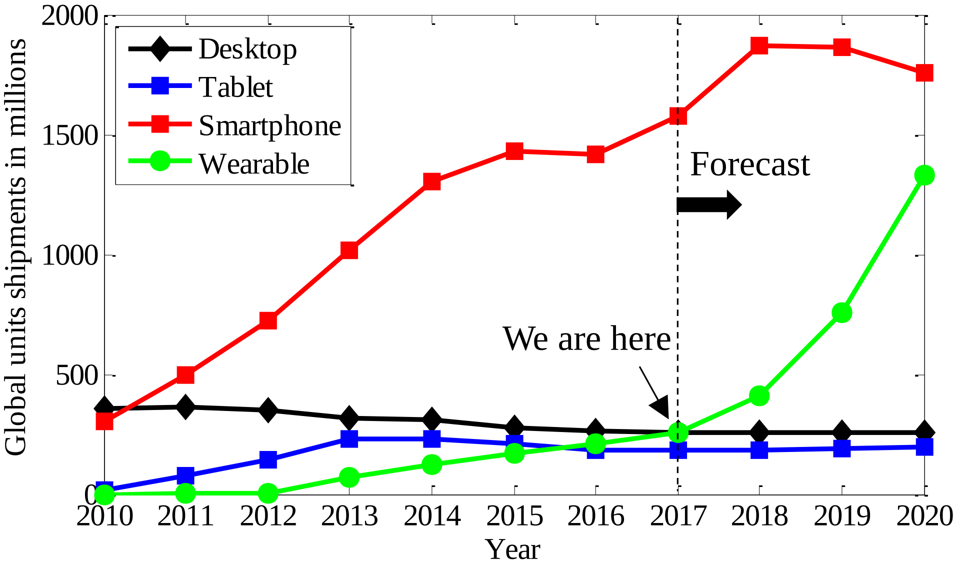

Fig. 1.2 Global unit shipments of electrical device from 2010s to 2020s

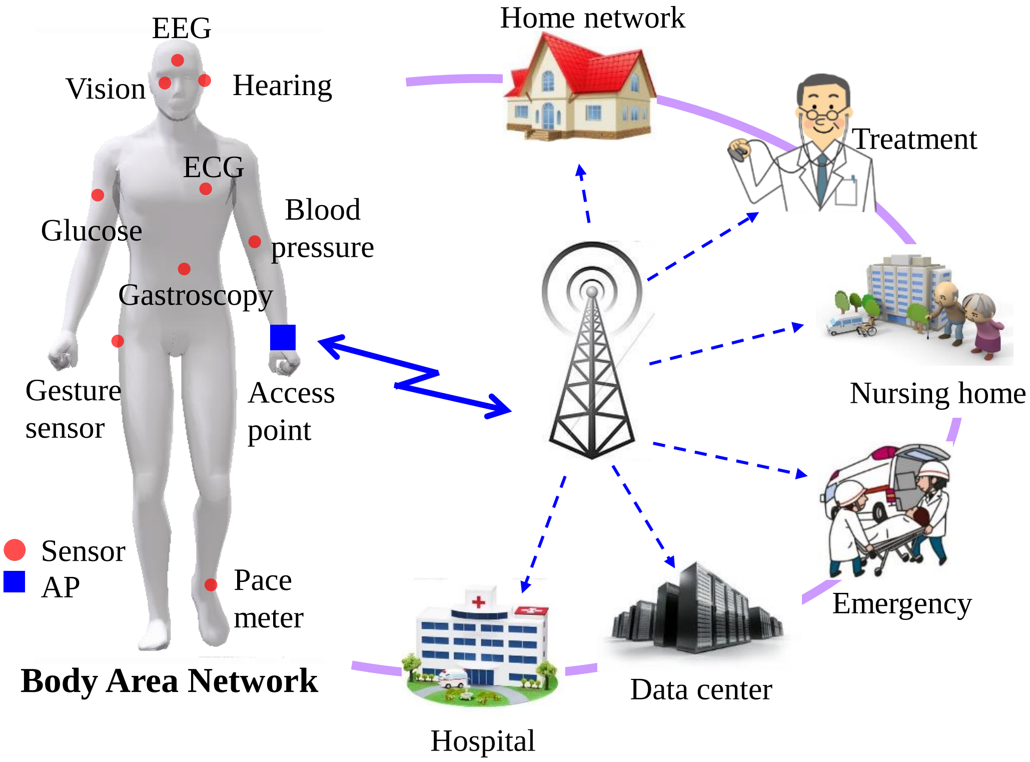

Fig. 1.3 Application mode of medical-healthcare system

1.1.2 Challenges in Wearable Antenna Assessment

In order to realize the mobile-healthcare wireless system, there are a lot of technical challenges in wearable BAN need to be solved. Especially in physical layer, how to design the appropriate antenna to fulfill the different wearable applications in various use scenarios is a significant subject.

Table 1.1 shows the communication system of wearable BAN radios. In general, wearable antenna in BAN applications is simply classified in three ways according to different antenna placement [9]: on-body; off-body; in-body. In on-body system, since both wearable devices are mounted on the same human body, efficient antenna design requires a good understanding of the properties of the propagation channel with human tissues and dynamic behavior involved. In off-body system, since the channel is off of the body and in the surrounding space, the antennas design should consider the shadowing effects of human body and multipath radio propagation environment. In in-body channel, major application area for this kind of communication is medical diagnostics and patient monitoring, where implantable medical devices, implanted transceivers are used for communicating with the outside world, are put inside the human body.

Due to a limited duration of PhD program, this thesis focus on the wearable antenna evaluation in on-body and off-body communication systems.

As shown in Table 1.1, in wearable BAN radios, at least one of the antenna is mounted on human body in either on-body or off-body situation. Thus, antenna engineers need to take human effects into consideration in channel modeling. In previous studies, P. S. Hall and Y. Hao have presented the on-body channel characterization for narrowband signal at 2.45 GHz [10], and path loss of each channel are given. Path gain for various paths and postures is also discussed in [11]. S. L. Cotton and W. G. Scanlon characterized and presented channel statistics for on-body in an indoor environment [12] [13]. All these studies highlight the evolving interest in on-body channel modeling to provide a guideline for wearable antenna design with high efficient performance. However, these investigations have been conducted in an anechoic chamber basis or field testing by propagation experiment, which ignored the important issue of multipath propagation environment in human vicinity. Moreover, less attention has been paid to the dynamic behaviors of human motion, which results in variation of on-body wireless link. For example, when the wearable antenna is located at a fluctuating place such as wrist, the arm-swinging motion will result in a polarization mismatch between two on-body antennas. On the contrary, when the antenna is attached at relative static place such as human torso, the arm-swinging motion will still cause the shadowing effects. All these conditions indicate that wearable antenna evaluation needs to consider the mutual interactions of the human property and the multipath effects in BAN use scenarios.

Fig. 1.4 (a) shows a propagation channel model of wearable antenna. It can be seen that the wearable antenna should be evaluated under a practical channel model in consideration of both the human dynamic motion and multipath propagation channel from surrounding objects. However, conducting the field tests in such as hospital room using actual test person has some drawbacks in terms of poor controllability and low accuracy, which will eventually degrades the development efficiency of wireless devices. Thus, in order to realize the equivalent level of radio wave propagation properties in BAN use scenarios, a reproducible evaluation system of antenna performance with high measurement accuracy instead of site specific field testing is strongly required. This evaluation device should include all the key factors of antenna, propagation, human body, and system, as shown in Fig. 1.4 (b).

Table 1.1 Physical layer: Antenna requirement in different BAN systems

System	On-Body	Off-Body	In-Body
Antenna location	Two or more devices mounted **on the same human body**	Devices on body with other devices **away from the human body**	Two or more devices **through the human body**
Core subject	Propagation channel properties with human dynamic behavior involved.	Shadowing effects of human body and multipath fading propagation environment	Electromagnetic characteristics of human tissue and electronic devices miniaturization

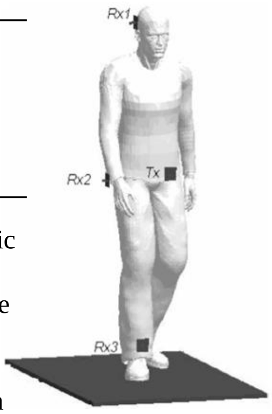

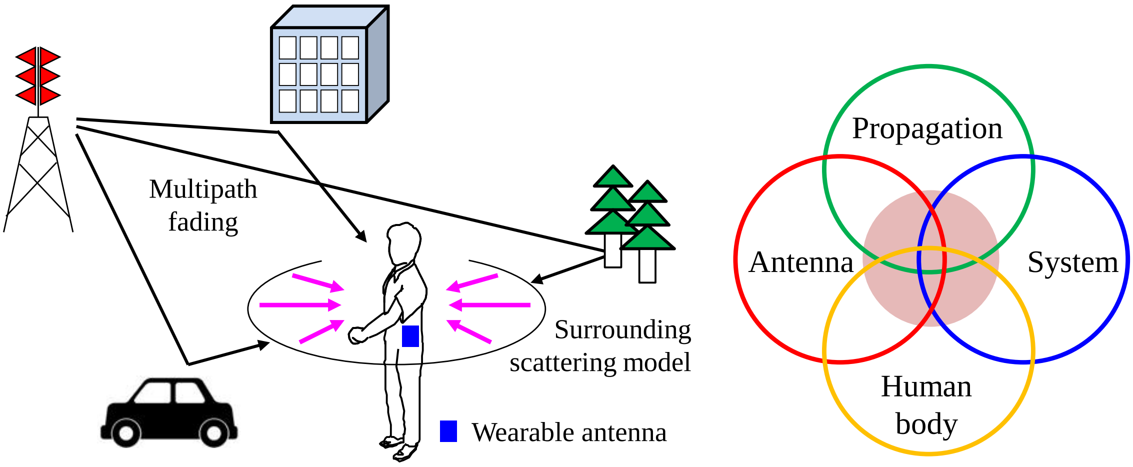

(a) Multipath propagation channel model (b) Key factors in BAN

Fig. 1.4 Core subjects in wearable antenna evaluation

1.1.3 What is Over-The-Air Testing

Over-The-Air Testing is a widely used method for the performance assessment of handset antenna [14]. Especially in multi-antenna terminals evaluation, such as MIMO, adaptive and diversity, OTA test was a very hot and popular topic since 2001s to 2010s. It has been standardized in both CTIA (International Association for the Wireless Telecommunication Industry) and 3rd Generation Partnership Project (3GPP) [15] [16]. The feature of OTA tests is that it is able to generate a fading propagation environment by varying time and spatial radio signals for evaluating complicated antenna performance in space, such as signal power, channel capacity, throughput or signal bit-error rate (BER) characteristics.

In general, OTA test methods have been classified into three categories: spatial fading emulator; reverberation chamber and two-stage method, as shown in Fig. 1. 5.

- Spatial fading emulator

  Fig. 1. 5 (a) shows the configuration of spatial fading emulator, which is developed by K. Ogawa and J. Takada in Panasonic and Tokyo Institute of Technology [17]. It is comprised of multiple antenna elements emulating the spatially distributed scatterers to generate the fading in a reproducible manner. The feature of spatial fading emulator with multi-probe configuration is in controlling the angular spread of incident waves and the XPR (cross-polarization power ratio), and in generating cluster and uniform spectra environments with considering the Doppler frequency.

- Reverberation chamber

  Fig. 1.5 (b) indicates the method of reverberation chamber invented by P. S. Kildal in Chalmers University of Technology [18]. In reverberation chamber, the DUT (device under test) antenna is located at the center of a metal box, where the emitted radio waves are completely reflected by the wall of metal box in random ways. The combination of different radio waves can create the desired radio wave probability distribution close to Rayleigh fading. The reverberation chamber examines a simple structure for an OTA apparatus at low cost but the poor controllability and repeatability because all of the reflected waves coming from one signal source are uncontrolled.

- Two stage method

  Fig. 1.5 (c) shows the two stage method [19]. In the first stage, the complex antenna radiation pattern of the DUT is measured in a traditional anechoic chamber. In the second stage, the measured radiation pattern will be convolved by a channel simulator with desired channel model to calculate the quasi-transmission properties such as channel capacity and throughput. The two-stage method can perform the required spatial channels with relatively low cost but more work on the concept verification is required for the practical setups.

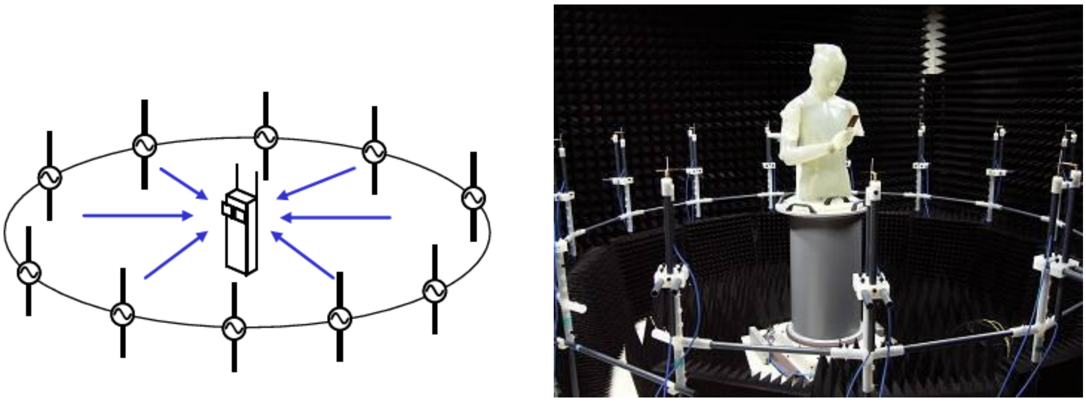

(a) Spatial fading emulator

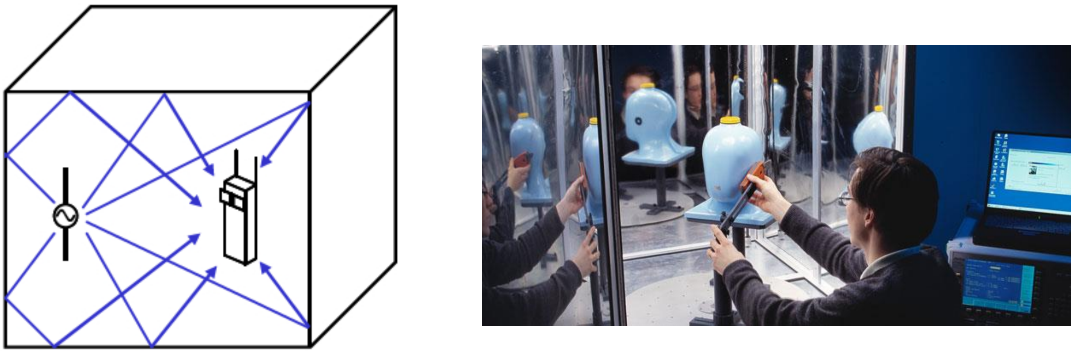

(b) Reverberation chamber

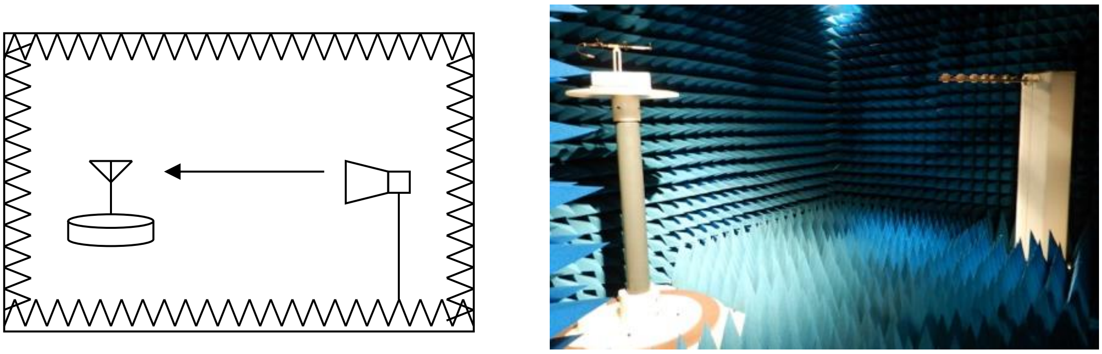

(c) Two stage method

Fig. 1.5 Typical approaches for over-the-air testing

In order to clarify the wearable antenna performance considering the influence of human-multipath mutual interactions, the control of incident wave with desired properties considering dynamic human motion is essential. Therefore, in this thesis, the method of spatial fading emulator is used as the OTA evaluation approach.

In terms of the spatial fading emulator, academic research in global leading institute are mainly contributed from Aalborg University (AAU) in Denmark, and Panasonic-Tokyo Institute of Technology in Japan. In AAU, Wei Fan with his supervisors G. F. Pedersen and J. Ø. Nielsen, have published many journals related to the measurement methodology using multi-probe fading emulator [20-24]. Their interests focus on the techniques to emulate 2D and 3D spatial channel models for MIMO-OTA testing, such as the realization of SCME (spatial channel model extended) models by setting probe weights. Also, the validity investigation of emulator such as test zone size, required number of probes and radiation pattern influence have been conducted. However, it seems that the evaluation of wearable applications are not included in their work.

In Japan, OTA test has been a hot topic for evaluation of multi-antenna handset terminals in fading environment since 2001s. In the early development, many approaches have been proposed for multipath fading generation. T. Ohira, and K. Gyoda proposed an ESPAR (electronically steerable passive array radiator) antenna as a spatial fading emulator [25]. This method was intended for simulating the multipath signal observed at the base station where the angular spread is relatively small [26], however, a strong coupling may occur due to the small physical size. C. Park has proposed CECA (cavity-excited circular array) using passive elements excited by radial cavity with center feeding, which overcome the proximity coupling in ESPAR antenna [27].

On the basis of these previous studies, it is concluded that it is better to feed the multiple antennas using the power divider together with the phase stretcher in the way of Jakes fading simulator. Since 2004s, Panasonic and Tokyo Institute of Technology has presented many papers related to a developed spatial fading emulator, with regards to the aspects of mobile terminal criterion such as diversity gain, BER performance and MIMO channel capacity [28-30]. Some related contributions were input to 3GPP and COST (European Cooperation in Science and Technology) for international standardization of this technology [31-37].

The above-mentioned work provided the research basis of OTA testing using spatial fading emulator. However, these studies have not involved the OTA assessment for wearable antenna in BAN system. Owing to different communication systems mentioned in Sect. 1.1.2, OTA testing methodology for wearable BAN radios should consider not only the emulation of the channel model in cellular system, but how to involve the mutual interactions of human and multipath influence. This is the core subject of this PhD thesis.

1.2 Aim of Work

The final goal of the study is to provide several OTA design methodologies for the performance evaluation of wearable antennas, taking the influence of human-multipath mutual interactions into account. The project is committed to construct a novel BAN-OTA evaluation system that is capable to realize both human dynamic behavior and multipath fading propagation environment.

Fig. 1.6 shows the OTA evaluation subjects for wearable BAN related to the configuration of this thesis. In addition to the trinity theory of mobile communication (antenna, propagation, system), this thesis involves the human body as another key impact factor, as shown in Fig. 1.4 (b). The main targets of the PhD project are listed and explained as follows.

- Application of weighted-polarization antenna for on-body channel (Chapter 2)

  In terms of the antenna, a weighted-polarization antenna has been developed, which is committed to improve the wireless communication quality in both off-body and on-body BAN use situations. My works aims at realizing the on-body wireless enhancement between two wearable terminals. The method focus on how to obtain the maximum received signal power considering the human dynamic motions that result in the variation of antenna rotation angle and polarization behavior.

- Development of fading emulator (Chapter 3)

  To evaluate the wearable antenna in general use scenarios with human and multipath effects involved, the first objective is to develop an actual device of spatial fading emulator, which is fundamental for all of the work in this PhD project. It is necessary to start from the basic model using radio wave synthesis principle, and the generation mechanism of multipath Rayleigh fading needs to be formulated. This will be applied to the actual device design and hardware implementation. After the OTA apparatus is manufactured, validity confirmation of Rayleigh fading is also needed.

- Rice on-body channel realization (Chapter 4)
  The Rice distribution is a specific nature to describe the BAN on-body propagation channel. To evaluate the wearable antenna in on-body communication system, the Rice factor defined as the power ratio of direct and reflected wave components must be implemented in a fading emulator using a calibration method in order to replicate an actual on-body channel in indoor propagation environment.

- 3D-OTA for 2D-arranged MIMO array (Chapter 5)
  Owing to an absence of uncorrelated incident waves in the elevation angles, two-dimensional cannot be applied to evaluate vertically-aligned multi-element antenna because of a unity correlation characteristic. Thus, a three-dimensional OTA test method that include the 3D incident wave properties needs to be developed for the assessment of vertically-arranged MIMO antenna.

- OTA method for BAN signal bit-error-rate (Chapter 6)
  In medical application, the signal bit error rate (BER) is generally

treated as a key index for evaluating an antenna's performance to ensure the high reliability and accuracy of medical data communication. Thus, an OTA measurement method for BER using commercial wireless module considering human shadowing and multipath fading effects are anticipated.

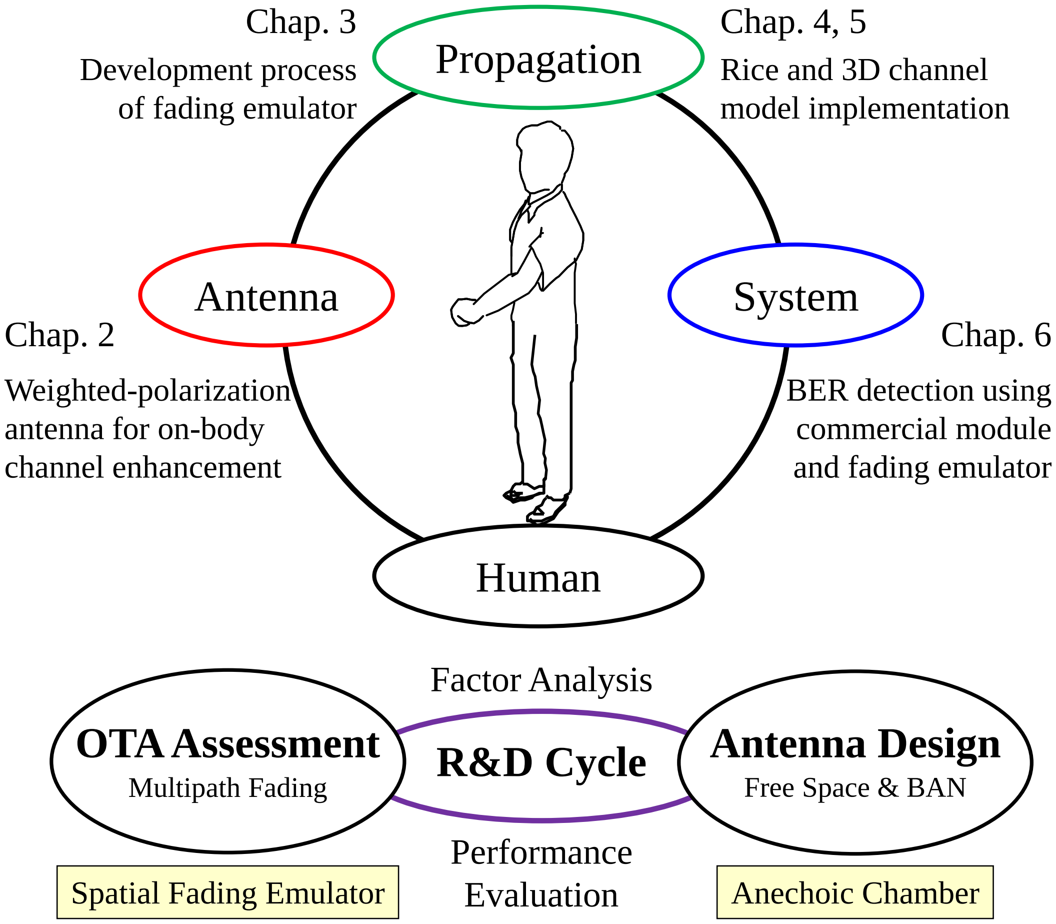

Fig. 1.6 OTA evaluation subjects for wearable BAN considering the harmonization of antenna, propagation, human body, and system

1.3 Related Funding

This thesis presents the OTA methodology for wearable antenna considering human and multipath combined influence. The research funding related to this PhD thesis is shown as below.

- JSPS KAHENHI (C)

  Research Title:

  A Study on the Development of a Fading Emulator for BAN Antenna Assessment

  Project Fiscal Year: 2013-04-01 – 2016-03-31

  Project / Area Number: 25420363

  Principal Investigator: Koichi Ogawa

  Collaborator: Kazuhiro Honda, Kun Li

  Relation with this thesis: This project provided a measurement instrument for wearable antenna assessment using the combined devices of human dynamic phantom and spatial fading emulator, as will be illustrated in Chapter 3. On the basis of the developed OTA apparatus, the experimental methodology of BAN on-body antenna considering the implementation of Rice factor, is illustrated in Chapter 4. Also, the developed fading emulator is utilized for signal BER measurement of BAN antennas in Chapter 6.

- SCOPE2013 PHASE I

  Research Title:

  Wrist-Mounted MIMO Array Antenna and OTA Assessment for Gigabit Channel Capacity by Adaptive Signal Processing Considering Human and Propagation Effects

Project Fiscal Year: 2013 – 2014

Grant Number: 135005102

Principal Investigator: Koichi Ogawa

Collaborator: Kazuhiro Honda

Relation with this thesis: The project supported the development of a multi-element weighted-polarization wearable antenna and the three-dimensional analytical channel model for this two-dimensionally arranged MIMO antenna array. The antenna design was included in Chapter 2 while the development of 3D fading emulator based on the analytical channel model will be mentioned in Chapter 5.

- SCOPE2014-2015 PHASE II

  Research Title:

  Wearable Antenna and OTA Assessment Considering Human Motion and Propagation Effects for MICT Network Establishment with Cooperation of Human and Social Infrastructure

  Grant Number: 145005101

  Principal Investigator: Koichi Ogawa

  Collaborator: Kazuhiro Honda, Yoshio Koyanagi, Hiroshi Sato, Ritsu Miura

  Project Fiscal Year: 2014 – 2015

  Budget Amount: 35,760,000 JPY

  Relation with this thesis: The project supported the development of the actual 3D fading emulator for the assessment of wearable MIMO antenna. Although, the content is not included in this thesis, it will be mentioned in Chapter 5 as a future work. In addition, an OTA measurement methodology for BER performance of wearable antenna considering combine shadowing-fading effects is conducted in this project, where a commercial FSK wireless module and a signal generator have been applied, as will be illustrated in Chapter 6.

The above-mentioned funding supported the most part of the researches conducted in this PhD program in Toyama University, and they also composed the configuration and contents of this thesis.

1.4 Layout of the Thesis

Fig. 1.7 shows the flowchart of this PhD thesis. It is composed of seven chapters. An overview of each chapter is given below.

Chapter 1 provides a brief preface of the entire thesis. The research background, aim of work, state of the art and layout of this thesis are illustrated, respectively.

Chapter 2 presents a weighted-polarization antenna applied to BAN on-body communication systems. The proposed antenna obtains an optimum signal level using a weight function considering the BP-XPR (Body Proximity Cross-Polarization Power Ratio) and antenna tilt angle. More than a 3-dB improvement of received signal power can be obtained by using the proposed method compared with the other types of antennas, regardless of the arm-swing motion and antenna placement, which verifies the effectiveness to enhance BAN on-body radio links. Moreover, an estimation method of BP-XPR using the three-dimensional radiation pattern of test antennas is proposed.

Chapter 3 shows a development process of spatial fading emulator. At first, the radio wave synthesis principle based on a simple analytical model is analyzed, which is utilized to clarify the generation mechanism of multipath Rayleigh fading. The actual device is developed by implementing these formulations. The design details of the fading emulator in both channel model and hardware manufacture have been conducted while the Rayleigh fading generation in the actual OTA device is confirmed.

Chapter 4 presents a preliminary experiment for realizing a Rice on-body channel in BAN-OTA testing using a fading emulator with a dynamic phantom. Using a calibration method, the appropriate Rice-factor that represents the actual propagation environment indoors, is implemented into a fading emulator. This work indicates that the developed fading emulator allows BAN-OTA testing to replicate the actual on-body propagation channel with the consideration of dynamic characteristics of human walking motion.

Chapter 5 presents a three-dimensional analytical channel model for vertically arranged MIMO array antennas. Particular emphasis is placed on how well handset MIMO antennas with a vertically arranged structure are characterized using the limited number of scatterers implemented in a fading emulator. Based on an analytical channel model, a suitable scatterers arrangement is determined for various conditions of multipath environments and numbers of array elements, and the arrangement can be employed for designing an actual three-dimensional OTA apparatus.

Chapter 6 presents an OTA experimental methodology to evaluate the BER characteristics of wearable antennas. A commercial FSK (frequency shift keying) wireless module is applied in the experiment. A dual-discrete control method to detect an instantaneous BER using a fading emulator with a dynamic human phantom is proposed. This proposal can replicate a realistic arm-shadowed fading channel with both instantaneous and average BER characteristics considering the dynamic BAN channel and multipath effects.

Chapter 7 summarizes some important conclusions derived from this thesis while Chapter 8 gives some possible future extension of the study.

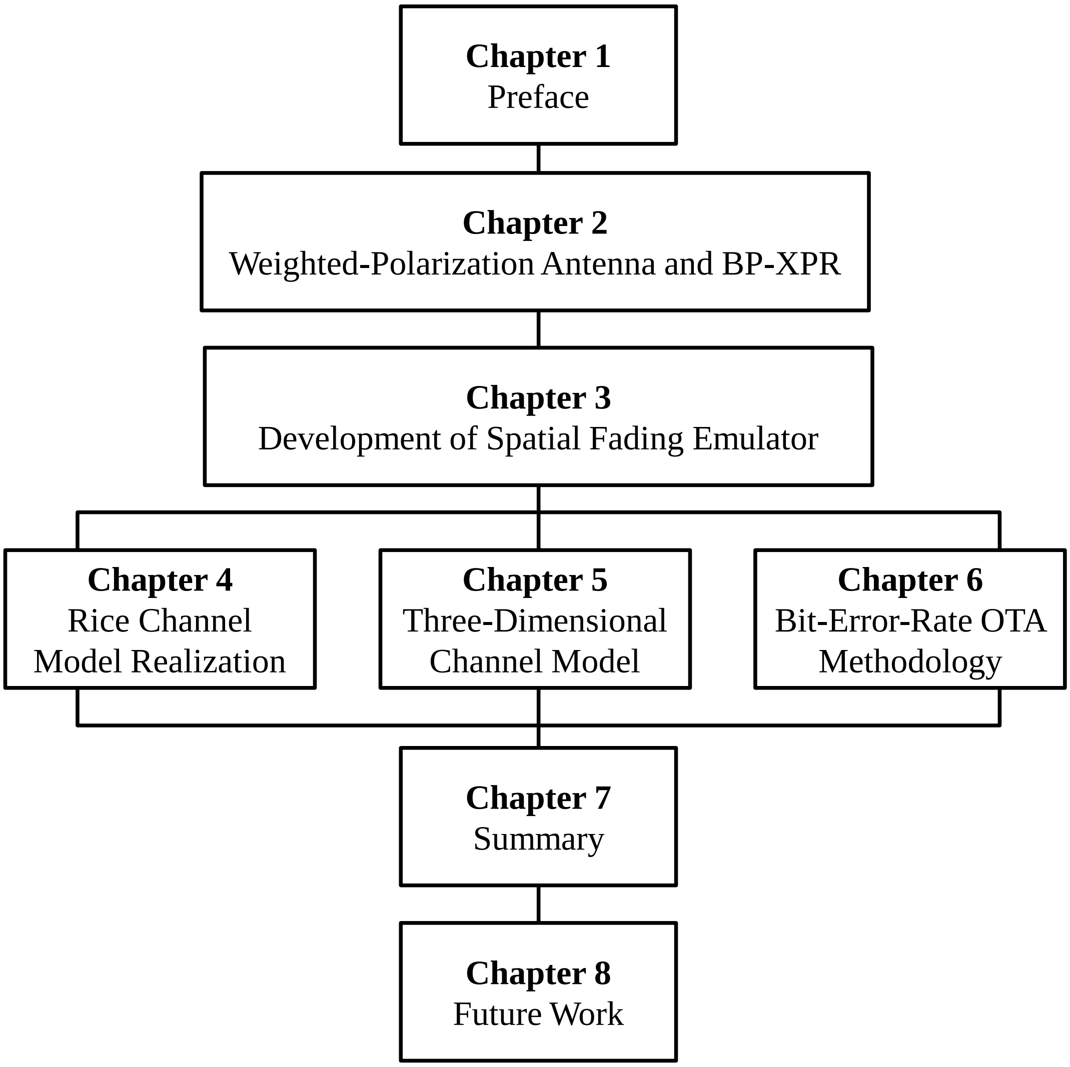

Fig. 1.7 Layout of this thesis

2. Weighted-Polarization Antenna and BP-XPR

2.1 Introduction

To realize the high reliability communication in dynamic BAN on-body channels, the enhancement of wireless connectivity between the wearable devices is an essential subject [38] [39].

Weighted-polarization wearable MIMO antenna [40] was proposed for upcoming 5G cellular systems. The concept of this antenna (see Fig. 1 in [40]) is aimed at realizing the high channel capacity in various conditions based on RF signal processing, where the cross polarization power ratio (XPR) and antenna inclination angle are considered as key parameters of obtaining the optimum weight functions. Using this method, high channel capacity can be obtained in both uplink and downlink channels between the base station and mobile terminal, without using the feedback from the received signal.

On the basis of this concept, in this work, I extend the application from off-body to on-body system. As shown in Fig. 2.1, the on-body channel indicates that the incident wave coming from sensor to access point, is totally different from the propagation mechanism compared with that in off-body cellular system. The most different point is that the polarization behavior is a time-variant value caused by the dynamic human motion and different wearable antenna placements, which may result in a severe variation of transmitting and receiving signal level [41] [42].

This study presents a weighted-polarization antenna applied to BAN on-body systems. A novel concept of the BP-XPR (Body Proximity Cross-

Polarization Power Ratio) [43] is proposed, which is quantified based on antenna locations and arm-swing angles. Using the BP-XPR, the weighted-polarization antenna achieves a high and stable signal power regardless of arm-swing motion and antenna placement, indicating that the proposed antenna is suitable for realizing a high reliable communication in future wearable BAN radio systems. Furthermore, an simple estimation method of BP-XPR using the three-dimensional radiation pattern of test antennas is proposed.

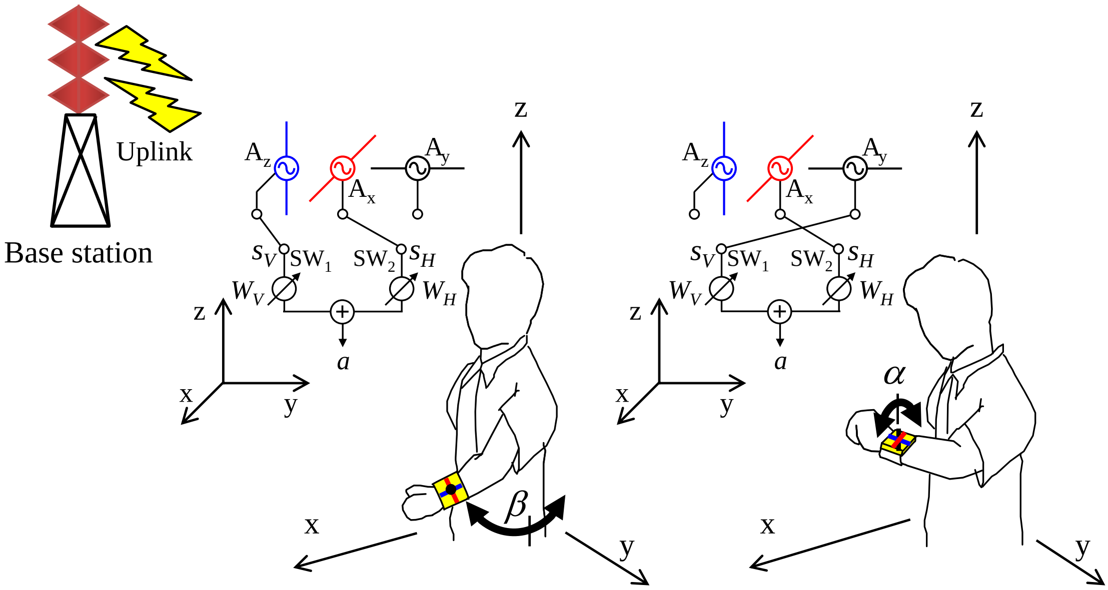

(a) Off-body channel

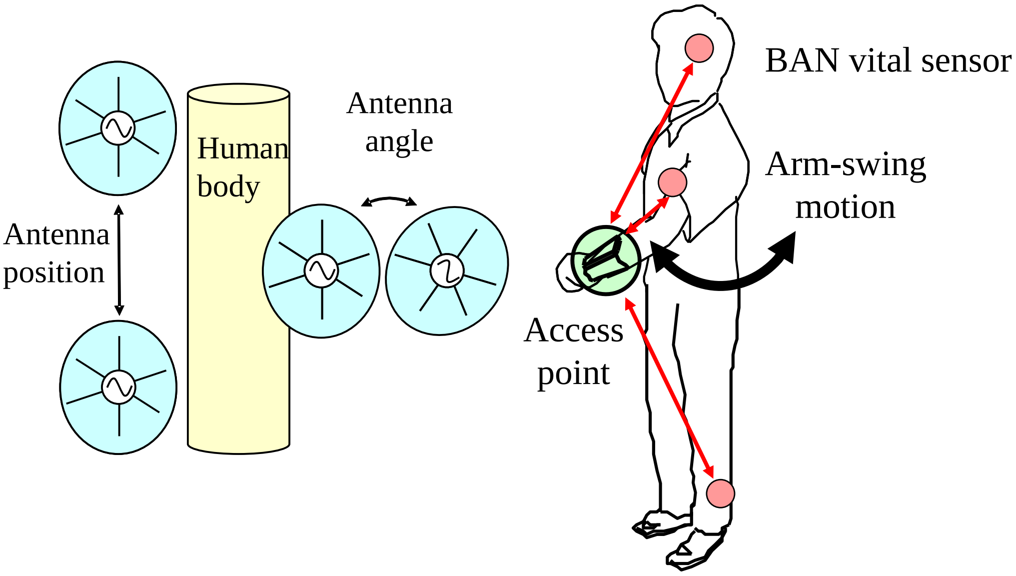

(a) On-body channel

Fig. 2.1 Difference between the usages of weighted-polarization antenna in off-body and on-body channels

2.2 Weighted-Polarization Antenna in Dynamic On-Body Channel

Fig. 2.2 (a) shows the channel model of a dynamic phantom [38] from the view of zx-plane. α denotes the arm-swing angle, which represents the antenna rotation angle simultaneously while β indicates the angle between z-axis and incident wave direction. The sensor modules are mounted on head and ankle while the access point is fixed at wrist. The received signal at wrist is decomposed into vertical and horizontal polarization components allocated in z-axis and x-axis respectively, as indicated by V-pol and H-pol. With different sensor antenna locations and arm-swing angles, the received power is changed whether the dipole A_z or A_x is used. Thus, the polarization controlled antenna for on-body link enhancement is desired.

Fig. 2.2 (b) indicates the configuration of a weighted-polarization antenna [40], which is comprised of three orthogonal dipole elements (A_x, A_y, A_z). When the antenna is rotated by an operator, two of the three dipole elements are selected using two switches (SW_1, SW_2). The received signals (s_V, s_H) are combined using the weight functions (W_V, W_H) created based on the variations in XPR and antenna inclination angle (α). The output signal is expressed as:

$$a = W_V s_V + W_H s_H e^{j\frac{\pi}{2}} \tag{2.1}$$

$$W_V = \left(\sqrt{\frac{XPR}{1+XPR}} |\cos\alpha| + \sqrt{\frac{1}{1+XPR}} |\sin\alpha| \right) \tag{2.2}$$

$$W_H = \left(\sqrt{\frac{XPR}{1+XPR}} |\sin\alpha| + \sqrt{\frac{1}{1+XPR}} |\cos\alpha| \right) \tag{2.3}$$

The derivation of weight function is illustrated in [40] in details. Since the antenna is utilized for on-body links, the value of XPR in Eqs. (2.2) and (2.3) is defined as BP-XPR (Body Proximity Cross-Polarization Power Ratio) [43] for describing the cross-polarization properties in on-body channel.

The general concept of XPR in a cellular system is proposed by T. Taga in 1990s [44]. It is defined as the power ratio between the mean incident powers of the vertically and horizontally polarized incident radio waves received while the antenna moves in the environment, averaged over a random route in a multipath environment. However, in the BAN on-body situation, two main reasons make it impossible to apply the common definition of XPR in cellular system, as shown below.

- Dynamic propagation channel caused by time-varied human motion
- RF performance degradation of both wearable Tx and Rx antenna

The above-mentioned features indicate that the XPR for on-body propagation is not a concept of average value in a certain sampling process, but a time-varied physical quantity determined by the instantaneous behavior human dynamic motion. This is the most specific aspect of on-body communication distinguished with the general cellular system. Therefore, the novel concept of BP-XPR, which aimed at describing the polarization nature of body proximity radio wave propagation, is applied to weighted-polarization on-body antenna, as will be illustrated in Sect. 2.3.

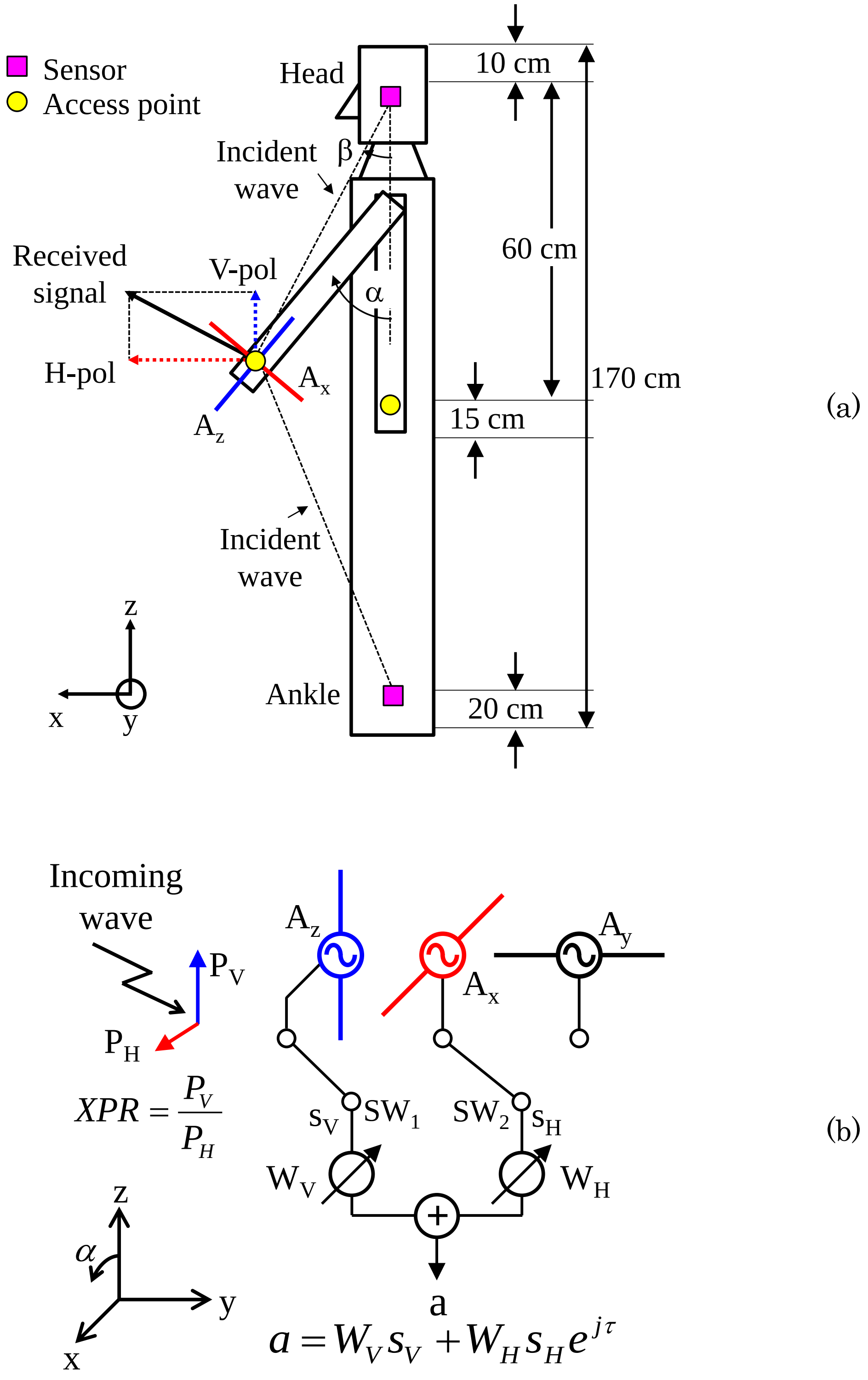

Fig. 2.2 Human on-body channel (a) Arm-swing dynamic phantom, (b) Weighted-polarization antenna

2.3 Anaytical Model

Figs. 2.3 shows the analytical model generated by the commercial EM solver FEKO [45]. The phantom has a height of 170 cm, where the homogeneous phantom is made of the dielectric properties of average muscle tissue, i.e., relative dielectric constant $\varepsilon_r = 55.8$ and conductivity $\sigma = 0.99$ S/m at 950 MHz [38].

In the transmitting side, a turn-style antenna is used as a sensor, which is comprised of two orthogonally-aligned half-wavelength dipoles with 90° out-of-phase excitation. Owing to its nearly omnidirectional radiation pattern with θ-polarization in the zx-plane shown in Figs. 2.3 (a-1) and 2.3 (b-1), the effects of the cross-polarization properties on the radiation patterns are eliminated.

Moreover, in the receiving side in Fig. 2.3 (a-2), vertical and horizontal dipoles along with z-axis and x-axis, are used at wrist for measuring the distributed polarization components V-pol and H-pol, as shown in Fig. 2.2 (a). Using the measured data, the BP-XPR of an incident wave is expressed as follows.

$$BP - XPR = \frac{P_V}{P_H} \tag{2.4}$$

where P_V and P_H indicate the received power in the link budget calculation using the vertical and horizontal dipole antennas, respectively.

Further, the weighted-polarization antenna shown in Fig. 2.2 (b), is applied considering the variation of BP-XPR and α caused by human motion. Here, the elements of A_z and A_x are selected, as shown in Fig. 2.3 (b-2), which are controlled using weight functions defined by Eqs. (2.2) and (2.3).

The left arm moved in the forward direction is varied from 0° to 90° while the backward situation is not investigated because the phantom has a symmetrical configuration. The separation between the antenna feed point and body surface is 3 cm. The simulation frequency is 950 MHz.

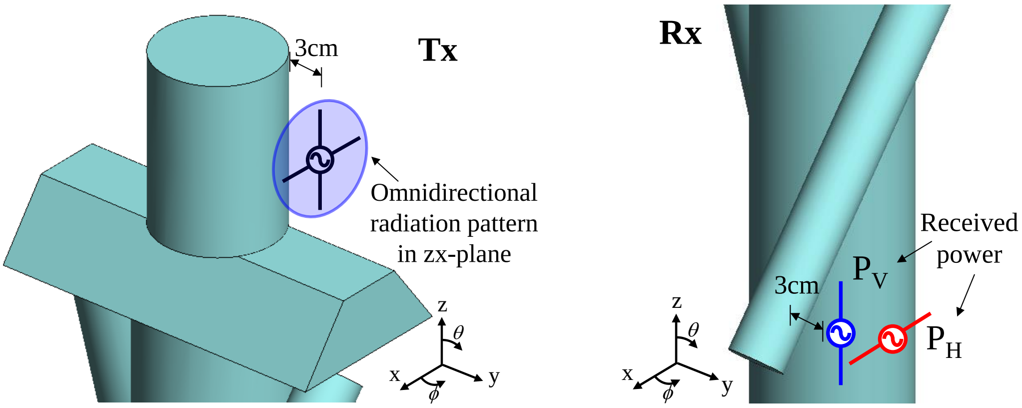

(a-1) Turn-style antenna (a-2) Vertical and Horizontal dipoles

(a) Analysis of BP-XPR

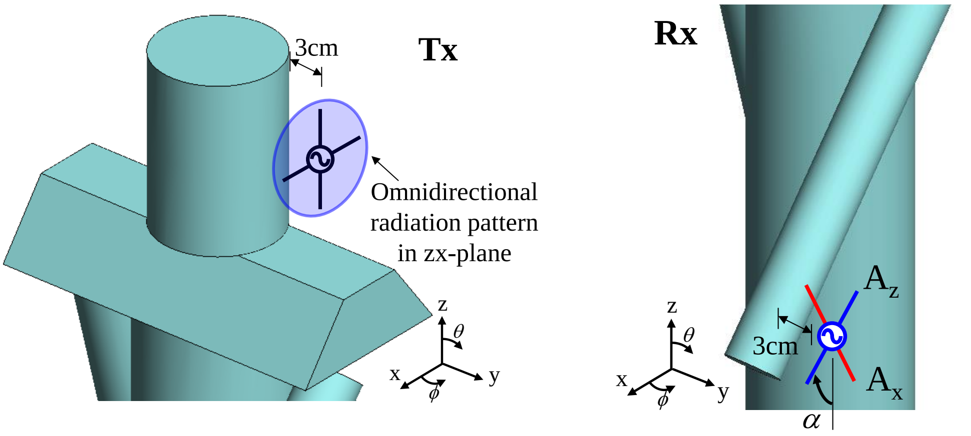

(b-1) Turn-style antenna (b-2) Weighted-polarization antenna

(b) Analysis of received signal power

Fig. 2.3 Analytical model using arm-swing phantom

2.4 Simulation Results

Fig. 2.4 shows the BP-XPR as a function of the arm-swing angle from 0° to 90° in head and ankle to wrist on-body channels, corresponding to Fig. 2.2 (a). In Fig. 2.4, BP-XPR varies obviously over 15 dB in each case occurs. When the antenna location is moved, a large difference of two curves is observed, indicating that the BP-XPR for on-body channel needs to be measured using Eq. (2.4) on a case-by-case basis, which is significantly different from the XPR in weight functions used for a MIMO antenna fixed at a certain on-body location when a specific use scenario is considered [40].

Fig. 2.5 shows the weight function (W_V, W_H) calculated by Eqs. (2.2) and (2.3) using the BP-XPR and α. Note that the weight functions of vertical and horizontal polarization components exchange at the position of $\alpha = 45°$. Based on these values, a simulation using the weighted-polarization antenna for on-body link enhancement is conducted.

Fig. 2.6 shows the results of radiation characteristics in zx-plane. The left arm is changed as $\alpha = 0°$, 40° and 90°, as shown in Figs. 2.6 (a-1) to (c-1). Figs. 2.6 (a-2) to (c-2) indicate the radiation patterns when the weighted-polarization antenna is used while Figs. 2.6 (a-3) to (c-3) indicate the results of the vertical dipole (A_z). The black markers ● indicate the radiation gain in the direction of incident waves (denoted by pink arrows), which determine the received power. In Figs. 2.6 (a-2) to (c-2), the weighted-polarization antenna achieves the strong gains of −0.6 dBd, −4.1 dBd and −4.9 dBd, respectively. However, using the vertical dipole (A_z), the incident wave approaches the null position, leading to the significant reduction in radiation gains of −15.4 dBd, −16.9 dBd and −10.4 dBd, as shown in Figs. 2.6 (a-3) to (c-3).

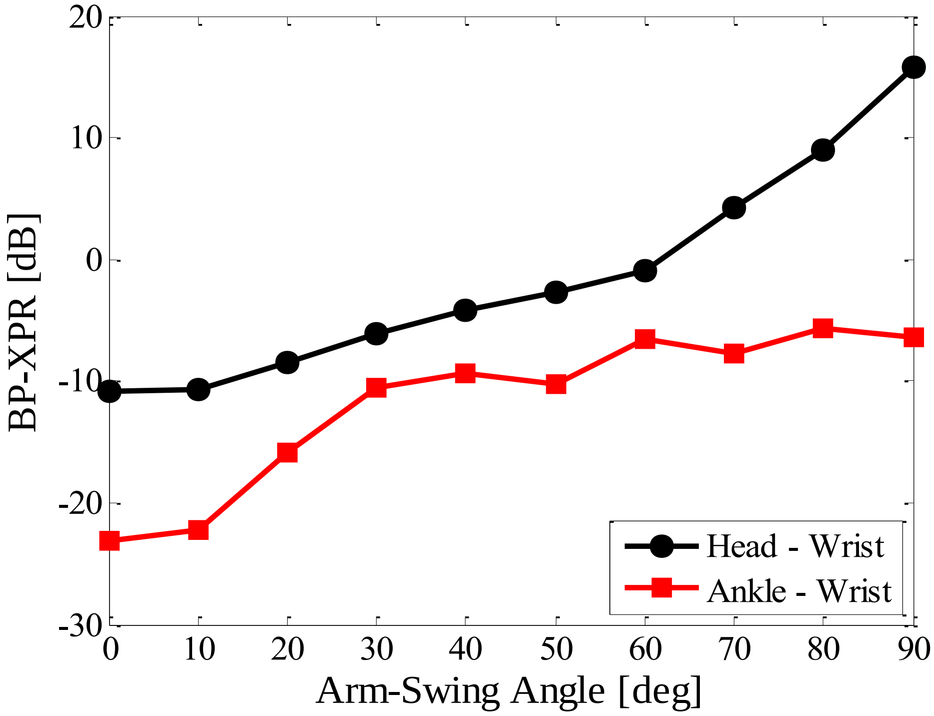

Fig. 2.4 BP-XPR vs. Arm-swing angle

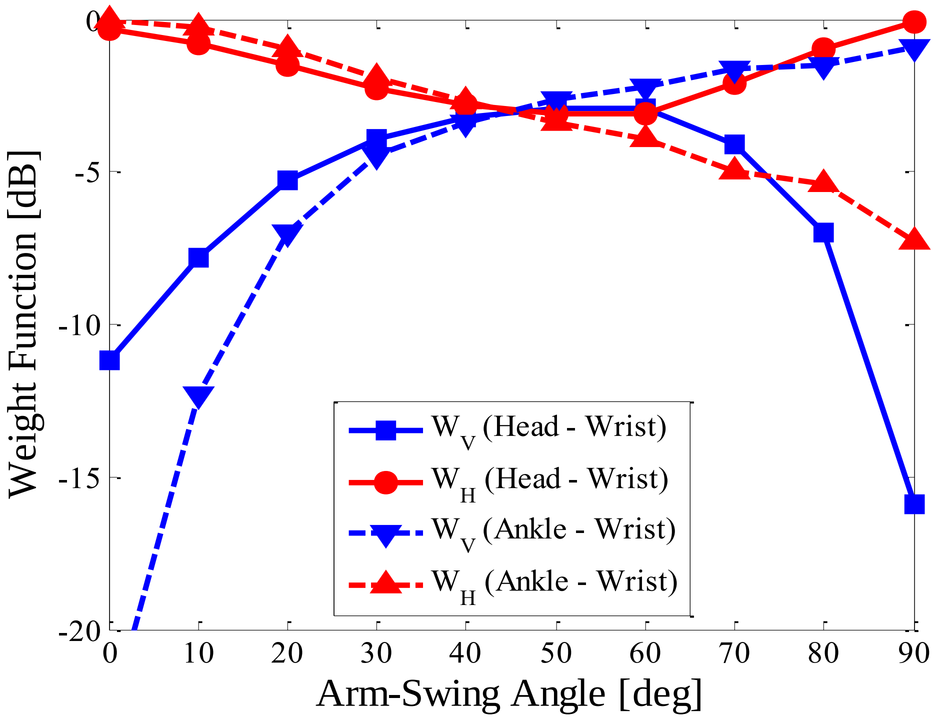

Fig. 2.5 Weight function vs. Arm-swing angle

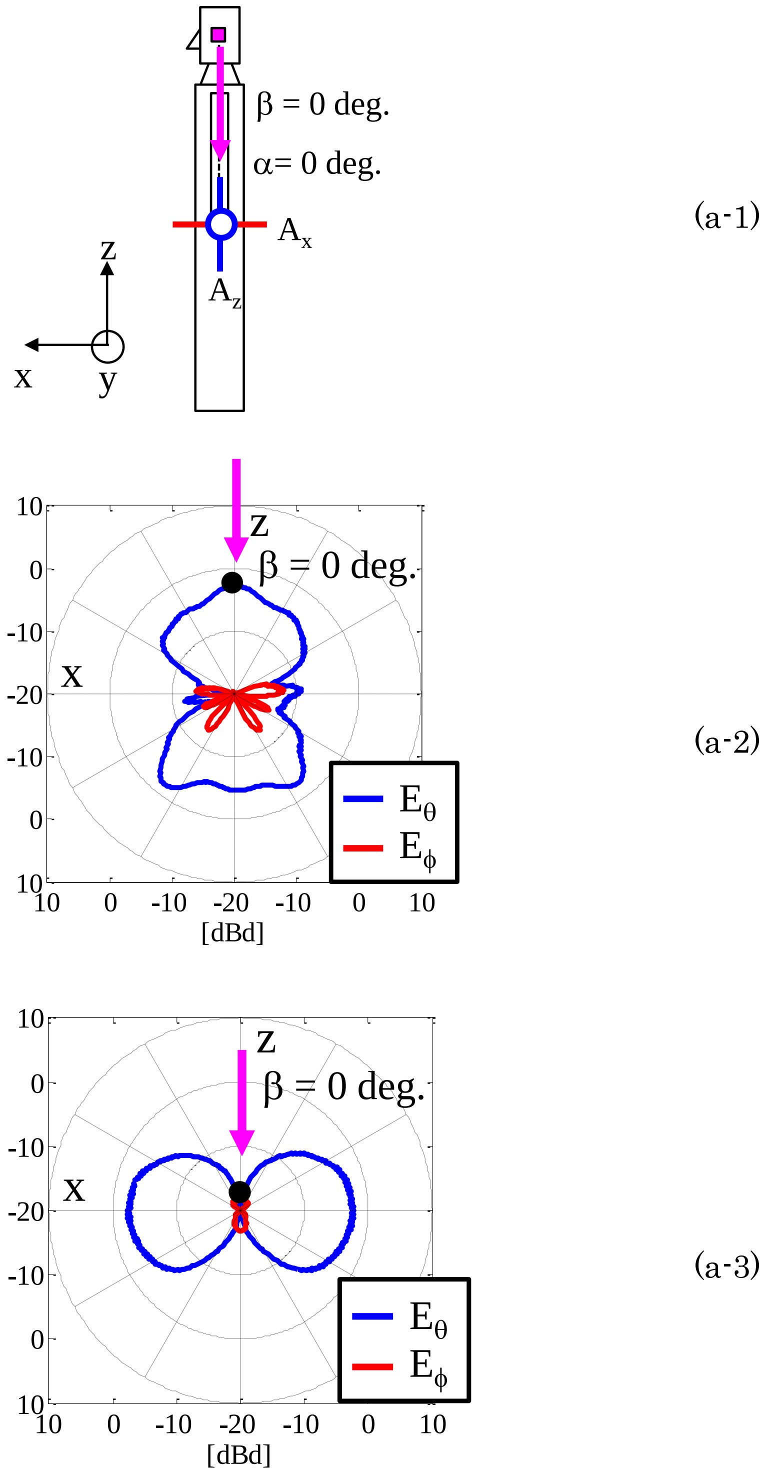

(a) α = 0 deg

Fig. 2.6 Simulated results of radiation characteristic

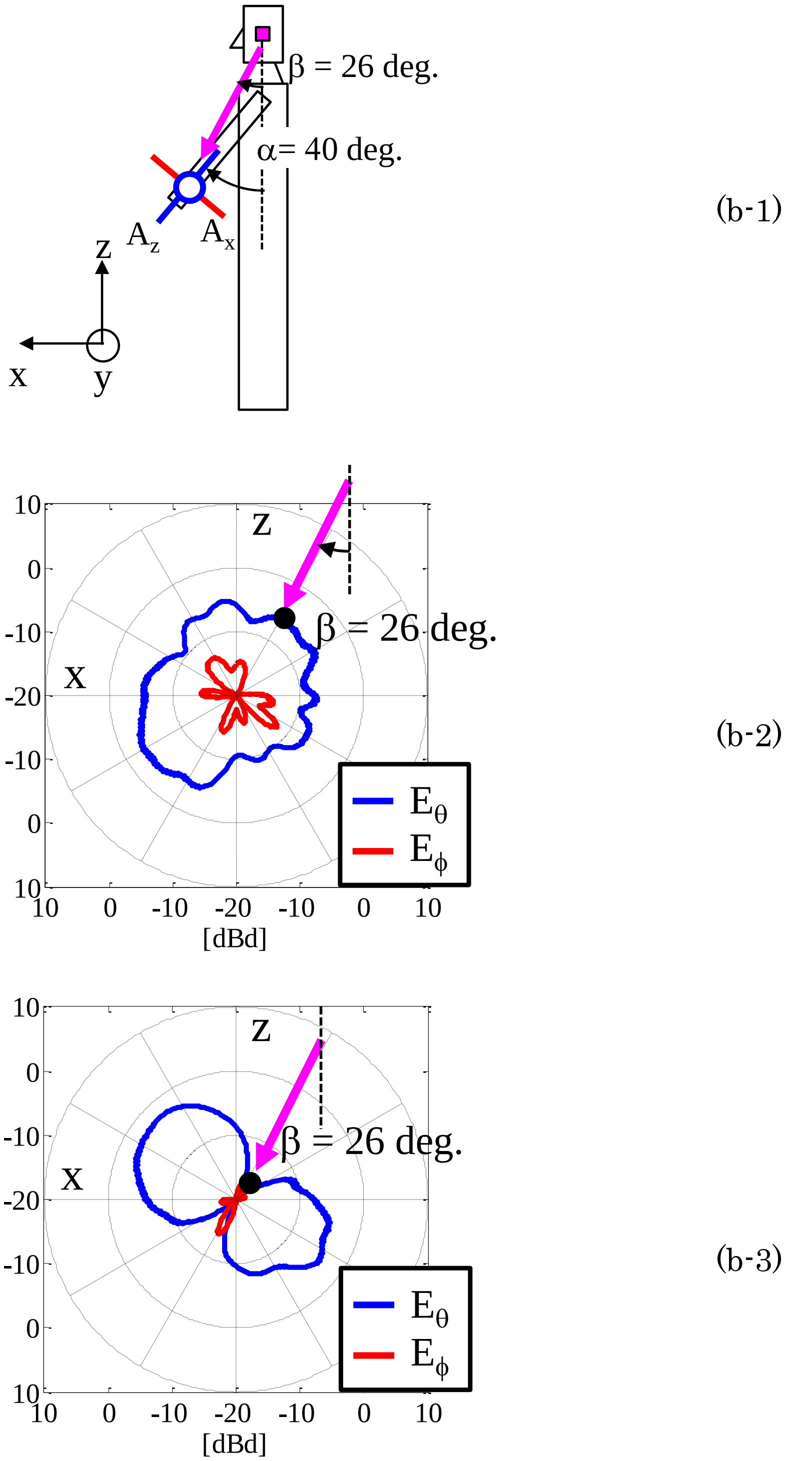

(b) α = 40 deg

Fig. 2.6 Simulated results of radiation characteristic

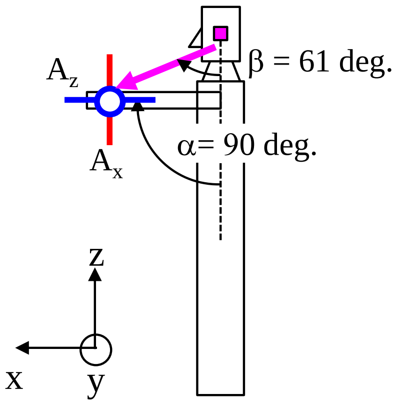

(c-1)

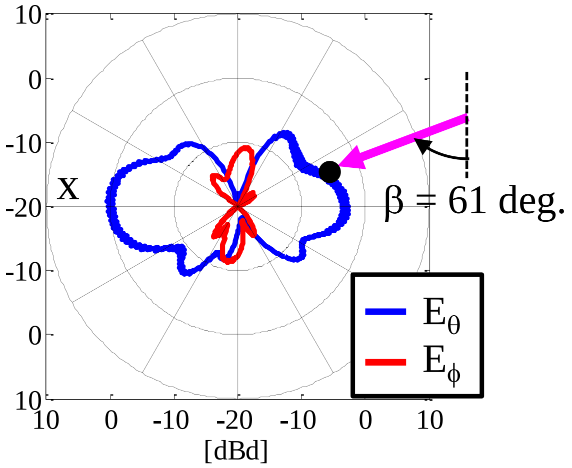

(c-2)

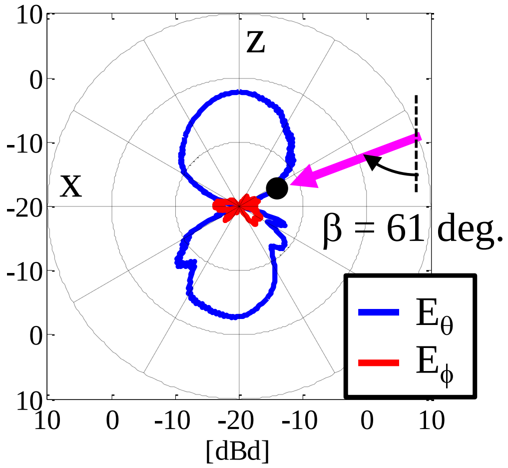

(c-3)

(c) α = 90 deg

Fig. 2.6 Simulated results of radiation characteristic

Fig. 2.7 indicate the received power normalized to that of an isotropic antenna, as a function of α varied from 0 to 90°. The free space propagation loss is included in the calculation. The curves with symbols ●, ■, ▲ and ▼ denote the results of four cases: the weighted-polarization antenna; the vertical dipole antenna (A_z); the horizontal dipole antenna (A_x), and the equal weight combined antenna ($W_V = W_H = 1/\sqrt{2}$), respectively.

In Fig. 2.7 (a), when the sensor antenna is located at head, the vertical dipole A_z gives a poor performance due to the absence of radiation gain in the direction of incident waves, as shown in Fig. 2.6. Fig. 2.7 (a) also shows that the horizontal dipole A_x provides a high received power owing to the benefit of radiation gain. In contrast to Fig. 2.7 (a), Fig. 2.7 (b) shows that there is a tradeoff behavior in the received power between the vertical and horizontal dipoles; the vertical dipole exhibits a low received signal power when α is less than 30° and a high received signal power when α is larger than 30°, and vice versa for the horizontal dipole. However, in Fig. 2.7, the weighted-polarization antenna can achieve a high and stable received power without regard to the antenna placement when the α is changed.

Further, Fig. 2.7 show that the received power of the equal weight combined antenna degrades at 0° and 90° compared with that of the proposed antenna because only vertical and horizontal polarization components with equal amplitude is utilized, resulting in a 3 dB enhancement when the proposed antenna is used. Moreover, the received power of the proposed antenna and equal weight antenna agrees with each other when α equals approximately 45°. The reason is that, as shown in Fig. 2.5, the same value of weight function ($W_V = W_H = -3$ dB) is produced at $\alpha = 45°$ for both cases even when the BP-XPR in Fig. 2.4 is varied significantly.

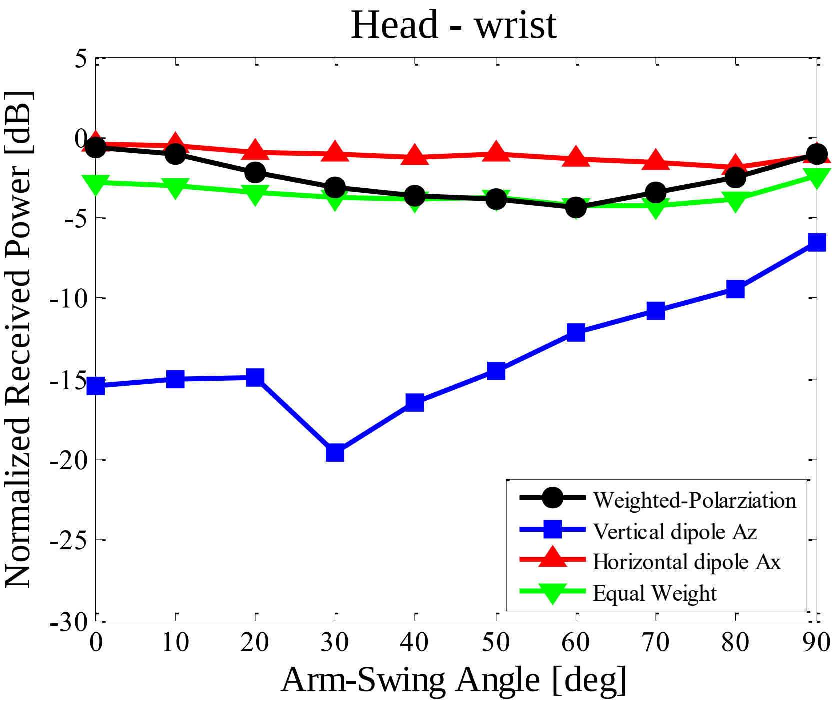

(a)

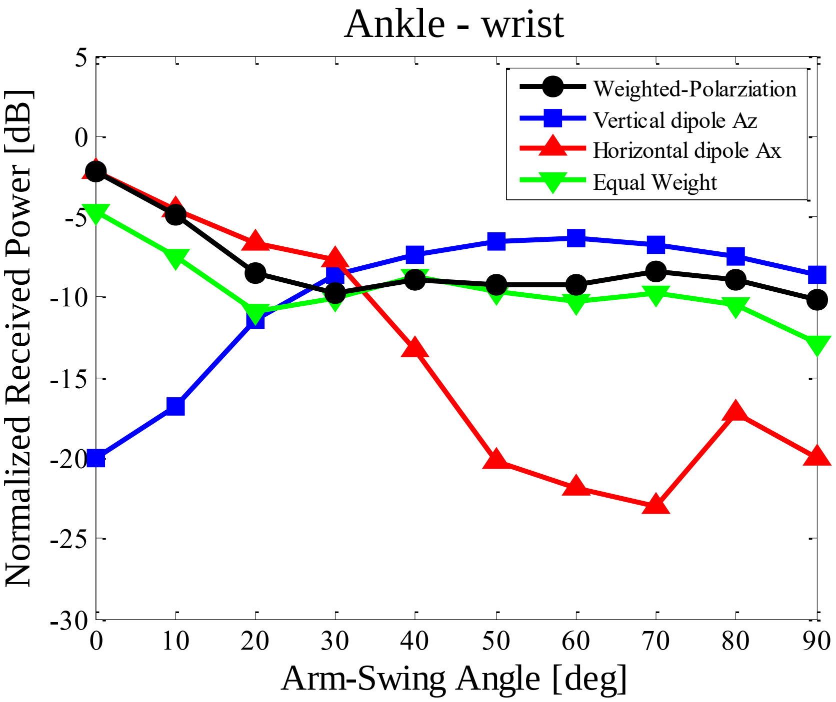

(b)

Fig. 2.7 Received power vs. arm-swing angle

(a) Head-wrist (b) Ankle-wrist

It is concluded from the abovementioned considerations that the proposed antenna achieves a high and stable received power compared with the other types of antenna, confirming the effectiveness of proposed weighted-polarization antenna, which is anticipated to be applied to future wearable BAN systems.

2.5 Estimation of BP-XPR

As mentioned in Sect. 2.4, since the proposed value of BP-XPR for on-body channel needs to be measured using Eq. (2.4) case-by-case, an estimation method for describing the polarization properties around the complicated human body is anticipated. As shown in Eq. (2.4), the received power (P_V and P_H) using the vertical and horizontal dipole antennas include the radiation gain of test antenna affected by human body effects. Thus, a simple method for estimating the value of BP-XPR is proposed as following equation

$$BP - XPR_{3D} = \frac{G_V(\theta,\phi)}{G_H(\theta,\phi)} \tag{2.5}$$

where $G_V(\theta,\phi)$ and $G_H(\theta,\phi)$ indicate the three-dimensional radiation gain of vertical and horizontal dipoles, respectively, according to the incident wave direction from various locations of sensor antennas. To verify the validity of Eq. (2.5), an EM simulation using the actual human body is carried out.

Fig. 2.8 (a) shows the analytical model of the human phantom, which is derived from an animation software, POSER [46]. The phantom is a male with a height of 170 cm, which is homogeneous made of the dielectric properties of average muscle tissue, i.e., relative dielectric constant $\varepsilon_r = 54.2$ and $\sigma = 1.51$ S/m at 2 GHz [47]. The sensor antenna is located at left head and left foot while the access point is mounted on left wrist.

The BP-XPR is applied to the weighted-polarization antenna [40]. The weighted-polarization antenna uses the antenna elements when the polarization of received signal is varied caused by antenna inclination. In Fig. 2.8 (a), since the antenna parallel to y-axis always receive the E_ϕ polarization component, this element is not selected.

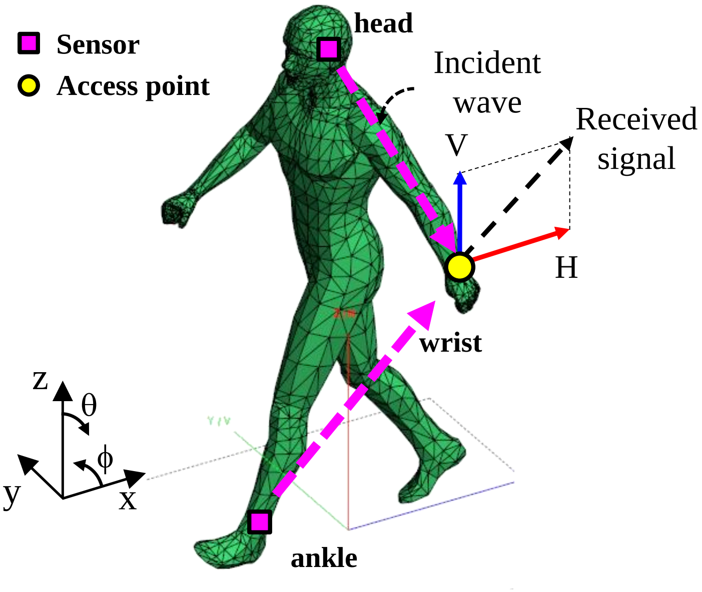

(a) Polarization distribution

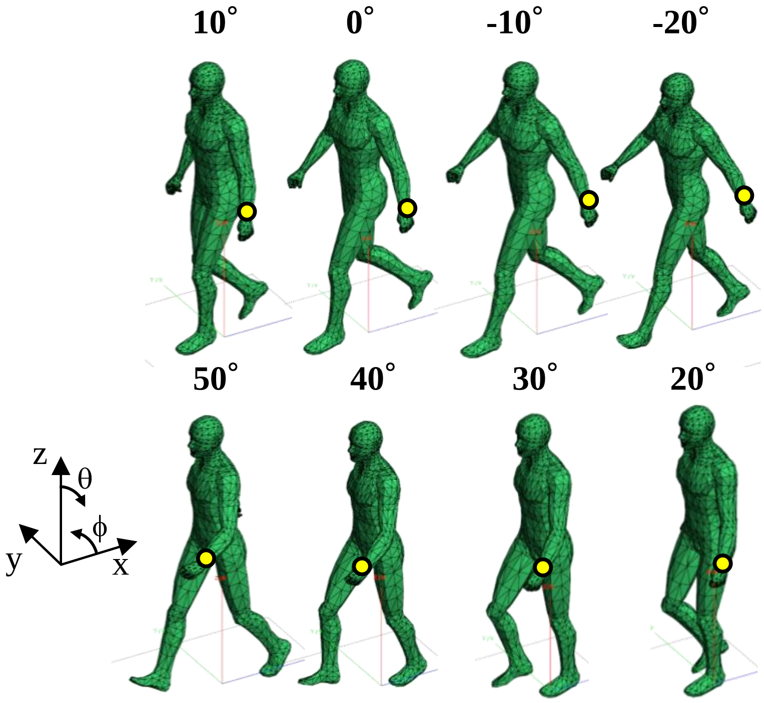

(b) Walking frames

Fig. 2.8 Human walking model

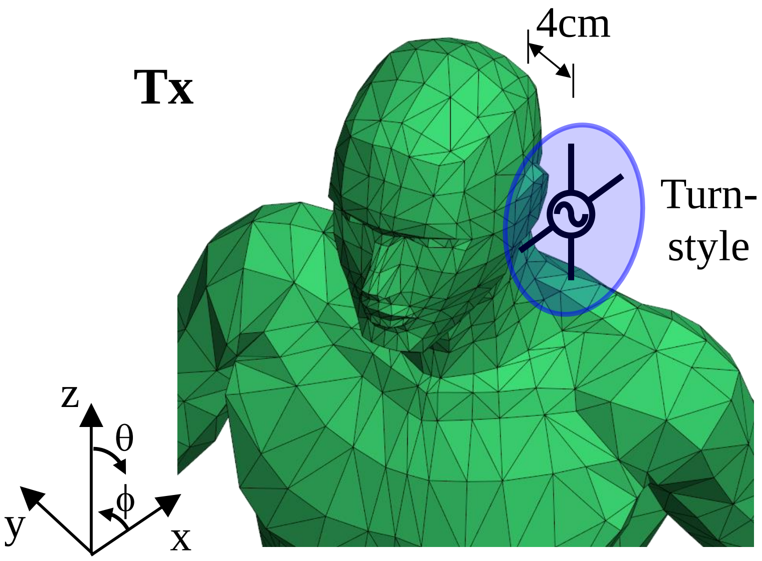

(c) Turn-style antenna at head

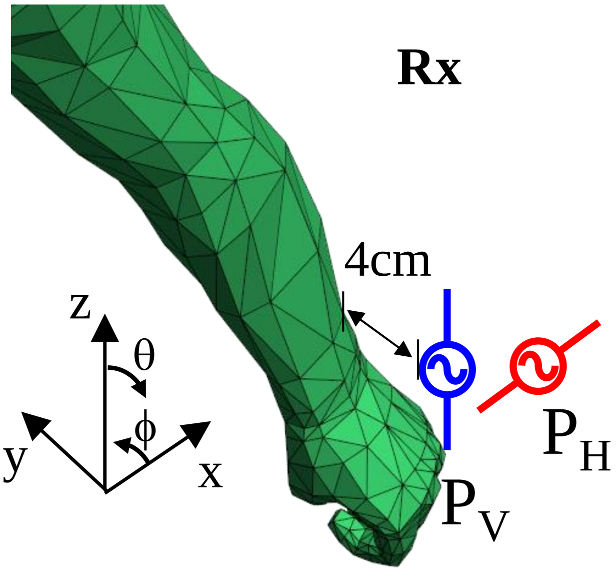

(d) Dipoles for measuring BP-XPR

Fig. 2.8 Human walking model

Fig. 2.8 (b) shows the a series of walking postures of the human model separated from frame 1 to 8. Each frame indicates the instantaneous arm-swing angle from –20° to 50° at 10° intervals, which represents a normal arm-swing angular range in a walking situation [48], where the arm-swinging angle is defined as the angle of a line that connects the wrist and the elbow with respect to the vertical direction.

In Fig. 2.8 (c), a turn-style antenna comprised of two orthogonally-aligned half-wavelength dipole antennas at 2 GHz with 90° out-of-phase excitation is used as a sensor module. This is because it has nearly omnidirectional radiation pattern with θ-polarization in the antenna operating plane, which can eliminate the effects on the cross-polarization properties caused by the radiation patterns, leading to the identical transmitting ability against to any angles of incident waves in the zx-plane. In the receiving side at wrist, as shown in Fig. 2.8 (d), the vertical and horizontal antennas are used for measured the received signal power P_V and P_H while the 3D radiation gains $G_V(\theta,\phi)$, $G_H(\theta,\phi)$ are also analyzed, simultaneously.

Based on the analytical model in Fig. 2.8, the link calculation between on-body antennas and simulation of radiation patterns of vertical and horizontal dipole antennas are carried out using the commercial EM solver FEKO [45]. The analytical frequency is 2 GHz. Since the human body is unsmooth, the antenna feed point to the surface of the human phantom is set with a separation of 4 cm. The analytical results will be illustrated hereafter.

Fig. 2.9 (a) indicates the analytical model from side and left-up views when the angle of left arm is 10°. Fig. 2.9 (b) shows the analytical radiation patterns of a turn-style antenna mounted on the head at 2 GHz in zx-plane.

Fig. 2.9 (c) shows the 3D radiation patterns of vertical and horizontal dipole antennas in the receiving point. In Fig. 2.9 (b), it can be seen that the omnidirectional radiation pattern with E_θ component of the turn-style antenna located at head can be obtained except –z direction. In Fig. 2.9 (c), the 3D radiation gain of $G_V(\theta,\phi)$, $G_H(\theta,\phi)$ in the incident wave direction from head to wrist is –25 dBi and –4.3 dBi, respectively. Therefore, the value BP-XPR_{3D} can be calculated as –20.7 dB based on Eq. (2.5).

Fig. 2.10 shows the results of the BP-XPR as a function of the arm-swinging angle from –20° to 50°. The black curve with symbol indicates the the calculated value of BP-XPR based on Eq. (2.4) using the received power of P_V and P_H measured by dipoles. The red curve shows the estimated value of the proposed BP-XPR_{3D} defined by Eq. (2.5) using the 3D radiation gain.

As shown in Fig. 2.10, with the variation of arm-swinging angle, a significant fluctuation over 20 dB can be observed in both cases of BP-XPR and BP-XPR_{3D}, indicating the dynamic property of on-body channel. Moreover, in the entire arm-swinging angular regions, the estimated values of BP-XPR_{3D} calculated from Eq. (2.5) agree well with that of BP-XPR in Eq. (2.4) regardless of different on-body channels.

Furthermore, in Fig. 2.10 (a), when the angle of left is 10°, there is a 10-dB difference between BP-XPR and BP-XPR_{3D} is observed. The reason of this phenomenon can be attributed to the shadowing effects caused by the human shoulder [49]. According to Fig. 2.9 (a), when the angle of left arm is 10°, the receiving antenna is moved to the –z direction of transmitting antenna. This means that the receiving antenna is moved to the null position of radiation pattern of transmitting antenna due to the shoulder shadowing effect. Thus, there is a difference occurred between the BP-XPR calculated by received power and the BP-XPR$_{3D}$ estimated by radiation gain. This phenomenon can be understood from Fig. 2.10 (b), where the turn-style antenna is mounted at foot. Since there is no significant shadowing effects on the link of the foot and wrist, the result of BP-XPR$_{3D}$ coincides well with the BP-XPR.

On the basis of the results above, it is confirmed that the using the 3-dimensional radiation pattern of test antennas (vertical and horizontal dipoles), the body proximity cross-polarization power ratio (BP-XPR) can be easily estimated when the direction wave between on-body antennas is not significantly obstructed by human body shadowing effects.

However, since only a special case of real human phantom is used, which is not representative of general human property, the calculated value of BP-XPR$_{3D}$ has not been applied to the weighted-polarization on-body antenna. The validity of proposed estimation method of BP-XPR$_{3D}$ needs to be confirmed in various human dynamic models, on-body use scenarios and different operating frequency in BAN radios. This will be addressed in future study.

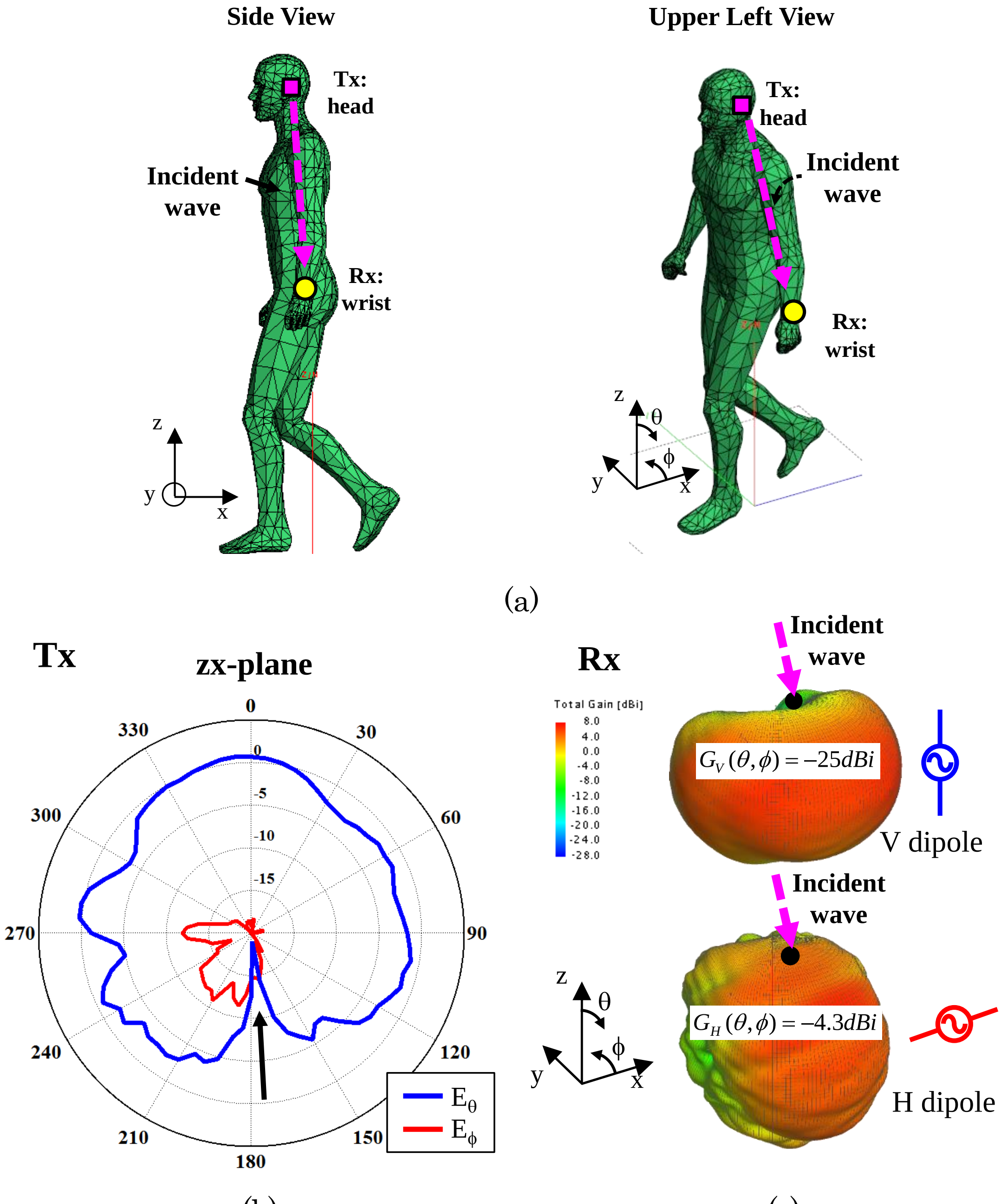

(a)

(b)

(c)

Fig. 2.9 Radiation characteristics of Tx and Rx antennas based on the analytical model when the arm-swing angle is 10 degrees

(a) Analytical model from side and upper left view, (b) Radiation pattern of Tx antenna (turn-style) in zx plane, (c) 3D radiation gain of Rx antenna (vertical and horizontal dipoles).

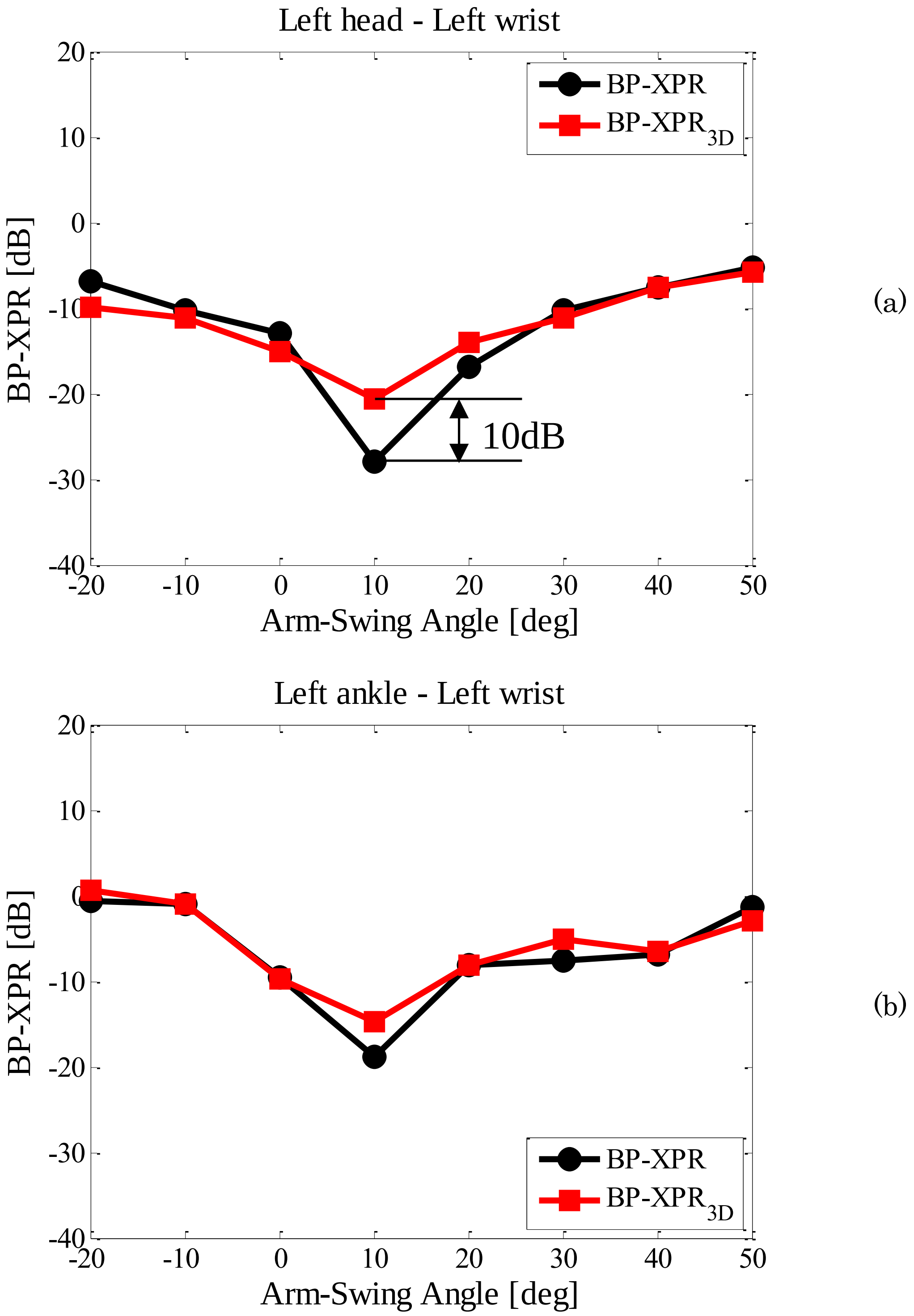

Fig. 2.10 BP-XPR vs. Arm-swing angle (a) left head to left wrist, (b) left ankle to left wrist.

2.6 Conclusion

This study presents a weighted-polarization antenna applied to BAN on-body communication systems. A primal objective is to achieve the radio link enhancement in both downlink and uplink on-body channels. The proposed antenna obtains an optimum signal level using a weight function considering the BP-XPR and antenna tilt angle. The results show that the proposed antenna achieved more than a 3-dB improvement of received signal compared with the other types of antennas, such as vertical dipole, horizontal dipole and equal weight combined antennas, regardless of the arm-swing motion and antenna placement, which verifies the effectiveness of the proposed method to enhance BAN on-body radio links.

Moreover, a simple estimation method of BP-XPR in consideration of human tissue effects and dynamic characteristics is proposed, which is quantified based on relative on-body antenna locations and human walking motion in an analytical way. The results show that the proposed BP-XPR can be estimated using the 3-dimensional radiation pattern of test antennas. Using the BP-XPR, the polarization behavior close to the human body is clarified. Future work will include the validation of BP-XPR_{3D} and scope of on-body applications.

3. Development of Spatial Fading Emulator

3.1 Introduction

Since wireless communications utilize radio waves propagating through the space as a medium, the propagation path characteristics are varied depending on the external conditions such as weather and geographical features. Further, in mobile communication system, with the moving placement of mobile terminal, fluctuation behavior of the propagation path becomes more severe. This phenomenon is named as fading (multipath propagation environment), which is generated by the variation of signal amplitude and phase. Due to fading effects, the quality of the received signal is significantly affected as the mobile moves over distances. To evaluate the wireless communication performance, fading effect is an un-ignorable impact factor. This is also the basic reason why the OTA device is required.

Fig. 3.1 (a) shows how fading effects might arise in practice [50]. A transmitter and receiver are surrounded by objects which reflect and scatter the transmitted energy, causing several waves to arrive at the receiver via different routes. This is multipath propagation. Since the direct wave from the transmitter to the receiver is blocked, this situation is called non-line-of-sight (NLOS) propagation. Each of the waves has a different phase and this phase can be considered as an independent uniform distribution, with the phase associated with each wave being equally to take on any value. In this case, the real and imaginary parts of the multipath components fulfill these conditions since they are composed of the sum of a large number of waves, leading to a Rayleigh distribution.

On the contrast, Fig. 3.1 (b) shows the line-of-sight (LOS) case, where a single strong path is received along with multipath energy from local scatterers. In this situation, the received signal is composed of a random multipath component, whose amplitude is described by the Rayleigh distribution, plus a coherent line-of-sight component which has essentially constant power. The power of this component will usually be greater than the total multipath power before it needs to be considered as affecting the Rayleigh distribution significantly, leading to a Rice distribution [50]. The ratio of direct single strong path and multipath components is often expressed as the Rice factor or the K-factor, which is an important parameter in Rice channel, as will be presented in Chapter 4.

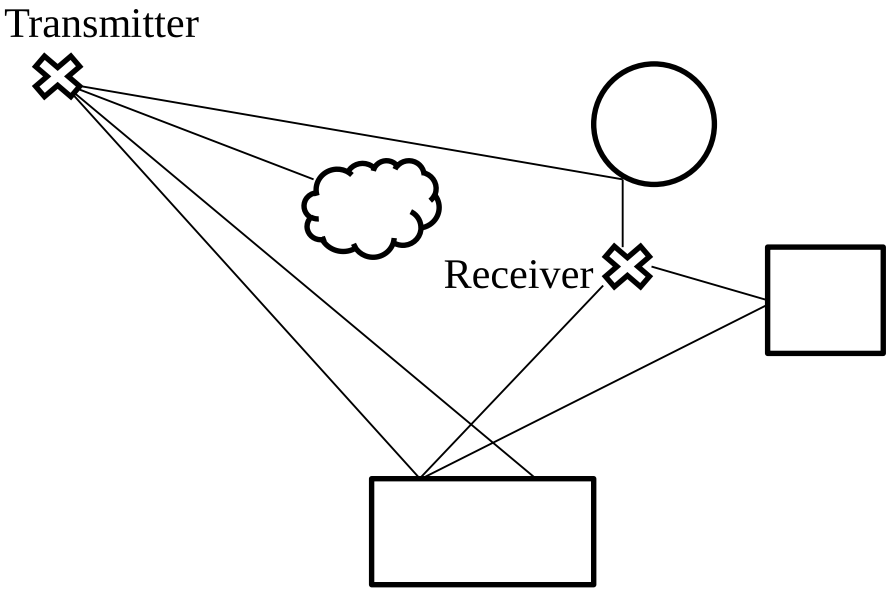

(a) Non-line-of-sight (NLOS)

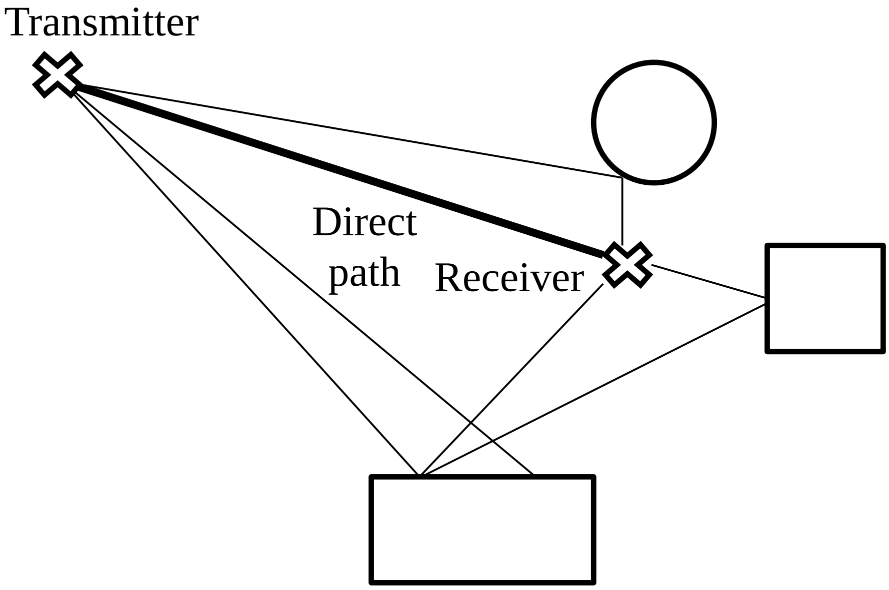

(b) Line-of-sight (LOS)

Fig. 3.1 Multipath radio wave propagation

3.2 Mechanism of Rayleigh Fading

As shown in Fig. 3.1(a), in NLOS situation, when the direct wave is obstructed, multipath propagation paths will be constructed by a large number of reflected waves (scattering waves) at receiving point, resulting in a combined electromagnetic wave distribution. To understand the phenomenon of Rayleigh fading, it is required to analyze the radio wave synthesis theory using a simple analytical model.

Fig. 3.2 shows the simplest case (two-source model) that an incident wave is reflected by a wall. Assuming that there is no reflection attenuation, the incident and reflected wave interfere with each other, generating a standing wave with periodically-fluctuated amplitude at half-wavelength of incident wave. Therefore, the peaks and valleys of the envelope distribution are observed. This is the basis of the fading wave.

Fig. 3.3 shows the calculation examples of fading waves when the reflected waves are 2, 3 and 6. In Fig. 3.3, it can be seen that the 6 waves synthesis eventually realize a randomly-varied envelope amplitude, which is close to situation of LOS environment. This fact indicates that at least 6 multipath waves are necessary for Rayleigh fading generation. In this way, an mathematical analysis is proposed to understand the multipath propagation caused by numerous waves interference phenomenon.

When multiple scattered waves are composed of many reflected waves, each individual reflected wave is called "elementary wave". Fig. 3.4 shows a receiving model of arriving waves in mobile terminal, where the carrier waves $s(t) = \mathrm{Re}[e^{j2\pi f_0 t}]$ with frequency f_0[Hz] come from the transmitter to a moving receiver. The n^th^ elementary wave $r_n(t)$ at the point of the mobile terminal, as shown by the dotted lines, can be expressed as follows.

$$r_n(t) = \mathrm{Re}\left[e_n(t)e^{j2\pi f_0 t}\right] = \mathrm{Re}\left[R_n e^{j2\pi f_0 t + j\alpha_n(t)}\right] \tag{3.1}$$

$$e_n(t) = R_n e^{j\alpha_n(t)} \tag{3.2}$$

Here, Eq. (3.1) indicates the carrier wave $s(t)$ modulated by the complex envelope $e_n(t)$ while R_n in Eq. (3.2) shows the amplitude of the complex envelope. Moreover, $\alpha_n(t)$ denotes the phase, which is determined by the phase shift ϕ_n caused by the path differences and the phase rotation component $2\pi f_0 t$ caused by Doppler shift f_d, as expressed by the following equations,

$$\alpha_n(t) = 2\pi f_d t + \phi_n \tag{3.3}$$

where the Doppler shift f_d, is given by the rate where the mobile crosses wave-fronts of the arriving signal,

$$f_d = \frac{v\cos\theta_n}{\lambda} \tag{3.4}$$

θ_n indicates the angle between the moving direction of the receiver and the incident wave. v denotes the moving speed of the receiver.

In Eq. (3.4), when the direction of incident wave is same as that of mobile terminal ($\theta_n = 0$), $f_d = -v/\lambda$; when the arriving wave direction is opposite ($\theta_n = \pi$), $f_d = -v/\lambda$. In this way, when $\theta_n = 0$ or π, the absolute value of the Doppler shift becomes maximum and this value is defined as the maximum Doppler frequency f_D,

$$f_D = \frac{v}{\lambda} \tag{3.5}$$

From Eqs. (3.2) to (3.5), the complex envelope $e_n(t)$ of the nth elementary wave $r_n(t)$ wave is obtained by

$$e_n(t) = R_n e^{j(2\pi f_d t + \phi_n)} = R_n e^{j(2\pi f_D \cos\theta_n t + \phi_n)} \tag{3.6}$$

Thus, as shown in Fig. 3.4, the multipath scatterering waves $r(t)$ can be expressed as a combination of N elementary waves,

$$
\begin{aligned}
r(t) &= \sum_{n=1}^{N} r_n(t) = \sum_{n=1}^{N} \mathrm{Re}\left[e_n(t)\, e^{j2\pi f_0 t}\right] \\
&= \mathrm{Re}\left[\sum_{n=1}^{N} R_n e^{j(2\pi f_D \cos\theta_n t + \phi_n)}\, e^{j2\pi f_0 t}\right]
\end{aligned}
\tag{3.7}
$$

The theory of Rayleigh fading is illustrated in details [50]. To understand the general nature of Rayleigh fading in actual propagation environment, a computer simulation is conducted using Eqs. (3.1) to (3.7), as shown in the next section.

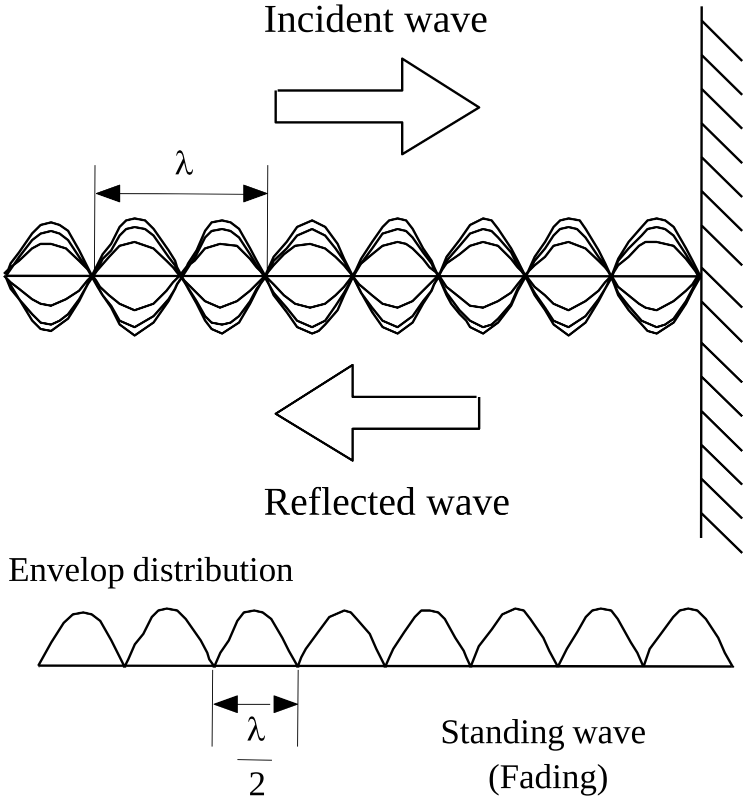

Fig. 3.2 Standing wave derived from incident and reflected waves

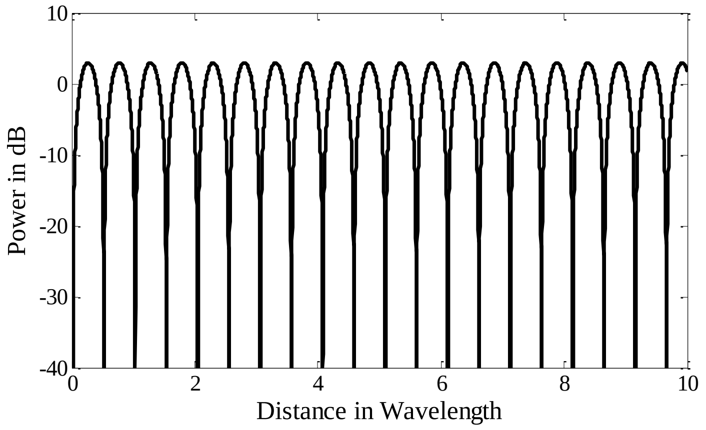

(a) 2 waves

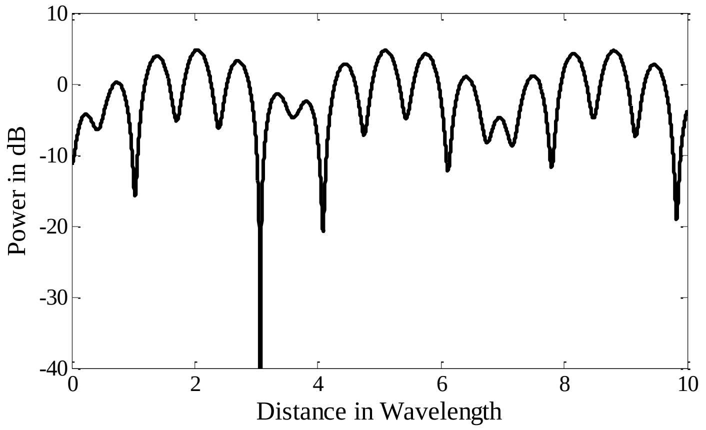

(b) 3 waves

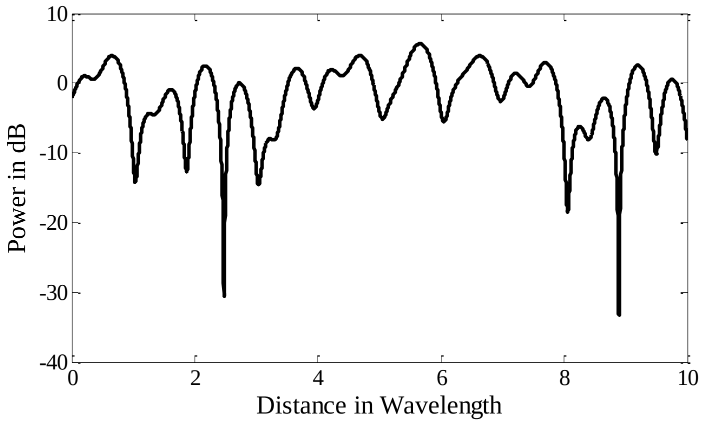

(c) 6 waves

Fig. 3.3 Variation of fading profile vs. number of reflected waves

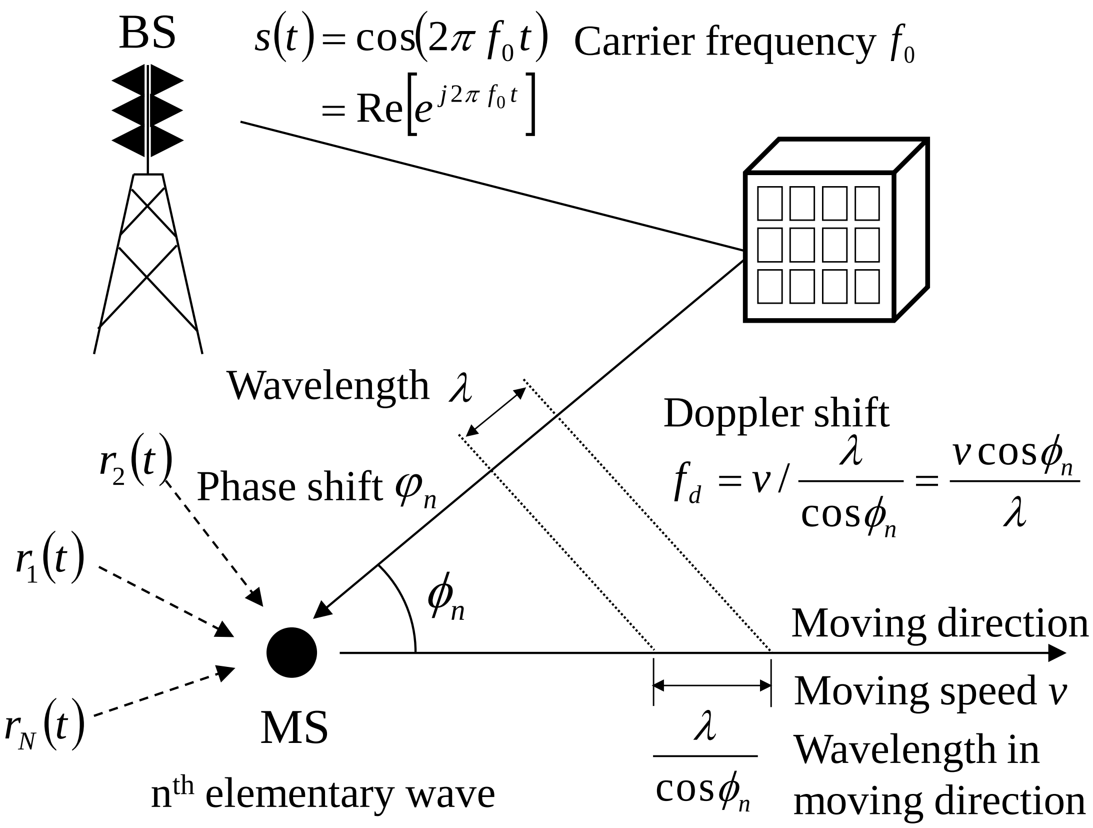

Fig. 3.4 Receiving model of arriving waves in mobile terminal

3.3 Simulation by Monte Carlo Method

In this section, a mathematical model to simulate the multipath fading characteristics in the actual radio wave propagation environment is presented.

Fig. 3.5 shows a multipath propagation model. In mobile communication system, when the distance between the base station and the mobile terminal is large, incident waves from the base station are assumed to be concentrated on the horizontal plane. N scatterers are arranged uniformly on a circle in a two-dimensional manner., which represent N reflected waves from base station caused by buildings and trees in urban areas.

On the basis of Figs. 3.4 and 3.5, as the same formulation mentioned in Sect. 3.2, the complex envelope $e_n(t)$ of the n^th^ elementary wave $r_n(t)$ wave, as shown by Eq. (3.6), is expressed by

$$e_n(t) = R_n e^{j(2\pi f_d t + \phi_n)} = R_n e^{j\{2\pi f_D \cos(\theta_n - \theta_v) t + \phi_n\}} \tag{3.8}$$

where R_n shows the amplitude of the complex envelope and ϕ_n denotes the phase shift caused by the path differences, as the same definition in Fig. 3.4. Assuming that the multipath lengths between transmitter and receiver are unity, R_n can be treated as a constant value. θ_n indicate the nth incident wave direction while θ_v shows the moving direction of the receiving antenna, as shown in Fig. 3.5. By analyzing the positions of scatterers with respect to the moving direction of receiving antenna, it is possible to evaluate the propagation characteristic according to the different traveling directions.

$$e_n(t) = e^{j\left\{2\pi \frac{v}{\lambda} \cos(\theta_n - \theta_v) t + \phi_n\right\}} = e^{j\left\{\frac{2\pi}{\lambda} \cos(\theta_n - \theta_v) v t + \phi_n\right\}} \tag{3.9}$$

For the convenience and generality of calculation program, the traveling distance of receiving antenna is defined as $z = vt/\lambda$. Thus, the simulation can be performed using the travel distance per wavelength regardless of wavelength (frequency).

$$e(t)=\sum_{n=1}^{N}e_n(t)=\sum_{n=1}^{N}e^{\,j\{2\pi\cos(\theta_n-\theta_v)z+\phi_n\}} \tag{3.10}$$

Using Eq. (3.9), the complex envelope $e_n(t)$ are successively generated according to the positions of receiving point. Consequently, the sum can be calculated by Eq. (3.10) to simulate the multipath propagation characteristic.

In Eq. (3.10), the key point is how to set the randomly-varied phase shift value ϕ_n caused by mobile terminal, as shown in Fig. 3.4. In terms of this aspect, the random numbers are used to randomly generate the ϕ_n to model the random propagation phenomena of mobile communication. The method using random numbers to simulate such complex physical phenomenon is called the "Monte Carlo simulation". This method provides the theoretical basis for the development spatial fading emulator. The usage of Monte Carlo method will be applied in the following chapters and will be introduced in details.

On the basis of the above-mentioned principles, the simulation results implemented by the MATALB program is shown hereafter.

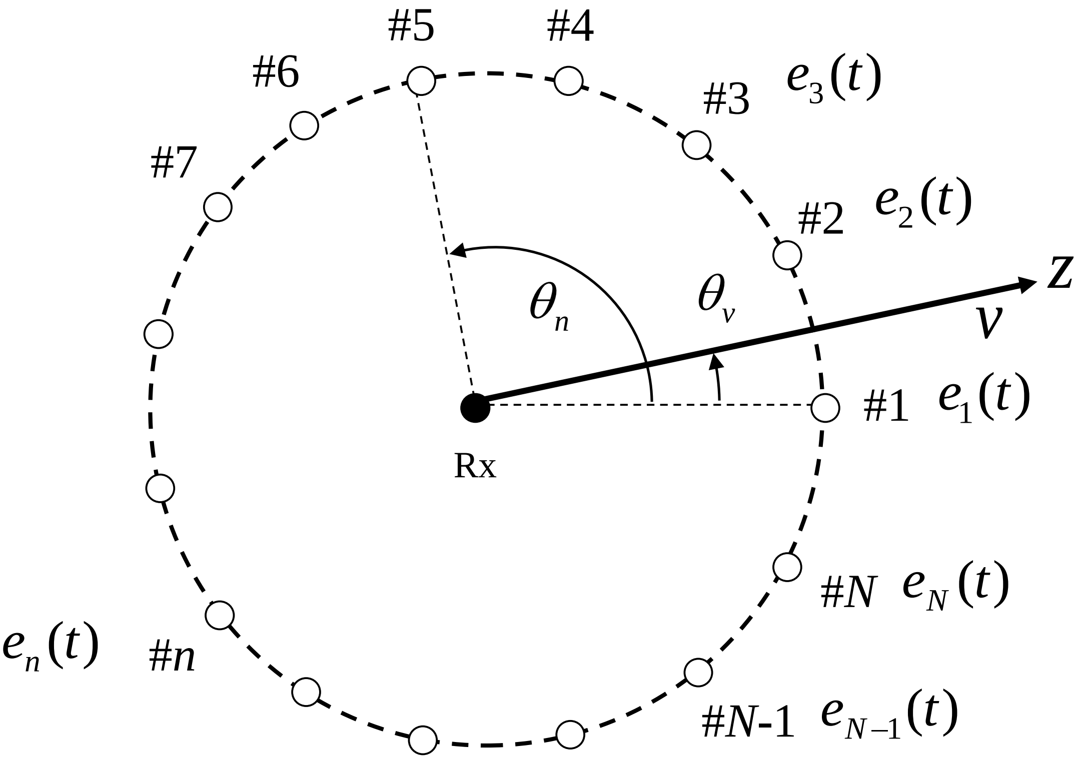

Fig. 3.5 Multipath propagation model for Monte Carlo simulation

Fig. 3.6 shows the Rayleigh wave generated by the Monte Carlo simulation based on Eq. (3.10). Fig. 3.6 (a) shows the scatterers distribution. The number of scatterers N is 15 while the moving direction θ_v is 10 degrees. The receiving antenna is moved in a distance of 50 wavelengths, where the generation of elementary waves is performed 5000 times at equal distance intervals (0.01λ). The PDF (possibility density function) of the received signal is shown in Fig. 3.6 (b), where the theoretical distribution in Fig. 3.6 (b) as a smooth line is the Rayleigh distribution [50], given theoretically by

$$p(R) = \frac{R}{\sigma^2} e^{-\frac{R^2}{2\sigma^2}} \qquad (0 \le R < \infty) \tag{3.11}$$

Fig. 3.6 (c) shows the instantaneous response of the received signal, where the average received power in the entire traveling distance is normalized to 0 dB. As shown in Fig. 3.6 (c), deep null positions of instantaneous response over −30 dB from the average received power can be observed.

Fig. 3.6 (d) shows the CDF (cumulative distribution function) curve using the calculated results of instantaneous response in Fig. 3.6 (c). The vertical axis shows the logarithmic display of the probability while the horizontal axis shows the received signal level normalized to 0 dB. The curve with square symbol shows the simulated results by using Monte Carlo method. The theoretical line of the CDF of Rayleigh distribution [50] is also included, as calculated by the following equation.

$$\begin{aligned} F(R) &= \int_{-\infty}^{R} p(x)\,dx = \int_{0}^{R} \frac{x}{\sigma^2} e^{-\frac{x^2}{2\sigma^2}} dx \\ &= 1 - e^{-\frac{R^2}{2\sigma^2}} \end{aligned} \tag{3.12}$$

In Fig. 3.6 (d), when the received signal level is less than −10 dB, the CDF value decreases with a gradient of one-tenth per 10-dB degradation of the received power. Also, this result agree well with the theoretical curve, indicating that the Monte Carlo simulation method has a sufficient accuracy compared with the analytical solution.

Based on the investigations mentioned above, an actual fading emulator is designed and manufactured by implementing the analytical model shown in Fig. 3.5, where the software for controlling the time-sequential varied signals for Rayleigh fading generation is also developed using the formulations in this section. The details of the development process will be introduced hereafter.

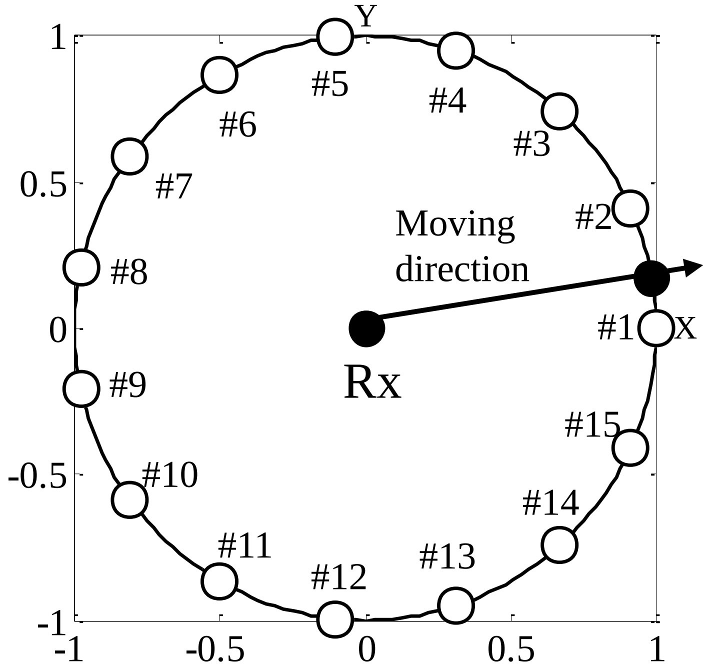

(a) Scatterers arrangement

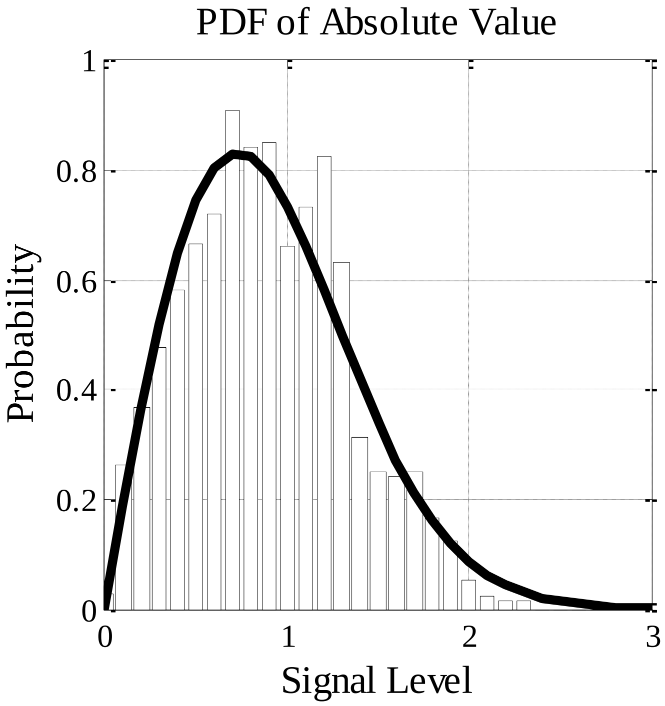

(b) Possibility density function

Fig. 3.6 Generation of Rayleigh fading using Monte Carlo simulation

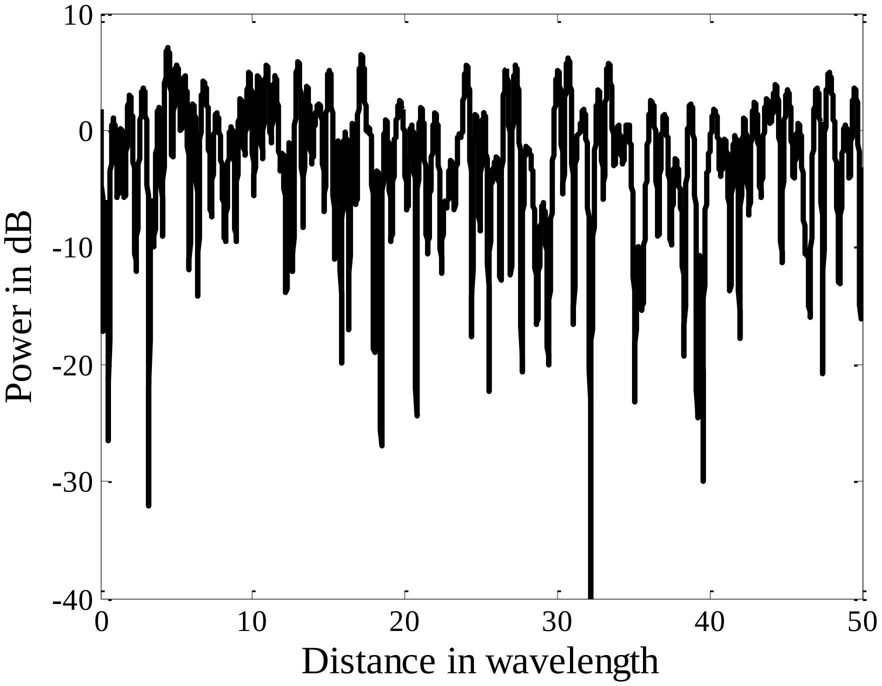

(c) Instantaneous response

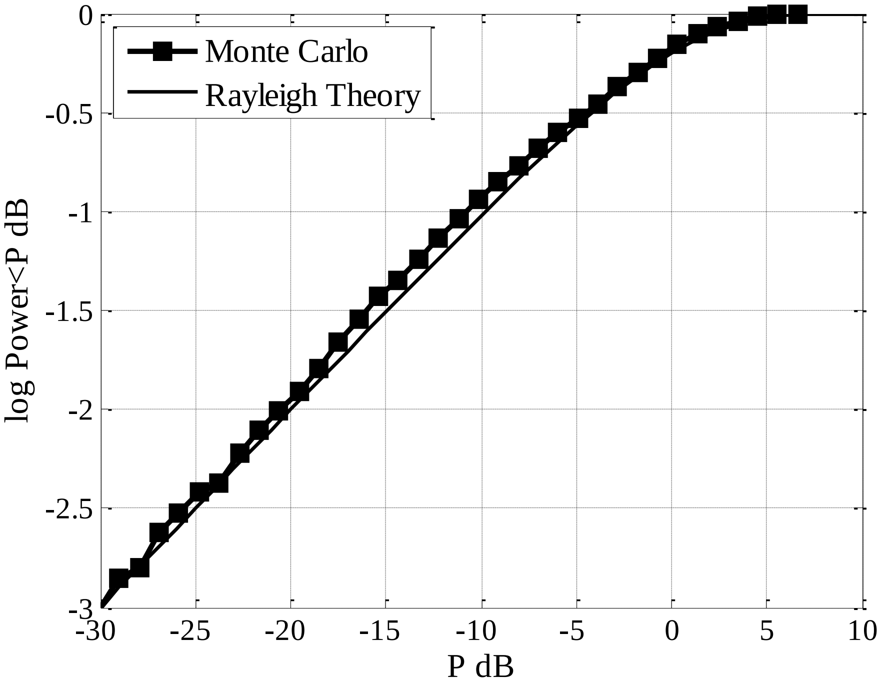

(d) Cumulative distribution function

Fig. 3.6 Generation of Rayleigh fading using Monte Carlo simulation

3.4 Design and Manufacture of the Actual Spatial Fading Emulator

The configuration of the developed fading emulator for BAN antenna assessment are illustrated in Figs. 3.7 and 3.8. The surrounding scatterers comprised of vertical and horizontal 950 MHz half-wavelength dipole antennas are fixed on the top of the resin pillars, which are located on the circumference at equal intervals. These orthogonally-arranged scatterers are used to realize cross-polarization power ratio (XPR) to represent different radio wave polarization components. The diameter of the fading emulator is 240 cm, and the height of each surrounding dipole antenna measured from the floor is 100 cm. The arm-swinging dynamic human phantom is located at the center of the fading emulator, which is developed by Panasonic [38]. The phantom is made of polypropylene with a thickness of 3mm for simulating the electrical properties of human, where both the arms are controllable to swing in order to emulate the dynamic shadowing effects caused by human behavior.

RF signals radiated from the scatterers are summed around the DUT (device under test) antenna attached at the human phantom, and the desired radio channel environment can be generated. The RF signal delivered from port 1 of a vector network analyzer (VNA) is separated by a power divider. Then, the radio waves are radiated from the antenna probes through the phase shifters and attenuators, which are used to control the phase and amplitude of each signal for emulating the multipath propagation environment.

The amplitude of each path was controlled by the attenuator according to the requirement of realizing Clark or Cluster channel model [51-54]. A computer was used to calculate the values of the phase shift of the signals from each scatterer to obtain a Rayleigh fading channel. In the measurement, the emulated radio waves radiated from the scatterers are received at receiving antenna (DUT) and measured its amplitude and phase, which means the S21 characteristics, using the VNA. In general, the experiment is performed using sinusoidal continuous wave (CW) signals. On the other hand, with different transmitting and receiving devices, the developed fading emulator can also perform other modulated signals, such as OFDM, CDMA, HSDPA, and MIMO formats in mobile communication system because of the RF-controlled configuration, rather than a digital-based architecture. Using this apparatus, a desired Rayleigh fading channel can be realized.

Fig. 3.9 shows a phase shifter utilized in the control circuit of the fading emulator. Fig. 3.9 (a) shows its photograph of the internal structure. One case of phase shifter is comprised of two phase shift unit (JSPHS-23+), where each unit can change the phase value from 0 to π. This means that the phase shift value of each path can be controlled in a range of 0 to 2π, which is sufficient to realize the Rayleigh fading generation. Fig. 3.9 (b) shows the voltage characteristic of the phase shifter, where the fitting function can be expressed by

$$V_{bias} = 0.0623\phi^3 - 0.7758\phi^2 + 4.18\phi - 2.0559 \tag{3.13}$$

where ϕ denotes the phase shift value. This function will be utilized to generate the bias voltage controlled by the D/A (digital/analog) converter, as shown in Fig. 3.9.

Fig. 3.10 shows an example of measured result using the developed fading emulator without human phantom, which means that only a sleeve dipole antenna at 950MHz located at the center of the OTA apparatus is used to receive the combined signals. 7 scattering units with radio wave absorbers behind them can create Rayleigh fading signals by varying the phases in the control circuit of fading emulator. The radio wave polarization environment was assumed to be vertical, which means that only vertical dipole antennas of the surrounding scatterers has been used.

Fig. 3.10 (a) shows the measured results of instantaneous response of a dipole antenna with a traveling distance of 50 wavelengths at 950 MHz. The sampling number is set to 5000. As shown in Fig. 3.10 (a), deep null positon over −30 dB can be observed, corresponding to the analytical result in Fig. 3.6 (c). Fig. 3.10 (b) indicates the CDF curve measured by the fading emulator, which agrees well with the theoretical value of Rayleigh distribution. This fact indicates that the Rayleigh fading propagation environment can be realized using the developed fading emulator.

Using this spatial fading emulator, the evaluation of wearable antenna performance in BAN system considering human and multipath environment mutual interactions have been conducted, as will be illustrated in the following sections.

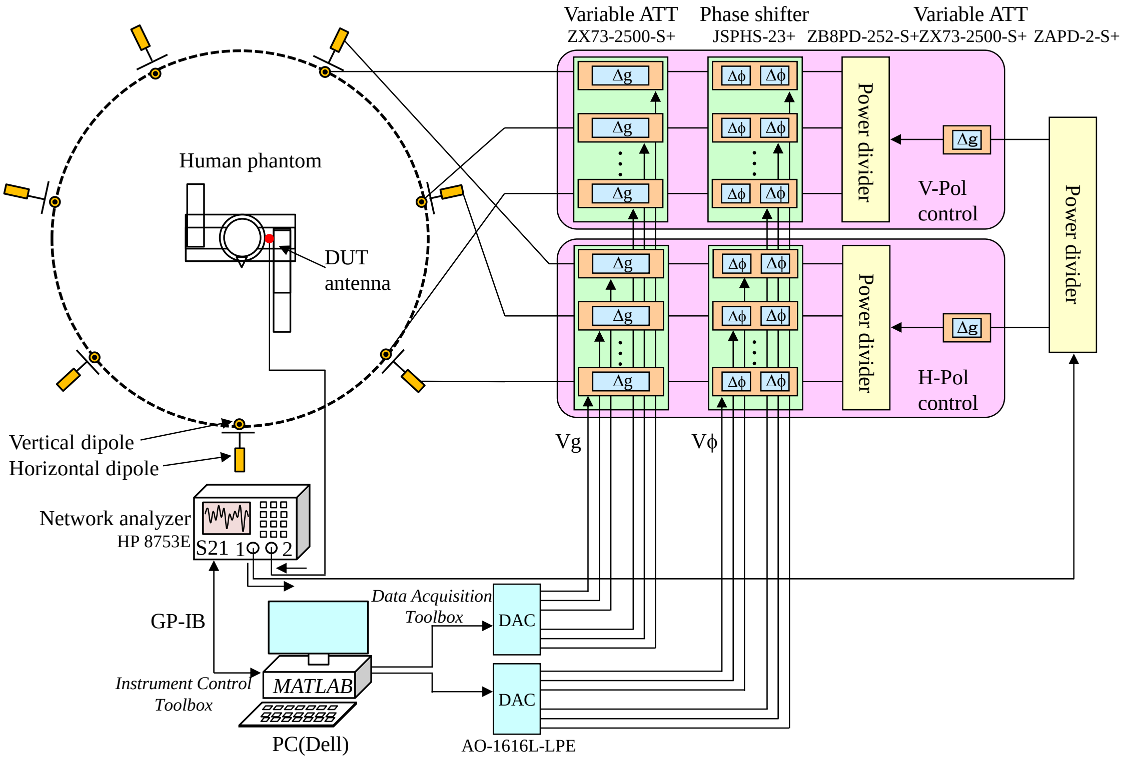

Fig. 3.7 Design chart of spatial fading emulator

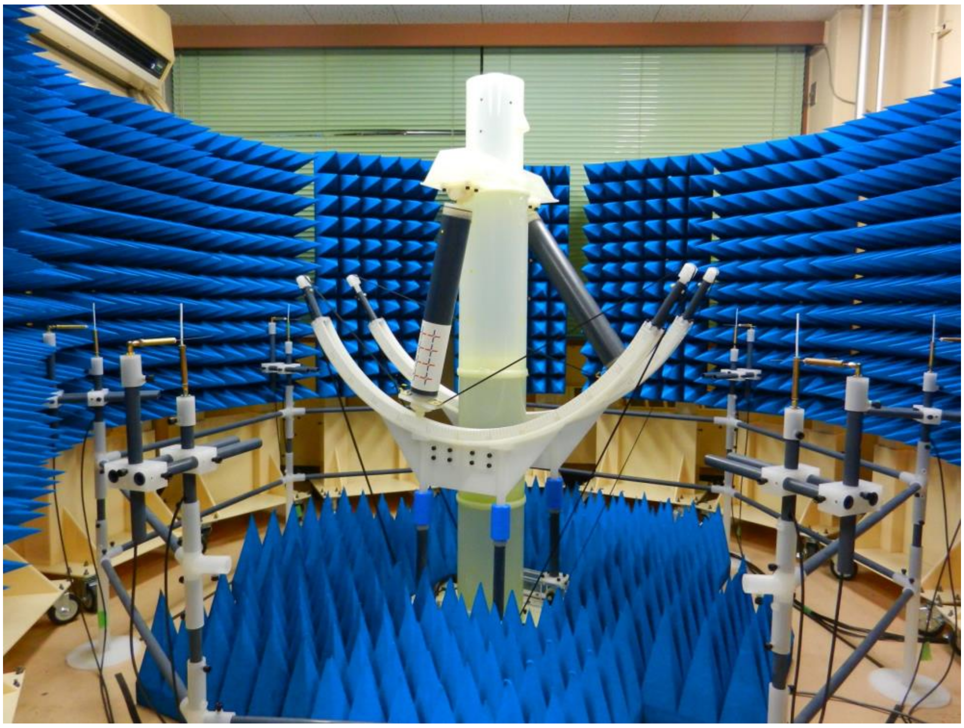

Fig. 3.8 Overview of the fading emulator for BAN antenna assessment

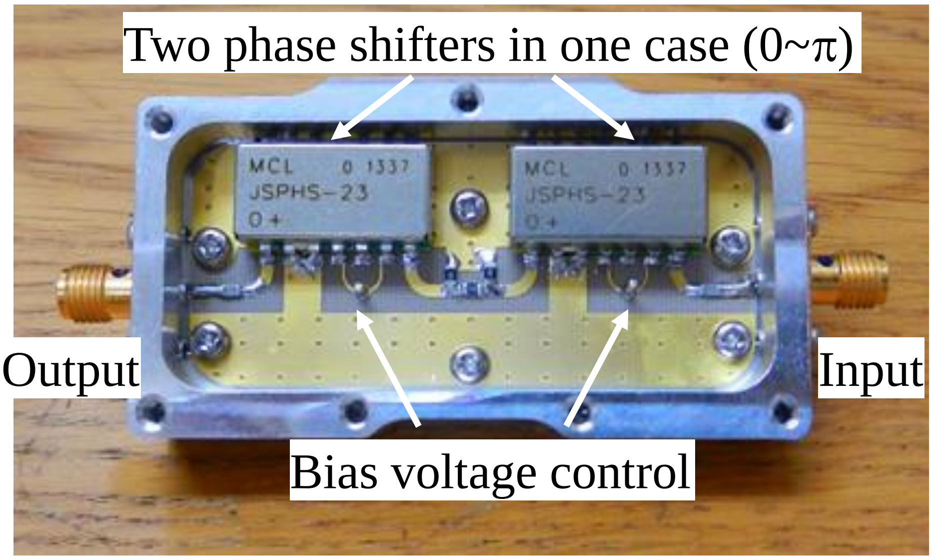

(a) Photograph of phase shifter

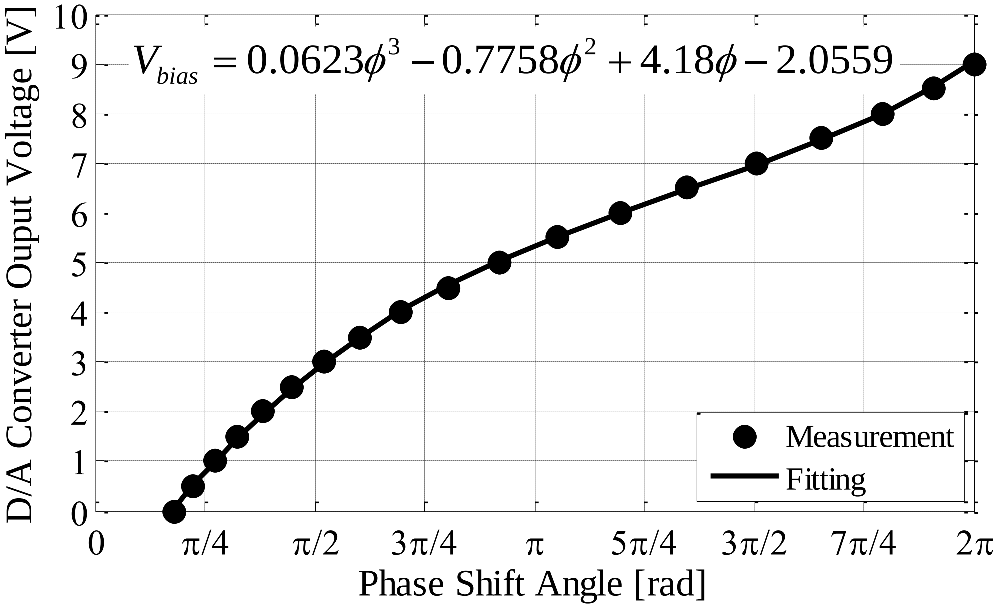

(b) Voltage characteristic and curving fitting

Fig. 3.9 Characteristics of phase shifters

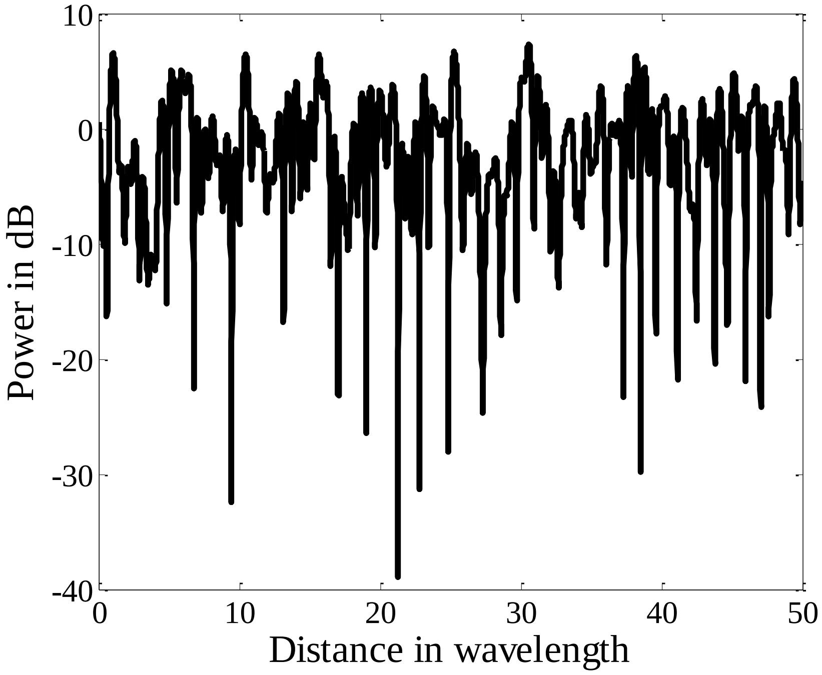

(a) Instantaneous response

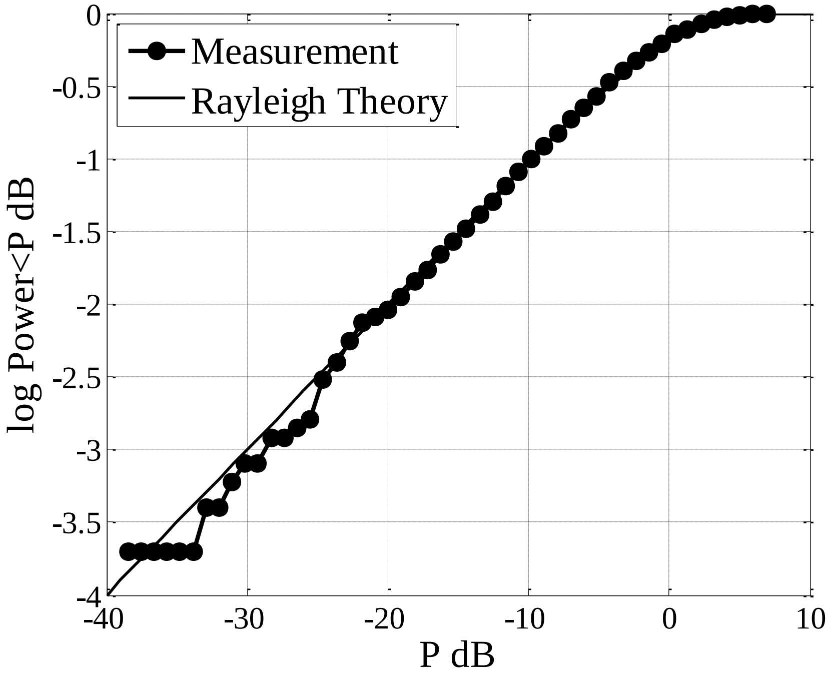

(b) CDF characteristics

Fig. 3.10 Measured result of Rayleigh wave using the developed fading emulator without human phantom

3.5 Conclusion

This chapter presents the development procedure of a spatial fading emulator in Toyama University.

Before the development of the actual device, the theoretical mechanism of multipath radio wave propagation phenomenon was analyzed, where the generation mechanism of multipath Rayleigh fading have been formulated. On the basis of the theoretical formulations, an analytical model using Monte Carlo simulation is constructed, which is confirmed to successfully realize the Rayleigh distribution property.

Using the theoretical and analytical investigations, the design and hardware implementation of an actual fading emulator was conducted. After the OTA device is manufactured, validity confirmation of Rayleigh fading is also needed. The result shows that a good nature of Rayleigh fading probability distribution can be performed by the developed fading emulator.

The developed OTA apparatus will be used to evaluate the wearable antennas considering different BAN use scenarios, as will be illustrated respectively in the following chapters.

4. Rice Channel Model Realization

4.1 Introduction

As mentioned in the previous chapters, OTA testing is a method of evaluating the general performance of a mobile device [15]. An OTA test to assess a multiple-input multiple-output (MIMO) handset antenna in multipath environments has been developed [17] [28] [55]. The study in [17] confirmed that the Rayleigh propagation environment indoors can be realized by setting a collection of random phases for the uniformly distributed scatterers. However, the OTA technique was not applied to body area network (BAN) systems in previous studies [38] [56]. In BAN systems, antenna characteristics are significantly altered by human body coupling or shadowing effects, and also the propagation environment. To determine the actual performance of BAN terminals in specific use scenarios is a complicated subject. Therefore, the objective of this study is aimed at developing an OTA methodology using a fading emulator for the accurate testing of BAN systems.

There are two major differences between an OTA test for cellular MIMOs and that for BAN radios. The first difference is that in BAN radios, we must consider dynamic channel variations, commonly referred to as shadowing, caused by the motion of an operator, such as the swinging of arms while walking. The second difference is that a BAN sensor module may be attached to the human body, such as on the head, torso, wrist, ankle or other positions, for collecting medical information where there is a strong direct wave coming from the sensor module to an access point attached at the waist, as shown in Fig. 4.1. This situation creates a Rice propagation environment in combination with the fields reflected from the surrounding objects.

In order to resolve the first issue, many studies have been published. Body dynamics are shown to significantly affect fading properties [10] [57]-[62]. Previously, an arm-swinging dynamic phantom that can simulate the natural walking style of humans was developed [38]. Using the phantom, shadowing-fading combined effects have been analyzed in [38] [56].

As for the second difficulty, there are also many related papers. A channel model for a wearable BAN based on the path loss model measured in an anechoic chamber is presented in [63]. However, the multipath component is not considered. Some studies for on-body propagation channels in a hospital environment are discussed in [57] [64-69]. Literature [57] proposed a statistical model for the on-body dynamic channel, which shows that the multipath bounces result in an additional energy contribution to the channel gain between two on-body antennas. The degradation of the Rice factor results in a fading statistic approaching a Rayleigh distribution (see Table 6 in [57]). However, these investigations have some drawbacks, such as low repeatability and accuracy because of the actual test persons and the specific measurement locations. Moreover, the K-factors shown in [69] indicate that the best-fitting statistical model depends on numerous parameters, such as the propagation channel, human subject, the antenna, and its orientation. Therefore, using the statistical channel model, it is difficult to conduct a precise evaluation of commercially available BAN devices in a specific use scenario. Thus, developing an experimental methodology and instrument that takes into account the combined effects caused by the direct path and multipath signals indoors, considering human dynamic characteristics, is an indispensable aspect of the evaluation of BAN radio systems, as will be illustrated later.

This work presents a new methodology for realizing a Rice channel in BAN-OTA testing using a fading emulator with a dynamic phantom. For the proposed apparatus to be effective, the fading emulator must be provided with an appropriate K-factor that represents the actual propagation environment indoors. Further, an implementation of the Rice channel to the proposed fading emulator in a BAN situation is presented. Thereafter, a calibration method for the fading emulator to adjust the actual K-factor of the on-body Rice channel is advanced. This calibration method is validated by analyzing the variations in the instantaneous K-factor attributed to the arm-swinging motion. Finally, an experiment is conducted for a continuous human walking motion with the fading emulator using an arm-swinging dynamic phantom. The results show that the developed fading emulator allows BAN-OTA testing to replicate the actual Rice channel propagation environment with the consideration of the dynamic characteristics of human walking motion.

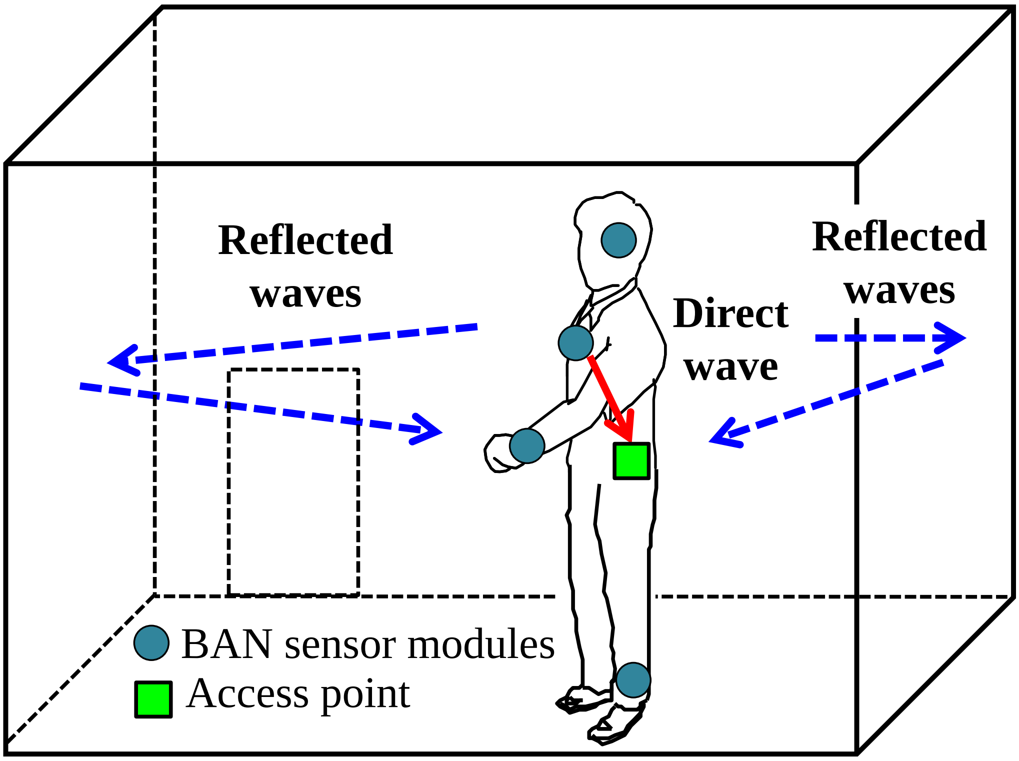

Fig. 4.1 Typical usage scenario of BAN radios

4.2 Configuration of the BAN Fading Emulator

The proposed fading emulator for BAN-OTA testing is shown in Fig. 4.2. The arm-swinging dynamic human phantom [38] is located at the center of the fading emulator. The phantom can swing both the arms to emulate the shadowing effects whereas the scatterers comprised of dipole antennas surrounding the phantom are used to create the cross-polarized fading signals at the Doppler frequency of walking. The diameter of the fading emulator is 240 cm, and the height of each surrounding dipole antenna measured from the floor is 100 cm. The signals radiated from the scatterers are summed around the phantom, and the desired radio channel environment can be generated, as shown by the blue dotted arrows. Additionally, a dipole antenna attached to the human body, e.g., on the chest, simulating a sensor module creates direct waves towards a dipole antenna simulating an access point located at the waist, as shown by the red solid arrow.

The fading emulator has two attenuators, ATT1 and ATT2, as shown in Fig. 4.2. The former is connected to the dipole antenna attached to the human body to control the direct wave component P_d, and the latter is connected to the dipole antennas used as scatterers located in the horizontal plane to control the multipath field components P_r. Therefore, the direct to the scattered field power ratio can be controlled with these two attenuators. Moreover, the K-factor representing the indoor radio propagation environment can be set with regard to the actual on-body Rice channel for BAN-OTA testing. The method of calibrating the fading emulator using the attenuators will be described in Sect. 4.4.

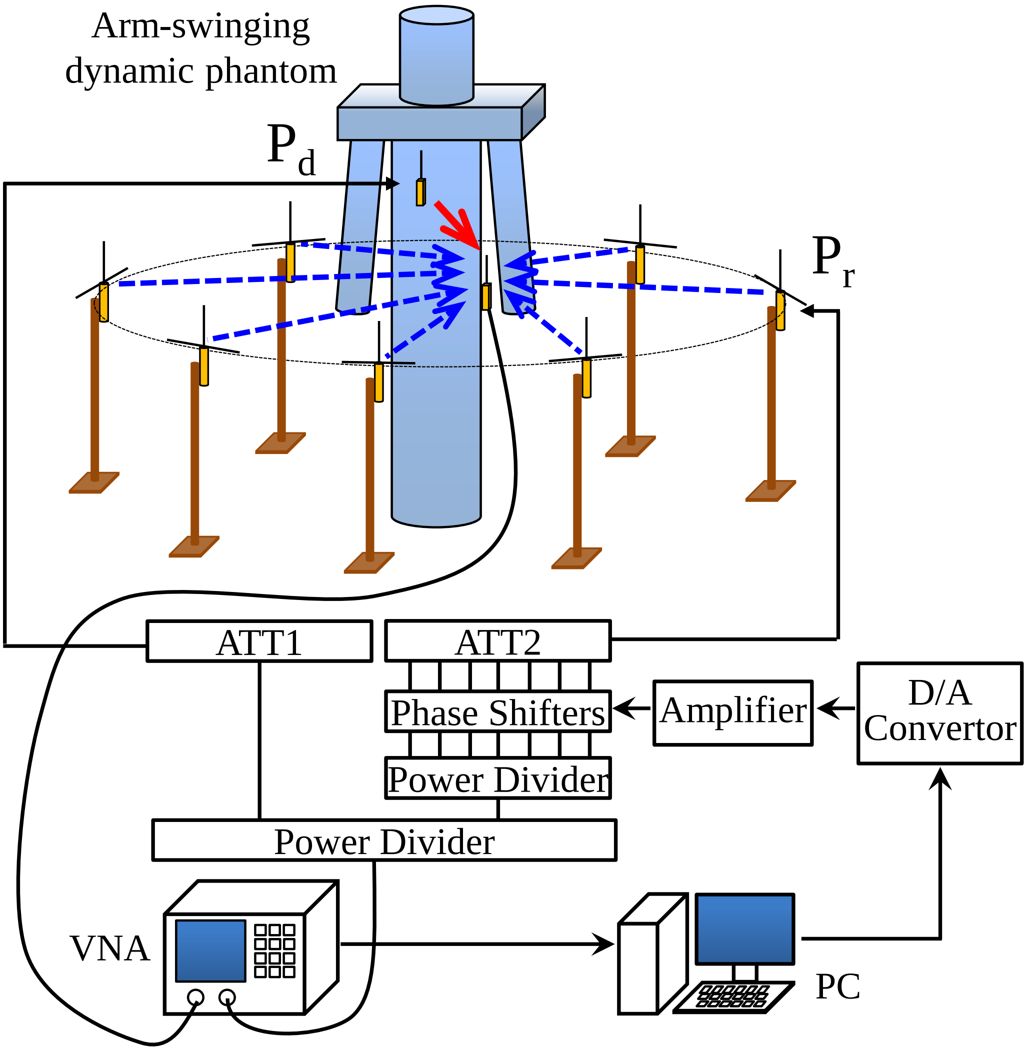

Fig. 4.2 Configuration of the BAN fading emulator

4.3 Implementation of Rice Channel to a Fading Emulator

Based on the configuration of the BAN fading emulator described in Sect. 4.2, an implementation of the Rice channel using the Monte Carlo method [38] [56] [70] considering the human walking motion in a BAN situation is presented in this section.

In general, BAN communications are classified into two major categories based on the different operational bandwidth: narrow band and wide band systems. In a narrow band system, the frequency is operated at 400 MHz or 950 MHz, leading to a low bit rate of communication. A frequency of 400 MHz is usually used for an implanted BAN system, such as capsule endoscopy; 950 MHz is generally applied to wearable devices. In this study, we focus on a narrowband system at 950 MHz for on-body BAN antenna evaluation, and thus the channel is considered to have a flat fading or time-invariant response in the absence of delay signals.

As shown in Fig. 4.3 (a), the BAN Rice channel is assumed to be surrounded by N scatterers uniformly arranged in the azimuth direction.

Initially, we focus on the reflected wave components P_r [71] [72], which indicate the multipath radio wave propagation environment, as shown in Fig. 4.3 (a). Assuming that the n-th path has a transfer function with vertical and horizontal components, its transfer function at the antenna can be given by

$$h_{Vn} = \sqrt{\frac{XPR}{1+XPR}} h_{ne} E_V(\theta_n, \phi_n) \exp(j\varphi_{Vn}) \tag{4.1}$$

$$h_{Hn} = \sqrt{\frac{1}{1+XPR}} h_{ne} E_H(\theta_n, \phi_n) \exp(j\varphi_{Hn}) \tag{4.2}$$

where $E_V(\theta_n, \phi_n)$ and $E_H(\theta_n, \phi_n)$ denote the complex electric field directivity of the antenna element for the θ and ϕ components, which are calculated by the method of moments [38]. Here, h_{ne} represents the equivalent amplitude of the incident waves and can be set to an arbitrary value; thus, it is assumed to have unity amplitude. Further, *XPR* is the cross-polarization power ratio [44]. The phases of the vertical (φ_{Vn}) and horizontal (φ_{Hn}) polarization components are independent of each other and uniformly distributed from 0 to 2π.

For each path, the two polarization components are combined as a complex sum of vertical and horizontal components as follows:

$$h_n = h_{Vn} + h_{Hn} \tag{4.3}$$

The resultant channel response h_s at the antenna is expressed as the sum of N paths using the following equation:

$$h_s = \sum_{n=1}^{N} h_n \exp\left\{ j \frac{2\pi d}{\lambda} \cos(\phi_n - \phi_m) \right\} = \sum_{n=1}^{N} h_{nr} \tag{4.4}$$

where λ is the carrier wavelength in free space, and d is the distance travelled by the dynamic phantom toward the azimuth direction (ϕ_m).

Therefore, the average power of the reflected waves (P_r) is obtained given by

$$P_r = \frac{1}{S} \sum_{s=1}^{S} |h_s|^2 \tag{4.5}$$

where S signifies the number of samples, which means the entire snapshots in a walking motion process.

On the other hand, the channel response of the direct wave can be expressed as

$$h_d = \sqrt{2KP_r} \tag{4.6}$$

where K is defined as the power ratio of the direct P_d and reflected wave components P_r, usually known as the Rician factor or the K-factor.

As shown in Fig. 4.3 (b), the combined signal response of each path at each arm-swinging angle can be obtained as a vector sum in the following form:

$$h_{nc} = h_d + h_{nr} \tag{4.7}$$

Therefore, the overall channel response in a Rice environment is expressed as follows:

$$\begin{aligned} h_{s,c} &= \sum_{n=1}^{N} h_{nc} = \sum_{n=1}^{N} \left(h_d + h_{nr} \right) \\ &= \sqrt{2KP_r} + \sum_{n=1}^{N} h_n \exp\{ j2\pi f_d t \cos(\phi_n - \phi_m) \} \end{aligned} \tag{4.8}$$

where $f_d = v/\lambda$ is the maximum Doppler frequency, and v denotes the velocity of the phantom.

Using this model, a Monte Carlo simulation can be carried out when the phantom is moving with the arms swinging, where the K-factor is used as an input variable to represent the relationship between P_d and P_r at each arm-swinging angle. The analytical results, presented in Sect. 4.5, will be compared with the measured results.

Furthermore, the software for controlling the fading emulator is also developed on the basis of the formulations mentioned above [Apx. A]. Specifically, time-sequential variations of signals for the surrounding dipole antennas (scatterers) and body-mounted dipole antenna (sensor module), depicted in Fig. 4.2, can be generated using a combination of Eq. (4.8), by varying the voltages applied to the phase shifters and attenuators (see Fig. 4.4), and the calibration method, as discussed in the next section.

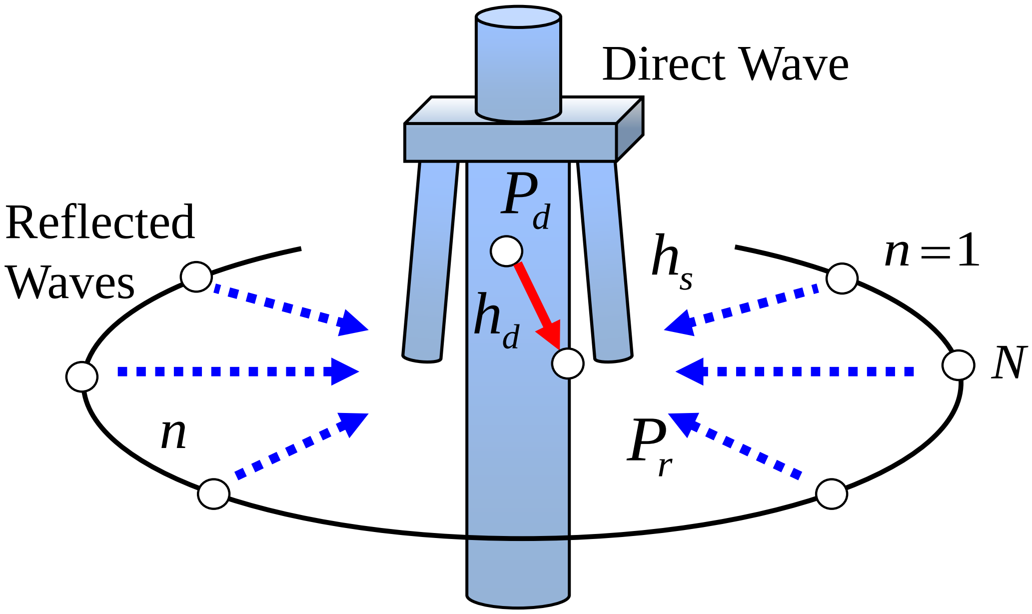

(a) BAN Rice channel model

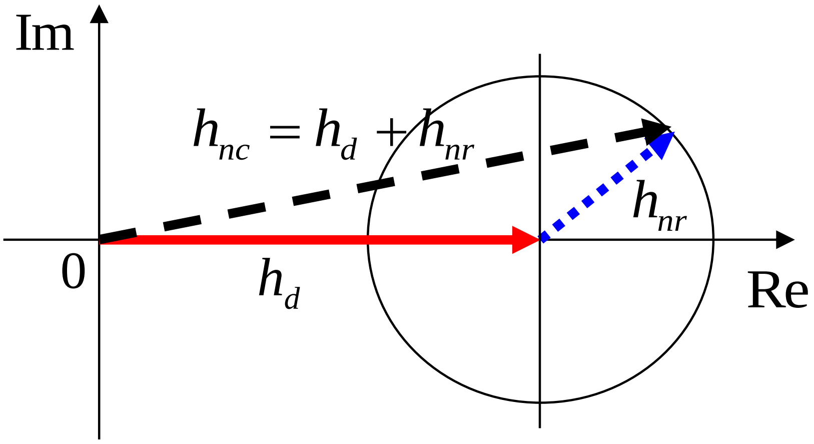

(b) Combination of direct and reflected wave components

Fig. 4.3 Implementation of Rice channel to the fading emulator

4.4 Calibration Method

Because there is a difference between the indoor radio wave propagation environment and usage scenarios of the fading emulator, calibration of the fading emulator is necessary for recreating the actual conditions of the other environments. Therefore, prior to the basic experiment, a procedure for calibrating the fading emulator is described in this section.

Fig. 4.4 shows the circuit of the fading emulator, which is composed of a power combiner, 7 phase shifters, and two attenuators. As can be seen, the power combiner is used to combine the signals from the surrounding dipole antennas with different phases obtained by using the phase shifters, as shown by the red diagram block. Here, ATT1 is used to control the direct wave (P_d), and ATT2 is used to control the reflected wave (P_r), as mentioned in Sect. 4.2.

The fading emulator can be calibrated by setting the values of the attenuators, shown in Figs. 4.2 and 4.4, using Eqs. (4.9) and (4.10) given below.

$$\begin{aligned} &\textit{If } P_d - P_r < K, \textit{ then} \\ &ATT1\ (\mathrm{dB}) = 0\ (\mathrm{dB}), \\ &ATT2\ (\mathrm{dB}) = K\,(\mathrm{dB}) - \{P_d\,(\mathrm{dBm}) - E[P_r]\ (\mathrm{dBm})\} \end{aligned} \tag{4.9}$$

$$\begin{aligned} &\textit{If } P_d - P_r > K, \textit{ then} \\ &ATT1\ (\mathrm{dB}) = \{P_d\,(\mathrm{dBm}) - E[P_r]\ (\mathrm{dBm})\} - K\,(\mathrm{dB}), \\ &ATT2\ (\mathrm{dB}) = 0\ (\mathrm{dB}) \end{aligned} \tag{4.10}$$

where P_d and P_r denote the power of the direct and scattered signals in dBm.

Here, E[x] signifies the expectation or average of the quantity x. The Rician factor or K-factor (K), in Eqs. (4.9) and (4.10), is defined as the ratio of P_d to P_r, and it can be measured during the propagation experiment, which will be described later in Sect. 4.4.3. Moreover, P_d can be measured with a vector network analyzer (VNA), and E[P_r] can be measured with the developed fading emulator, shown in Fig. 4.2, which will be discussed in Sects. 4.4.1 and 4.4.2, respectively. With the actual value of the K-factor in a certain situation as a reference, the attenuators in the fading emulator, shown in Fig. 4.4, can be used to adjust the ratio of P_d to P_r to create a realistic radio propagation environment as required. For example, if $P_d - P_r$ is less than K-factor as shown in Eq. (4.9), the signal level of reflected wave will be larger than that in the actual propagation environment. Thus, we need to set the value of difference into ATT2 to reduce the signal level of reflected wave components to adjust the measured K-factor in the actual propagation experiment. On the contrary, if $P_d - P_r$ is larger than the actual K-factor as indicated in Eq. (4.10), it means that the direct wave is so large that the value of difference needs to be set into ATT1 to reduce the signal level of direct wave components to adjust the measured K-factor.

In order to confirm the proposed method of calibration mentioned above, some basic experiments have been carried out.

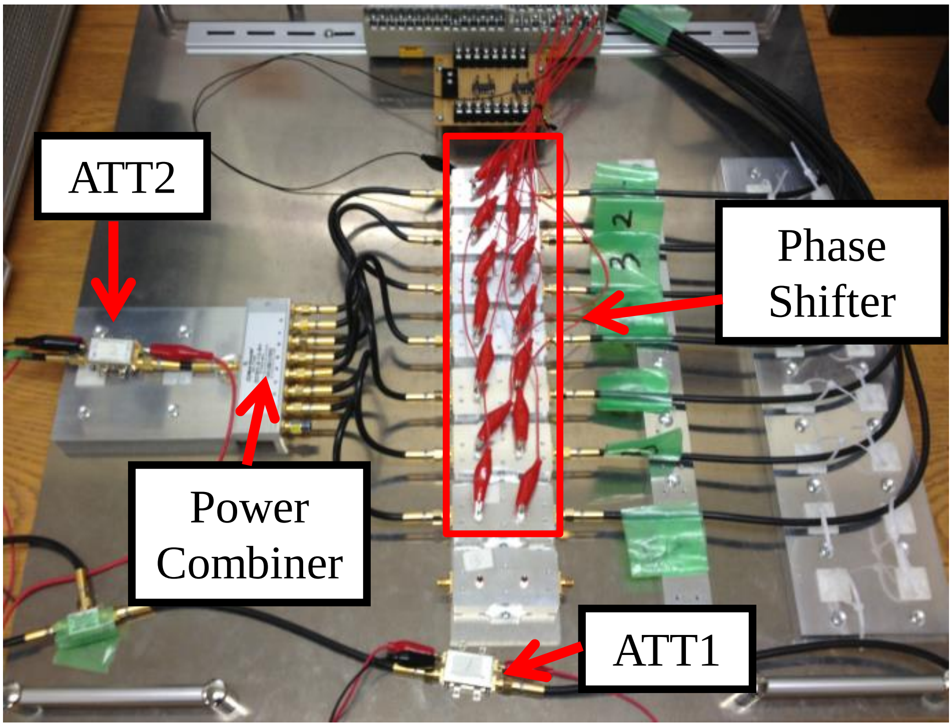

Fig. 4.4 Photograph of the developed fading emulator

First of all, a basic experiment for confirming the realization of the Rice channel has been conducted using the proposed calibration method by the developed fading emulator, where the human effects are not considered.

Fig. 4.5 shows the measurement setup, which is the prototype of fading emulator developed in Toyama University [73]. A sleeve antenna at 950MHz located at the center is used to receive the combined signals, where another sleeve antenna beside is used to create a strong direct radio wave. 7 scattering units with radio wave absorbers behind them can create Rayleigh fading signals by varying the phases and amplitudes in the control circuit of fading emulator, as shown by Fig. 4.4.

Fig. 4.6 shows a vector diagram of both Rayleigh and Rice distribution created by the fading emulator. The black points indicate the entire snapshots of received signals. The points plotted at the center of the diagram shows the Rayleigh distribution situation while the points plotted away from the center of the diagram shows the Rice distribution results when $K = 13$ dB. As an example, the red arrow denoted by h_d shows the channel response of direct wave while the white arrow indicated by h_{nr} shows that of the multipath wave components. The green arrow denoted by h_{nc} shows the combined outcome. In Fig. 4.6, the relationships of three vectors indicate that the proposed Rice channel can be realized using the proposed calibration method by using the fading emulator

Fig. 4.7 shows the various instantaneous response of a dipole antenna with a walking distance of 50 wavelengths at 950 MHz in different values of K-factor using the method of calibration by the fading emulator using Eqs. (4.9) and (4.10). As shown in Fig. 4.7, with the value of K-factor increasing, the deep nulls disappear owing to an increase in the power ratio of direct and reflected waves controlled by the fading emulator.

Fig. 4.8 shows the CDF characteristics of received signals corresponding to the instantaneous responses shown in Fig. 4.7. The theoretical curve for the I-zero response [50], defined as the modified Bessel function of the first kind with order zero, is also included as the dotted curve, which is generally used to describe the Rice distribution. It can be seen that measured results indicated by the red curves in different values of K-factors agree well with their theoretical curves, indicating the effectiveness of proposed calibration method.

After the calibration method is validated by using dipole antenna, the experiments using the dynamic human phantom considering the arm-swinging motions have been carried out.

In previous studies [38] [56], the shadowing effects attributed to the arm-swinging motion are shown to simultaneously affect the direct wave between the two on-body antennas and reflected wave components from the surrounding objects. Therefore, it is necessary to measure the direct and multipath signals individually and analyze the relationship between the value of K-factor, P_d and $\mathrm{E}[P_r]$, to confirm the validity of proposed method of calibration. The measurements are presented in five sections, 4.4.1, 4.4.2, 4.4.3, 4.4.4, and 4.4.5, as follows.

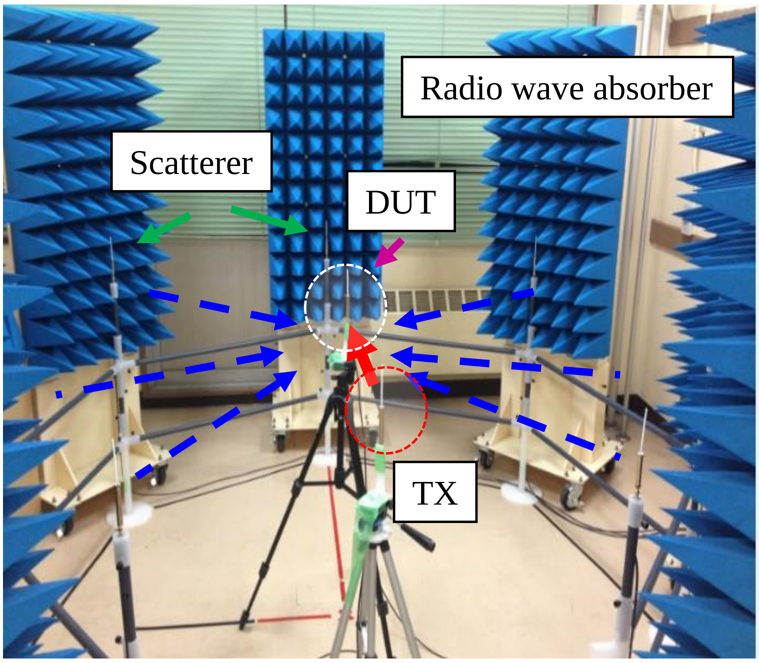

Fig. 4.5 Rice confirmation experiment without human phantom

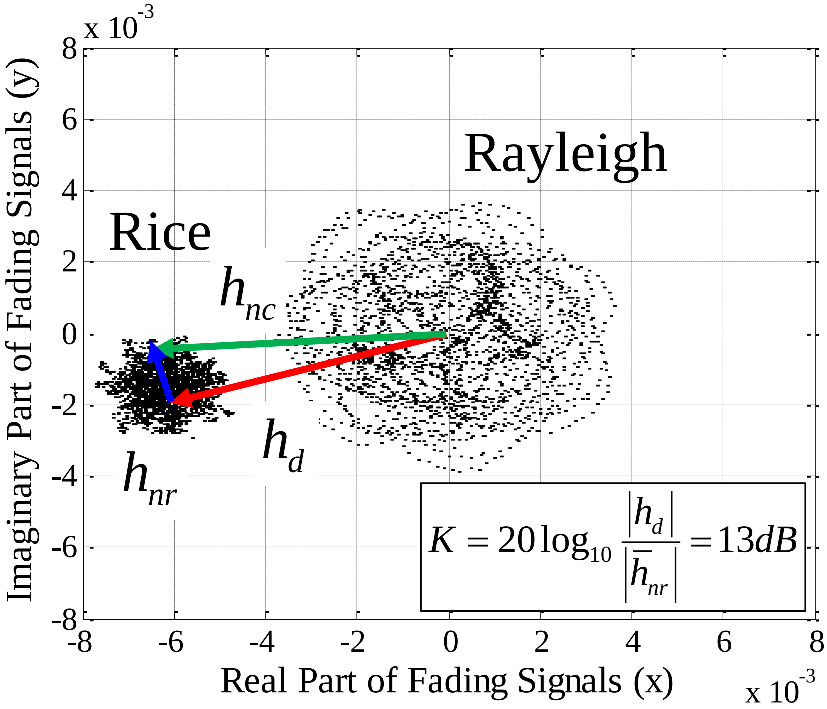

Fig. 4.6 Vector diagram of received signals in Rayleigh and Rice distribution realized by fading emulator

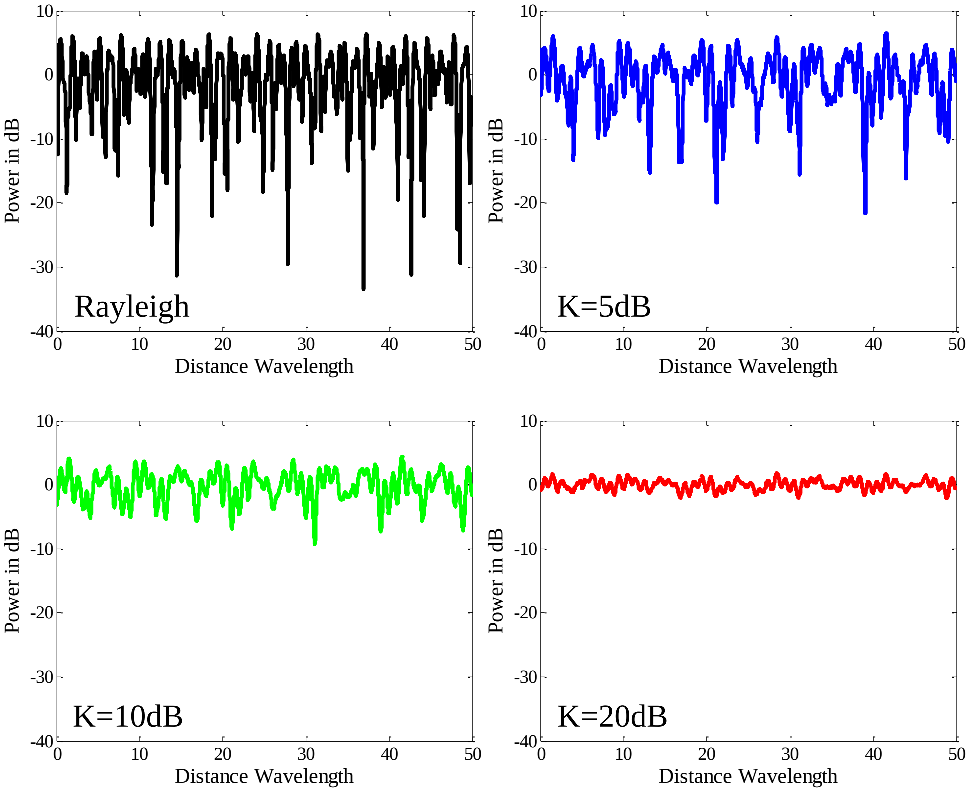

Fig. 4.7 Instantaneous response with different values of K-factors calibrated by the fading emulator

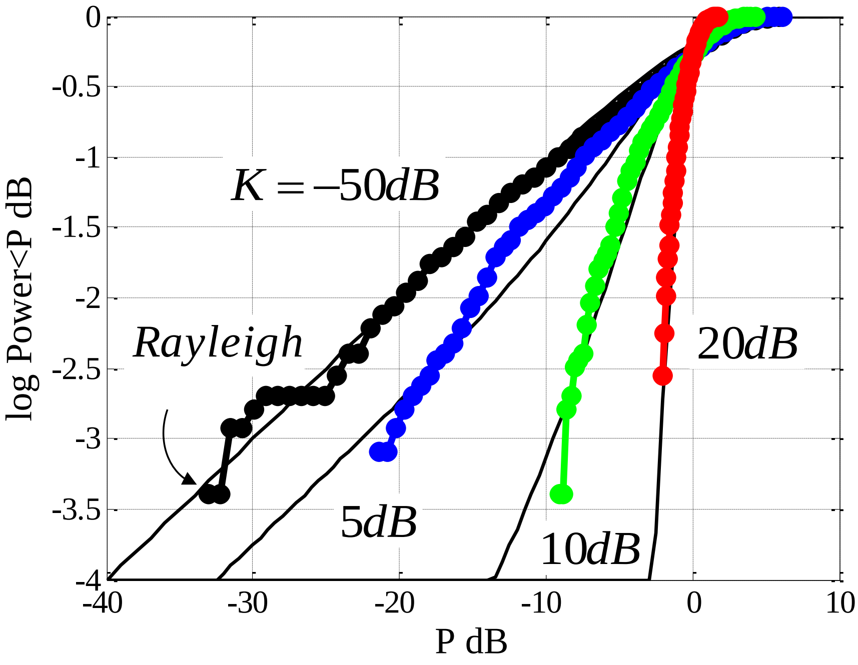

Fig. 4.8 CDF characteristics with different values of K-factors

4.4.1 Measurement of P_d

Initially, the path loss between the two BAN antennas that represents the power of the direct wave (P_d) was measured considering the arm-swinging motion in BAN on-body situation. We chose a half-wavelength dipole antenna as a test antenna because of an easy understanding of the physical mechanism with regard to the measured results owing to simple radiation properties.

In Fig. 4.9, the picture on the left-hand side shows the photograph of the arm-swinging dynamic phantom [38], and the figure on the right-hand side shows its configuration. The receiving half-wavelength dipole antenna at 950 MHz in the vertical orientation was located at position A on the left-hand side of the waist of the structure. The transmitting antenna was mounted at positions B and C, which are 45° and 135° away from position A in the same horizontal plane around the torso, as shown in the right-hand side figure of Fig. 4.9. The distances from A to B and A to C around the torso of the phantom can be calculated as 17.3 cm and 51.8 cm, respectively. The separation between the dipole antenna and the surface of the phantom is set to 1 cm. The impedance characteristics when the separation is 1 cm are shown in Fig. 4.10 for three cases: the results calculated by the method of moments, those measured by the phantom, and the results for a human (22-year-old Japanese male, 70 kg in weight and 175 cm in height). Furthermore, the analytical results when the distance between the antenna and the phantom was 3 cm [38] are also included in Fig. 4.10. It can be seen that there is little difference between the result of VSWR when the separation is 1 cm and that of 3 cm, which indicates that the separation between the antenna and phantom does not have a serious impact on the impedance characteristics because the design uses a dipole antenna with relatively wideband characteristics. Thus, for a more realistic wearable situation, in this study, the separation is set to 1 cm in all analyses and measurements.

Additionally, two coaxial cables were used to connect the two dipole antennas to a VNA for measuring the S21 characteristic. Detailed descriptions of the measurement model and procedures are given in [39]. The phantom can swing both the arms to create the shadowing effects. The angle of left arm was changed from –15 to 40 degrees at 5 degrees intervals while the right arm was changed from 40 to –15 degrees simultaneously as the same manner, which has been confirmed by analyzing the statistical measurements of walking motion using the real test persons [56].

Fig. 4.11 shows the measured results with two different positions of the two dipole antennas (A-B and A-C) and the angle of left arm as parameters. As can be seen, when the angle of left arm is varied from –15° to 40°, the curves of path loss change correspondingly for each position. In A-C position, the path loss is greater with considerable variation because of the obstruction of the phantom body and shadowing effects caused by the arm, as shown by the curve with the ■ symbol. On the other hand, if the two antennas are placed close to each other, in position A-B (shown by the curve with symbol ●), the level of path loss decreases, indicating a strong direct wave level. The characteristics of path loss at these two positions (A-B and A-C) will be used to verify the proposed calibration method, as will be presented later in Sects. 4.4.4 and 4.4.5.

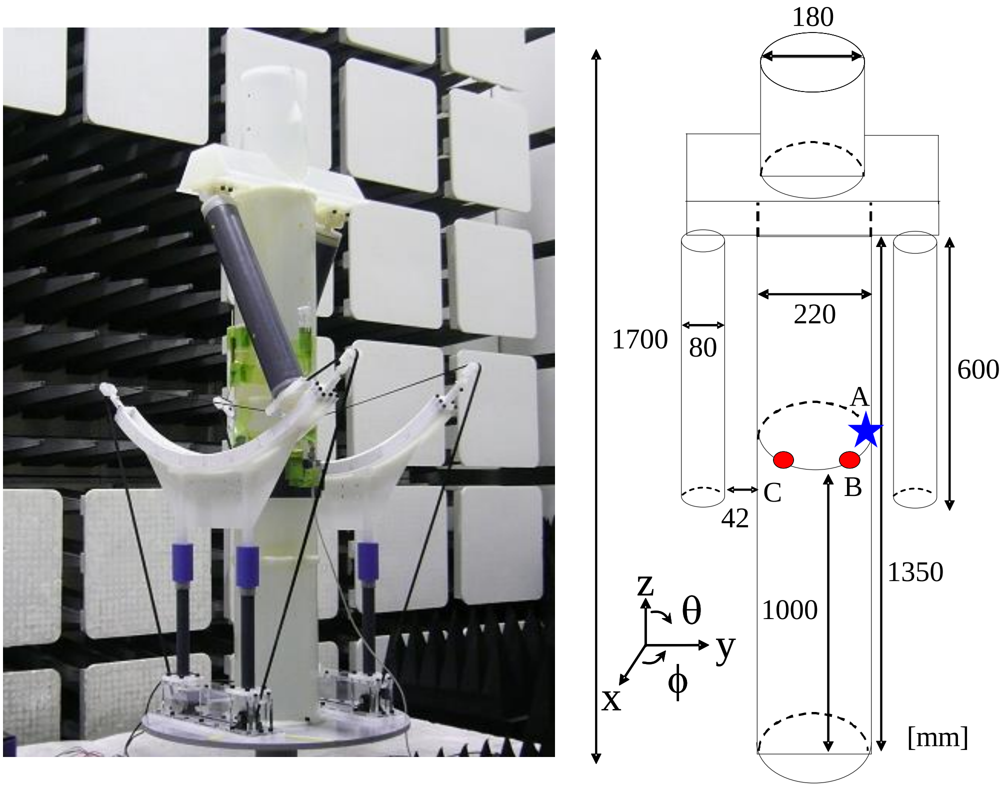

Fig. 4.9 Photograph and configuration of the arm-swinging dynamic phantom

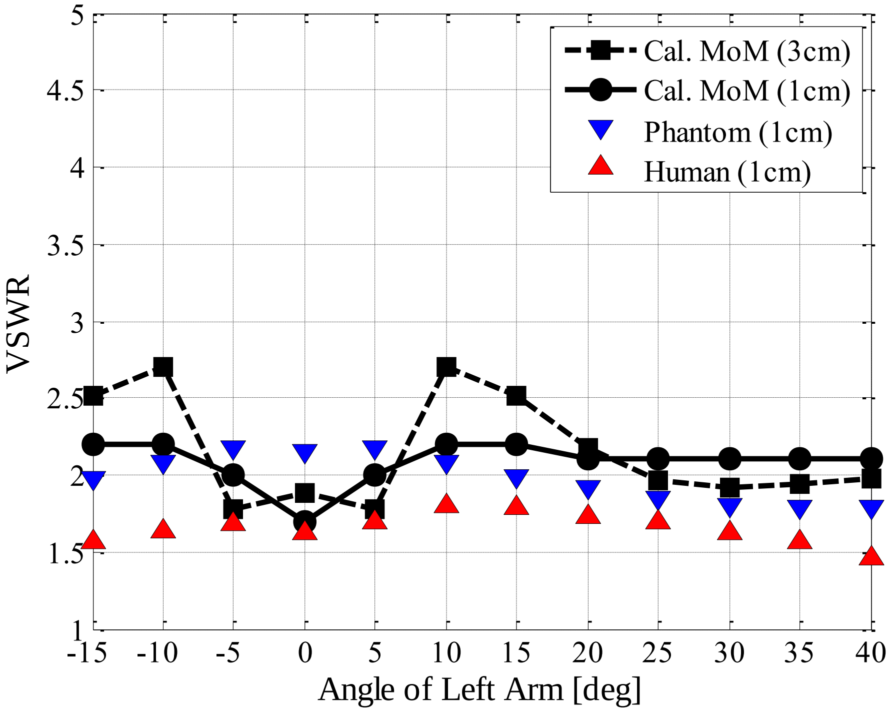

Fig. 4.10 VSWR vs. angle of the left arm at location A

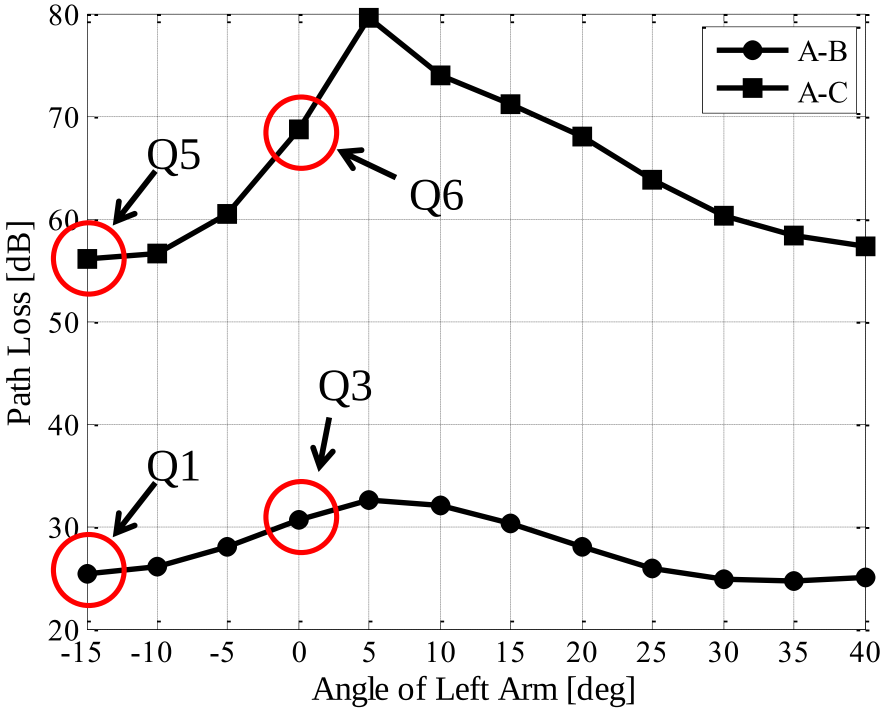

Fig. 4.11 Path loss vs. angle of left arm for different antenna positions

4.4.2 Measurement of P_r

The average power of the reflected waves (E[P_r]) at different angles of the left arm also needs to be measured.

In this case, only the receiving antenna located at position A, shown in Fig. 4.9, is used for collecting the combined multipath radio waves created by the scattering antennas using the developed RF-controlled fading emulator.

As shown in Fig. 4.12, when the angle of the left arm is varied from −15° to 40° in intervals of 5°, a significant degradation of approximately 15.5 dB can be observed. The reason is that when the left arm is close to the dipole antenna attached to the waist, the radiation efficiency reduces significantly because of the shadowing effects caused by the arm [38].

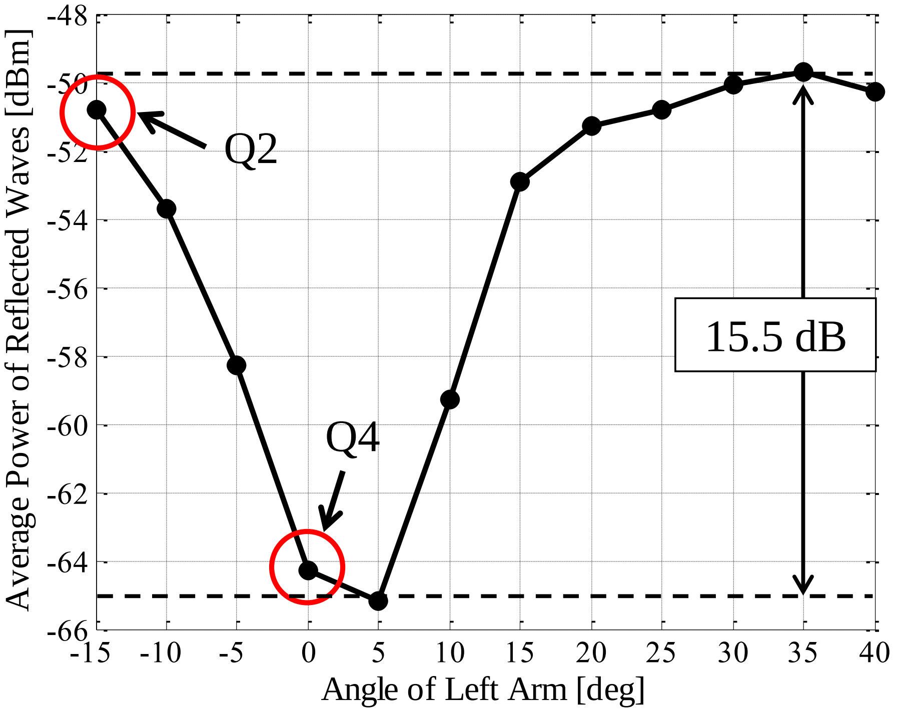

Fig. 4.12 Variation of multipath signals vs. angle of the left arm

4.4.3 Preliminary Experiment using a Phantom

To obtain the actual value of the K-factor in indoor on-body Rice channel situations, a preliminary experiment has been conducted using the human phantom with a fixed arm angle. As shown in Fig. 4.13, an arm-swinging dynamic phantom with salt water inside, which is close to the electrical property of the human body, is used instead of a real test person because of better repeatability [38].

The phantom's torso has a diameter of 22 cm and a height of 120 cm. The receiving antenna was located at position A shown in Fig. 4.9 whereas the transmitting antenna was located at positions B and C. The two antennas attached to the phantom were separated by 1 cm from the surface for the experiment. Moreover, the left and right arms were fixed at –15° and 40° angles, respectively. For the measurement, the frequency was set to be 950 MHz. The data of the received signals were collected and analyzed on the receiving side.

Fig. 4.14 shows the top view of the indoor measurement environment, which is an 8 m × 6.5 m classroom at Toyama University. The distance from the floor to ceiling is 3 m. The distance from the human phantom to the wall is set to 1.8 m on the right side and 1 m on the back side. Fig. 4.15 shows the measurement scenarios. The arms of the human phantom can be fixed at any desired angle, as shown in Fig. 4.15 (a). The phantom was pushed by a person along a distance of 6 m for 20 s with two dipole antennas attached to the phantom, as shown in Fig. 4.15 (b).

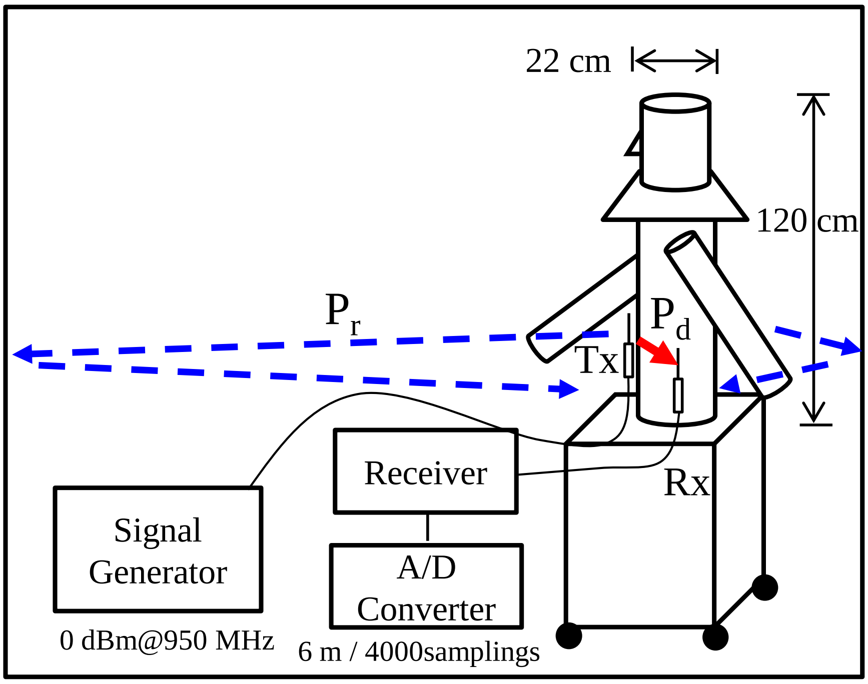

Fig. 4.13 Setup for indoor measurement of K-factor

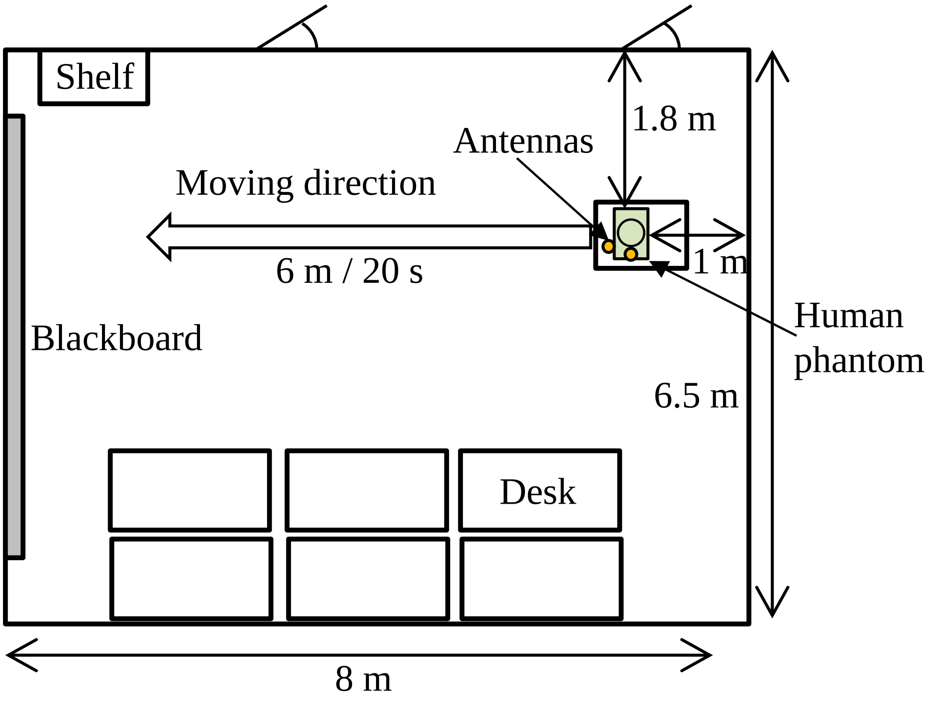

Fig. 4.14 Measurement environment in a classroom

(a) Arm-fixed human phantom

(b) Experiment scenario

Fig. 4.15 Photograph of propagation experiment

Fig. 4.16 shows the measured results of the propagation experiment. Figs. 4.16 (a) and (b) indicate the instantaneous response and cumulative distribution function (CDF) characteristics when the left arm is fixed at −15° and the antennas are mounted at position A-B, shown in Fig. 4.9. Further, Figs. 4.16 (c) and (d) indicate the instantaneous response and CDF characteristics when the left arm is also fixed at −15° and the antennas are mounted at position A-C, shown in Fig. 4.9. The theoretical curve for Rayleigh response is also included. For each case, measurements have been taken thrice so as to reduce the error of measurement. During the measurement time of 20 s, the number of samples in the receiver was set to be 4000, which means that we recorded data every 0.005 s, as indicated by the horizontal axes in Figs. 4.16 (a) and (c). The CDF curves shown in Figs. 4.16 (b) and (d) indicate that the measured values of K-factor are 18 dB and 5 dB in the two antenna positions A-B and A-C, respectively.

Moreover, with this propagation experiment, the actual values of K-factor can be measured for different relative antenna positions and different instantaneous angular positions of the arms, which will then be used for the validation of the proposed calibration method in the Sects. 4.4.4 and 4.4.5.

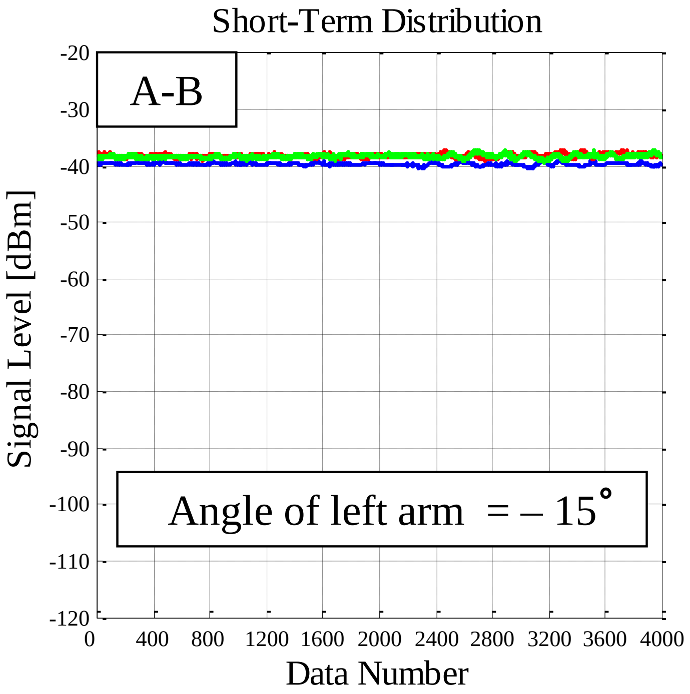

(a) Instantaneous response at position of A-B

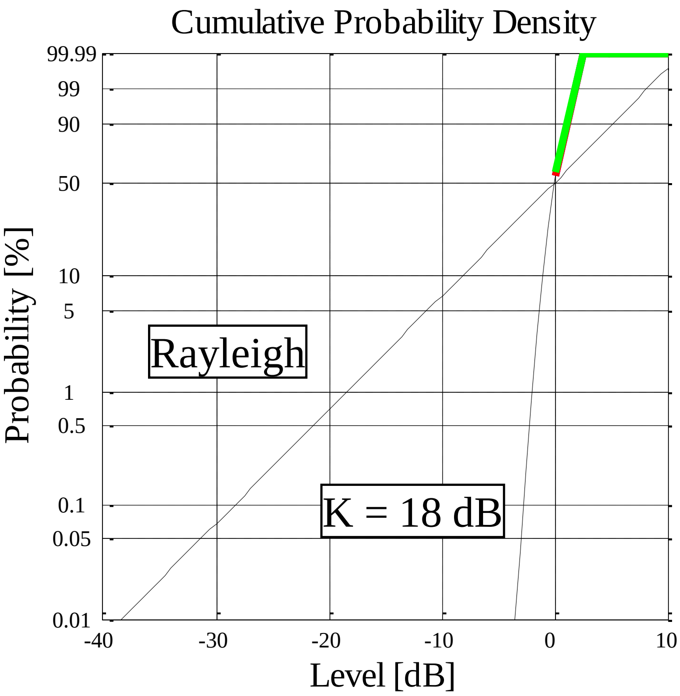

(b) CDF characteristics at position of A-B

Fig. 4.16 Measurement results of the propagation experiment in a classroom

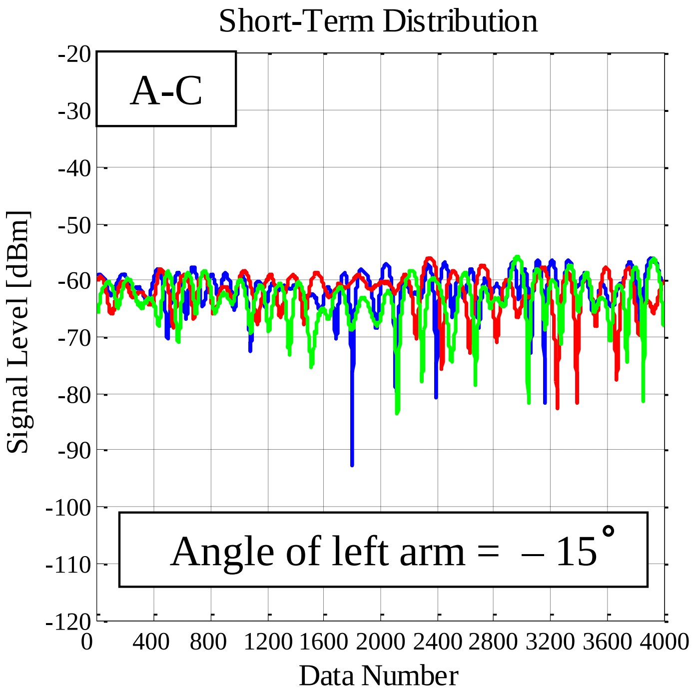

(c) Instantaneous response at position of A-C

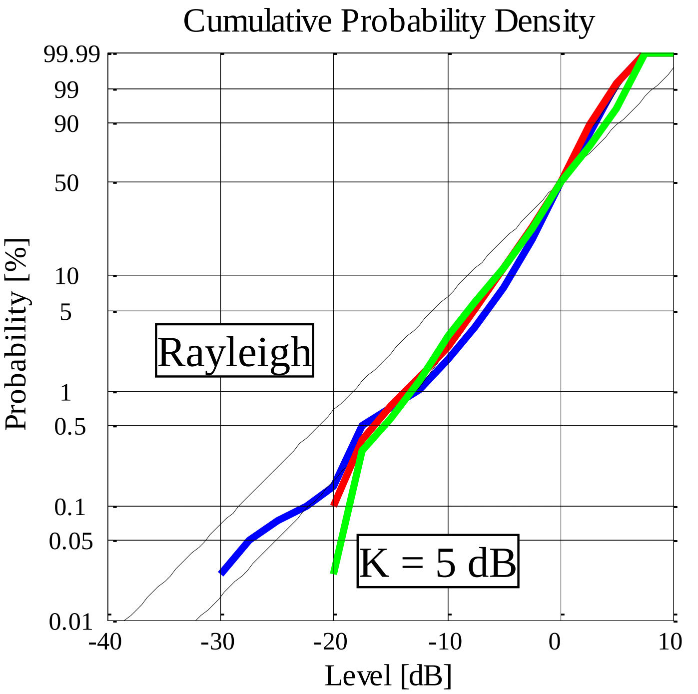

(d) CDF characteristics at position of A-C

Fig. 4.16 Measurement results of the propagation experiment in a classroom

4.4.4 Calibration in Fading Emulator

After P_d and $E[P_r]$ are analyzed as mentioned above, the K-factor can be achieved on the basis of these two parameters by adjusting the attenuator in the fading emulator. For example, we choose a specific situation when the angle of the left arm is at a reference position of –15°. The receiving and transmitting antennas are placed in positions A and B, respectively, as shown in the right figure of Fig. 4.9. From the propagation experiment described in Sect. 4.4.3, the K-factor is measured as 18 dB for this case, as indicated by Fig. 4.16 (b). As can be seen in Fig. 4.11, when the angle of the left arm is –15°, the path loss is 25.3 dB shown as Q1. Because the transmission power was set to be 0 dBm, the signal level of the direct wave (P_d) is calculated to be –25.3 dBm. Moreover, the average reflected wave $E[P_r]$ is –50.8 dBm as shown by position Q2 in Fig. 4.12 when the angle of the left arm is –15°. Thus, the difference between P_d and $E[P_r]$, which is equivalent to the K-factor, is 25.5 dB. This value is larger than the actual measured K-factor value of 18 dB. Therefore, Eq. (4.10) can be selected to calibrate the fading emulator. Using Eq. (4.10), the value we set to ATT1 can be calculated as [{–25.3 dBm – (–50.8 dBm)} – 18 dB] = 7.5 dB, and ATT2 is set to be 0 dB.

Fig. 4.17 (a) and (b) indicate the results measured with the fading emulator using Eq. (4.10). It can be seen that both the instantaneous response and CDF characteristics obtained by calibrating the fading emulator coincide well with the measured results from the propagation experiment shown in Figs. 4.17 (a) and (b). Therefore, the K-factor, obtained from the propagation experiment, can be realized by setting the attenuators in the fading emulator with the proposed method of calibration.

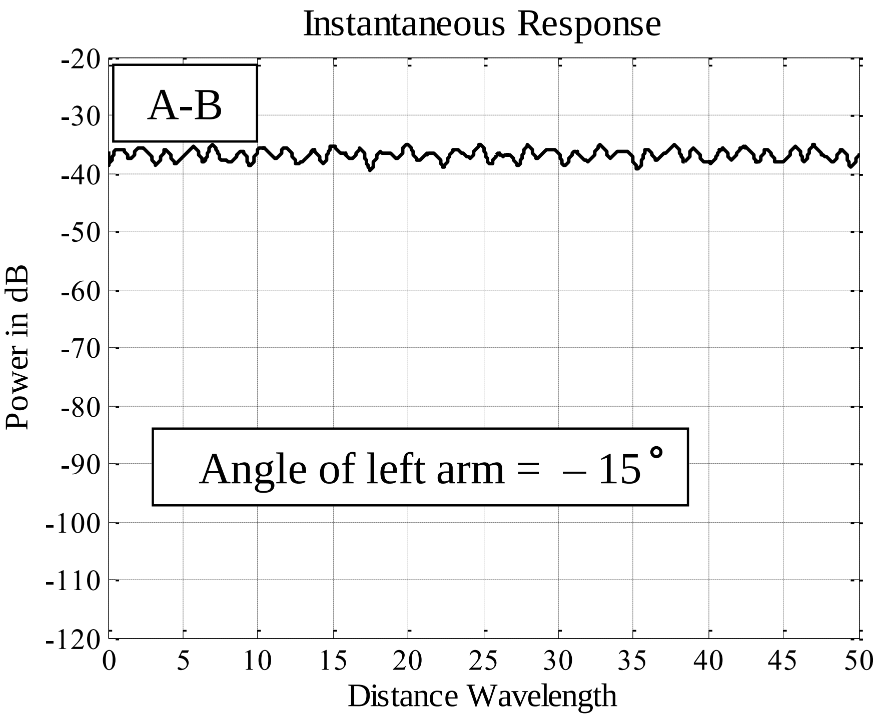

(a) Instantaneous response at position of A-B

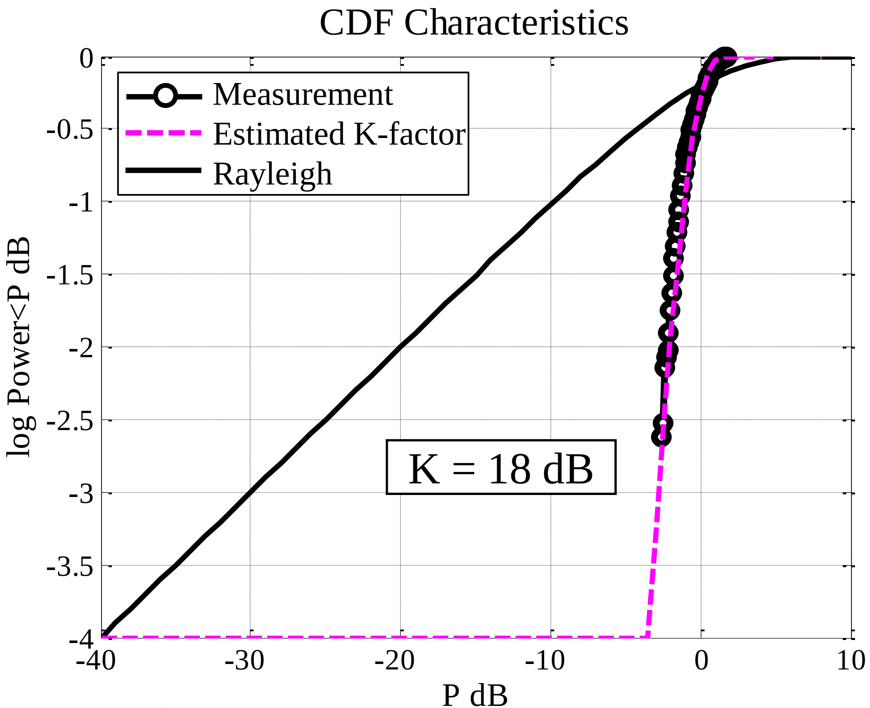

(b) CDF characteristics at position of A-B

Fig. 4.17 Calibration of K-factor when angle of left arm = −15°

4.4.5 Verification of the Proposed Method

After obtaining the values set in the attenuators, the instantaneous K-factors can be estimated for situations where the phantom swings both arms by transforming Eqs. (4.9) and (4.10) as follows:

$$\text{If } P_d - P_r < K, \text{ then}$$

$$K\,(\mathrm{dB}) = P_d\,(\mathrm{dBm}) - \{E[P_r]\,(\mathrm{dBm}) - ATT2\,(\mathrm{dB})\} \tag{4.11}$$

$$\text{If } P_d - P_r > K, \text{ then}$$

$$K\,(\mathrm{dB}) = \{P_d\,(\mathrm{dBm}) - ATT1\,(\mathrm{dB})\} - E[P_r]\,(\mathrm{dBm}) \tag{4.12}$$

Here, Eq. (4.12) is selected because we will analyze the same situation mentioned in Sect. 4.4.4 with the left arm at −15° angle and antennas at position A-B. Thus, the K-factors at other angles of the left arm at 5° degrees intervals can be estimated using Eq. (4.12), which are illustrated in Table 4.1. Thereafter, we conduct the actual experiment, where the human phantom is walking for a distance of 50 wavelengths at 950 MHz, using the fading emulator to confirm the accuracy of the estimated K-factors, shown in the right column of Table 4.1.

For a certain position, calibrated with the fading emulator, taken as a reference position, as shown in Fig. 4.17, we only need to change the angle of left arm at 5° intervals to measure the combined signal levels of P_d and E[P_r] created by the fading emulator at every instantaneous angular position. The measured K-factor will be automatically set by the direct wave P_d and reflected waves E[P_r] caused by the movement of the left arm, as shown in Table 4.1. For example, from position Q3 in Fig. 4.11 and position Q4 in Fig.

4.12, we can infer the values of P_d and E[P_r] to be –30.6 dBm and –64.3 dBm, respectively, when the left arm is at an angle of 0°. Because ATT1 is set to be 7.5 dB, the K-factor can be calculated as ((–30.6 dBm – 7.5 dB) – (–64.3 dBm)) = 26.2 dB, as shown in Table 4.1.

The estimated K-factors at position A-C are also included in Table 4.2. On the basis of the calibration method at position A-B, we chose the same angle of the left arm at –15° as a reference position. From the propagation experiment described in Sect. 4.4.3, the K-factor is measured as 5 dB for this case, as indicated by Fig. 4.16 (d). As can be seen in Fig. 4.11, when the angle of the left arm is –15°, the signal level of the direct wave (P_d) is found to be –56 dBm, as shown by position Q5. The average reflected wave E[P_r] is –50.8 dBm as shown by position Q2 in Fig. 4.12, when the angle of the left arm is –15°. Thus, the K-factor can be calculated to be –5.2 dB. This value is less than the actual measured K-factor value of 5 dB. Therefore, Eq. (4.9) is selected to calibrate the fading emulator. Using Eq. (4.9), the value we set to ATT2 can be calculated as 5 dB – (–56 dBm – (–50.8 dBm)) = 10.2 dB, and ATT1 is set to be 0 dB in this case. After the K-factor at the reference position is calibrated, the K-factors at each arm-swinging angle are estimated, as shown in the right column of Table 4.2. For example, from position Q6 in Fig. 4.11 and position Q4 in Fig. 4.12, we can infer the values of P_d and E[P_r] to be –68.7 dBm and –64.3 dBm, respectively, when the left arm is at an angle of 0°. Because ATT2 is set to be 10.2 dB, using Eq. (4.11), the K-factor can be calculated as ((–68.7 dBm) – (–64.3 dBm – 10.2 dB)) = 5.8 dB, as shown in Table 4.2.

Table 4.1 K-factor estimation for different angles of the left arm with antennas at position A-B

Angle of Left Arm (deg)	Pd (dBm)	Pd (dBm)–ATT1(dB)	E[Pr](dBm)	K(dB) = (Pd (dBm) – ATT1 (dB)) – E[Pr] (dBm)
– 15	– 25.3 **(Q1)**	– 32.8	– 50.8 **(Q2)**	**18 (Measured by propagation experiment)**
– 10	– 26.1	– 33.6	– 53.7	20.1
– 5	– 27.9	– 35.4	– 58.3	22.9
0	– 30.6 **(Q3)**	– 38.1	– 64.3 **(Q4)**	26.2
5	– 32.5	– 40	– 65.2	25.2
10	– 32.1	– 39.6	– 59.3	19.7
15	– 30.3	– 37.8	– 52.9	15.1
20	– 27.9	– 35.4	– 51.3	15.9
25	– 25.8	– 33.3	– 50.8	17.5
30	– 24.8	– 32.3	– 50.1	17.8
35	– 24.6	– 32.1	– 49.7	17.6
40	– 25.0	– 32.5	– 50.3	17.8

Table 4.2 K-factor estimation for different angles of the left arm with antennas at position A-C

Angle of Left Arm (deg)	Pd (dBm)	E[Pr](dBm) –ATT2(dB)	E[Pr](dBm)	K(dB) = Pd (dBm) – (E[Pr] (dBm) – ATT2(dB))
– 15	– 56 **(Q5)**	– 61	– 50.8 **(Q2)**	**5 (Measured by propagation experiment)**
– 10	– 56.6	– 63.9	– 53.7	7.3
– 5	– 60.5	– 68.5	– 58.3	8
0	– 68.7 **(Q6)**	– 74.5	– 64.3 **(Q4)**	5.8
5	– 79.5	– 75.4	– 65.2	–4.1
10	– 74.0	– 69.5	– 59.3	–4.5
15	– 71.1	– 63.1	– 52.9	–8
20	– 67.9	– 61.5	– 51.3	–6.4
25	– 63.8	– 61.0	– 50.8	–2.8
30	– 60.3	– 60.3	– 50.1	0
35	– 58.4	– 59.9	– 49.7	1.5
40	– 57.2	– 60.5	– 50.3	3.3

Fig. 4.18 (a) and (b) show the CDF variations for four different left arm angles (–15°, 0°, 15°, and 40°), when the dipole antennas are located at positions A-B and A-C, respectively. The theoretical curve for Rayleigh response is shown with the solid line. The curves with symbol ○ indicate the data obtained from the fading emulator whereas the broken lines show the estimated values of K-factor, shown in Table 4.1 and 4.2, which are calculated from I-zero response. As can be seen, the measured data agree well with the estimated values of K-factor both in positions A-B and A-C, indicating that the method of estimating the K-factor using measured results of P_d and E[P_r] is correct. It can also be seen that when the K-factor is negative, such as the case where the angle of the left arm is 15° as shown in Fig. 4.18 (b), the CDF curve coincides with the Rayleigh distribution. This is attributed to the fact that when the position of two dipole antennas is changed from A-B to A-C, a longer link distance results in an obvious increase of the path loss as shown in Fig. 4.11, leading to a significant degradation of K-values due to a large reduction of the direct wave compared with the multipath components.

Based on the extensive investigations mentioned above, the proposed method of calibrating the fading emulator is confirmed to be valid. This method can be used for BAN-OTA testing to realize the actual radio wave propagation scenarios such as for dynamic characteristics attributed to human motion.

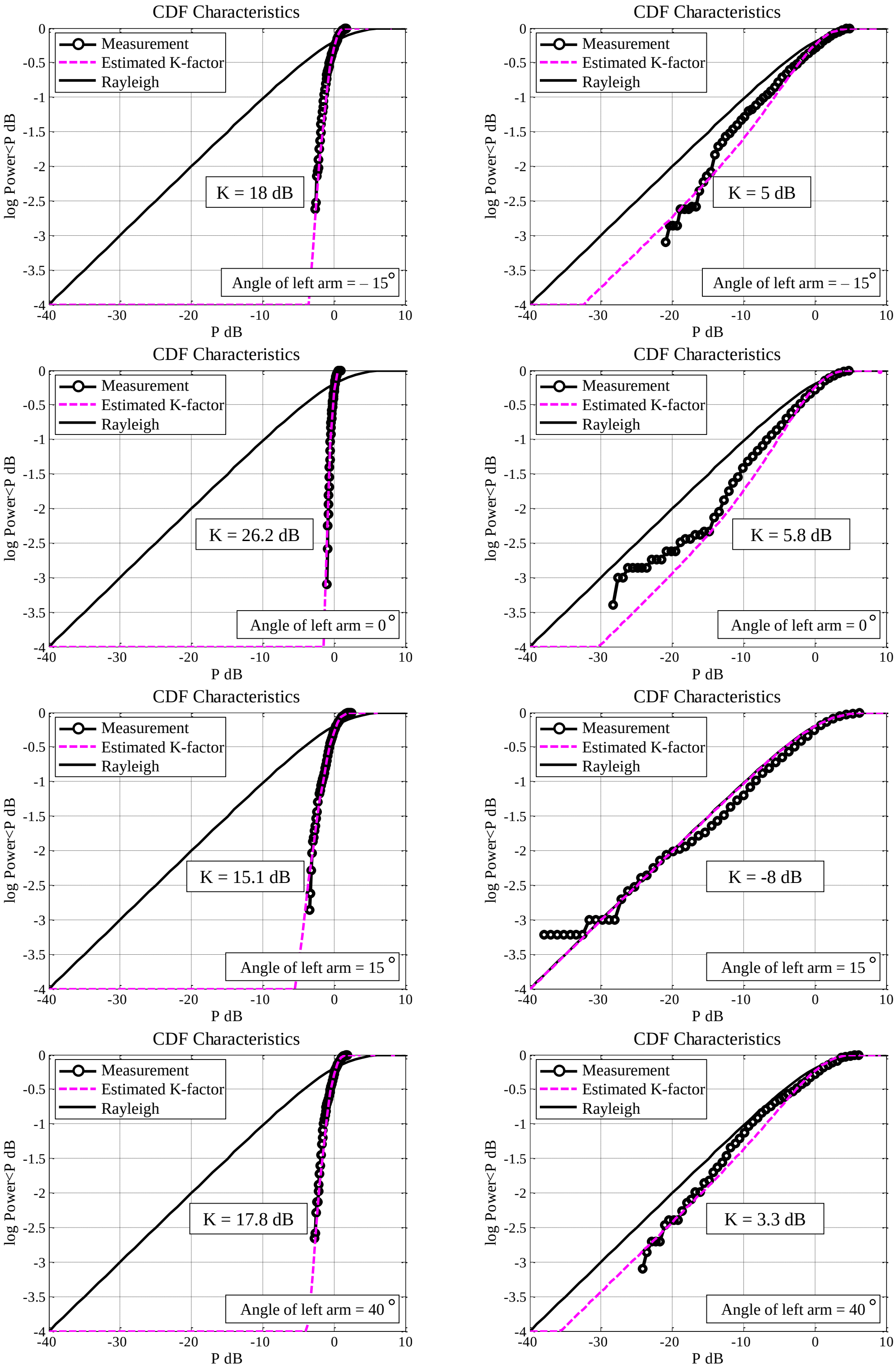

(a) (b)

Fig. 4.18 CDF variations measured using the fading emulator for different angles of the left arm: (a) position A-B, (b) position A-C

4.5 Experiment When Phantom is Walking

After the proposed calibration method is verified, an experiment to realize the actual Rice channel in the developed fading emulator with continuous human walking motion has been conducted, as presented in this section.

Fig. 4.19 shows the top view of the BAN fading emulator, as introduced in Fig. 4.2. The dynamic phantom placed at the center is controlled by a computer and can swing both the arms. In addition, 7 scattering half-wavelength sleeve dipole antennas at 950 MHz with radio wave absorbers behind them can create Rayleigh fading signals by varying the phases and amplitudes in the control circuit of the fading emulator. The receiving dipole antenna is fixed at position A, and the transmitting dipole antennas are mounted at positions B and C, in the same manner shown in Fig. 4.9.

After the K-factor (with values 18 dB and 5 dB), shown in Fig. 4.16, is calibrated at the reference position where the left arm is at –15°, as described in Sect. 4.4, the experiment can be conducted using the fading emulator for a continuous arm-swinging motion. The left arm was varied from –15° to 40° and back to –15° while the right arm was changed from 40° to –15° and back to 40° simultaneously in the opposite direction based on the statistical measurements on the actual human walking motion using real test persons [56]. The speed of arm-swing motion is 20 seconds per cycle. On the other hand, the measurement time of the fading emulator is 260 seconds. Therefore, the arms need to swing continuously for 13 cycles to fit the measurement time.

Furthermore, a Monte Carlo simulation based on the proposed analytical Rice channel model, mentioned in Sect. 4.3, has been carried out. The method of analyzing the combined effects of shadowing-fading is explained in detail in [38] [56]. The phantom walks at a stride length of 60 cm. Two strides, equivalent to a two-way swing, are equal to 120 cm, corresponding to 1 cycle of arm-swinging motion. Therefore, during the 13 cycles of arm-swinging motion, the moving distance can be calculated as 1560 cm, which is about 49 wavelengths at 950 MHz. The number of snapshots is set to be 100 samples per wavelength. The XPR is set to be 50 dB, which means that the polarization is assumed to be vertical because only the vertical polarization of the dipole antennas is used in the fading emulator. The values of the initial phases and angle of direction of motion are set the same as those of the actual setup of the fading emulator. The results are analyzed as follows.

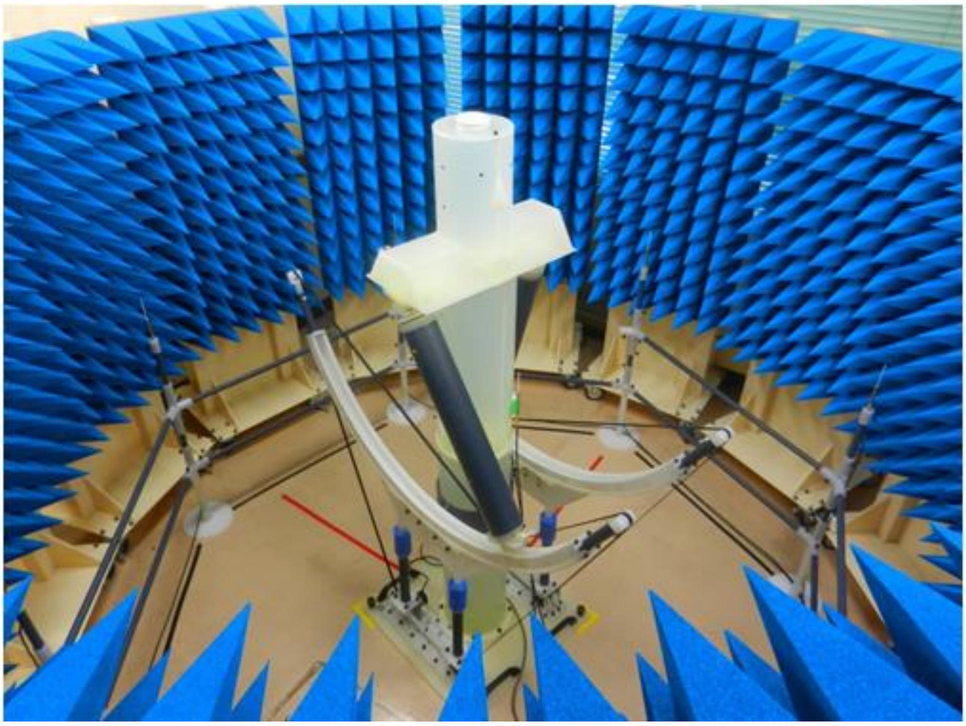

Fig. 4.19 Top view of the BAN fading emulator with the arm-swinging dynamic phantom

Figs. 4.20 (a) and (c) (shown by the black curve) illustrate the results of instantaneous response measured in the fading emulator for a walking distance of 50 wavelengths at 950 MHz when the dipole antennas are located at positions A-B and A-C, as shown in Fig. 4.9. Further, Figs. 4.20 (b) and (d) (shown by the red curve) illustrate the analytical results using the Monte Carlo simulation.

As can be seen in Figs. 4.20 (a) and (b), in situation A-B, the distance between the transmitting and receiving antennas is small, but P_d is strong enough to enable all the K-factors to be maintained at a high level even after being affected by the shadowing effects caused by arm-swinging motion, as can be inferred in Table 4.1. However, in situation A-C, shown with Figs. 4.20 (c) and (d), because P_d almost disappears, as can be inferred by Fig. 4.11, the received signal level is mainly contributed by the multipath radio wave components leading to a significant variation of received signals, as shown in the instantaneous response plot.

Fig. 4.21 shows the CDF characteristics of the combined signals when the phantom walks at a strike length of 60 cm during the 13 cycles of arm-swinging motion. The profile with symbol ○ shows the measured results obtained from the fading emulator corresponding to Figs. 4.19 (a) and (c) whereas the dotted curve with symbol △ indicates the analytical outcome calculated by Monte Carlo simulation corresponding to Figs. 4.20 (b) and (d). The theoretical Rayleigh response curve is illustrated with the solid line in the graph. We can see from Fig. 4.21 that for both the antenna positions, A-B and A-C, the measured results agree well with the analytical outcome indicating that the Rice channel of BAN on-body situation considering human dynamic characteristics can be realized using the developed fading emulator, which is extremely useful for evaluating actual BAN radio modules in BAN-OTA testing.

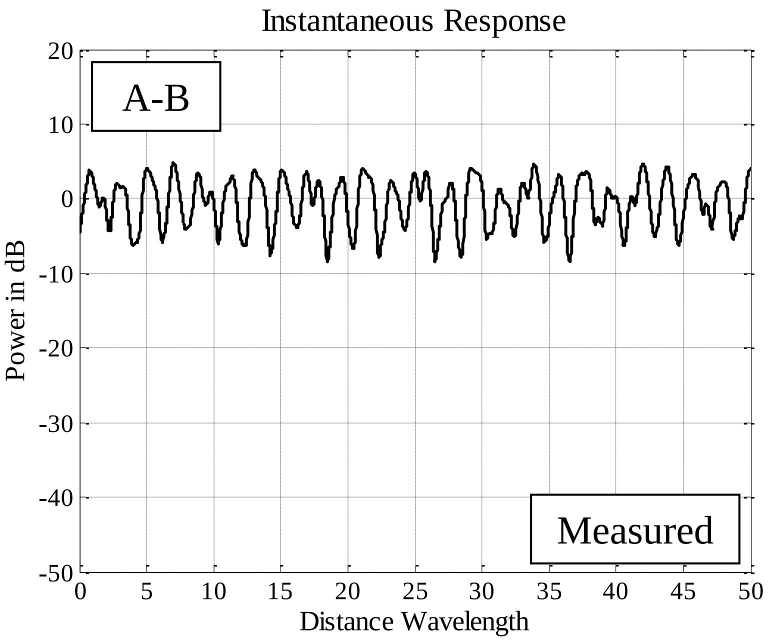

(a) Measured results of instantaneous response at position of A-B

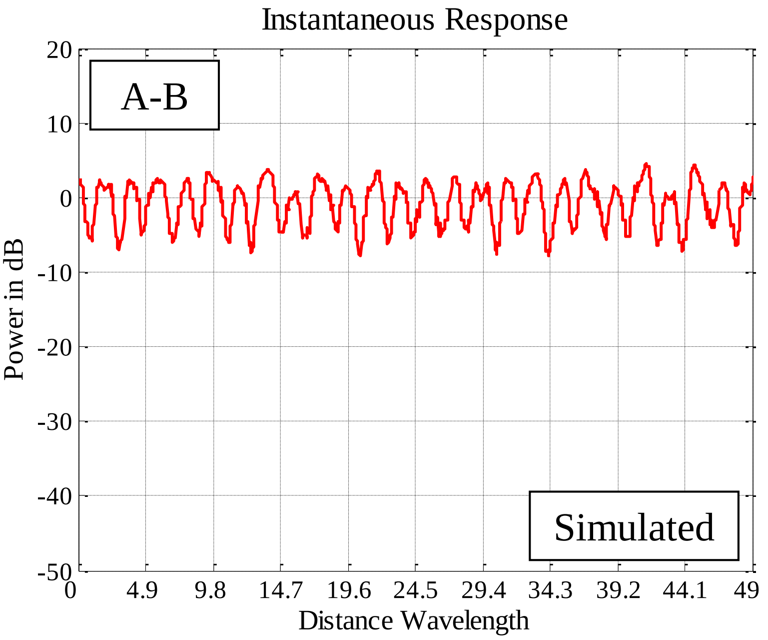

(b) Analytical results of instantaneous response at position of A-B

Fig. 4.20 Measured and analytical results of instantaneous response

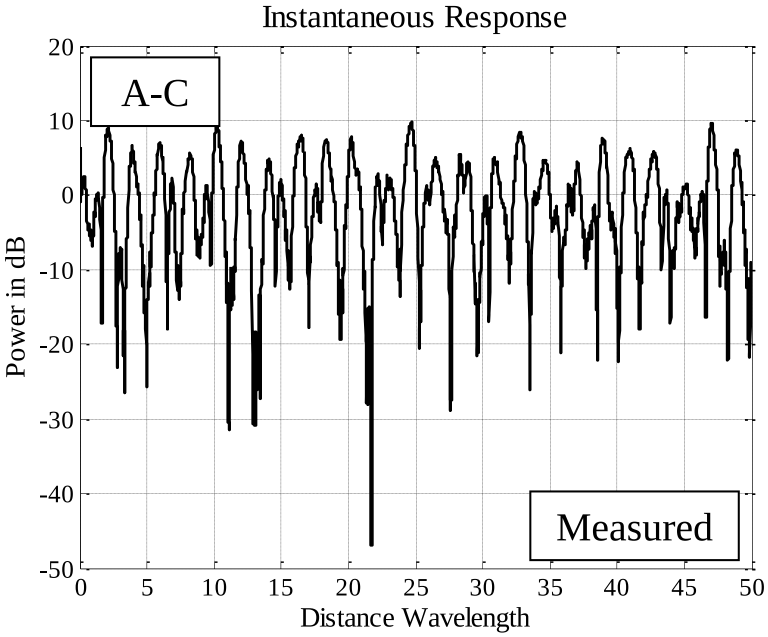

(c) Measured results of instantaneous response at position of A-C

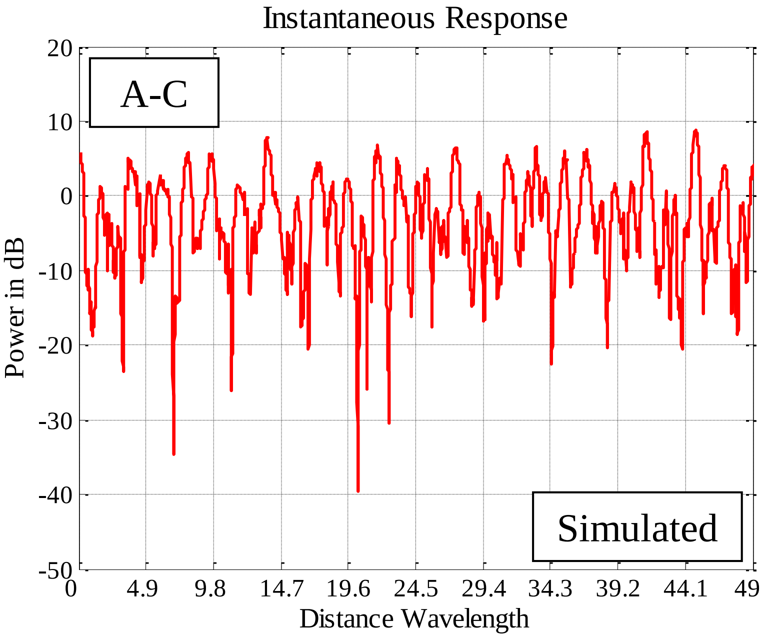

(d) Analytical results of instantaneous response at position of A-C

Fig. 4.20 Measured and analytical results of instantaneous response

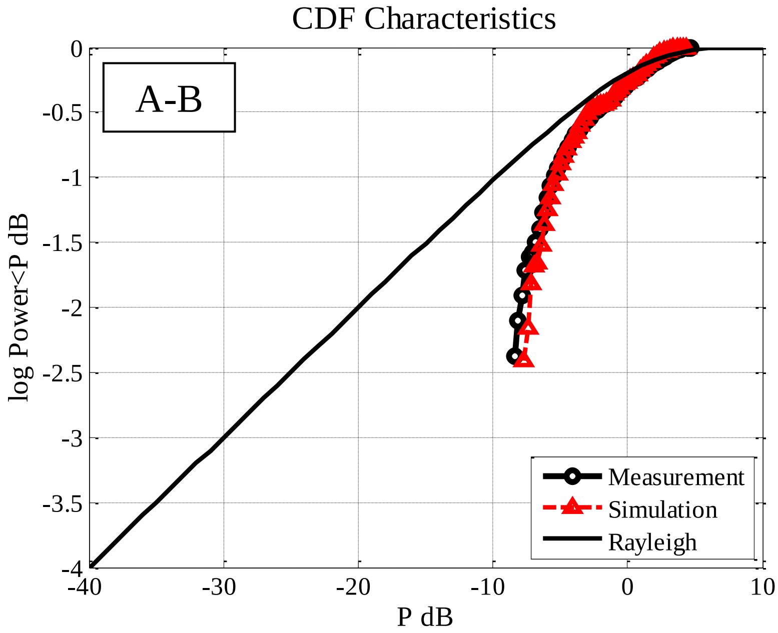

(a) CDF of position A-B,

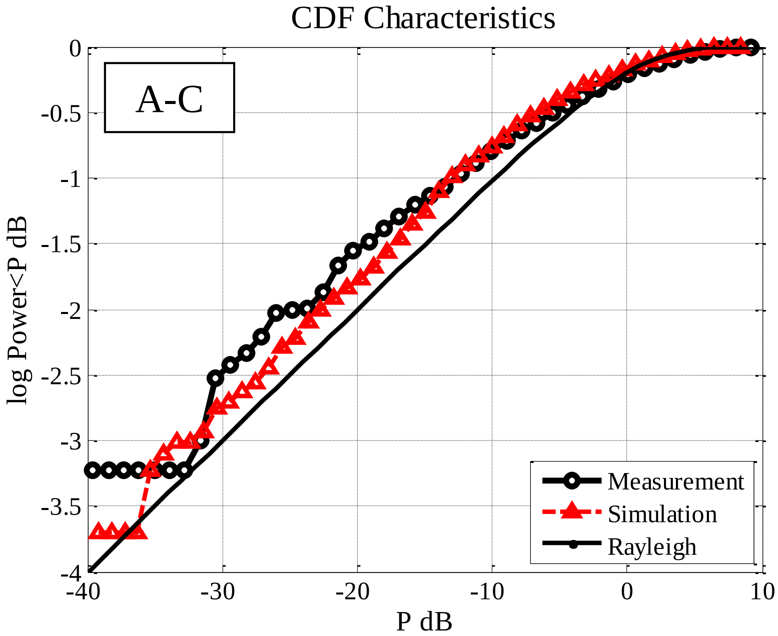

(b) CDF of position A-C

Fig. 4.21 Measured and analytical results of CDF characteristics

4.6 Conclusion

This study presents a new methodology for BAN-OTA testing using a developed fading emulator with a dynamic phantom. Providing the fading emulator with an appropriate K-factor that can represent the actual propagation environment indoors is essential. In addition, an implementation of Rice channel to the developed fading emulator in the BAN situation is presented. Then, a method of calibration where the attenuators in the fading emulator are adjusted to achieve the actual K-factor values of the on-body Rice channel is advanced, which is confirmed by analyzing the variation of instantaneous K-factor for each angle of the arm. Finally, an experiment was conducted on the fading emulator when the human phantom is walking with a continuous arm-swinging motion. The results show that using the proposed fading emulator, the actual Rice channel propagation environment considering dynamic characteristics of human walking motion can be realized in BAN-OTA testing. The aim is to realize a BAN-OTA apparatus that can assess the communication quality of commercially available BAN radio modules for on-body communication considering human dynamic characteristics. This will be address in future studies.

5. Three-Dimensional Channel Model

5.1 Introduction

The development of simple and appropriate OTA testing apparatus for mobile terminals with a MIMO system is indispensable to the success of upcoming LTE-Advanced and 5G cellular systems [74-79]. As illustrated in Chapter 1, the method of OTA testing can be classified into two categories: the reverberation chamber and the spatial fading emulator. Several studies for OTA evaluation using the reverberation chamber have been reported [80-84]. These studies examine a simple structure for an OTA apparatus at low cost. However, the apparatus has some drawbacks in terms of difficulties in controlling the angular spread of incident waves and the XPR, and in generating cluster and uniform spectra environments because all of the reflected waves coming from one signal source are uncontrolled.

A fading emulator is one of the other solutions to directly producing a radio multipath environment with high controllability and high accuracy [17] [28] [85] [86]. In the literatures [17] [28], a spatial fading emulator was successfully implemented to evaluate the channel capacity of MIMO antennas. The fading emulator is created based on a two-dimensional channel model in which incident waves coming from a base station are confined to a horizontal plane. Hence, in the apparatus, a number of uncorrelated waves that ensure parallel transmission using MIMO streaming channels exist only in the azimuth angles. This means that a vertically aligned MIMO array cannot be evaluated using a conventional fading emulator [17] because adjacent elements in the array located in the vertical direction exhibit a unity correlation owing to an absence of uncorrelated incident waves in the elevation angles. This eventually degrades the channel capacity.

In future MIMO standardization, a MIMO array implemented in a handset is anticipated to be in commercial use in a system with an increasing number of array elements, such as 4 × 4 and 8 × 8 MIMO systems to achieve gigabit high-speed communications. Thus, the evaluation of a MIMO antenna arranged in the column direction is necessary because a two-dimensional array is advantageous for multi-element compactness.

Another important topic is the diversity of applications. An eight-element MIMO antenna mounted on the wrist for the purpose of gigabit transmission of wearable applications in body area networks (BANs) has been studied [87], as shown in Fig. 5.1 (a). Wearable antennas have a remarkable feature different from conventional antennas used in cellular handsets: their directions mounted on the human body cannot be determined as a specific value, which means that a MIMO antenna fabricated as a linear array located horizontally may change as a vertical array at the time of a practical use. Fig. 5.1 (b) shows a 2-element MIMO array in free space while Figs. 5.1 (c) and (d) shows the analytical results of correlation characteristics and channel capacity at 2 GHz using a conventional 2-dimensional analytical model, when the inclination angle of the antenna α in Fig. 5.1 (b) is changed from -90° to 90°. The results show that the 2-dimensional analytical model cannot be applied for the assessment of wearable MIMO antenna due to the rotation of MIMO array caused by a specific use scenario of operator. In order to evaluate the vertically arranged MIMO array antenna, a three-dimensional OTA test method needs to be developed.

In previous research, several methods for 3D-OTA assessment have been proposed [88-90]. Previous literature [90] provides an analytical model for the assessment of a 3D spatial channel emulator for OTA tests, where the impact of the installation range and interval of probe rings on the spatial correlation characteristics between reception points is presented. However, the variation of MIMO channel capacity caused by different scatterers arrangement is not analyzed. Further, the index for designing an OTA apparatus considering multipath environments and DUT array elements is not advanced.

This study presents a new methodology of the OTA assessment for vertically arranged MIMO array antennas. Particular emphasis is placed on how well handset MIMO antennas with a vertically arranged structure are characterized using the limited number of scatterers implemented in a fading emulator [91]. First we studied the mechanism of the arrangement of scatterers on the variation of channel responses using a proposed three-dimensional analytical model. It is shown that the condition of a 3D-OTA with the prescribed parameters allows the correlation to be reduced, which permits the channel capacity to increase in the same manner that sufficient scatterers are distributed over the entire solid angle. Then the appropriate scatterers arrangement for a 3D-OTA instrument considering the number of DUT antenna elements and multipath characteristics is investigated. The analytical results show that a suitable scatterers arrangement can be determined for various conditions of multipath environments and numbers of array elements, and that the arrangement can be employed for designing an actual 3D-OTA apparatus.

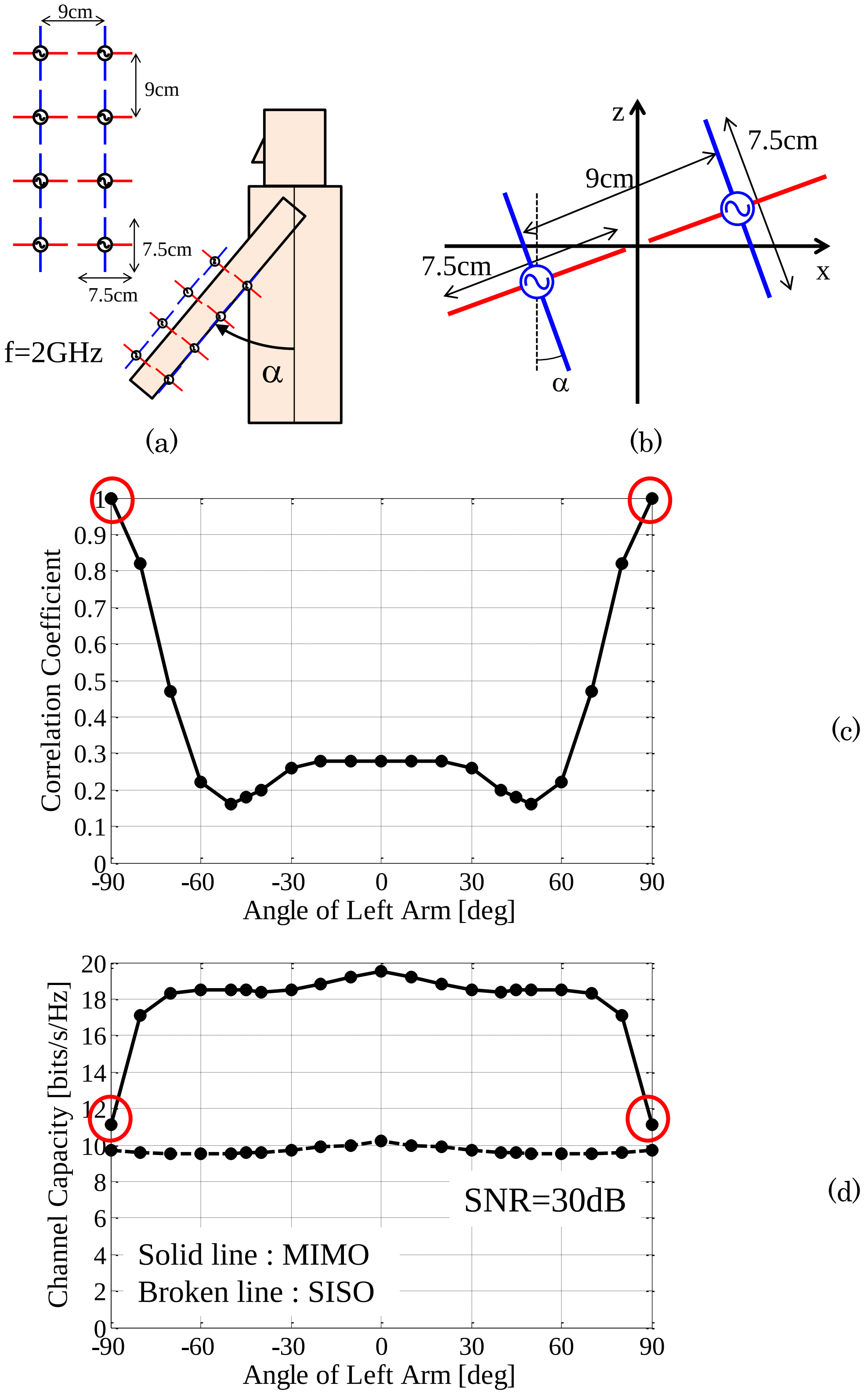

Fig. 5.1 3D channel model for wearable MIMO antenna (a) 8x8 element wearable MIMO (b) 2x2 MIMO (c) Correlation (d) Channel capacity

5.2 3D-OTA Channel Model for Vertical MIMO Array

In previous studies of MIMO-OTA testing [17] [28], it was determined that the array elements of a DUT antenna arranged in the row direction is related to the scatterers placed in the azimuth direction. Therefore, in this paper, we focus on a discussion of the scatterers arrangement in the elevation direction, which is related to the array elements arranged in the column direction.

Fig. 5.2 shows the three-dimensional channel model for assessing a vertically arranged MIMO array antenna. In Fig. 5.2 (a), the MIMO antenna with N-element is arranged in one column in the z-direction, which is comprised of vertically oriented half-wavelength dipole antennas. The antenna element spacing d_s is set to 9 cm, while the frequency for the analysis is 2 GHz. The radiation characteristics of each element are calculated using the method of moments [92].

In Fig. 5.2 (b), the vertically arranged MIMO antenna shown in Fig. 5.2 (a) is located at the center of the channel model where a number of scatterers are distributed in space in a three-dimensional manner. The angular power distribution of the incident wave in the channel model is assumed to be a uniform in azimuth and a Gaussian in elevation [92], where m_s represents the average elevation angle of the incident wave, and σ_s signifies the standard deviation. In the elevation direction, the scatterers used in an actual fading emulator are distributed within a limited angular range between pl and ph in a symmetrical manner with respect to m_s. The number of scatterers is set to nh in azimuth and nv in elevation at an equal interval. The phase of the radio waves from each scatterer is randomly distributed to realize the uncorrelated condition among all paths between the scatterers and the array elements.

Fig. 5.3 shows an example of the incident wave distribution and the scatterers arrangement in an OTA apparatus. The red circles indicate the scatterers placement. Figs. 5.3 (a) and (b) show the scatterers arrangement in the azimuth and elevation directions, respectively. The average elevation angle $m_s = 20^{\circ}$, and the standard deviation of incident waves $\sigma_s = 20^{\circ}$. The number of scatterers is set to $nh = 7$ in azimuth and $nv = 5$ in elevation. Five scatterers in the elevation direction are arranged from $pl = -10^{\circ}$ to $ph = 50^{\circ}$, indicating that $\Delta\alpha = ph - pl = 60^{\circ}$, where $\Delta\alpha$ is defined as the separation between ph and pl shown in Fig. 5.3 (b).

In order to obtain useful knowledge of the required conditions of a 3D-OTA channel model, we focus on the key parameters of ph, pl, nv, m_s, σ_s, and N, which may determine the channel capacity of MIMO array antennas, as will be presented in Sect. 5.4.

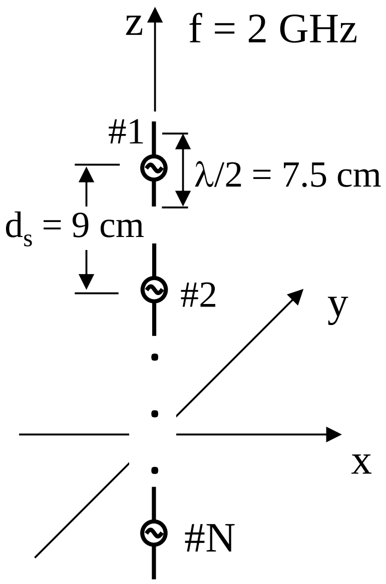

(a) Vertical MIMO array antenna

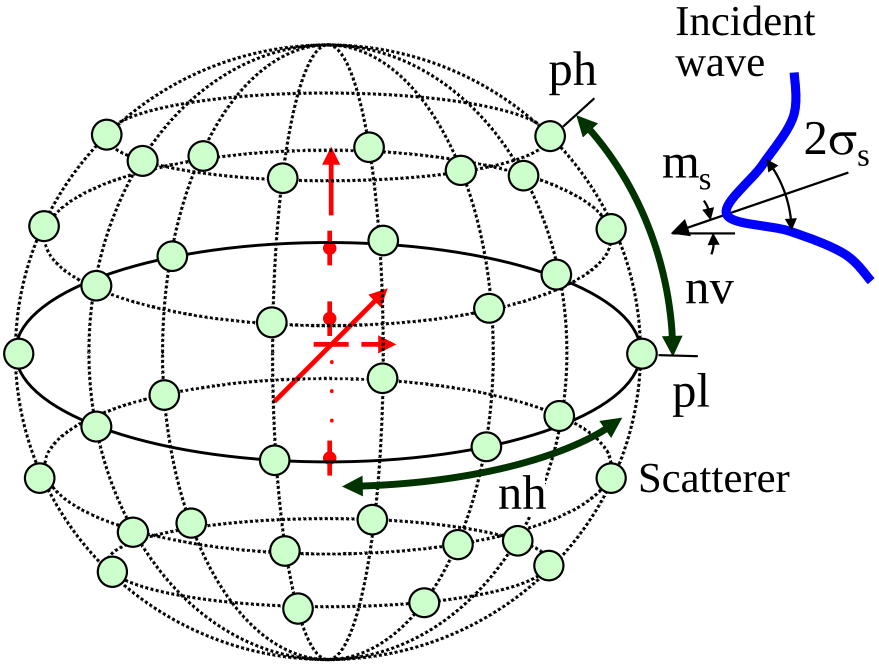

(b) Analytical channel model

Fig. 5.2 Three-dimensional channel model for OTA assessment of vertically arranged MIMO array antenna

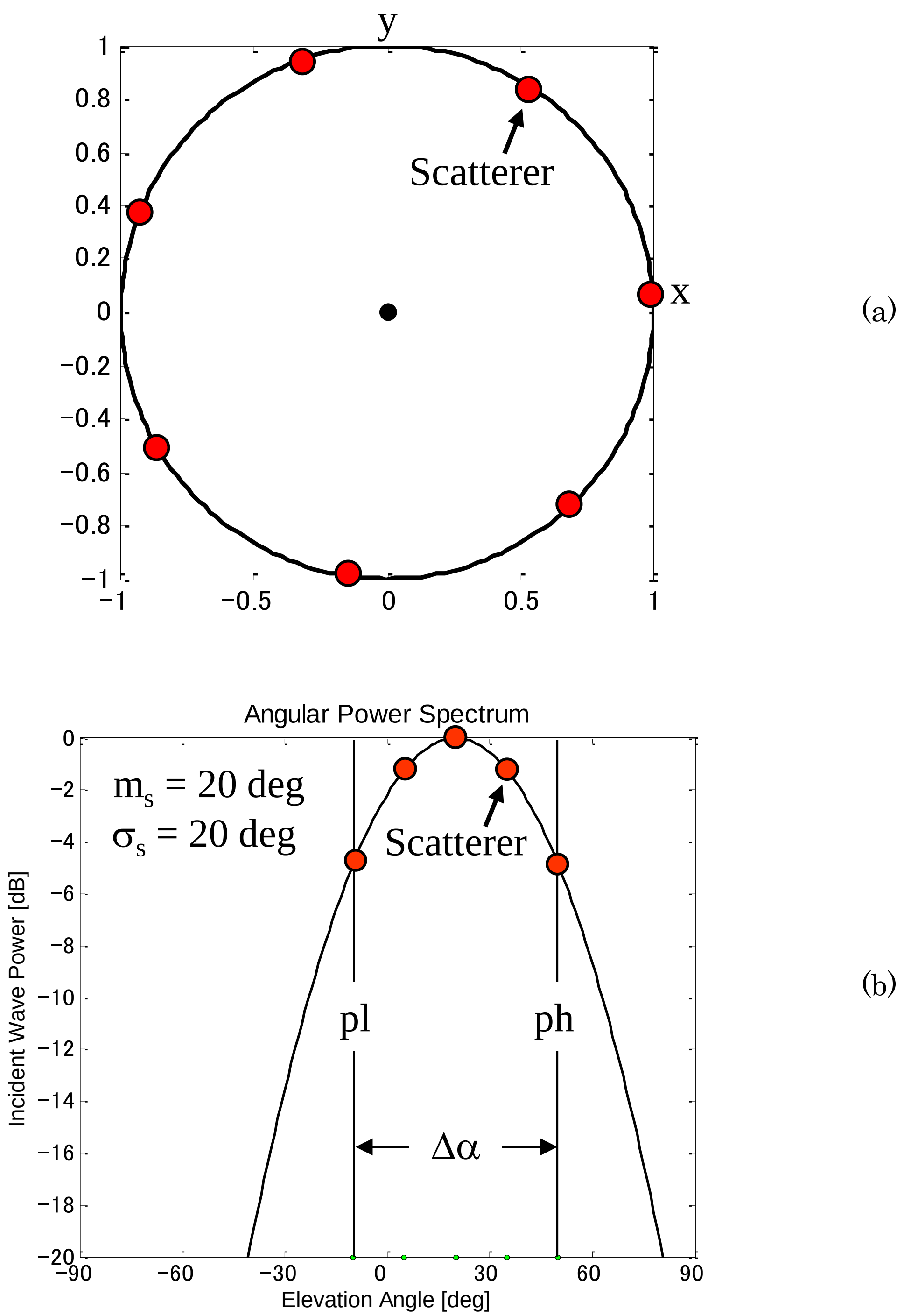

Fig. 5.3 Incident wave distribution and scatterers arrangement

$ph = 50°$, $pl = -10°$, $nv = 5$, $nh = 7$

(a) Azimuth (b) Elevation

5.3 Analytical Method

In the literature [17], the authors investigated the radius of a two-dimensional fading emulator in a cluster environment in which incident waves with a small angular spread exist in the azimuth direction. To do this, they analyzed the average received power ratio between two MIMO antenna elements. Their investigation corresponds to the scenario where the incident waves of the three-dimensional channel model, described in Fig. 5.2, have a small angular spread in the elevation direction. Hence, we can estimate the required radius of the 3D-OTA apparatus discussed in this paper on the basis of the outcomes given in [17]. The estimation results show that the error of the received power can be suppressed within 1 dB when the radius is larger than 1.0 m, 1.5 m, and 2.0 m at 2 GHz, where the element spacing between the two quasi-dipole arrays is less than 10 cm, 17 cm, and 30 cm, respectively (see Fig. 9 in [17]).

These element spacings correspond to the total array size when $N = 2$, 3, and 4 for the MIMO array antenna illustrated in Fig. 5.2 (a), where the total array size is defined as the distance between the exciting port of element #1 and that of element #N. From the quantitative relationship between the radius and the element spacing, the required radius for the array with N = 8 (total array size of 60 cm) is estimated to be 2.8 m by means of the extrapolation method. On the basis of this knowledge, the analysis hereafter is performed under the condition that the criterion for the radius of the emulator mentioned above is satisfied, which results in a situation where incoming waves emitted from the emulator scatterers arriving at a DUT terminal can be assumed to be plane waves [90].

Fig. 5.4 (a) shows the channel model of an $M \times N$ MIMO system in a three-dimensional scatterers arrangement, in which the MIMO array at the MS side is arranged in the vertical direction [93]. The number of array elements in a base station (BS) and a handset antenna are defined as M and N, respectively. In this paper, an NLOS situation between the base station and terminal antenna is assumed. M BS antennas create a set of M uncorrelated waves where each wave comprises K_m scatterers as shown in Fig. 5.4 (a), which surround N handset antennas, constructing second-wave sources around the moving terminal. Thus, M uncorrelated waves are subject to independent identically distributed (i.i.d.) complex Gaussian processes. Note that K_m scatterers share M waves coming from M BS antennas, but the uncorrelated conditions among the M waves is achieved by giving random phases to the scatterers [93]. Fig. 5.4 (b) shows the coordinate of the k-th scatterer with the handset moving toward the azimuth direction ϕ_V. The multipath property modeled by the angular power spectrum. The spectrum is uniform in azimuth and Gaussian in elevation as shown below:

$$P_\theta(\theta,\phi) = \frac{XPR}{1+XPR} A_\theta \exp\left[\frac{\left\{\theta - \left(\frac{\pi}{2} - m_V\right)\right\}^2}{2{\sigma_V}^2}\right] \tag{5.1}$$

$$\left(0 \le \theta \le \pi, 0 \le \phi \le 2\pi\right)$$

$$P_\phi(\theta,\phi) = \frac{1}{1+XPR} A_\phi \exp\left[\frac{\left\{\theta - \left(\frac{\pi}{2} - m_H\right)\right\}^2}{2{\sigma_H}^2}\right] \tag{5.2}$$

$$\left(0 \le \theta \le \pi, 0 \le \phi \le 2\pi\right)$$

where XPR is the cross-polarization power ratio. m_V and m_H are the mean angles of the θ and ϕ-component elevational power spectra, as shown in Fig. 5.4 (c). σ_V and σ_H are the standard deviations of the θ and ϕ-component elevational power spectra. A_θ and A_ϕ are the normalization constants to satisfy

$$\oiint P_\theta(\theta,\phi)d\Omega = \frac{XPR}{1+XPR}$$

$$\oiint P_\phi(\theta,\phi)d\Omega = \frac{1}{1+XPR} \tag{5.3}$$

$$\oiint \left[P_\theta(\theta,\phi) + P_\phi(\theta,\phi)\right]d\Omega = 1$$

In this work, the same parameters are used for the incident waves, which means that $m_V = m_H = m_s$, $\sigma_V = \sigma_H = \sigma_s$.

In the Monte Carlo simulation, as a similar procedure to Eqs. (4.1) and (4.2), it can be assumed that k-th path has the transfer functions of vertical and horizontal components, h_{Vn} and h_{Hn}, as illustrated in Fig. 5.4 (d). Then, the transfer functions of the k-th path at the n-th antenna of two components are expressed as

$$h_{\mathrm{V}k,nm} = \sqrt{\frac{XPR}{1+XPR}}\, h_{k,\mathrm{m}}\, E_{\theta k}(\theta_{k,m},\phi_{k,m})\exp\left(j\varphi_{\mathrm{V}k,m}\right) \tag{5.4}$$

$$h_{\mathrm{H}k,nm} = \sqrt{\frac{1}{1+XPR}}\, h_{k,\mathrm{m}}\, E_{\phi k}(\theta_{k,m},\phi_{k,m})\exp\left(j\varphi_{\mathrm{H}k,m}\right) \tag{5.5}$$

As a complex sum of the vertical and horizontal components

$$h_{k,nm} = h_{Vk,nm} + h_{Hk,nm} \tag{5.6}$$

Thus, the resultant channel response of the n-th handset antennas can be expressed as the sum of the K_m paths under the nearby m-th scatterers groups, as follows:

$$h_{nm} = \sum_{k=1}^{K_m} h_{k,nm} \exp\left\{ j \frac{2\pi d}{\lambda} \cos(\phi_{k,m} - \phi_v) \sin(\theta_{k,m}) \right\} \tag{5.7}$$

where λ is the carrier wavelength in free space, and d is the distance travelled by the handset antenna toward the azimuth direction ϕ_v shown in Fig. 5.4 (b).

$h_{k,nm}$ in Eq. (5.7) is determined by the combination of the complex electric field directivity of the antenna element for the θ and ϕ-polarization components, as shown in Eq. (5.6), which can be calculated by the method of moments. Hence, we can analyze an arbitrary DUT antenna by replacing $h_{k,nm}$ in Eq. (5.7) in accordance with the type of antenna to be investigated [68], indicating that the DUT antenna shown in Fig. 5.2 (a) is separated from the channel model illustrated in Fig. 5.2 (b). This means that the three-dimensional channel model presented in this paper possesses broad generalities in analyzing 3D-OTA responses of different types of DUT antennas treated in this article. The phases of different polarization components are independent of each other to realize the uncorrelated characteristics among all the paths between the scatterers and handset antennas.

h_{nm} in Eq. (5.7) indicates the channel response between the m-th base station antennas and n-th terminal antennas. Therefore, the channel response of the arrays at the s-th snapshots can be calculated by the following matrix:

$$\mathbf{H}_s = [h_{nm}] = \begin{bmatrix} h_{11} & h_{12} & \cdots & h_{1\mathrm{M}} \\ h_{21} & h_{22} & \cdots & h_{2\mathrm{M}} \\ \vdots & \vdots & \ddots & \vdots \\ h_{\mathrm{N}1} & h_{\mathrm{N}2} & \cdots & h_{\mathrm{NM}} \end{bmatrix} \tag{5.8}$$

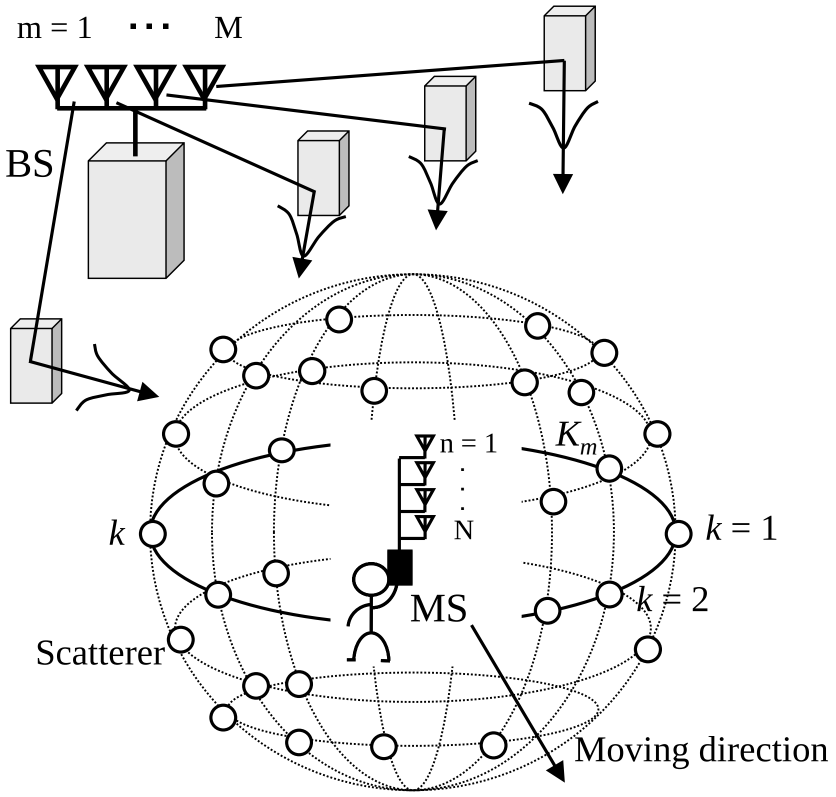

(a) Channel model of an $M \times N$ MIMO

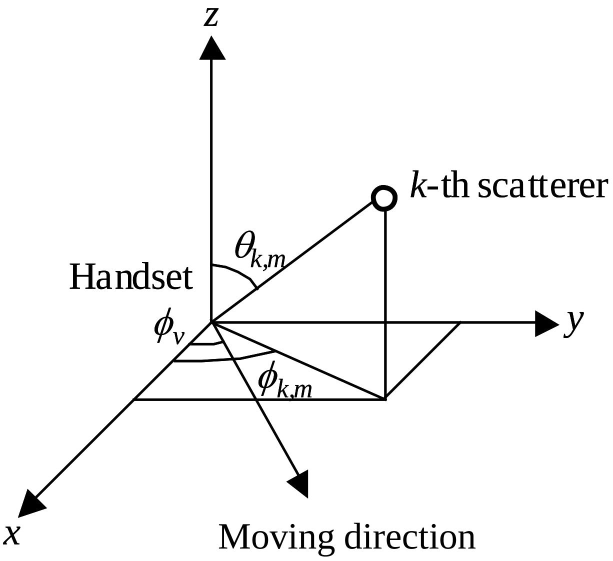

(b) Coordinate of scatterers

Fig. 5.4 Radio propagation 3D model

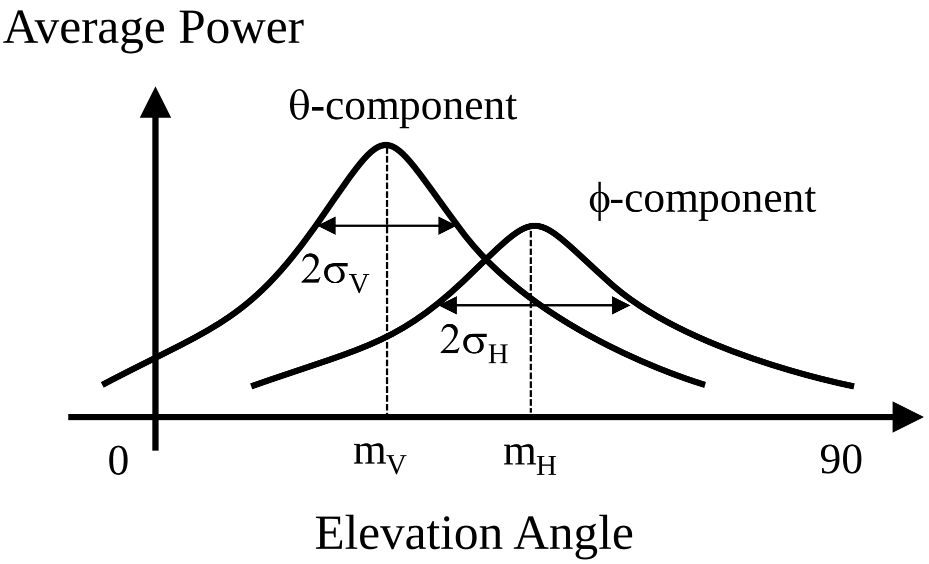

(c) Incident wave model in elevation direction

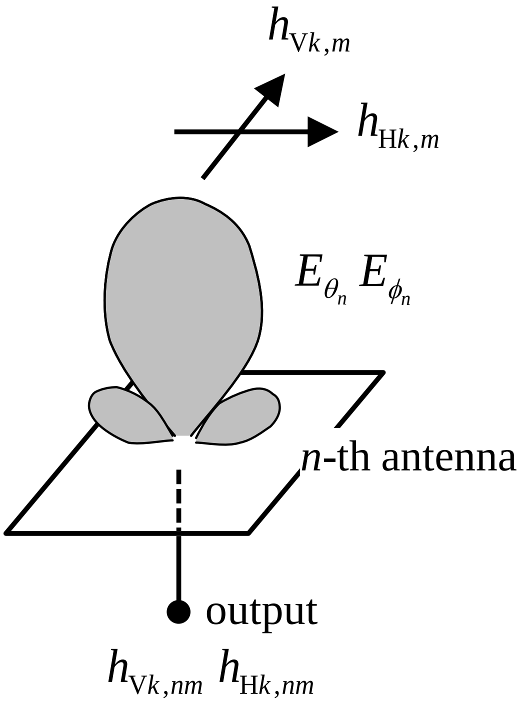

(d) Transfer functions of vertical and horizontal components

Fig. 5.4 Radio propagation 3D model

The eigenvalues λ_i are obtained based on the singular value decomposition derived from Eq. (5.8), as expressed below:

$$\mathbf{H}_s = \mathbf{U}_s \mathbf{D}_s \mathbf{V}_s^H \tag{5.9}$$

$$\mathbf{U}_s = \left[e_{r1}, \cdots, e_{r\mathrm{L}}\right] \tag{5.10}$$

$$\mathbf{V}_s = \left[e_{t1}, \cdots, e_{t\mathrm{L}}\right] \tag{5.11}$$

$$\mathbf{D}_s = \mathrm{diag}\left\lfloor \sqrt{\lambda_1}, \cdots, \sqrt{\lambda_\mathrm{L}} \right\rfloor \tag{5.12}$$

Using the above-mentioned formulas, the obtained eigenvalues λ_i can be used to infer the instantaneous Shannon capacity (without feedback) in the s-th snapshots as follows:

$$C_s = \sum_{i=1}^{L} \log_2\left(1 + \frac{\gamma \lambda_i}{M}\right) \quad \text{[bits/s/Hz]} \tag{5.13}$$

where $L = \min(N, M)$, and γ denotes the input signal-to-noise ratio (SNR). Here, the SNR is defined as an average value of instantaneous SNRs when an isotropic antenna (antenna gain is 0 dBi) is used for receiving the coherent incident waves with vertical polarization (XPR = ∞), which are assumed to be radiated from a single antenna at the base station. The analysis is executed successively until the handset antenna arrives at the end point of the moving direction. The average value of the channel capacity when the terminal antenna moving in a distance can be obtained by the following equation:

$$\overline{C} = \frac{1}{S} \sum_{s=1}^{S} C_s \tag{5.14}$$

where S signifies the number of samples.

5.4 Analytical Results

Based on the channel model and analytical method mentioned in Sects. 5.2 and 5.3, some analyses for 3D-OTA tests are carried out. We focus on two viewpoints: mechanism analysis and determination of scatterers arrangement, which are presented in Sects 5.4.1 and 5.4.2, respectively.

5.4.1 Mechanism Analysis

Fig. 5.5 shows the cumulative distribution function (CDF) of the eigenvalue and channel capacity of a 4 × 4 MIMO antenna in the vertically arranged array configuration, as shown in Fig. 5.2.

In Fig. 5.5 (b), the curves shown on the left side indicate the single-input single-output (SISO) channel capacity, while the black curve on the right side shows the MIMO channel capacity. The symbols C_{mimo} and C_{siso} drawn in the figure indicate the calculated values of MIMO and SISO channel capacity, respectively. A vertically polarized incident wave with an SNR of 30 dB is considered. The average elevation angle is assumed to be $m_s = 20^{\circ}$ with an angular spread of $\sigma_s = 20^{\circ}$. The scatterers are distributed with the parameters of $ph = 90^{\circ}$, $pl = -90^{\circ}$, $nv = 37$, and $nh = 30$. Hence, the total amount of 1,110 scatterers is arranged in the entire space.

As shown in Fig. 5.5, dense eigenvalues and a large capacity are observed when distributing a large number of scatterers over the entire solid angle. The 4 × 4 MIMO achieves a large channel capacity of 36.1 bits/s/Hz, which is equivalent to a channel capacity of 3.6 Gbps when a 100-MHz bandwidth is considered.

Fig. 5.6 shows the CDF of the eigenvalue and channel capacity when $ph = 25^{\circ}$, $pl = 15^{\circ}$ ($\Delta\alpha = ph - pl = 10^{\circ}$), $nv = 5$, and $nh = 7$. The average elevation angle is assumed to be $m_s = 20^{\circ}$ with an angular spread of $\sigma_s = 20^{\circ}$. As shown in Fig. 5.6, sparse eigenvalues and a small capacity are given when distributing a small number of scatterers over a small angular range. The eigenvalue has a sparse distribution, which is different from that in Fig. 5.5. Specifically, compared with the first and second eigenvalues, the third eigenvalue is 1/100 or less, while the fourth eigenvalue cannot even be observed on the graph. This yields a small channel capacity of 24.1 bits/s/Hz.

The abovementioned phenomenon seen in Fig. 5.5 and Fig. 5.6 can be understood very clearly by considering the correlation coefficient. Table 5.1 shows the correlation coefficient between the i-th and j-th elements, where the element index is defined in Fig. 5.2 (a). Tables 5.1 (a) and (b) show the analytical results corresponding to the key parameters described in Fig. 5.5 and Fig. 5.6, respectively.

We can find a small correlation of less than 0.66 in Table 5.1 (a) throughout the entire results. By contrast, Table 5.1 (b) indicates that the correlation between the two elements aligned in column is higher than 0.9. This fact provides a physical picture for explaining why Fig. 5.6 (a) shows a sparse eigenvalue. It also indicates that, if the angular range of the scatterers is confined to a narrow angle such as $\Delta\alpha = 10^{\circ}$, the OTA assessment cannot be carried out. Therefore, the angular range of the scatterers needs to be extended.

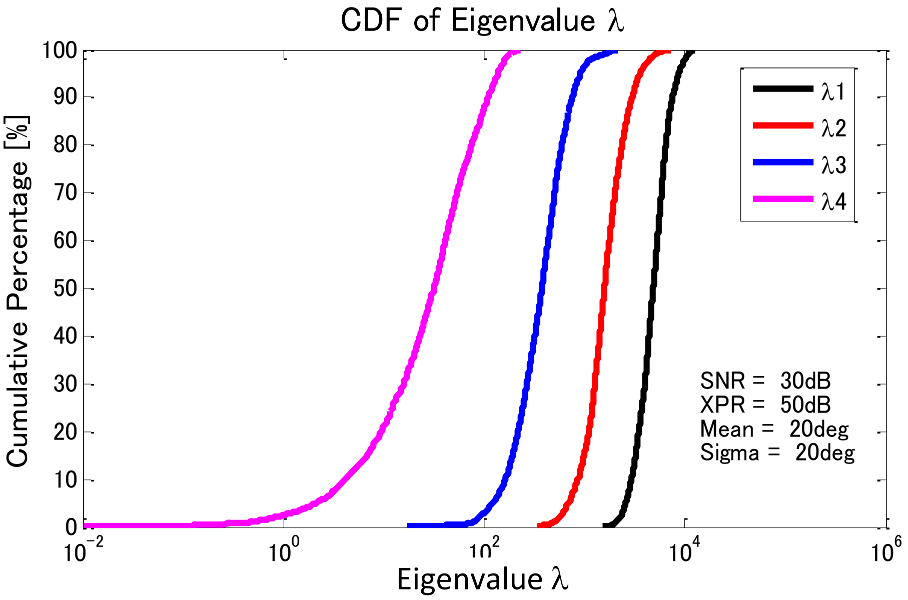

(a) CDF of Eigenvalue λ

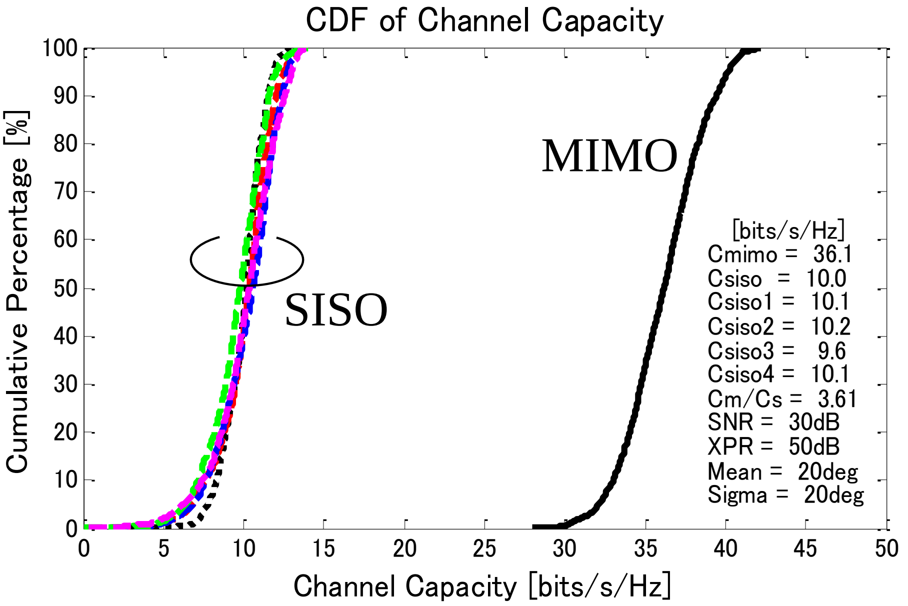

(b) CDF of Channel Capacity

Fig. 5.5 Eigenvalue and channel capacity of the 4 × 4 MIMO array

($ph = 90^{\circ}$, $pl = -90^{\circ}$, $nv = 37$, $nh = 30$)

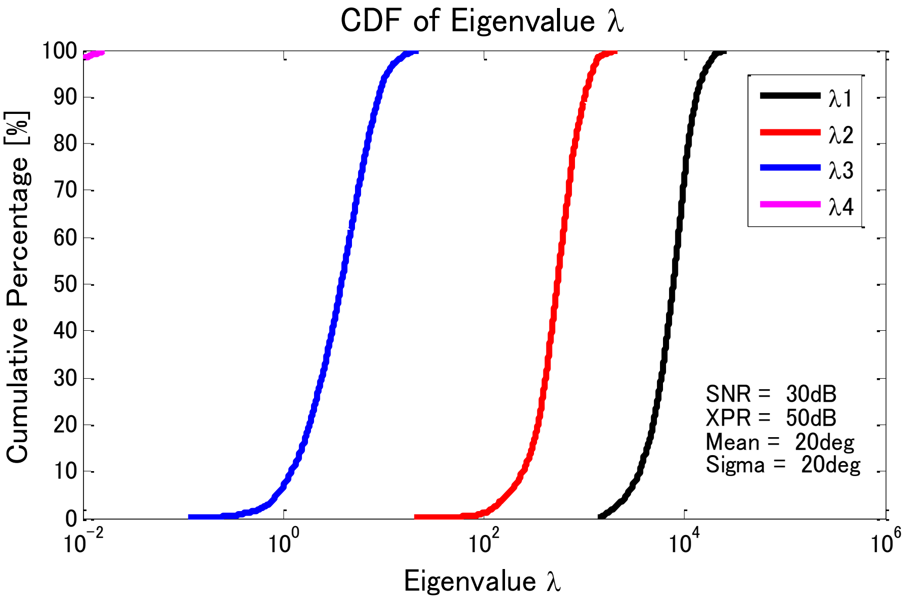

(a) CDF of Eigenvalue λ

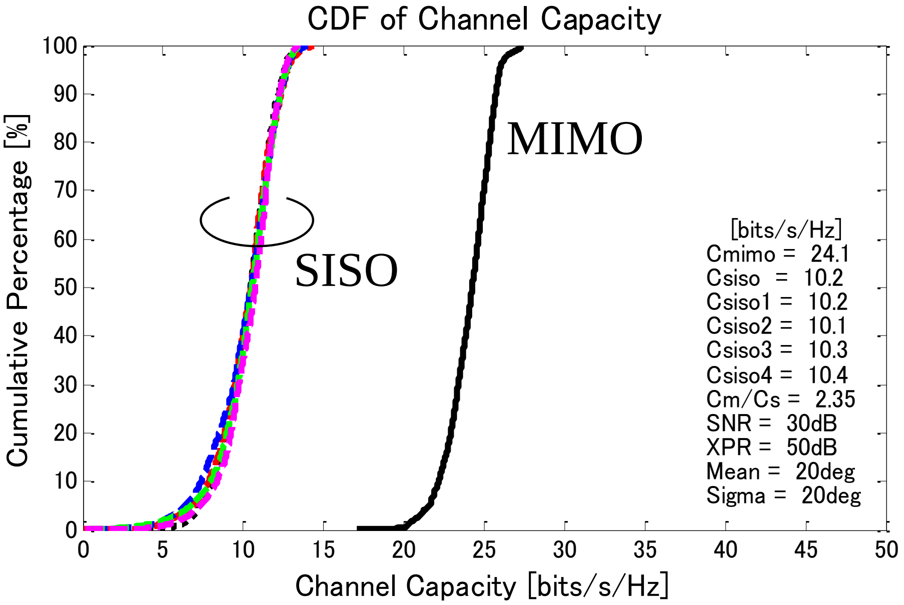

(b) CDF of Channel Capacity

Fig. 5.6 Eigenvalue and channel capacity of the 4 × 4 MIMO array

($ph = 25^{\circ}$, $pl = 15^{\circ}$, $nv = 5$, $nh = 7$)

Table 5.1 Absolutes of complex correlation coefficient between elements

(a) ph = 90 deg, pl = –90 deg, nv = 37, nh = 30

	j = 1	j = 2	j = 3	j = 4
i = 1	1.00	0.54	0.22	0.29
i = 2	0.54	1.00	0.66	0.19
i = 3	0.22	0.66	1.00	0.55
i = 4	0.29	0.19	0.55	1.00

(b) ph = 25 deg, pl = 15 deg, nv = 5, nh = 7

	j = 1	j = 2	j = 3	j = 4
i = 1	1.00	0.97	0.89	0.78
i = 2	0.97	1.00	0.97	0.90
i = 3	0.89	0.97	1.00	0.98
i = 4	0.78	0.90	0.98	1.00

Fig. 5.7 shows the eigenvalue and channel capacity when $ph = 50^\circ$, $pl = -10^\circ$ ($\Delta\alpha = 60^\circ$), $nv = 5$, and $nh = 7$. The average elevation angle is set to $m_s = 20^\circ$ with an angular spread of $\sigma_s = 20^\circ$. In Fig. 5.7, we have dense distribution of the eigenvalues, resulting in a large capacity of 35.1 bits/s/Hz, which is very close to the idealized value in Fig. 5.5. Thus, the limited number of scatterers of the 3D-OTA apparatus has a good ability to assess a vertically arranged MIMO array antenna.

Table 5.2 shows the correlation coefficients corresponding to the parameters described in Fig. 5.7. As shown in Table 5.2, we have very small correlations between the elements aligned in the vertical direction, which is the same behavior that was observed in Table 5.1 (a). This supports the hypothesis that correlations are reduced owing to uncorrelated waves in the vertical plane.

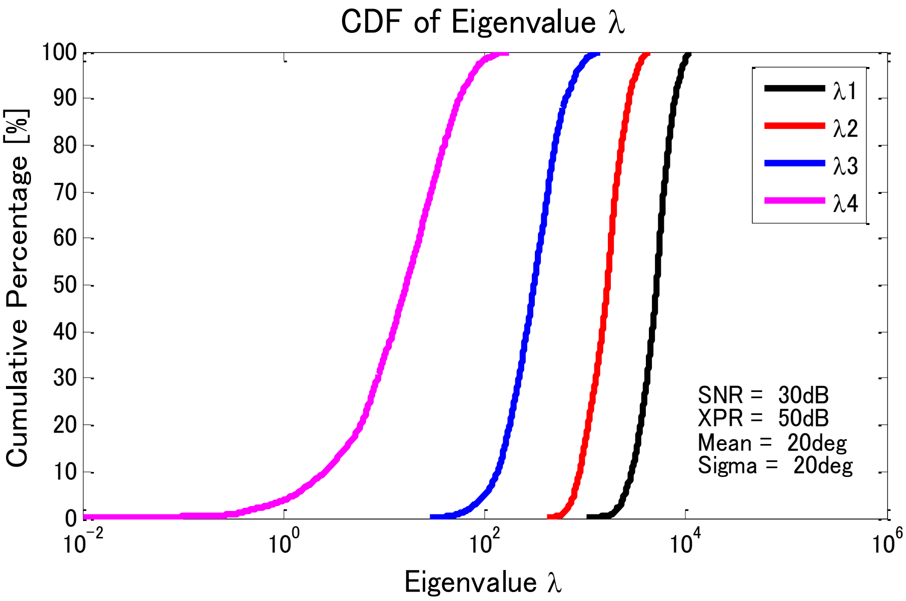

(a) CDF of Eigenvalue *λ*

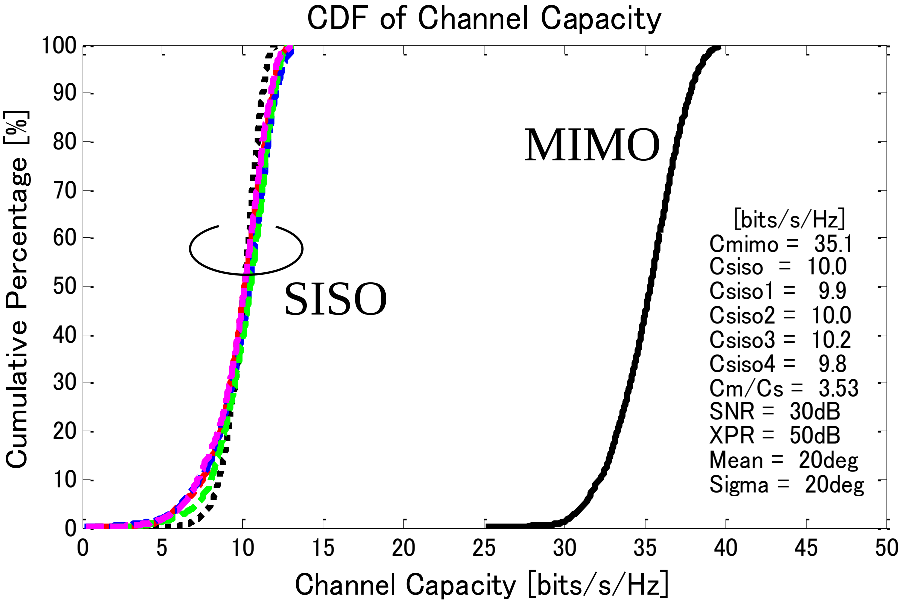

(b) CDF of Channel Capacity

Fig. 5.7 Eigenvalue and channel capacity of the 4 × 4 MIMO array

($ph = 50^\circ$, $pl = -10^\circ$, $nv = 5$, $nh = 7$)

Table 5.2 Absolutes of complex correlation coefficient between elements

ph = 50 deg, pl = –10 deg, nv = 5, nh = 7

	j = 1	j = 2	j = 3	j = 4
i = 1	1.00	0.63	0.13	0.06
i = 2	0.63	1.00	0.64	0.10
i = 3	0.13	0.64	1.00	0.60
i = 4	0.06	0.10	0.60	1.00

Fig. 5.8 shows the average channel capacity as a function of the angular region of scatterers, defined as $\Delta\alpha = ph - pl$, as shown in Fig. 5.3 (b), with the number of scatterers nv as parameters when the number of vertical arrays $N = 4$. The average elevation angle is set to $m_s = 20^\circ$ with an angular spread of $\sigma_s = 20^\circ$.

In Fig. 5.8, it can be seen that $\Delta\alpha$ of 80° with $nv = 5$ or 7 is found to be suitable for 3D-OTA, as shown by position P2, because almost the same performance can be achieved as that observed when distributing over the entire solid angle, as indicated by the diamond-shaped symbol plotted on the right axis.

However, considering practicability and cost of manufacture, the size of the instruments needs to be as small as possible. Therefore, $nv = 3$ with $\Delta\alpha$ of 50° is another choice for the realization of an OTA apparatus, as shown by position P1 in Fig. 5.8, because 89.8 % of the target value of the channel capacity can be obtained there.

Since in this paper we focus on the scatterers arrangement in the elevation direction, $nv = 3$, 5, and 7 have been investigated as key parameters. Here, only odd numbers are used because the scatterer is required at the peak position of the Gaussian distribution in the elevation direction, as shown in Fig. 5.3 (b). Further, the odd number of scatterers is suitable for the symmetrical arrangement on the left and right sides of the peak position.

On the other hand, the number of scatterers in the azimuth direction nh is fixed at seven. The reason is that in a two-dimensional channel model, the sum of more than six or seven waves is sufficient to realize the Rayleigh distribution in the azimuth direction [50].

The SNR is set to 30 dB. The diamond mark on the right axis in Fig. 5.8 indicates the average channel capacity value calculated with the parameters of $ph = 90^\circ$, $pl = -90^\circ$, $nv = 37$, and $nh = 30$, which means that a total of 1,110 scatterers are arranged throughout the entire space, as shown in Fig. 5.5. Hence, the goal of the OTA apparatus development is to obtain a capacity that is close to the value analyzed based on these parameters.

Additionally, MIMO channel capacity may be changed when a different number of DUT antenna arrays N is employed in different multipath environments, such as various m_s and σ_s. Thus, the multipath characteristics and the number of arrays need to be considered as the parameters for determining an appropriate scatterers arrangement (nv, $\Delta\alpha$) in the design of an OTA apparatus, as will be introduced in Sect. 5.4.2.

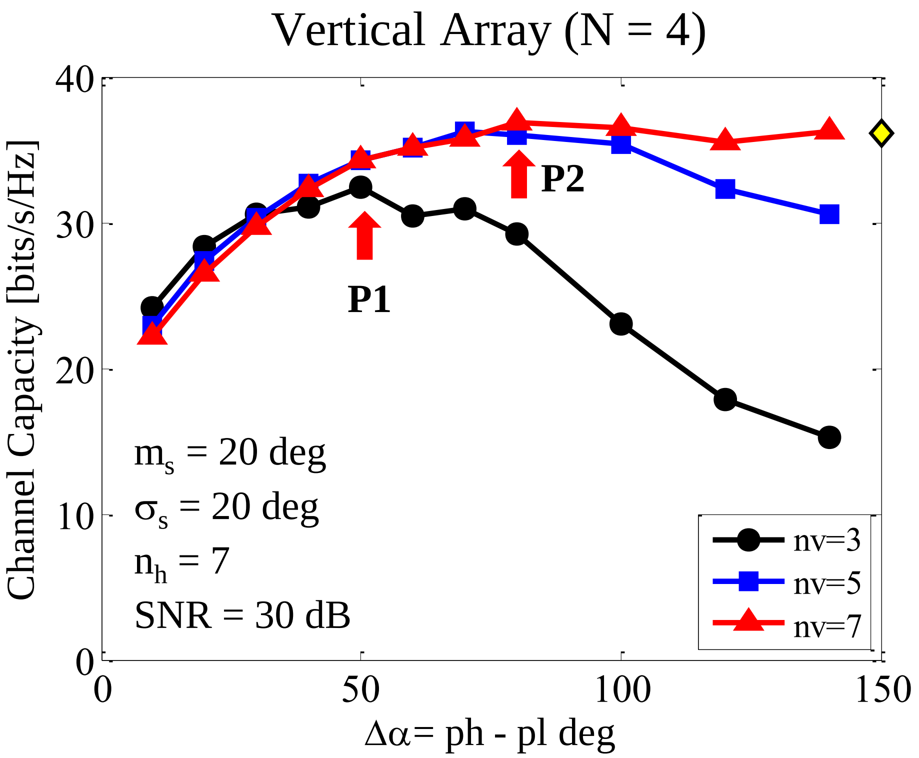

Fig. 5.8 Channel capacity vs. number of scatterers and angular region

5.4.2 Determination of Scatterers Arrangement

Since the idealized value of the channel capacity may be changed because of different conditions (N, m_s, or σ_s), in order to describe the effective degree to which the MIMO channel capacity is evaluated, we define the channel capacity ratio r_c, which indicates the percentage of the channel capacity as compared with the target value, as follows:

$$r_c = \frac{\overline{C}}{\overline{C_t}} \tag{5.15}$$

where $\overline{C}$ indicates the average channel capacity calculated using Eq. (5.14), while $\overline{C_r}$ indicates the idealized value calculated with the parameters of $ph = 90°$, $pl = -90°$, $nv = 37$, and $nh = 30$, as shown in Fig. 5.5.

Fig. 5.9 shows the variations in the channel capacity ratio r_c when the number of arrays N is increased from 2 to 8 considering σ_s, m_s, and $\Delta\alpha = ph - pl$ as parameters. nh is 7, while the SNR is set to 30 dB with XPR = 50 dB. Figs. 5.9 (a) and (b) represent the two cases when $nv = 3$ and 5, respectively. In Fig. 5.9, the angular spread σ_s is set to 10°, 20°, and 30°. The figures (1) (2) (3) on the left side indicate when $m_s = 20°$, while the figures (4) (5) (6) on the right side indicate the case of $m_s = 40°$. These are selected as examples that represent the general characteristics of incident waves in the elevation direction in multipath environments in an urban macro cellular environment [44]. The results r_c calculated by Eq. (5.15) are represented by symbol ●. Based on these data, the approximate curved surfaces are created using the least-mean-square (LMS) method.

In Fig. 5.9, an obvious fluctuation of r_c is observed owing to various σ_s and m_s. Thus, the suitable scatterers arrangement (nv, $\Delta\alpha$) based on the desired

(σ_s, m_s) for evaluating different numbers of array N needs to be determined. The useful information from the raw data in Fig. 5.9 will be abstracted and reorganized.

As shown in Figs. 5.9 (a) - (1) and (4), $nv = 3$ is sufficient to evaluate the array with $N = 2$ because more than 80 % of channel capacity ratio r_c is obtained in most part of entire data. However, with the number of arrays N increasing from 2 to 8, a significant reduction of the entire r_c can be observed.

In particular, when $N = 8$, as shown in Figs. 5.9 (a) - (3) and (6), the entire r_c are almost less than 60 %, indicating that the number of scatterers $nv = 3$ is not sufficient to evaluate the MIMO array with a large number of elements arranged in the vertical direction. Thus, nv needs to be increased for the case when N is very large.

In Fig. 5.9 (b), when $nv = 5$ is used, the entire r_c are increased compared with the r_c for $nv = 3$ in Fig. 5.9 (a) even when $N = 8$. This indicates that $nv = 5$ is necessary to ensure the evaluation of the channel capacity when $N = 8$.

However, Figs. 5.9 (a) - (1), (a) - (2), and (b) - (3) show that r_c can be maintained at a high level only when $\Delta\alpha$ is fixed in a certain range, as shown by the vertical dotted arrows. Thus, an appropriate scatterers arrangement $\Delta\alpha$ needs to be determined for different conditions. The mechanism was illustrated in Sect. 5.4.1, where the positions of P1 and P2 in Fig. 5.8 can be found in Figs. 5.9 (a) - (2) and (b) - (2), respectively.

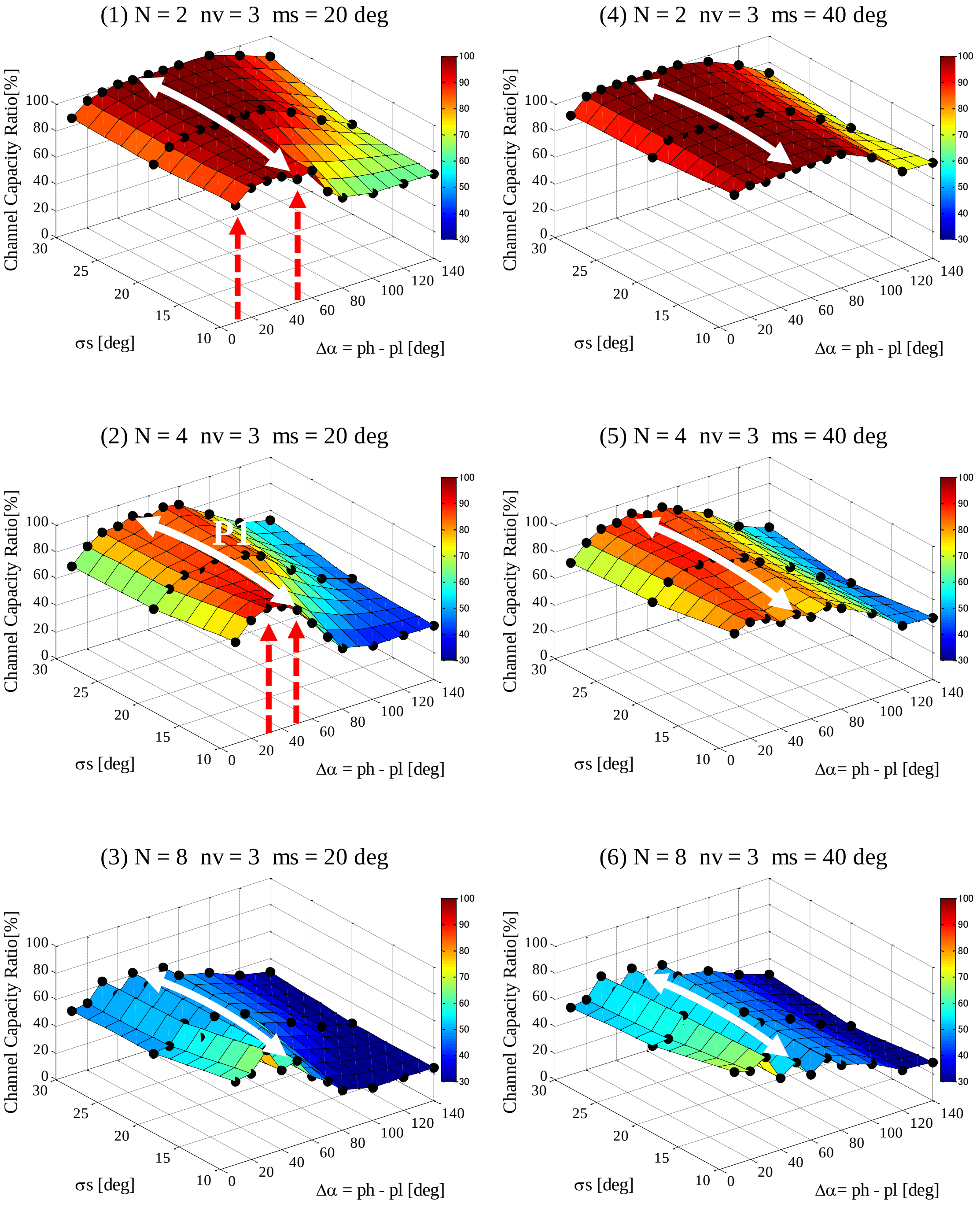

(a) $nv = 3$

Fig. 5.9 Channel capacity ratio vs. number of array elements and scatterers angular region

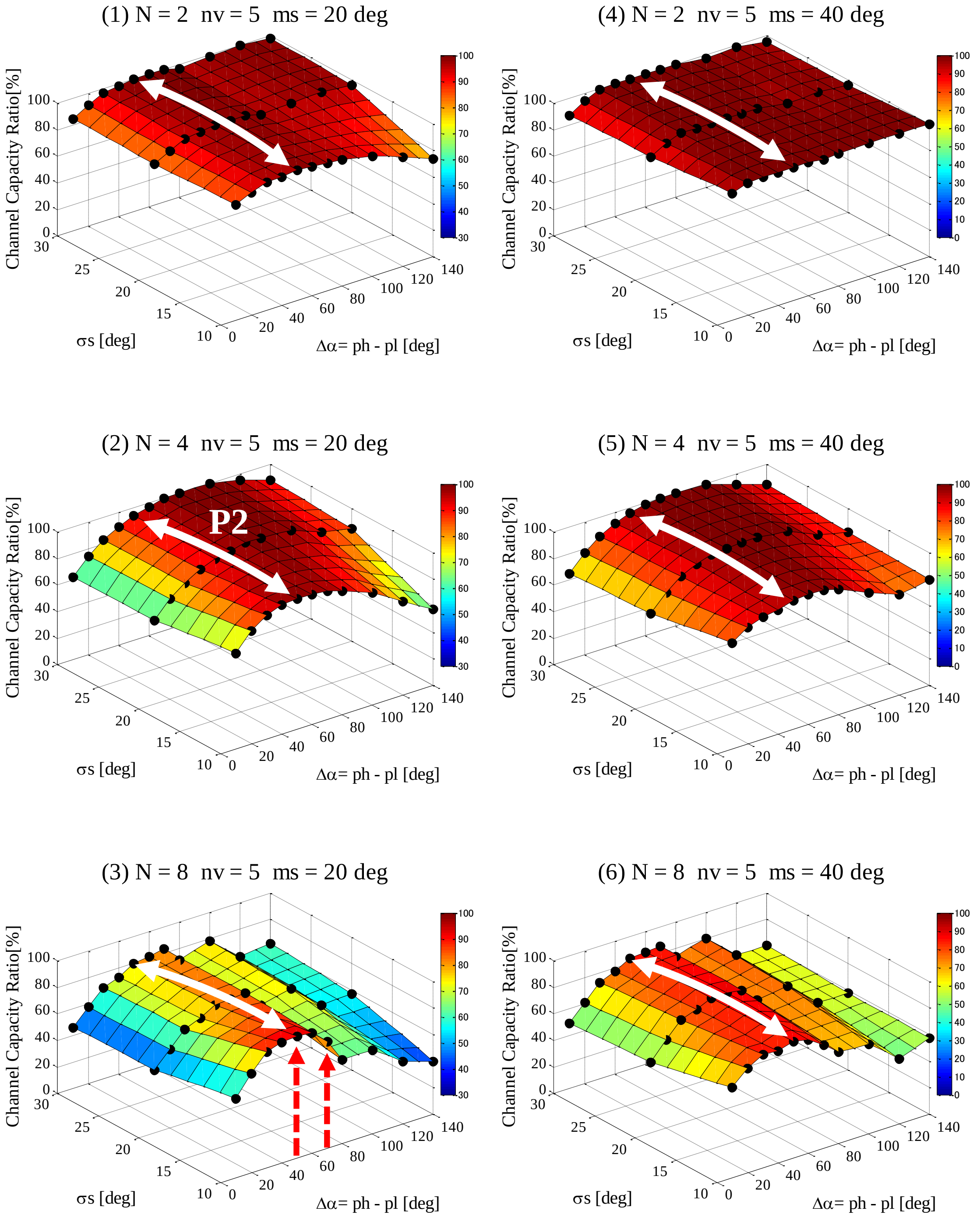

(b) $nv = 5$

Fig. 5.9 Channel capacity ratio vs. number of array elements and scatterers angular region

Table 5.3 shows how to determine the appropriate scatterers arrangement (nv, $\Delta\alpha$) using the data of channel capacity ratio r_c exhibited in Fig. 5.8 in different situations of σ_s when $m_s = 20°$. Tables 5.3 (a), (b), and (c) list three cases: $N = 2$ and $nv = 3$, $N = 4$ and $nv = 3$, and $N = 8$ and $nv = 5$. These correspond to Figs. 5.9 (a) - (1), (a) - (2), and (b) - (3), which are determined in order to cover the optimum (nv, $\Delta\alpha$) considering the possibility and commonality in different conditions of N and σ_s.

In Table 5.3 (a) where $N = 2$ and $nv = 3$, a large range of $\Delta\alpha$ from 10° to 60° can be selected because more than 80 % of r_c is obtained in any case of σ_s corresponding to Fig. 5.9 (a) - (1). However, in Table 5.3 (b) where $N = 4$ and $nv = 3$, $\Delta\alpha$ where the channel capacity is evaluated with more than 80 % of r_c is reduced to a range from 30° to 50°. Moreover, in Table 5.3 (c) where $N = 8$ and $nv = 5$, the optional $\Delta\alpha$ is changed to a range from 50° to 70°. These appropriate ranges of $\Delta\alpha$ are indicated by the dotted boxes in Table 5.3, which correspond to the separation of the vertical dotted arrows in Fig. 5.9.

As mentioned in Fig. 5.8, considering the manufacture of the actual OTA assessment apparatus, the number of scatterers in the elevation direction nv needs to be as small as possible. Moreover, the scatterers angular region $\Delta\alpha$ is also anticipated to be smaller as possible to reduce the size of the device. In addition, it is convenient for the design of the actual apparatus if the scatterers angular region $\Delta\alpha$ is fixed at a certain value.

Thus, it can be concluded that $\Delta\alpha = 50°$ is the most suitable scatterers arrangement, because in any conditions of N and σ_s, at least 80 % of the channel capacity ratio can be achieved even when N is increased to 8, as shown by the horizontal arrow in Table 5.3. In Fig. 5.9, it can be seen that when $\Delta\alpha$ is fixed at 50°, as indicated by the two-way arrows, r_c is maintained at the mountain ridge of the approximate curved surfaces in each case of σ_s. This indicates that a valid proposed scatterers arrangement has $\Delta\alpha = 50^\circ$.

Fig. 5.10 shows the channel capacity ratio r_c as a function of nv and σ_s when $\Delta\alpha = 50^\circ$. Figs. 5.10 (a) and (b) show the cases when $m_s = 20^\circ$ and 40°, respectively. The solid curve shows that $nv = 3$, while the dotted line shows that $nv = 5$. The curve with symbols ■, ●, and ▲ indicates the case when $\sigma_s = 10^\circ$, 20°, and 30°, respectively.

In Fig. 5.10 (a), it can be seen that when $\Delta\alpha$ is fixed at 50°, if N is less than 4, $nv = 3$ is sufficient to evaluate the channel capacity because these parameters can yield an r_c of more than 80 %. However, if a large number of array elements such as $N = 8$ is used, $nv = 5$ is needed to ensure an r_c of more than 80 %.

Furthermore, when a high incident wave angle $m_s = 40^\circ$ is considered as shown in Fig. 5.10 (b), $nv = 5$ with $\Delta\alpha = 50^\circ$ is found to be necessary for evaluating the case when $N = 8$. This conclusion can be observed in Fig. 5.9 (b) - (6), where the two-way arrow representing the position of $\Delta\alpha = 50^\circ$ passes through the mountain ridge of the approximate curved surface when $N = 8$ with $m_s = 40^\circ$ and various σ_s.

It can be concluded from the above investigations that when the number of DUT antenna arrays N is less than 4, $nv = 3$ is adequate to realize a 3D-OTA assessment, while if N is increased to 8, $nv = 5$ is necessary. Further, it is found that $\Delta\alpha = 50^\circ$ is the optimum parameter for a convenient apparatus design because the scatterers can be fixed in each case of $m_s = 20^\circ$ and 40°.

Since a small-cell era is coming for future wireless communication systems, the approach between the mobile terminal and base station will lead to variations in the m_s and σ_s of incident waves in the elevation direction, while the number of arrays N will be increased to realize ultra-high-capacity. The proposed scatterers arrangement (nv, $\Delta\alpha$) for a 3D-OTA apparatus can be applied to evaluate the multi-element MIMO antenna in various multipath conditions (σ_s, m_s) as desired.

Table 5.3 Determination of scatterers arrangement (nv, $\Delta\alpha$)

for various N and σ_s when $m_s = 20^\circ$

(a) $N = 2$, $nv = 3$

σs Δα	10°	20°	30°
10°	87.5%	84.3%	85.7%
20°	96.7%	94.2%	95.2%
30°	98.4%	97.4%	98.4%
40°	97.8%	99.5%	100%
50°	**92.4%**	**99.5%**	**100%**
60°	84.8%	100%	100%
70°	75.5%	100%	100%
80°	67.9%	100%	100%
100°	63.6%	90.6%	100%
120°	63.6%	78.0%	92.6%
140°	63.6%	67.0%	84.7%

Table 5.3 Determination of scatterers arrangement (nv, $\Delta\alpha$)

for various N and σ_s when $m_s = 20^\circ$

(b) $N = 4$, $nv = 3$

σs Δα	10°	20°	30°
10°	75.5%	66.8%	65.7%
20°	88.4%	78.4%	77.1%
30°	93.7%	84.8%	83.7%
40°	91.5%	86.1%	85.0%
50°	**85.0%**	**89.8%**	**89.1%**
60°	71.5%	84.2%	84.2%
70°	57.4%	85.6%	88.3%
80°	45.5%	80.9%	86.1%
100°	40.4%	63.7%	71.9%
120°	40.4%	49.6%	57.8%
140°	40.4%	42.1%	52.9%

(c) N = 8, nv = 5

σs Δα	10°	20°	30°
10°	59.4%	47.7%	46.3%
20°	74.3%	59.7%	57.9%
30°	86.9%	71.0%	69.0%
40°	90.5%	75.3%	73.2%
50°	**91.5%**	**81.6%**	**80.0%**
60°	90.3%	82.9%	81.0%
70°	80.4%	83.5%	83.2%
80°	63.3%	70.9%	71.2%
100°	63.1%	75.8%	78.4%
120°	47.4%	56.2%	59.6%
140°	40.0%	57.6%	62.1%

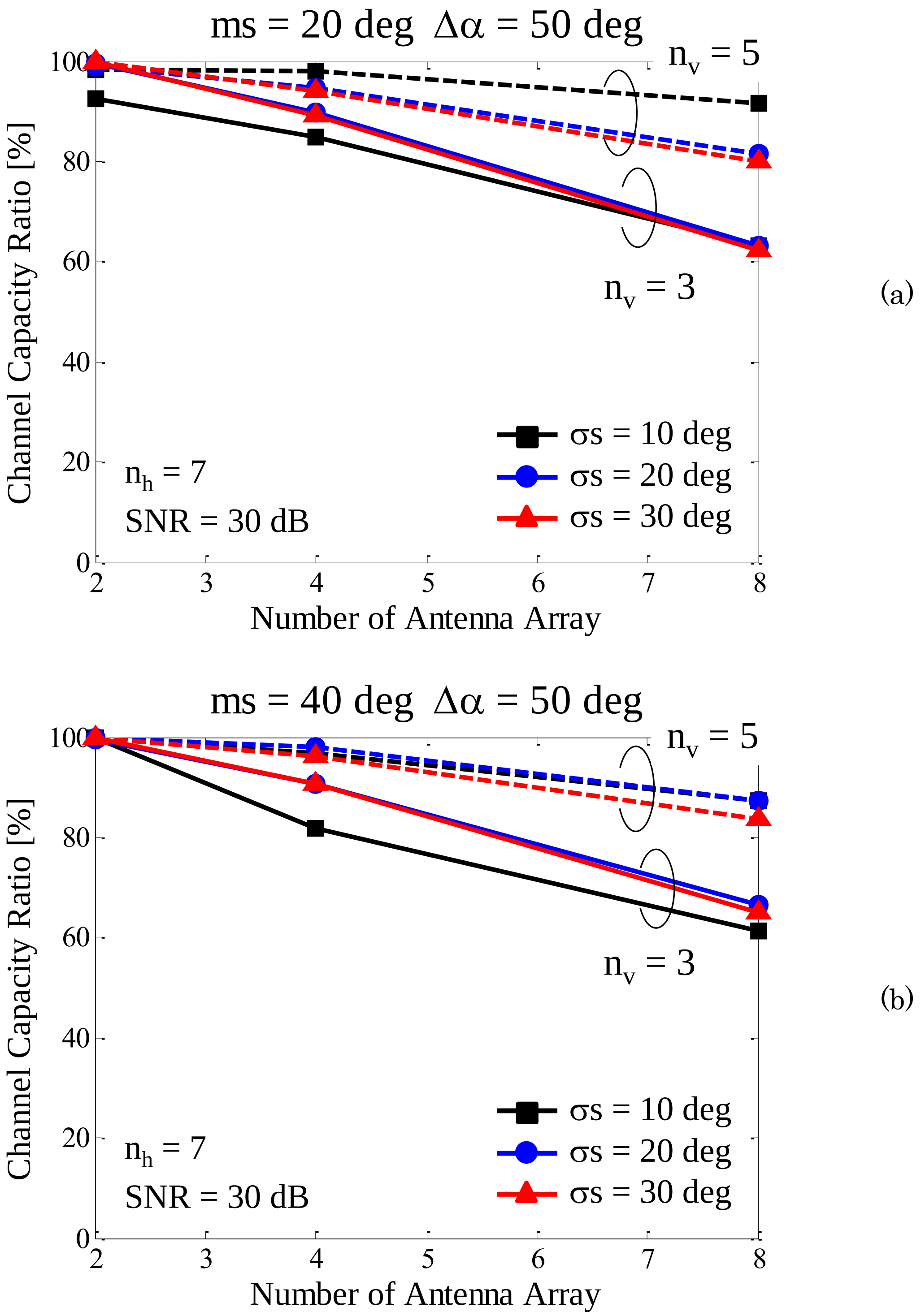

Fig. 5.10 Channel capacity ratio vs. the number of array elements and scatterers angular region when $\Delta\alpha = 50^\circ$: (a) $m_s = 20^\circ$ and (b) $m_s = 40^\circ$

5.5 Characterization of 2-Dimensional MIMO Array

As mentioned in Sect. 5.4, the minimum number of probes required in a practical apparatus that the number of scatterers in the elevation direction $nv = 3$ is a candidate for the development of OTA apparatus. Based on this precondition, the separation of probes in the elevation direction was investigated to further minimize an OTA device [94]. Particular emphasis is placed on the mutual interactions between the incident wave power distribution in the elevation direction and the radiation pattern of terminal antenna elements. In this section, a performance analysis of a two-dimensionally arranged MIMO array antenna is conducted using the proposed channel model in Fig. 5.2 (b).

Fig. 5.11 shows the structure of the two-dimensional MIMO array antenna as an extended version from Fig. 5.2 (a), where the MIMO array antenna is comprised of vertically-oriented half-wavelength dipole antennas. 4 elements are arranged in column in the z-direction and 2 elements are arranged in row in the y-direction, constructing an 8-element MIMO array antenna in the vertical and horizontal arrangement. The vertical and horizontal array spacing d_{s1} and d_{s2}, are set to 9 cm. The frequency for the analysis is 2 GHz.

Fig. 5.12 shows the average channel capacity as a function of the elevation probes angular region $\Delta\alpha$, with the incident waves angular spread, σ_s, as a parameter. The probe parameters values of $nh = 7$ and $nv = 3$ were chosen. The diamond in Fig. 5.12 indicates the target capacity value calculated by the same parameters with that in Fig. 5.5, which indicates an idealized 3D-OTA system.

As shown by the solid curve with symbol ● in Fig. 5.12, when σ_s is 20°, the degradation in channel capacity can be observed in both sides of the elevation probes angular region with respect to 50°, as a similar phenomenon shown in Fig. 5.8. This may be due to the power variation of incident waves in the elevation direction because of a small standard deviation of $\sigma_S = 20°$.

Therefore, we expand the angular spread σ_S from 20° to infinity to transform the Gaussian distribution to a uniform distribution to ensure the equivalent power of incident waves in the elevation direction. This can increase the MIMO channel capacity compared with that at $\sigma_S = 20°$, as shown by the broken curve with symbol ■ in Fig. 5.12, but the channel capacity does not reach the target value as supposed. In order to clarify the mechanism responsible for this fact, the mutual effects of the multipath propagation environment and antenna radiation characteristics of a MIMO antenna to be tested using an OTA apparatus is analyzed.

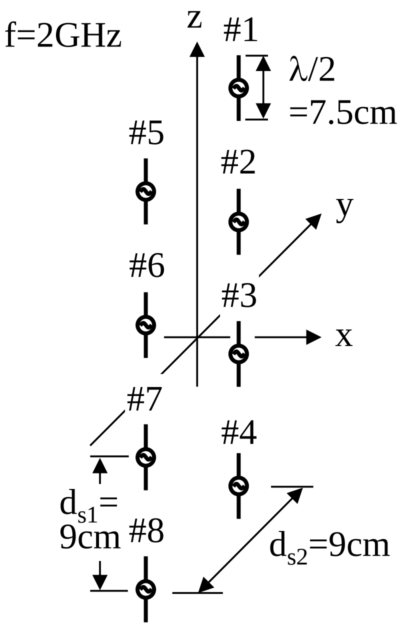

Fig. 5.11 2-by-4 vertically-arranged MIMO array antenna

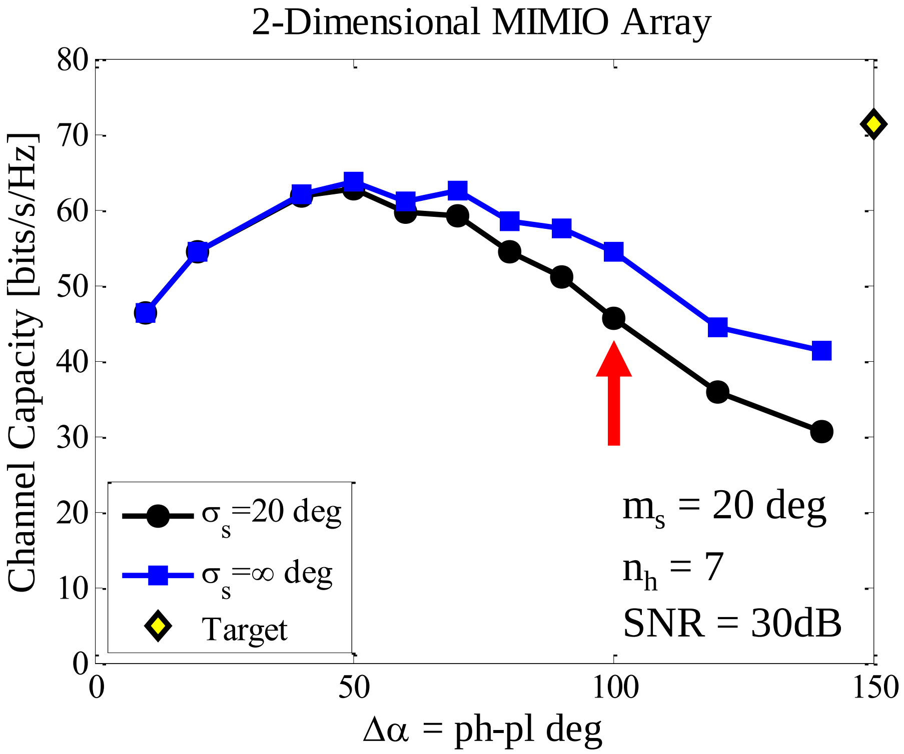

Fig. 5.12 Channel capacity of 2D MIMO antenna as a function of $\Delta\alpha$ with

incident waves angular spread σ_s as parameters

Fig. 5.13 (a) shows the radiation pattern of a half-wavelength dipole antenna in the vertical plane with θ-polarization that is a single unit of the 8-element MIMO array antenna shown in Fig. 5.11 (a). The analytical frequency is 2 GHz. Three incident waves with equivalent power ($\sigma_S = \infty$) are assumed coming from the elevation directions.

As seen in Fig. 5.13 (a), although the power level of the three incident waves are the same, the received signal level is different owing to the radiation pattern in the vertical plane, as shown by points Q1, Q2, and Q3, when the elevation probes angular region is set to 100°. Therefore, when the elevation probes angular region increases, the incident waves in the vicinity of the *ph* and *pl* directions will approach the null position of radiation patterns. This degrades the channel capacity owing to a reduction in the received signal power, as indicated by the arrow in Fig. 5.12.

The abovementioned considerations imply that if the MIMO antenna shows an omnidirectional radiation pattern in the vertical plane, the channel capacity increases. To verify this, a turn-style antenna was used. The turn-style antenna is comprised of two orthogonally aligned half-wavelength dipole antennas in the horizontal plane with 90° out-of-phase excitation, as illustrated by an inset in Fig. 5.13 (b). As shown in Fig. 5.13 (b), the turn-style antenna has an omnidirectional radiation pattern in the zx-plane with ϕ-polarization. This suggests that the received signals will have identical amplitudes if the ϕ-polarized incident waves follow a uniform distribution, as shown by points Q4, Q5, and Q6, as shown in Fig. 5.13 (b). Using the turn-style antenna, an 8-element MIMO antenna operating at 2 GHz was arranged in the same configuration as the vertically-oriented dipole antennas shown in Fig. 5.11 to create a quasi-MIMO array for analyzing the channel capacity.

Fig. 5.14 shows the channel capacity of the 8-element MIMO antennas using vertically-oriented dipole antennas and quasi-turn-style antennas as a function of the elevation probes angular region. The XPR was set to −50 dB in the analysis of the turn-style antenna, implying that only horizontally-polarized waves were considered. An increased and stable channel capacity was observed as shown by the solid curve with symbol ▲ as the scatterers angular region increased when the turn-style antenna was used, confirming the validity of our presumption.

The abovementioned phenomena seen in Figs. 5.12 and 5.14 can be understood by analyzing the average correlation coefficient, defined as an average of the correlation coefficients between elements arranged in the longitudinal direction. Fig. 5.15 shows the calculated results. As seen in Fig. 5.15, when we used the dipole array antennas, the average correlation coefficient was decreased significantly when σ_s was increased from 20° to infinity, as indicated by the solid curve with symbol ■, which resulted in an increased channel capacity corresponding to the analytical results shown in Fig. 5.12. An abrupt change in the correlation coefficient, where $ph - pl$ approached 80°, denoted by points Q7 and Q8, can be attributed to a cancellation phenomenon of incident waves that occurred owing to the reverse phase on the opposite sides of the radiation pattern of the dipole antenna. This allowed the multipath effects to disappear, leading to the abrupt change in the correlation coefficient.

Further, when the σ_s was set to infinity, the average correlation coefficient of the turn-style array was almost the same as that of the dipole array, as presented by the solid curve with symbol ▲. This suggests that the stable channel capacity after $\Delta\alpha$ of 50° for the turn-style array was not caused by the change in the correlation coefficient, but by an increase in the received signal power due to the omnidirectional radiation pattern of the turn-style array. This presumption is also supported by the fact that, as seen in Fig. 5.14, with $\Delta\alpha$ decreasing to less than 50°, the channel capacity of the dipole array was larger than that of the turn-style array owing to the directivity of the dipole antenna, as indicated by position Q1 in Fig. 5.13 (a) when the three incident waves approach the average elevation angle m_s.

Based on the abovementioned considerations, we conclude that the variation in the MIMO channel capacity in the 3D-OTA tests was caused by the power distribution of incident wave σ_s and the radiation patterns in relation to the different types of antennas. These two mechanisms interact with each other; therefore, they should be taken into consideration in the process of designing the 3D-OTA probe arrangement.

Specifically, for example, when $nv = 3$, to test the antenna with irregular radiation characteristics such as a dipole antenna, the probes in the elevation direction need to be arranged with a large angular separation, such as 50 degrees, to ensure a high MIMO channel capacity. On the contrary, if the DUT antenna has an omnidirectional radiation pattern in the vertical plane, such as a turn-style antenna, the probes in the elevation direction can be appropriately arranged with a smaller angular separation, such as 30 degrees, as shown by the arrow in Fig. 5.14.

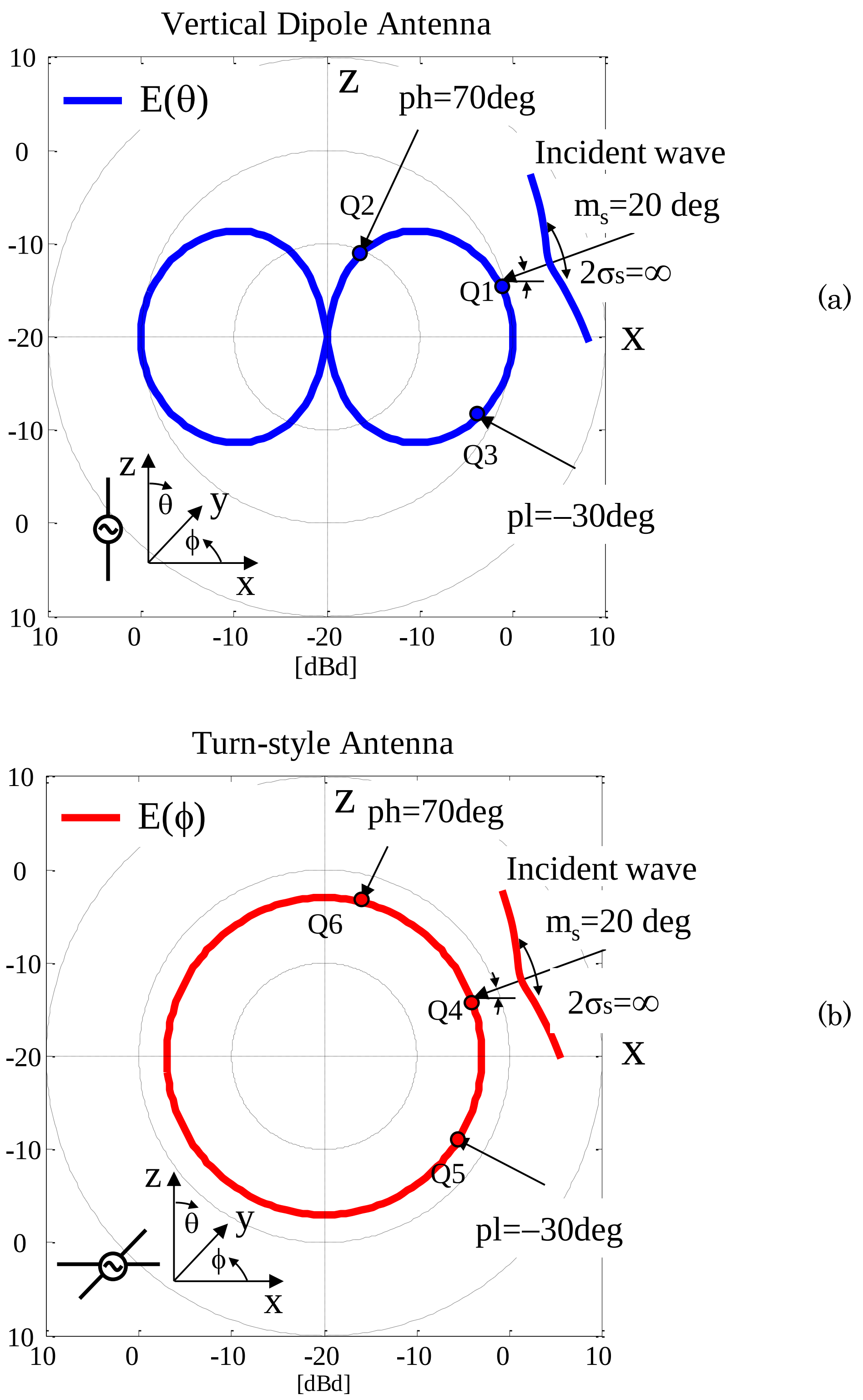

Fig. 5.13 Radiation pattern with incident waves in the elevation directions

(a) vertical dipole antenna; (b) turn-style antenna

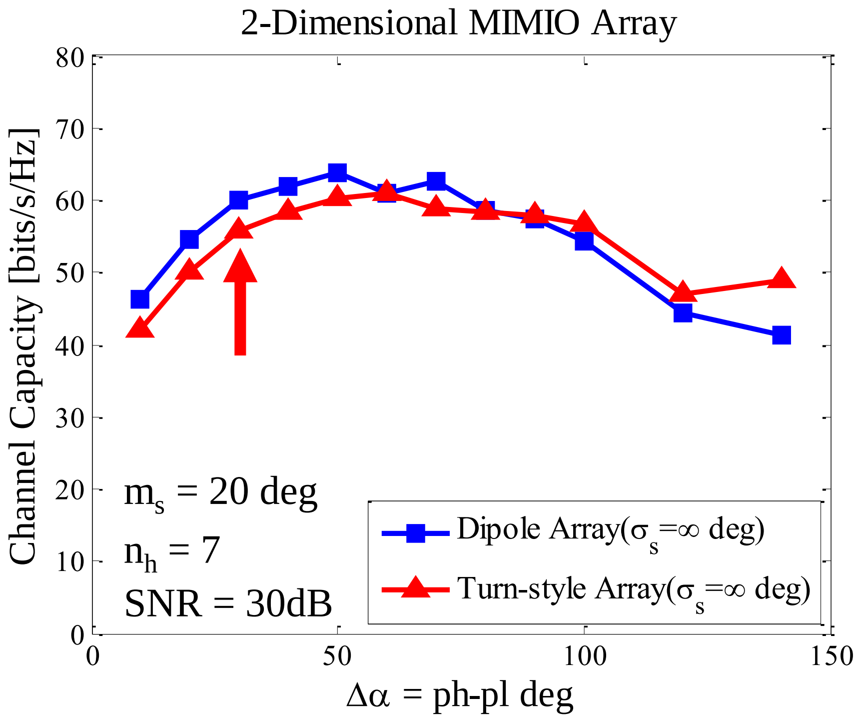

Fig. 5.14 Channel capacity of vertical dipole and turn-style array vs. *Δα*

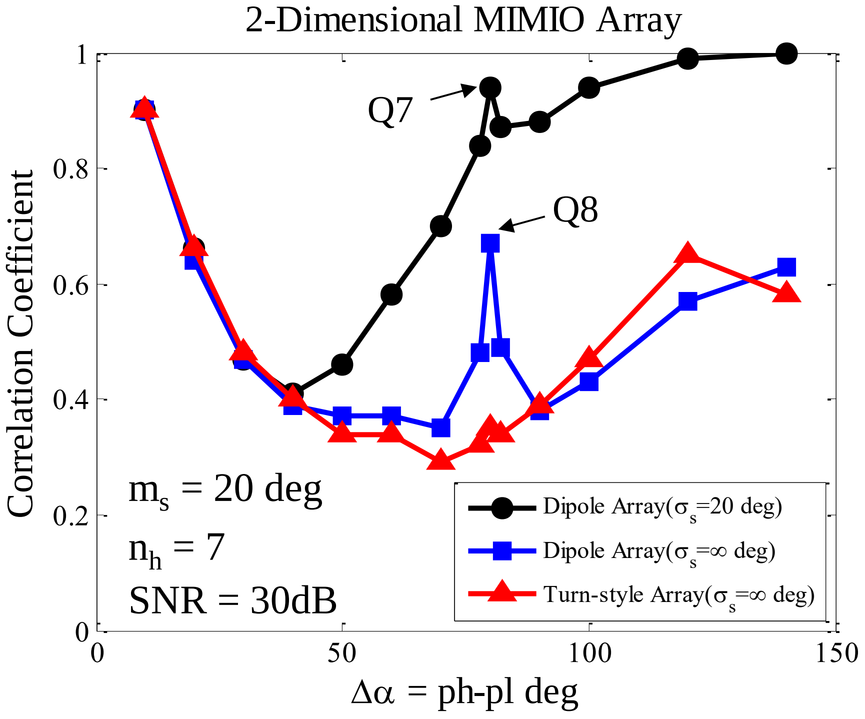

Fig. 5.15 Average correlation coefficient of vertical dipole and turn-style array antennas vs. elevation probes angular region *Δα*

5.6 Design and Manufacture of 3D-OTA Apparatus

On the basis of the knowledge obtained from this work, the configuration of an OTA apparatus for evaluating a two-dimensional MIMO array antenna is designed, as shown in Fig. 5.16. In Fig. 5.16, nv is set to 3 while $\Delta\alpha = ph - pl$ is set to 50 degrees in consideration of the miniaturization of an actual OTA device.

As shown in Fig. 5.16, three sets of dipoles are arranged in the longitudinal direction. The nv scatterers are integrated as one module for the generation of desired incident waves power distribution σ_s in the elevation direction controlled by using attenuators. The signal of each path is distributed to vertical and horizontal polarization components for the realization of XPR. The variable phase shifter module is connected by a coaxial cable, which will be used to calculate the channel response of each path h_{nm} (see Eq. (5.7)) according to the moving direction and moving distance of the terminal by a computer. Therefore, the entire electromagnetic waves radiated from the scattering units can be controlled.

Fig. 5.17 shows the photograph of developed 3D-OTA apparatus based on the analytical results presented in this study, where the multi-element MIMO array antenna will be mounted on the dynamic human phantom in order to realizing the ultra-high-speed communication in future mobile medical-healthcare system. This will be addressed as a future work.

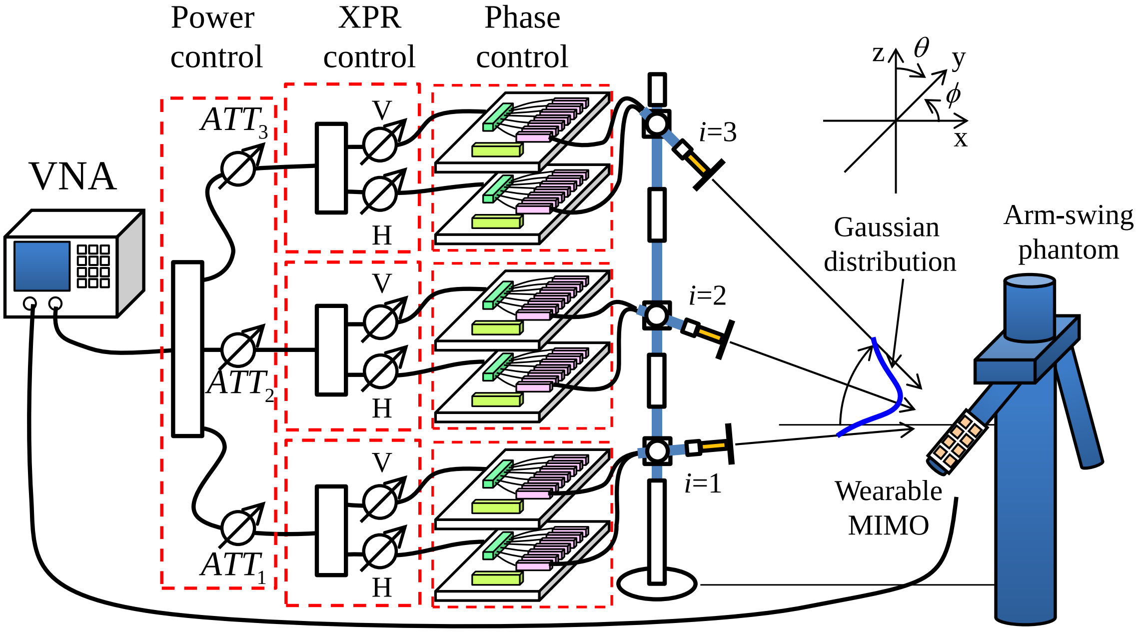

Fig. 5.16 Configuration of 3D-OTA apparatus for wearable MIMO antenna

Fig. 5.17 Photograph of 3D-OTA apparatus with dynamic human phantom

5.7 Conclusion

This paper presents a new methodology of OTA assessment for vertically and two-dimensionally arranged MIMO array antennas. The appropriate scatterers arrangement considering multipath characteristics and the number of DUT antenna elements required for evaluating vertically arranged MIMO array antennas has been studied. Useful knowledge has been obtained that can be employed in the design of an actual 3D-OTA apparatus.

A great quantity of analytical data for the appropriate scatterers arrangement are proposed. The arrangement can be determined based on the actual conditions of multipath characteristics and the number of DUT antenna elements as desired. A choice of scatterers arrangements such that when we test the vertically arranged MIMO array antenna is provided, the angular range of 50° is found to be suitable for 3D-OTA testing. Based on this investigation, when the number of vertically arranged antenna arrays N is less than 4, the number of scatterers $nv = 3$ is adequate to realize a 3D-OTA assessment, while if N is increased to 8, $nv = 5$ is necessary.

In the view of the analytical results presented in this study, it is anticipated to obtain the optimization of the structure of the OTA device. An actual 3D-OTA has been developed using the knowledge obtained in this paper [95].

6. Bit-Error-Rate OTA Methodology

6.1 Introduction

In the upcoming 5G communication system, wearable terminals such as watch-type and body-attached devices operated in BAN systems have received considerable attention owing to the increasing demand for wireless applications in medical information communication technology (MICT) [9]. To ensure the safety of patients in hospital, high reliability and high accuracy of medical data obtained from body-worn wireless devices is essential. The signal bit error rate (BER) is generally treated as a key index for evaluating an antenna's communication quality.

So far, analytical studies of the BER performance of mobile antennas in a multipath environment in a non-line-of-sight (NLOS) case have been carried out [96] [97]. In a previous study [98], assessments of BER characteristics of BAN antennas were conducted by using a Monte Carlo simulation. However, because of an absence of equipment for BER measurement, few studies have been conducted using an empirical method for a multipath-fading channel. Therefore, an evaluation system for the BER performance of BAN antennas is anticipated.

There are two difficulties in evaluating the BER performance of BAN radios. As shown in Fig. 6.1 (a), the first is that we must consider dynamic channel variation, commonly referred to as shadowing, caused by human motion [61] [62]. The second is the multipath radio components (fast fading) due to reflections and diffractions from surrounding objects, as shown in Fig. 6.1 (b). In real-world BAN scenarios indoors, objects such as walls and furniture will cause severe deterioration in the communication quality of

BAN antennas. These difficulties indicate that the key target of BER evaluation is the realization of instantaneous BER performance under a continuous dynamic BAN channel in realistic fading scenarios.

With regard to the first issue, many studies have been published to clarify dynamic behaviors of the human body [10], [58]. However, an assessment using a real human has a drawback in terms of poor controllability for realizing repeatable human dynamic motions such as walking. We developed an arm-swinging dynamic phantom that can simulate the natural walking style of a human, with controllable arm-swinging angles [38].

With regard to the second difficulty, some efforts have been made to derive a channel model using statistical approaches [64], [99]. In propagation measurement using an actual human, the statistical modeling depends on numerous parameters, such as the propagation channel, the human body and the antenna types or orientation. Therefore, it is difficult to determine the true reasons for variations in antenna performance in BAN dynamic channels. In order to consider the combined effects that occur in BAN dynamic channels, the systemization of a measurement procedure needs to be developed.

Over-the-air (OTA) testing is a good candidate for evaluating the general performance of mobile devices [17]. A spatial fading emulator can directly produce a radio multipath environment with higher controllability and accuracy [17]. An OTA test to assess a BAN on-body antenna in a Rice channel model using a fading emulator has been conducted. This test successfully constructed an assessment system that took into account both the human dynamic channel and the fading process [100]. However, the continuous arm-swinging motion in [100] was operated separately from the

OTA measurement using a different GPIB control system, as illustrated in Sect. 3.5. Thus, the matching between the arm-swing control and signal detection in the fading process was not taken into account. This will eventually degrade the measurement accuracy when conducting highly sensitive OTA tests, such as BER.

Another study [101] proposed a BER measurement apparatus for a handset adaptive antenna evaluation. However, the details of the BER measurement procedure were not clarified. Compared to an OTA evaluation for general mobile terminals [101], the probability of synchronism loss for BER detection in a dynamic BAN radio channel will increase due to the significant arm shadowing effects. It is critical to restore the instantaneous BER performance overlapped with the time-variant fading profile. To eliminate the synchronism loss in a dynamic BAN channel, the detection of instantaneous BER must be embedded into the fading process in a discrete-continuous manner.

This study presents a methodology for BER-OTA testing to evaluate the communication quality of BAN antennas. A novel dual-discrete control method to detect the instantaneous BER by using a fading emulator with a dynamic human phantom for the off-body communication system between the wearable terminal and base station is proposed. Emphasis is placed on how to implement the proposed method while simultaneously considering the dynamic BAN channel and multipath effects. The empirical results show that the proposed method replicates a realistic arm-shadowed fading channel with both instantaneous and average BER characteristics.

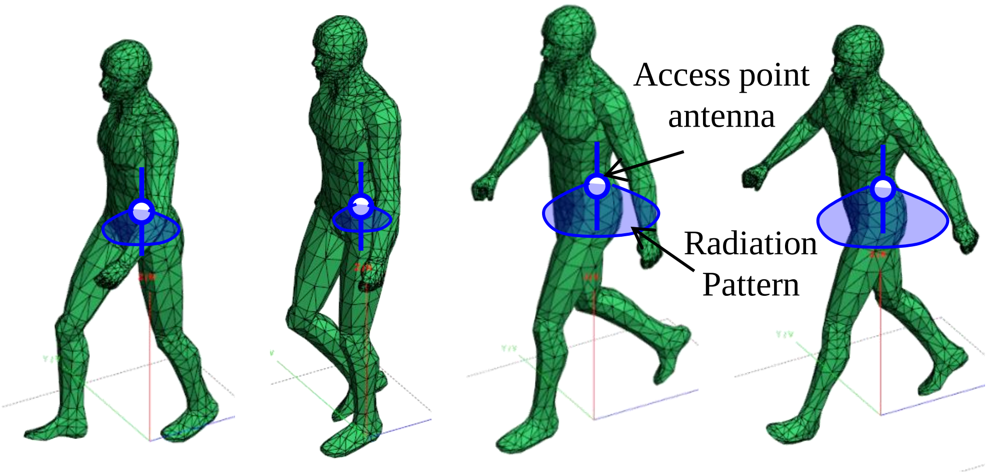

(a) Shadowing effects caused by arm-swinging motion

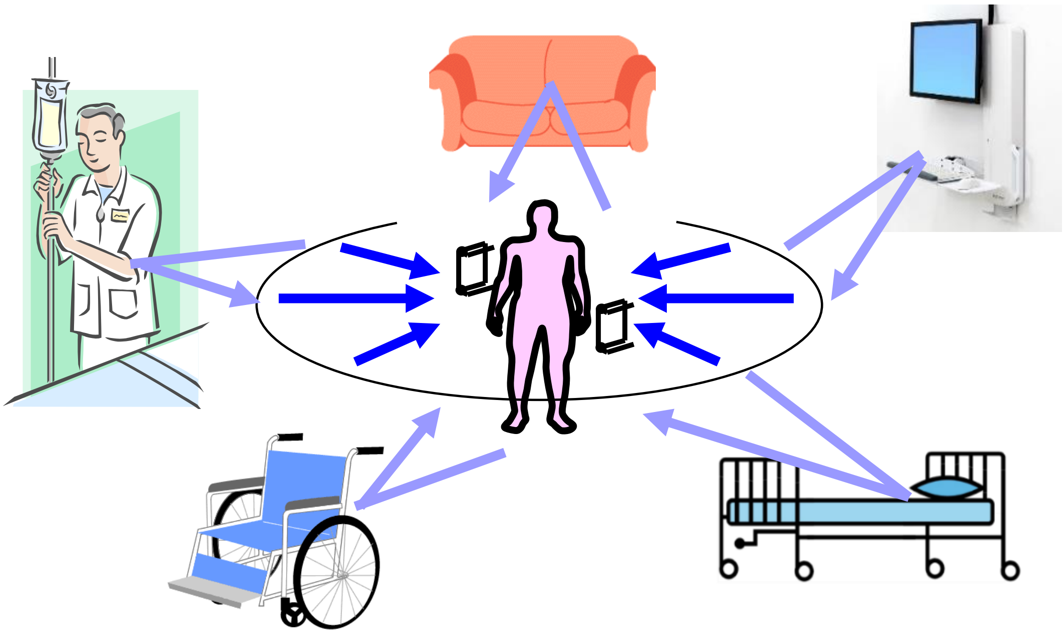

(b) Multipath effects from surrounding objects indoors

Fig. 6.1 Subjects of wearable BAN in medical propagation environment

6.2 BER-OTA Assessment Apparatus

Fig. 6.2 (a) shows the configuration of the proposed BER-OTA apparatus. The diameter of the fading emulator is 240 cm, and the height of each surrounding dipole antenna from the floor is 100 cm. A dipole antenna is attached to the human body, e.g., to the left waist, simulating an access point of wireless application for off-body communication with the external terminals. The arm-swinging dynamic human phantom [38] is located at the center of the fading emulator. The phantom can swing both arms to emulate the shadowing effects.

The 14 scatterers comprising dipole antennas surrounding the phantom are used to produce the radio waves with a Doppler shift by continuously varying the phase of the RF signals. In an indoor walking situation, a decrease in the Rice factor results in a fading statistic approaching a Rayleigh distribution (see Table 6 in [57]). Thus, the propagation properties of the off-body system are similar to those of a standard cellular system. In this study, to represent a canonical model of mobile communication systems, the angular density function of incident waves is assumed to be uniform in azimuth. The phase shift values of each path are determined by random numbers using a computer to generate uncorrelated waves with uniformly distributed scatterers (Clark model), confirming that the summation of all the paths results in multipath signals with the properties of Rayleigh fading.

Table 6.1 summarizes the specifications for the wireless device used in the experiment. A frequency shift keying (FSK) signal with a PN9 pattern at 926 MHz is created using a signal generator (Anritsu, MG3710A) at the transmitting side. This signal is detected using an FSK module (Silicon Labs, Si4432) at the receiving side, as shown in Fig. 6.2 (b). FSK modulation is commonly applied to low-data-rate, low-power radio frequency wireless devices such as the wearable applications in BAN radio systems. A DUT (device under test) antenna is connected to the wireless IC (Integrated Circuit) via a coaxial cable, as indicated by a photograph in Fig. 6.2 (a). Using this equipment, the instantaneous BER performance in a specific BAN scenario can be detected. The procedure to set up the link of FSK wireless module and signal generator is illustrated in [Apx. C] in details.

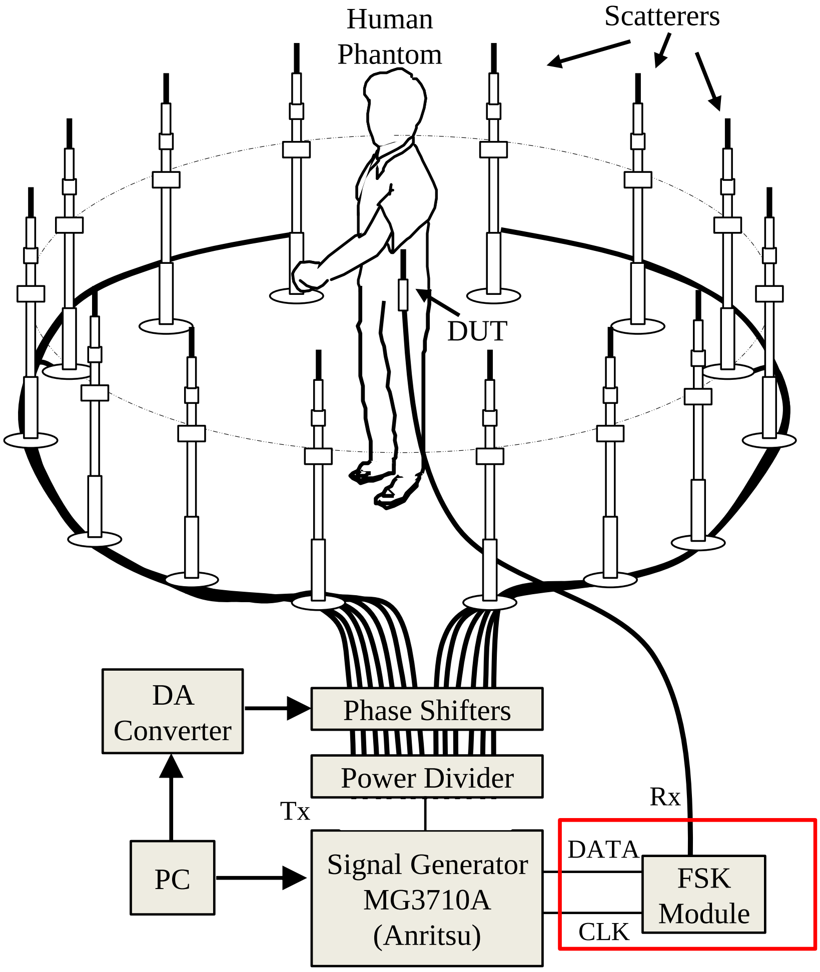

(a)

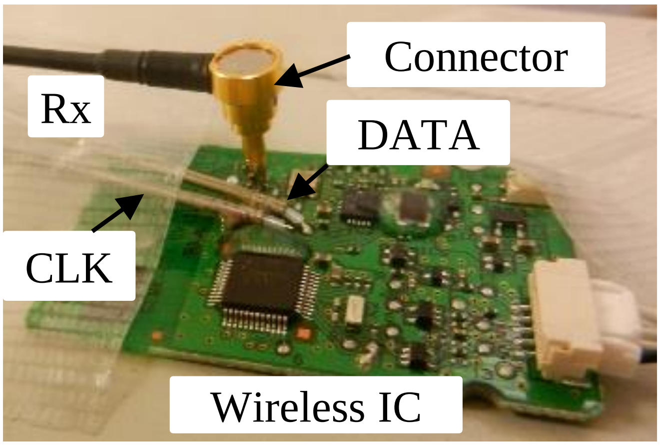

(b)

Fig. 6.2 Two-dimensional fading emulator for BER measurement

(a) BER-OTA apparatus (b) FSK module

Table 6.1 Specifications for Wireless Device

Frequency	**926 MHz**
Wireless IC	**Si4432**
Modulation	**FSK**
Signal pattern	**PN9**
Transmission rate	**40 kbps**
Sensitivity	**-105 dBm (BER<10^{-3})**
Antenna	**Half-wavelength dipole**

6.3 Dual-Discrete Control Method

In general, in field testing of mobile terminals, BER is treated as a time-averaged value in a real-time continuous measurement under certain sampling numbers. However, in a dynamic BAN channel, the received signal level of a wearable application is extremely sensitive to human motion. In that case, in addition to multipath fading effects, the synchronism loss in a real-time continuous BER detection process increases significantly. After the re-synchronism operation, the restarted BER measurement will deviate from the original location of the fading snapshot. Consequently, the instantaneous BER overlapped with fading profile cannot be clearly obtained. This eventually degrades the accuracy and reliability of the measured BER data in a dynamic BAN channel.

To reduce the probability of synchronism loss in BER experiment, the detection of instantaneous BER is conducted at the interval when fading process is stopped. Since the transmission rate of the FSK module (see Table 6.1) is extremely high compared with the maximum Doppler frequency caused by the natural human walking speed [102], the random FM noise produced by received signal phase variation is not superimposed on the desired modulation. In that case, it can be inferred that there is no significant impact on the average BER performance of the receiver due to the Doppler effects because the error floor is sufficiently low [103].

In order to guarantee the accuracy of a BAN antenna evaluation, in this paper we propose a novel dual-discrete processing method for detecting the instantaneous BER performance of a dynamic BAN channel in a Rayleigh fading propagation environment.

Fig. 6.3 shows the hybrid analytical model of fading signals that simultaneously takes into account the arm-swinging and the walking motion using Monte Carlo simulation (see Fig. 4 in [98]). The two-way swing is divided into many small angular fragments, with each fragment occupying a 5-degree swing motion. In all the 5-degree angular regions, the radiation patterns are calculated using the method of moments. Employing a constant-radiation pattern within a 5-degree region, fading signals are created using a Monte Carlo simulation that calculates every snapshot by summing all the paths between the i-th surrounding scatterer and the wearable dipole antenna. The procedure for the Monte Carlo simulation is described in detail in literature [93]. Based on this analytical method, the experimental dual-discrete processing method is shown below.

Fig. 6.4 (a-1) shows the first discrete processing for instantaneous BER detection in a fading channel, which simultaneously takes the arm-swinging motion into account [38], [100]. The red curve shows an image of the continuous fading signals in single-cycle arm-swinging motion, whereas the black line indicates the divided arm-swinging angular fragments. The left arm angle α, which is defined as the angle of a line that connects the shoulder and the hand in the vertical direction, swings forward ($\alpha = 40^{\circ}$) and backward ($\alpha = -10^{\circ}$) on the human phantom. Fig. 6.4 (a-1) indicates an example of a two-stride human walking motion, corresponding to two-way arm-swinging from $\alpha = 40^{\circ}$, passing through $\alpha = -10^{\circ}$ in between, and terminating at $\alpha = 40^{\circ}$ at the end. Each stride is set to 70 cm (2.16 λ). Thus, the phantom walks over a distance of $d = 140$ cm, which is equivalent to 4.32 λ at 926 MHz. As shown in Fig. 6.4 (a-1), d is defined as the summation of all section distances d_n in each arm-swinging angular fragment, as expressed by the following equation:

$$d = \sum_{n=1}^{N} d_n \tag{6.1}$$

where N denotes the number of separate arm-swinging angular sections. Although the human arm-swinging motion follows different statistical models such as a continuous sinusoidal variation [98], to simplify the experiment, all arm-swinging angular regions are set to equal intervals ($d_1 = d_2 \ldots = d_N$). In Fig. 6.4 (a-1), since the number of snapshots is set to 50 samples per wavelength, the two strides cover 4.32 × 50 = 216 snapshots. Therefore, when each arm-swinging angular region is set to 10°, there are $N = 12$ intervals from $\alpha = 40°$ to $-10°$ and back to 40°, resulting in 18 snapshots per angular section, as shown in Fig. 6.4 (a-1). BER detection for every arm-swinging section overlapped with a fading channel was conducted until the end of 18 sampling snapshots. Then BER detection moved to the next arm-swinging angle.

Fig. 6.4 (a-2) shows the second discrete processing for instantaneous BER detection in the fading channel. As can be seen in Fig. 6.4 (a-1), in each snapshot of the fading profile, the DA converter for the phase control is stopped, which implies that there is a pause in the fast fading process. At this interval, the measurement of a time-averaged BER value is calculated, as shown in Fig. 6.4 (a-2). Since the synchronism is completed at a different time (T_0) in every snapshot owing to the different received signal levels caused by channel variations, the stop time is expanded to 6 s as an exit condition in a way that the time of synchronism and actual BER measurement are sufficient. After the synchronism is completed, the BER measurement is switched from fluctuating to stable state with the increasing sampling data, as shown in Fig. 6.4 (a-2). This method improves the accuracy of instantaneous BER detection overlapped with fading signals. For the sake of the 40-kbps transmission rate of the wireless IC, the maximum sampling data is calculated as 240,000 at this interval. Thus, a high degree of accuracy in the BER value up to 10^{-6} can be detected. When the time-averaged BER detection shown in Fig. 6.4 (a-2) is finished, the fading process is moved to the next snapshot with a separation of λ / 50, as shown in Fig. 6.4 (a-1), until the antenna has covered the prescribed traveling distance *d*.

Fig. 6.4 (b) shows the BER detection in numerous arm-swinging cycles in Fig. 6.4 (a-1). The entire traveling distance D is defined as follows:

$$D = kd \tag{6.2}$$

where k indicates the number of arm-swinging cycles, as shown in Fig. 6.4 (b). Thus, the traveling average BER value (BER_m) of all instantaneous BER (BER_s) values in the entire human walking distance D is calculated as follows:

$$BER_m = \frac{1}{S}\sum_{s=1}^{S} BER_s \tag{6.3}$$

where S signifies the number of entire snapshots, as indicated by the lateral axis in Fig. 6.4 (b). In this paper, k is set to 1, and thus S is calculated to be $4.32 \times 50 = 216$.

Based on this dual-discrete method, the BER evaluation of a BAN dynamic channel can easily be carried out because the BER detection procedure is effectively embedded into a combined arm-swinging and fading channel. The details of BER measurement software using fading emulator and dynamic phantom is illustrated in [Apx. B2]

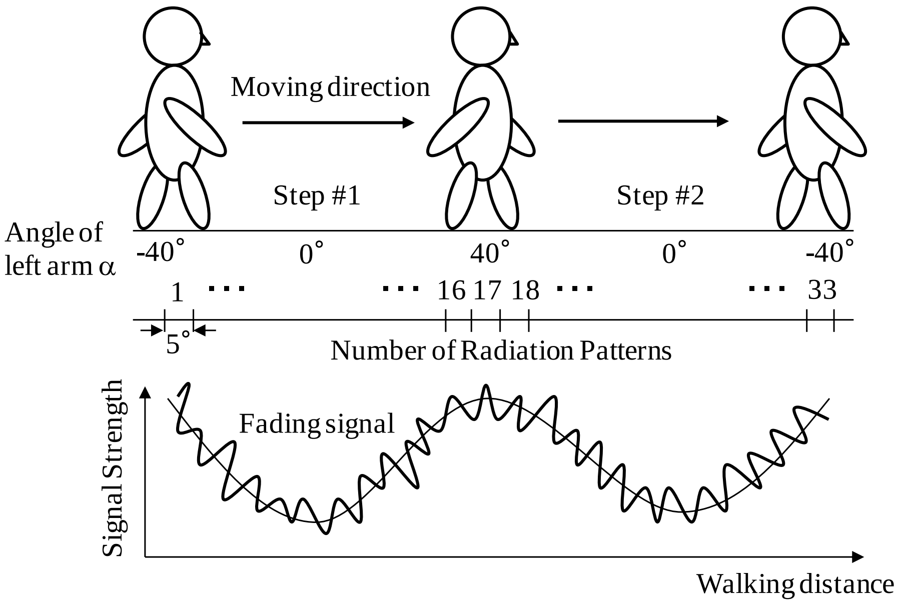

Fig. 6.3 Monte Carlo simulation method

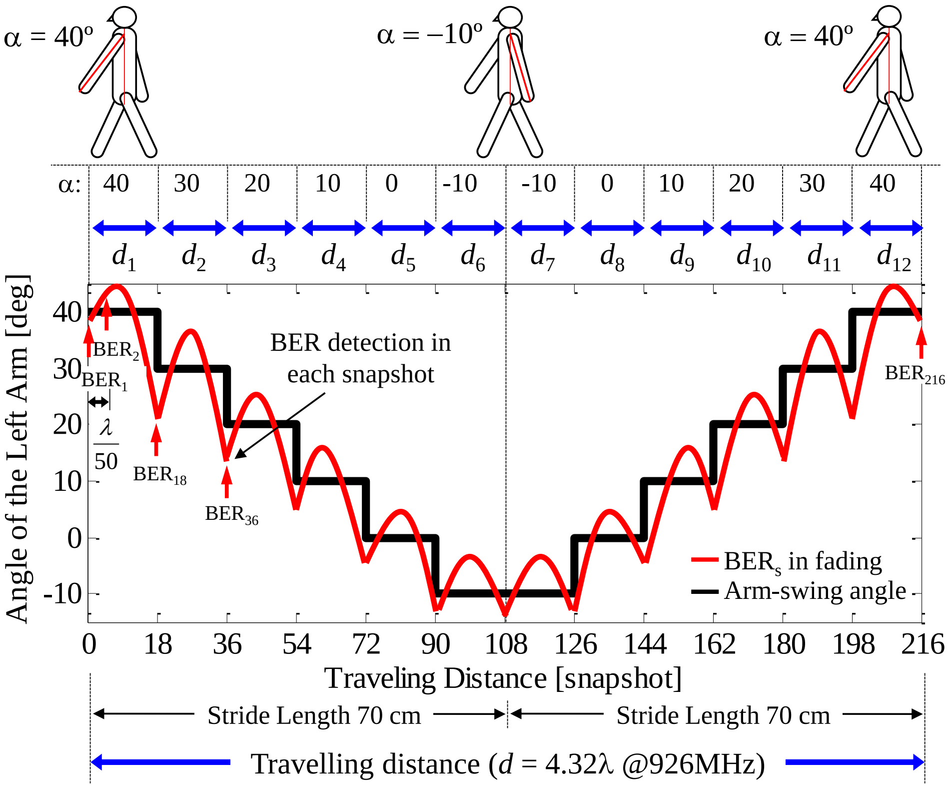

(a-1) 1st processing in a dynamic BAN channel

Fig. 6.4 Dual-Discrete control method using BER-OTA apparatus

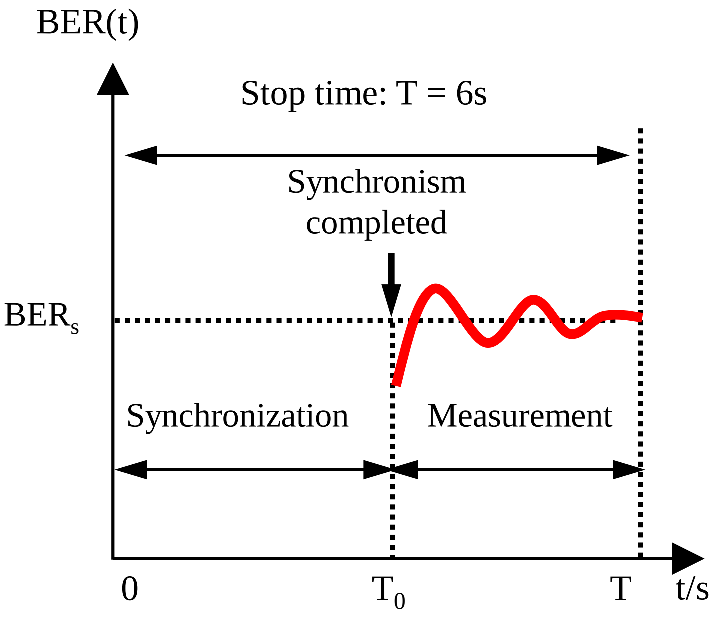

(a-2) 2nd processing for instantaneous BER in a fading channel

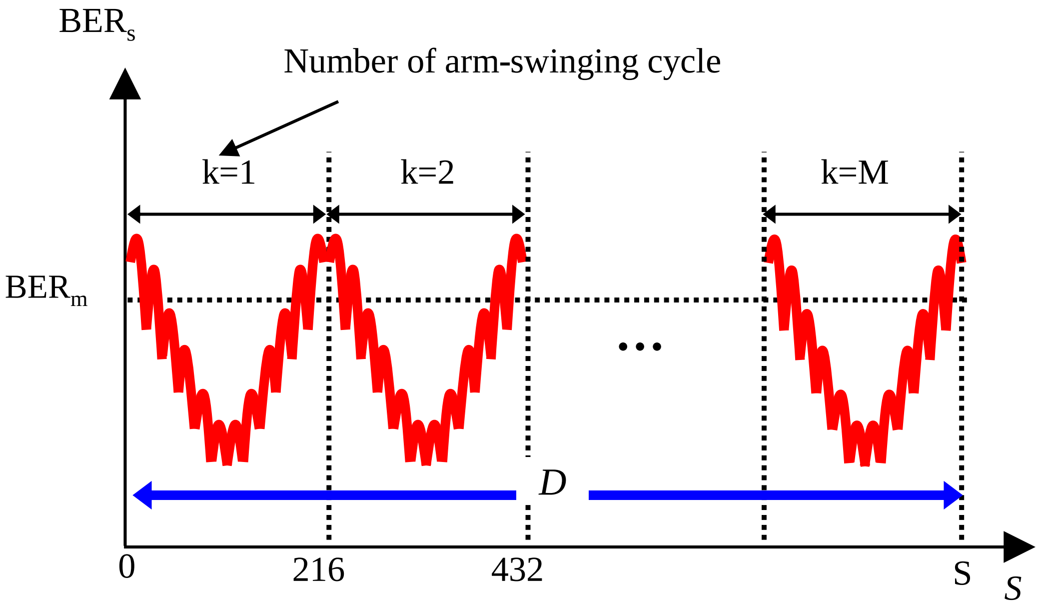

(b) BER detection in numerous arm-swinging cycles

Fig. 6.4 Dual-Discrete control method using BER-OTA apparatus

6.4 Method to set CNR

Before the BER experiment using a human phantom, a method to set the CNR (carrier to noise ratio) for the developed fading emulator [104] is illustrated in this section, as shown in Fig. 6.5.

As Step 1 in Fig. 6.5 (a), in the non-fading situation, where only one of the scatterers is connected to the SG, the power of noise P_N when BER = 10^{-3}, is calculated as follows.

$$P_N = \frac{P_{t0} L_0}{CNR_0} \tag{6.4}$$

Here, P_{t0} denotes the transmitting power when the BER equals 10^{-3}. L_0 indicates the path loss from one scatterer to DUT antenna. In this case, CNR_0 is 10 (10 dB).

As Step 2 in Fig. 6.5 (b), in the fading situation when the developed BER-OTA apparatus is used, the CNR can be calculated by following equation.

$$CNR = \frac{P_t L_r}{P_N} \tag{6.5}$$

where P_t indicates the transmitting power of SG for BER measurement in the fading situation. L_r indicates the average value of path loss in a certain walking distance of 10λ using a vertical dipole at 950 MHz, as shown in Fig. 6.5 (b). Based on this method, the average BER characteristic in the Rayleigh fading propagation environment can be investigated.

Fig. 6.6 shows the measured results of BER_m with the FSK modulation signals. The circle symbols show the results of average BER in the AWGN situation while the triangle symbols indicate those of the fading environment. Since FSK is non-linear modulation, the theoretical value of BER does not exist. Thus, an approximation formula by fitting the measured data in

AWGN channel is provided, as shown below.

$$P_e = erfc\left(\sqrt{\frac{\gamma}{2}}\right) \tag{6.6}$$

where γ indicates the instantaneous value of CNR. As shown in Fig. 6.6, the black curve coincides well with the measured result, indicating the effectiveness of Eq. (6.6). Using the Eq. (6.6), the analysis of BER_m in the Rayleigh fading environment can be calculated by Monte Carlo simulation [56] [98] [104], as shown by the red line in Fig. 6.6.

In Fig. 6.6, it can be seen that the BER performance decreases as the CNR increases with a gradient of one-tenth of the BER per 10 dB increment of the input CNR, which is identical to the gradient for a single antenna in a Rayleigh environment. However, when the CNR is larger than 25 dB, the gradient is increased. The reason is that the sampling data of each transmitted power is set to 500 points in this paper, which may not be enough to obtain the low value of BER even the CNR is increased. The optimum number of data sampling for BER OTA measurement will be investigated in future.

On the other hand, as shown in Fig. 6.6, the measured BER curve eventually coincides with the theoretical value of Rayleigh curve, indicating the validity of the proposed procedure to set the CNR using the developed BER OTA apparatus. Based on the abovementioned method, the BER measurement considering the combined effects of arm-swinging shadowing and multipath fading effects using the developed OTA apparatus is carried out, which will be illustrated in Sect. 6.5 hereafter.

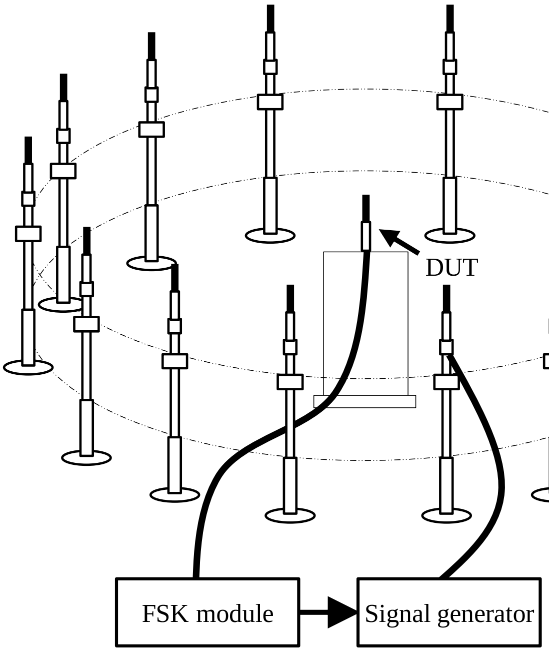

(a) AWGN channel

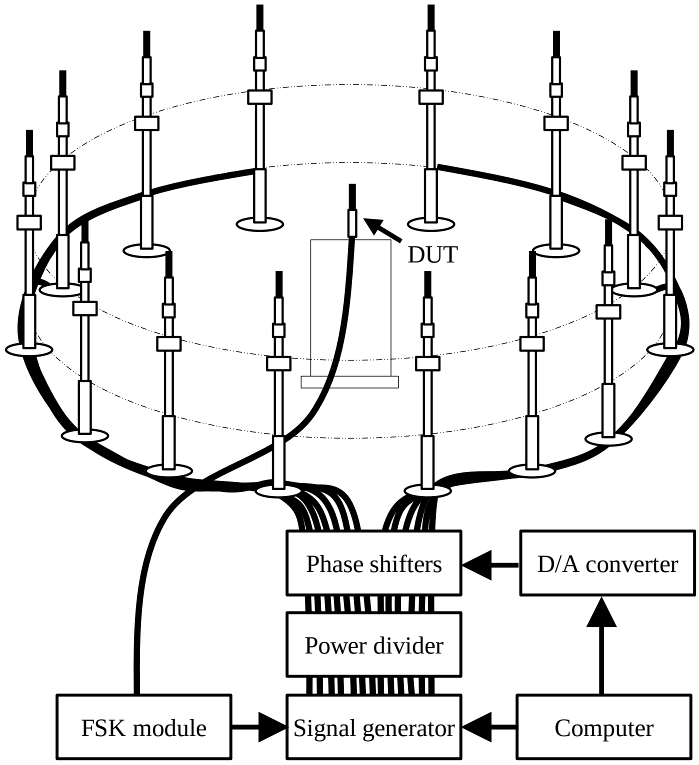

(b) Fading channel

Fig. 6.5 Method to set the CNR of fading emulator for BER measurement

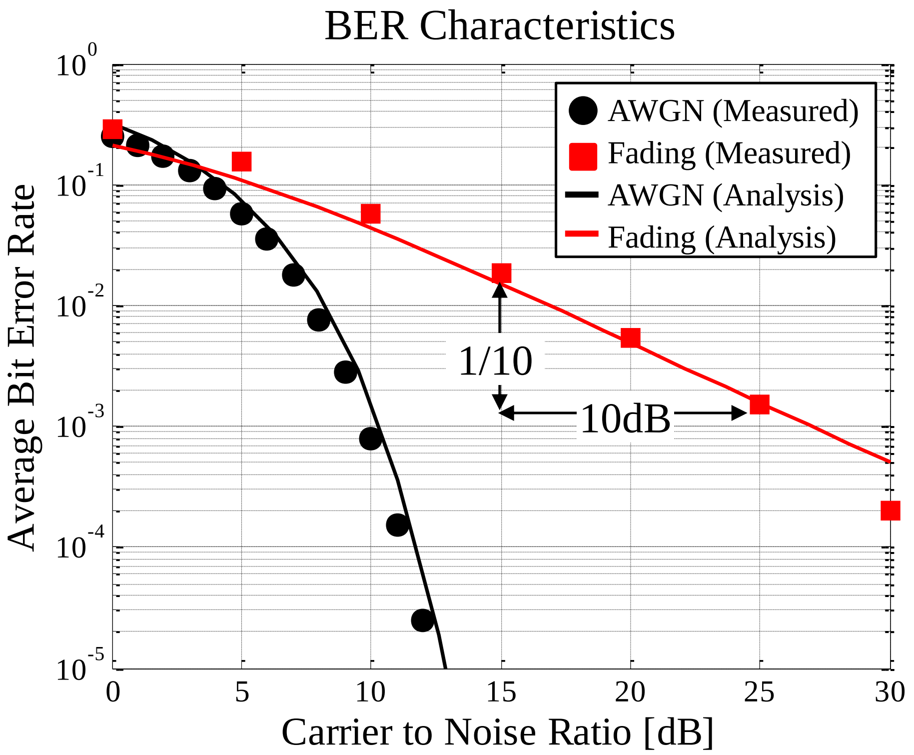

Fig. 6.6 Average BER characteristics using a vertical dipole antenna

6.5 BER Evaluation in Shadowing-Fading Dynamic BAN Channel

In this section, the BER experiment with the arm-swinging motion in a Rayleigh fading channel is carried out using the proposed dual-discrete control method for the first time.

Fig. 6.7 shows an entire view of the BER-OTA apparatus with the dynamic phantom and proposed fading emulator. The human phantom placed at the center of the fading emulator is set with a specific arm-swing angle (α). The DUT antenna (half-wavelength sleeve dipole antenna) is fixed at the left waist. The separation between the antenna and the surface of the phantom is 3 cm. The polarization is assumed to be vertical because only the vertically polarized dipole antennas are used in the fading emulator, as shown in Figs. 6.2 and 6.7.

Fig. 6.8 shows the analytical model of the dynamic human phantom and the radiation characteristics with varied angle of left arm. A half-wavelength sleeve dipole antenna at 950MHz is utilized as a DUT antenna attached to the left waist of a human phantom, as shown by in Fig. 6.8 (a). Fig. 6.8 (b) shows the radiation pattern simulated by the method of moments when the angle of left arm is 40° and 0°, respectively, which has been analyzed in previous study [56]. The electrical properties of the model are chosen such that the relative permittivity is 55.8 and conductivity is 0.99 S/m, which are the average values for human muscle at 950 MHz [38]. Due to the significant shadowing effects caused by the arm at 0°, the antenna shows a poor performance so that the radiation gain for all angles in the xy-plane is less than −20 dBd.

To clarify the Rayleigh propagation environment, the received signal status is addressed at a static scene (fixed-arm). Figs. 6.9 (a) and (b) shows the measured instantaneous response and cumulative distribution function (CDF) when the arm angle α is fixed at 40, 20 and 0°, respectively. The number of sampling snapshots S in each case is set to 216, corresponding to the sampling process of 1-cycle arm-swinging motion, as shown in Fig. 6.3 (a-1).

In Fig. 6.9 (a), the deep null positions below −20 dB can be observed. Moreover, without regards to arm angles α, the measured results indicate a well-performed Rayleigh fading environment in comparison with the theoretical curve, as shown in Fig. 6.9 (b).

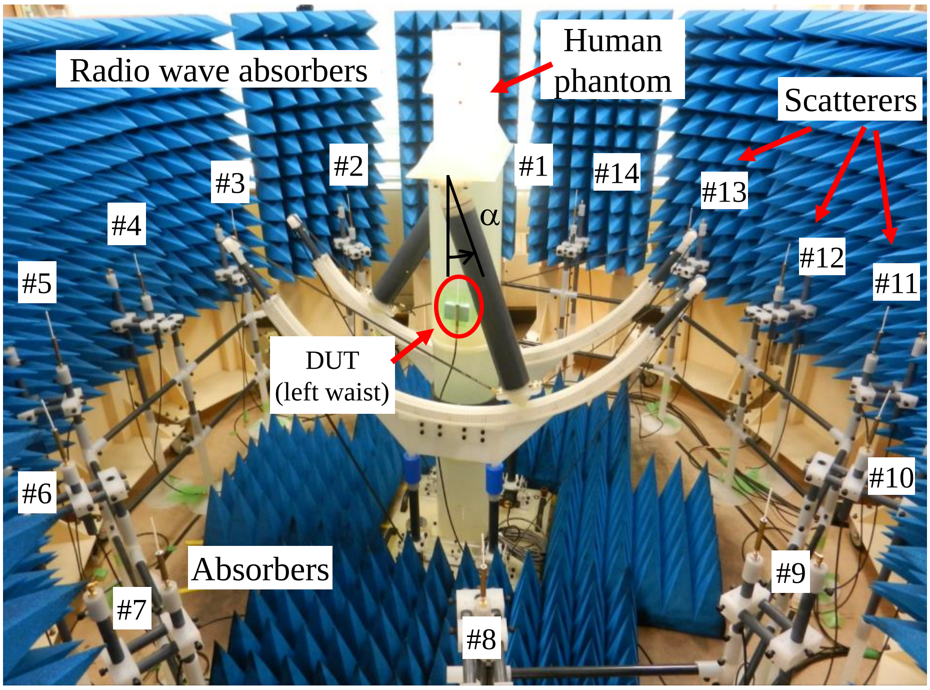

Fig. 6.7 Photograph of measurement setup.

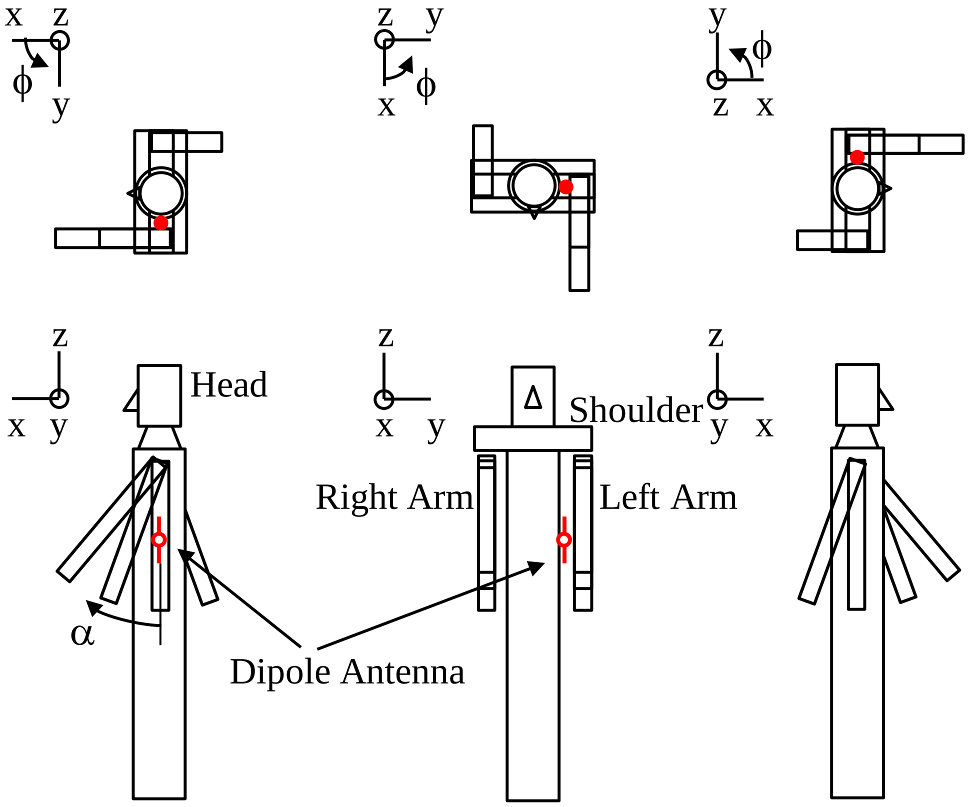

(a) Human phantom

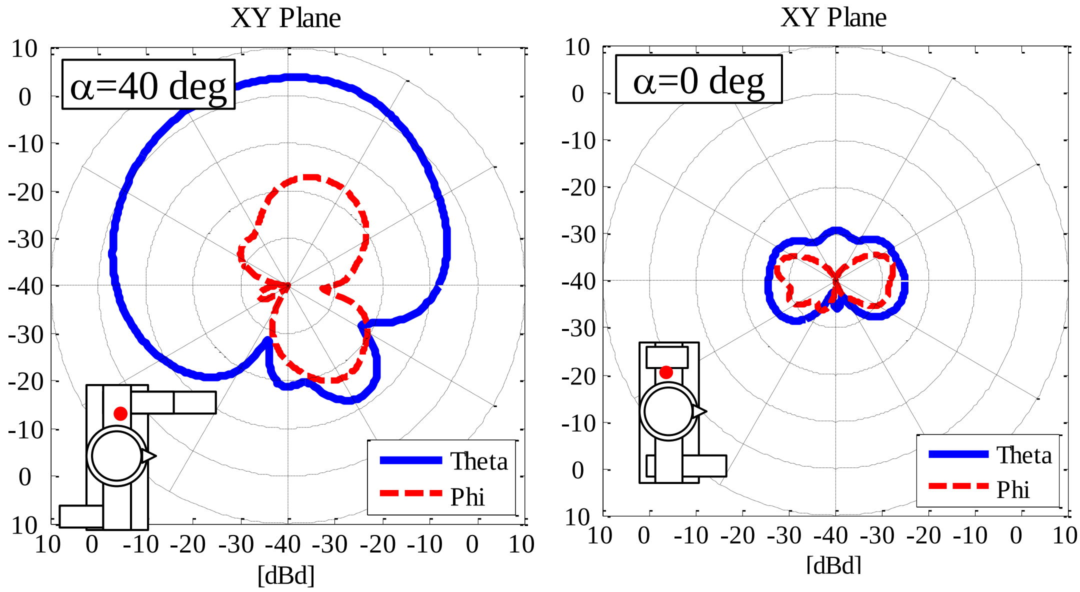

(b) Radiation pattern

Fig. 6.8 Analytical model and radiation characteristics vs. angle of left arm

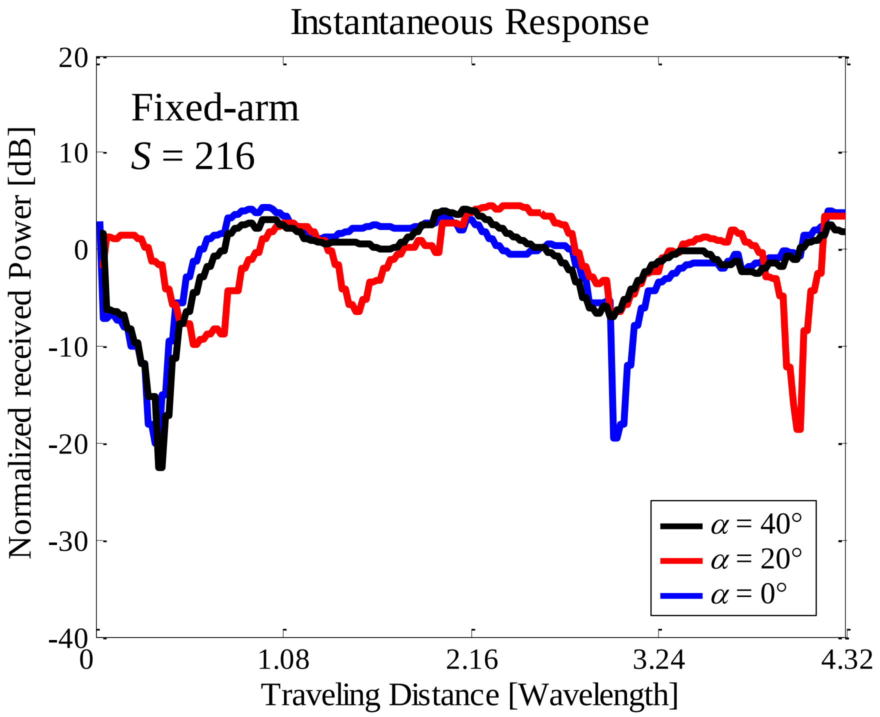

(a)

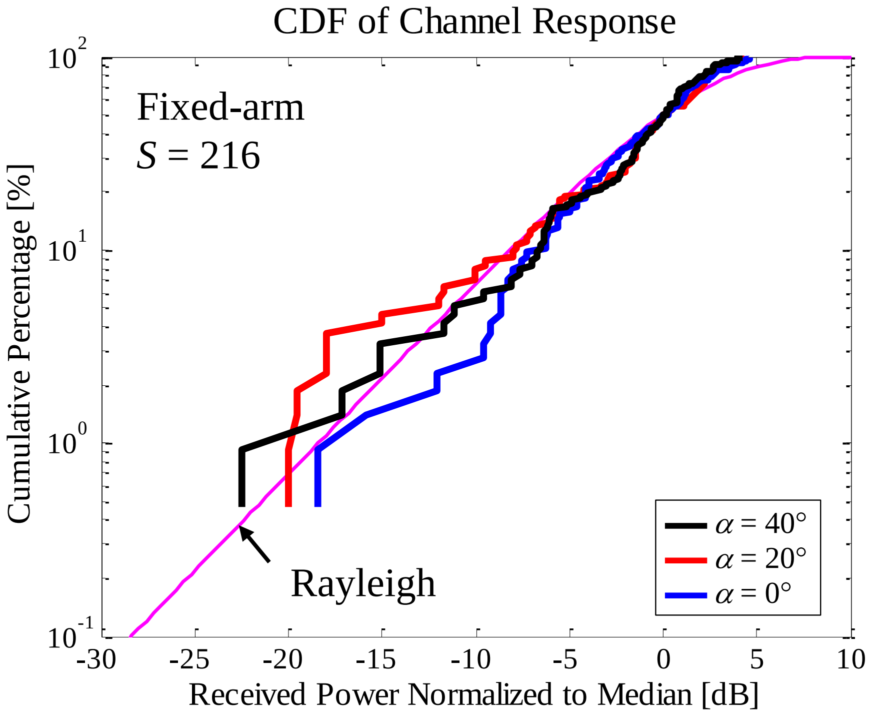

(b)

Fig. 6.9 Status of received signal power vs. fixed arm angles

(a) instantaneous response (b) CDF characteristics

Fig. 6.10 shows the instantaneous response when the phantom moves with changing arm-swing angle α. Fig. 6.10 (a) shows the received power, while Fig. 6.10 (b) indicates the instantaneous BER performance (BER_s). The phantom walks over a distance of 140 cm, equivalent to 4.32 λ at 926 MHz, based on the conditions introduced in Fig. 6.3 (a-1).

The instantaneous BER_s in Fig. 6.10 (b) shows that a fluctuation profile owing to the fading characteristics is clearly observed where the peak positions of the BER curve coincide with the null positions of the fading profile. As can be seen in Fig. 6.10 (b), when the left arm passes through the angular region of $\alpha = 10^\circ$ to $\alpha = -10^\circ$, a significant reduction in the instantaneous BER is observed owing to the degradation of received power caused by the arm shadowing effect. In particular, when $\alpha = 0^\circ$, as indicated by the arrows, a severely shadowed fading channel occurs. In addition, the BER falls off rapidly when the angle of the left arm α is outside this range.

In Fig. 6.10, even the signal level varies significantly owing to a shadowing-fading BAN channel, on the basis of the proposed dual-discrete control method in Fig. 6.3, a stepwise-continuous instantaneous BER profile is attained owing to the well-controlled measurement at each arm-swing fragment. This feature indicates that the proposed dual-discrete processing using the developed BER-OTA apparatus can successfully evaluate the BAN dynamic channels in a Rayleigh fading environment.

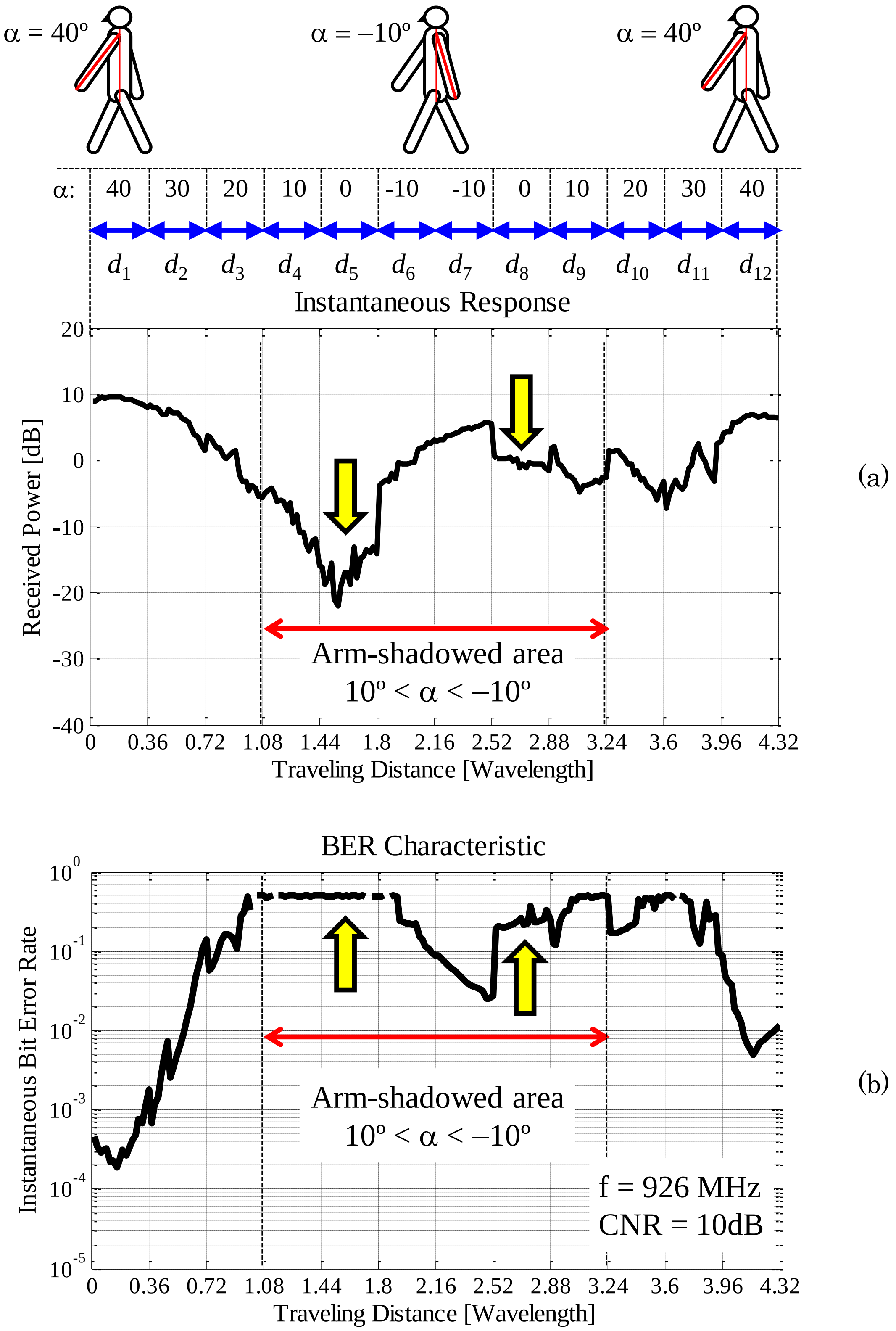

Fig. 6.10 Instantaneous response vs. arm-swinging angle

(a) instantaneous received power, (b) instantaneous BER$_s$

Fig. 6.11 shows the average BER characteristics (BER_m) of the FSK signals when the CNR is varied. The details to set the CNR for the developed BER-OTA system are illustrated in Sect. 6.4. In Fig. 6.10, the triangle symbols indicate the measured results when the phantom walks in the same conditions shown in Fig. 6.10. The circle and square symbols denote the cases of additive white Gaussian noise (AWGN) and a Rayleigh fading situation, respectively, where only the DUT antenna is used (without human effects). The theoretical curves for the AWGN and Rayleigh responses are also included, corresponding to those in Fig. 6.6.

As can be seen in Fig. 6.11, when the human effects are not included, the average BER_m decreases as the CNR increases with a gradient of one-tenth of the BER_m per 10-dB increment of the input CNR, which is identical to the gradient for a single antenna in a Rayleigh fading environment. On the other hand, when the left arm is fixed at $\alpha = 40^{\circ}$, which is out of the arm-shadowed angular region (see Fig. 6.10), the measured result of average BER_m also coincides well with the Rayleigh distribution. This fact indicates that without considering the shadowing effects, the Rayleigh fading propagation can be performed by the proposed BER-OTA apparatus even when a huge size of human phantom is used.

Note that when the CNR is greater than 25 dB, the gradient of the measured results is increased compared with the theoretical Rayleigh response. The reason for this is that the deep null positions in a fading profile may not be achieved due to insufficient snapshots ($S = 216$). In that case, the number of errors in the demodulated data streaming may be lost, i.e., $BER_s = 0$, which results in the reduction in the measurement accuracy of the average BER at a high CNR level. Therefore, when the system criterion is limited at $BER_m = 10^{-3}$, such as for conventional low data rate wearable BAN radios, $S = 216$ is satisfied to achieve the desired high accuracy for the BER experiment. However, when $BER_m = 10^{-5}$ is required, e.g., for next-generation high-speed wearable BAN radios for advanced medical applications, S needs to be increased. The optimum sampling number for different applications will be investigated in future work.

Furthermore, in Fig. 6.11, it is shown that owing to the significant shadowing effects caused by the arm-swing motion, the desired CNR is increased for BER_m measurement. When BER_m equals 2×10^{-2}, a 15-dB increase in CNR is observed. This result agrees well with the analytical outcome (see Fig. 6 in [98]), indicating that the proposed dual-discrete control method enables a highly reliable BER evaluation with respect to sensitive shadowing-fading dynamic BAN channels.

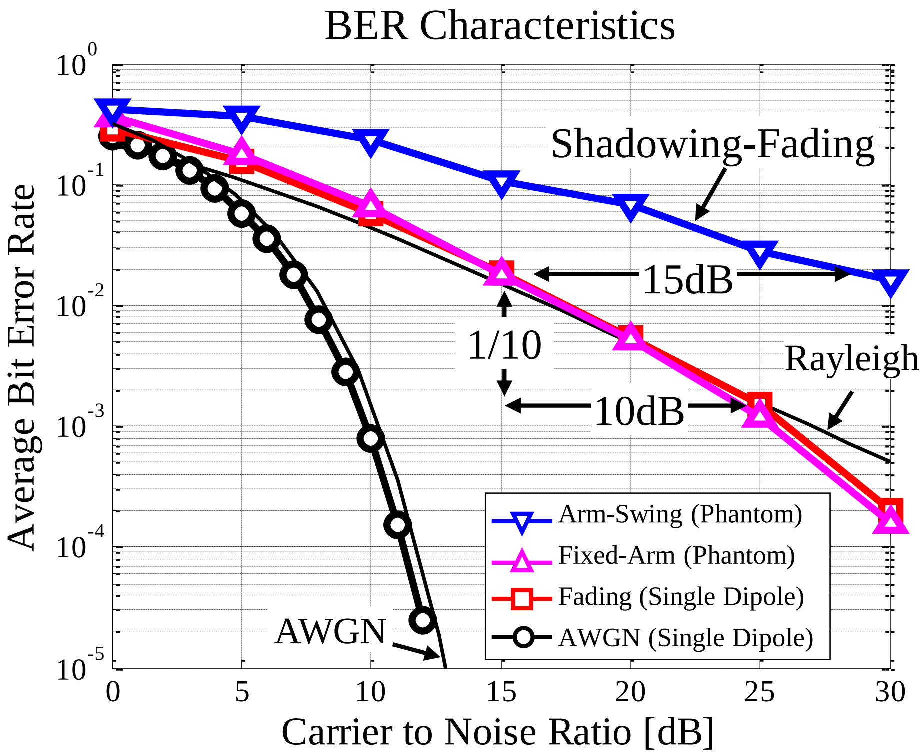

Fig. 6.11 Average BER characteristics in dynamic BAN channel.

6.6 Conclusion

This study presents an experimental methodology for BER-OTA testing to evaluate the communication quality of BAN antennas. A novel dual-discrete control method to detect the instantaneous BER by using a fading emulator with a dynamic human phantom for the off-body communication system between the wearable terminal and base station is proposed. Emphasis is placed on how to implement the proposed method while simultaneously considering the dynamic BAN channel and multipath effects. The empirical results show that the proposed method replicates a realistic arm-shadowed fading channel with both instantaneous and average BER characteristics. The developed method is anticipated to be used for the assessment of commercial BAN wireless applications.

7. Summary

This PhD thesis presents an OTA design methodology for wearable antennas considering the influence caused by human and multipath mutual interactions. Through the analysis and measurement of channel model and antenna performance, a development and research cycle of wearable antenna design and OTA methodology is formed. Based on the knowledge obtained from this thesis, the concept of wearable antenna design considering various index of use scenarios and applications is widely expanded. The contributions of this thesis will be illustrated as below.

In Chapter 2, a weighted-polarization wearable antenna applied to BAN on-body communication systems to achieve the radio link enhancement in both downlink and uplink on-body channels is proposed. This antenna obtains an optimum signal level using a weight function considering the BP-XPR and antenna tilt angle. The results show that the proposed antenna achieved more than a 3-dB improvement of received signal compared with the other types of antennas, such as vertical dipole, horizontal dipole and equal weight combined antennas, regardless of the arm-swing motion and antenna placement, which verifies the effectiveness of the proposed method to enhance BAN on-body radio links. Moreover, a simple estimation method of BP-XPR is provided. The results show that the proposed BP-XPR can be estimated using the 3-dimensional radiation pattern of vertical and horizontal test antennas.

In Chapter 3, to evaluate the performance of wearable antenna in multipath propagation environment, a spatial fading emulator was developed. Chapter 3 shows the development process of spatial fading emulator from the theoretical basis to manufacture. At first, the radio wave synthesis principle based on a simple analytical model was analyzed, which was utilized to clarify the generation mechanism of multipath Rayleigh fading. The actual device was developed by implementing these formulations. The design details of the fading emulator in both channel model and hardware manufacture have been conducted while the Rayleigh fading generation in the actual OTA device has been confirmed.

In Chapter 4, in order to represent an actual on-body propagation channel, a new methodology for realizing a Rice channel in BAN-OTA testing using a fading emulator with a dynamic phantom is proposed. An appropriate K-factor that represents the actual propagation environment indoors obtained from the propagation experiment, is implemented into the fading emulator based on a calibration method. This calibration method is validated by analyzing the variations in the instantaneous K-factor attributed to the arm-swinging motion. Finally, an experiment is conducted for a continuous human walking motion with the fading emulator using an arm-swinging dynamic phantom. The results show that the developed fading emulator allows BAN-OTA testing to replicate the actual Rice channel propagation environment with the consideration of the dynamic characteristics of human walking motion.

In Chapter 5, to obtain the high speed and large capacity in off-body communication system, a three-dimensional analytical channel model for vertically arranged MIMO array antennas is presented. A vertically arranged structure are characterized using the limited number of scatterers implemented in a fading emulator. The mechanism of the arrangement of scatterers on the variation of channel responses is studied using a proposed three-dimensional analytical model. Moreover, the appropriate scatterers arrangement for a 3D-OTA instrument considering the number of DUT antenna elements and multipath characteristics is investigated. The design parameters obtained from this study provide a suitable scatterers arrangement for designing an actual 3D-OTA apparatus.

In Chapter 6, to realize the high communication quality in off-body channel, an experimental methodology for BER-OTA testing to evaluate wearable antennas is presented. As a measurement procedure, a dual-discrete control method to detect an instantaneous BER using a fading emulator with a dynamic human phantom. Particular emphasis is placed on how to implement the proposed method while simultaneously considering the dynamic BAN channel and multipath effects. It is confirmed that the BER measurement of a BAN dynamic channel in a Rayleigh fading environment is easily conducted using the proposed dual-discrete control method. This method is anticipated to be used for the assessment of commercial BAN wireless applications.

Based on the knowledge obtained from this thesis, diverse evaluation system for various wearable antenna considering the mutual interactions of human dynamic motion and multipath propagation environment is proposed. The achievement of this study will provide an improved evaluation systems for practical wearable terminals in theoretical, analytical and experimental approaches. It is expected to establish a good R&D of OTA testing and wearable antenna design, which is benefit for the development of commercial wireless medical device, and this will significantly promote the mobile medical-healthcare system network in future society.

8. Future Work

Since the antenna in BAN system is utilized in biomedical domain, communication index cannot be defined as “protect the minimum” as mobile terminals per usual, but needs to ensure that “nothing dangerous will happen”. To fulfil this requirement, particular emphasis must be placed on how to achieve the high reliable communication of medical wireless devices in variety of BAN applications. With respect to specific challenges in physical layer, there are four subjects need to be studied as below.

(1) Shadowing modeling of realistic human walking motion.
(2) Three-dimensional Rice channel for wearable diversity antenna evaluation in indoor environment. (On-Body)
(3) Three-dimensional cluster channel model for wearable MIMO antenna assessment in street small cell. (Off-Body)
(4) Implantable MIMO antenna design and development for medical data wireless transmission. (In-Body)

Subject (1):

Fig. 8.1 shows the method to obtain the probability density function (PDF) of human shadowing response. Using a realistic human dynamic modeling created by animation software, such as Poser [46], the shadowing response of walking motion can be assumed as a periodic function of physical values such as path loss or mean effective gain (MEG). This function will be used to calculate the cumulative distribution function (CDF) of the shadowing model. Since CDF is an integral value of PDF, the PDF can be differentiated easily.

Through the derived shadowing model, theoretical analysis of BER performance of a diversity antenna can be developed. This way of thinking is very helpful for antenna engineers to verify the true reason that degrades antenna performance in BAN dynamic channel, such as power or correlation.

Subject (2):

Fig. 8.2 shows a three-dimensional Rice channel model representing a typical usage scenario of BAN on-body radios, where multipath reflected waves are coming from not only azimuth but also elevation directions with various power distribution and cross-polarization power ratio (XPR). The proposed 3-dimensional analytical channel model combines the arm-swinging shadowing effects and multipath fading phenomenon successfully, which is expected to simulate the BER performance of diversity antennas in realistic BAN radios. Based on this channel model, the actual BER experiment will be conducted by a 3-dimensional BER-OTA evaluation system at Toyama University. A dynamic human phantom can swing both arms to emulate the shadowing effects whereas the scatterers surrounding the phantom are used to create the desired fading signals in both azimuth and elevation. The 3D-OTA apparatus denotes that BER performance of BAN diversity antenna can be evaluated not only in an anechoic chamber base but also in a realistic BAN use scenarios.

Subject (3):

Fig. 8.3 shows the commercial use scenarios of wearable MIMO antenna in street small cell environment, which has a small spatial angular power spectrum (APS) of incident wave in both azimuth and elevation angles. In addition, considering human random-directional movement and shadowing effects caused by arm-swinging motion, MIMO channel capacity will be significantly affected. This work aims at the channel characterization of wearable MIMO antennas in such environment by giving several simulation solutions using a three-dimensional analytical channel model based on cluster model. The three-dimensional coordinate in Fig. 8.3 representing the moving angle (ϕv) of the MIMO antenna in azimuth, where the cluster is employed to simulate a set of discrete waves with a narrow angular spread (σ) arriving at the MIMO terminal in both azimuth and elevation directions. Using this method, the decisive factor of Shannon channel capacity determined by the mutual interactions of human movement, antenna placement and incident wave characteristics in future street small cell MIMO system can be clarified. Future work can also commit to the empirical approaches of over-the-air testing and propagation measurement for wearable MIMO evaluation.

Subject (4):

Since the implantable applications will become the hottest topic in future, I also aim at developing a capsule endoscope MIMO antenna for high quality image transmission through the human body to outside wearable terminals. In Fig. 8.4, the implantable MIMO antenna will be comprised by helical antenna, with an RF-controlled method to deal with the issue of polarization mismatch caused by the creeping motion in the intestinal of human body. There are many difficulties in implantable system, such as the antenna miniaturization, inclination behavior, impedance mismatch and large path loss. It will be an extremely interesting aspect in my future research life.

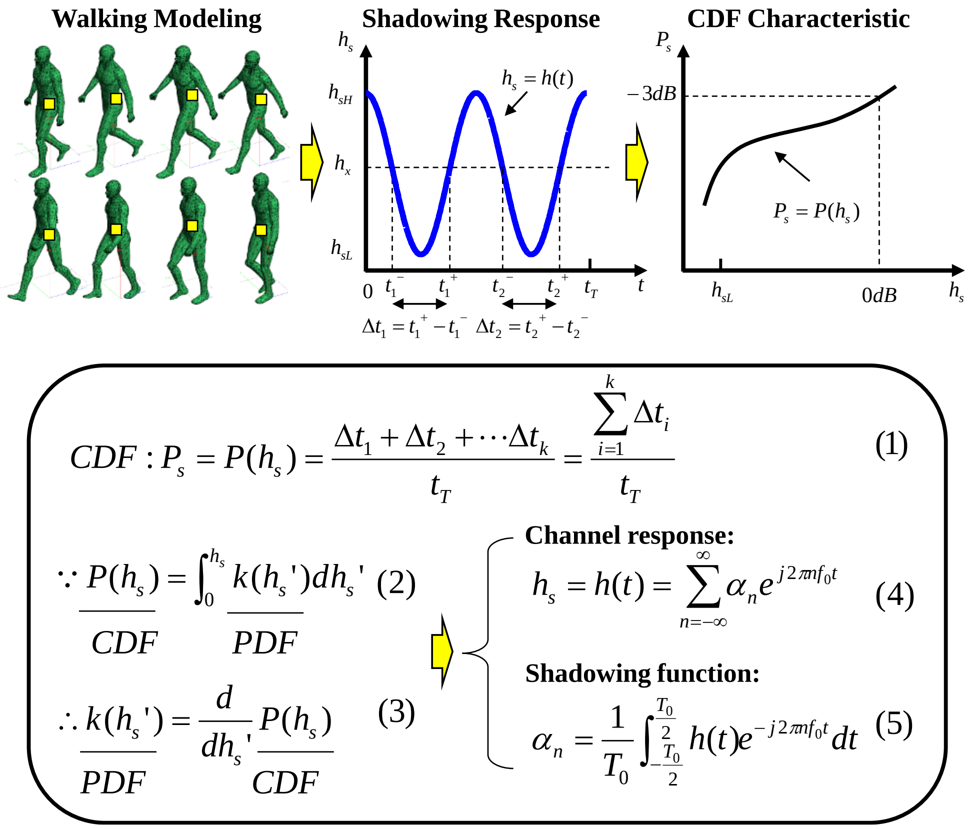

$$CDF : P_s = P(h_s) = \frac{\Delta t_1 + \Delta t_2 + \cdots \Delta t_k}{t_T} = \frac{\sum_{i=1}^{k} \Delta t_i}{t_T} \qquad (1)$$

$$\because \underbrace{P(h_s)}_{CDF} = \int_0^{h_s} \underbrace{k(h_s')dh_s'}_{PDF} \qquad (2)$$

$$\therefore \underbrace{k(h_s')}_{PDF} = \frac{d}{dh_s'} \underbrace{P(h_s)}_{CDF} \qquad (3)$$

Channel response:

$$h_s = h(t) = \sum_{n=-\infty}^{\infty} \alpha_n e^{j2\pi n f_0 t} \qquad (4)$$

Shadowing function:

$$\alpha_n = \frac{1}{T_0} \int_{-\frac{T_0}{2}}^{\frac{T_0}{2}} h(t) e^{-j2\pi n f_0 t} dt \qquad (5)$$

Fig. 8.1 Derivation process of arm-swinging shadowing model

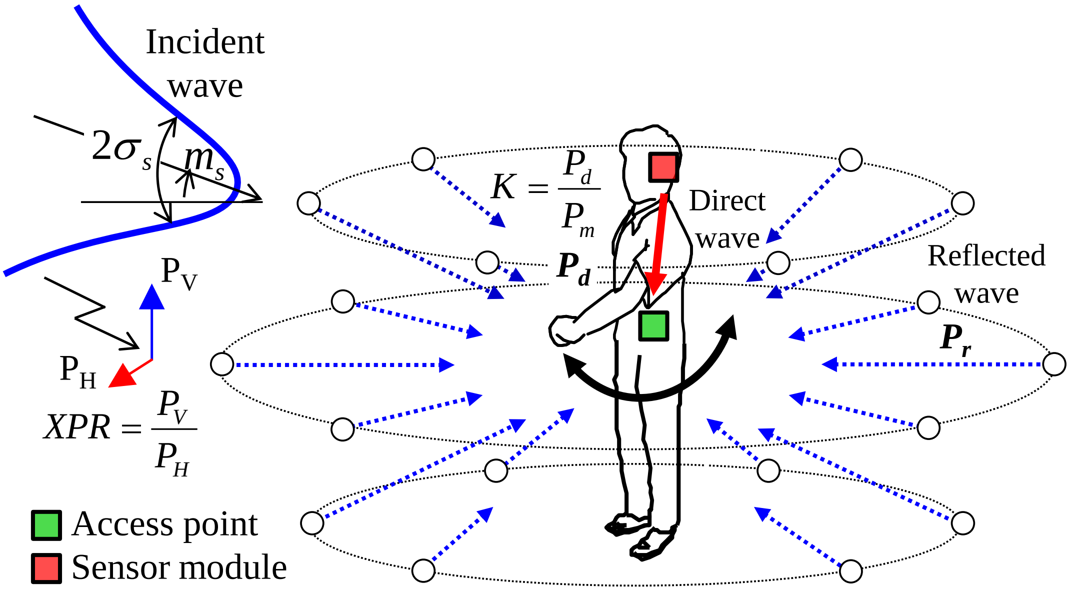

Fig. 8.2 Three-dimensional Rice channel model

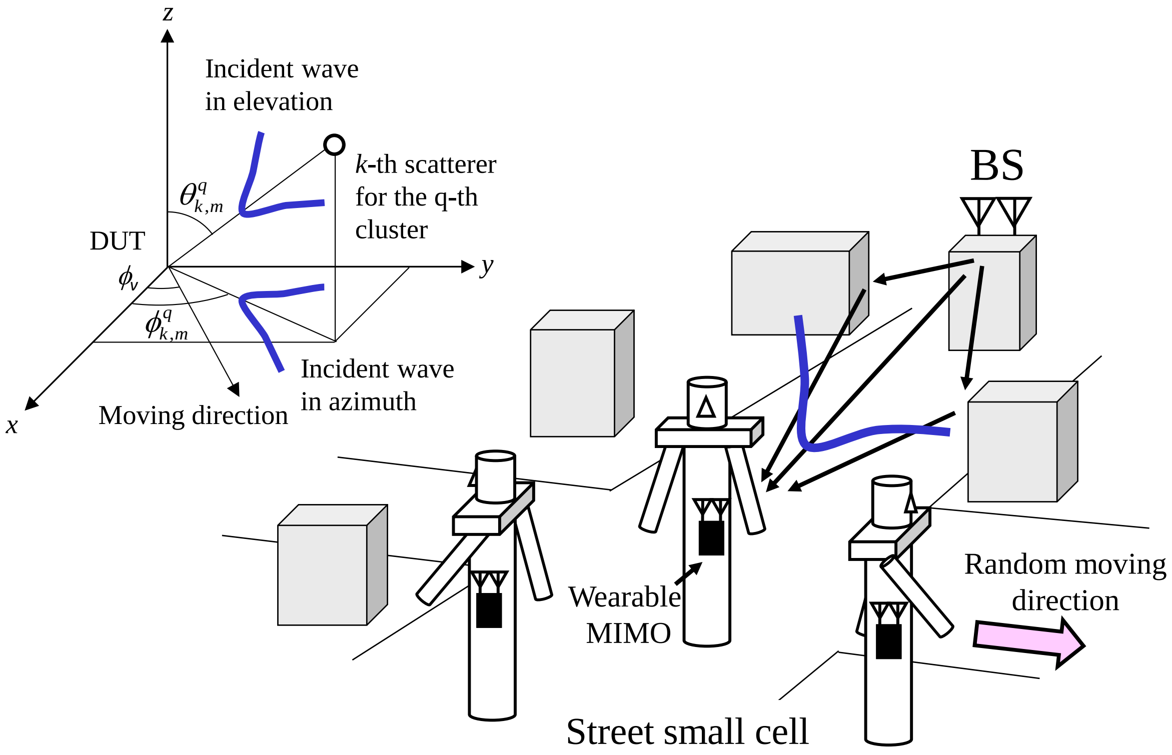

Fig. 8.3 Wearable MIMO antenna in street small cell environment

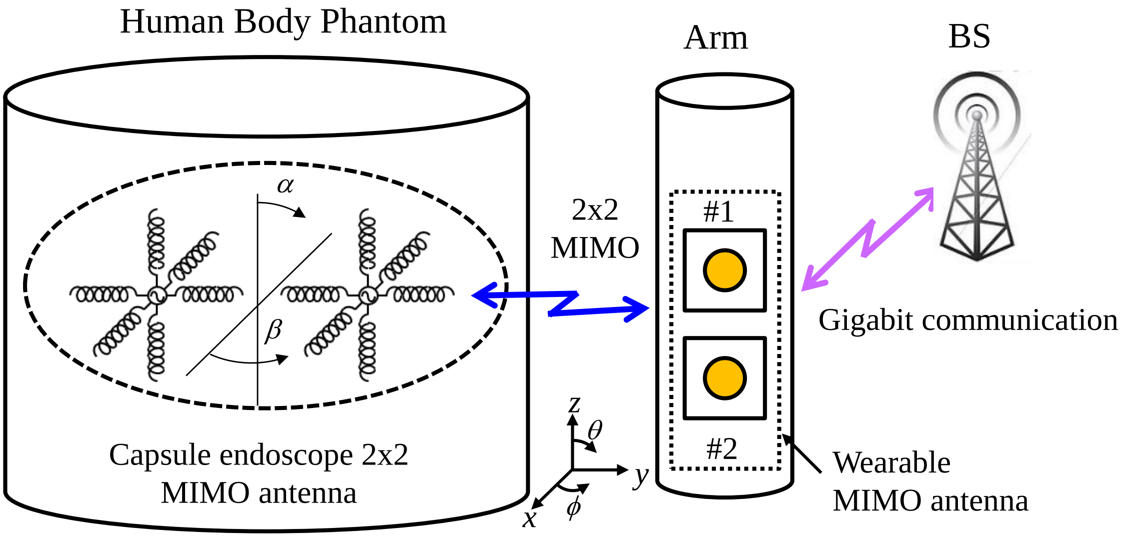

Fig. 8.4 Design of implantable capsule endoscope MIMO antenna

Acknowledgement

First of all, I would like to express my gratitude to Dr. Ogawa for his support and invaluable guidance during the period of Master and PhD course in Toyama University. Not only the professional knowledge, the way of his thinking, passion and attitude let me know how to work as a researcher and educator. He always emphasizes the importance of “view of things”, which will have a significant impact on my rest research career.

I want to thank Dr. Ando, Dr. Hirobayashi, Dr. Maezawa in Toyama University, and Dr. Takada in Tokyo Institute of Technology for being the examination committee members of my PhD defense.

I want to thank Dr. Honda for his kind guidance and numerous advices in the student career in Toyama University. He spent a lot of time teaching me the technical skills, correcting my papers and discussing with me. It has been a wonderful experience for me to work with him.

Finally, I must express the appreciation to my father Ruijie Li and mother Lewen Wu, who always support me unconditionally even I willfully chose the tough research life. I want to thank my uncle Dr. Ruixue Li in Hosei University, for bringing me to Japan and giving me a chance to study abroad. I need to thank my wife Sisi Sun, who is extremely patient and supportive for my PhD work, and married with me when I have nothing.

Reference

[1] D. Gesbert, M. Shafi, D. S. Shiu, P. Smith, and A. Naguib, “From Theory to Practice: An Overview of MIMO Space-time Coded Wireless Systems,” IEEE J. Sel. Areas Commun., Vol. 21, No. 2, pp. 281–302, Apr. 2003.

[2] [IoT] http://www.postscapes.com/internet-of-things-examples/

[3] [The Statistics Portal] https://www.statista.com/

[4] [World Health Organization] http://www.who.int/en/

[5] [United Nations Population Fund] http://www.unfpa.org/

[6] [Ministry of Health, Labour and Welfare] http://www.mhlw.go.jp/

[7] T. G. Zimmerman, Personal Area Networks (PAN): Near-Field Intra-Body Communication, M.S. thesis, MIT Media Laboratory, Cambridge, MA (September 1995)

[8] [IEEE 802.15 WPAN™ Task Group 6 (TG6) Body Area Network] http://www.ieee802.org/15/pub/TG6.html

[9] P. S. Hall and Y. Hao, Antennas and Propagation for Body-Centric Wireless Communications, Artech House, Inc., 2006.

[10] Y. I. Nechayev, P. S. Hall, C. C. Constantinou, Y. Hao, A. Alomainy, R. Dubrovka, C. G. Parini, “On-Body Path Gain Variations with Changing Posture an Antenna Position”, the 2005 IEEE AP-S International Symposium on Antennas and Propagation and USNC/URSI National Radio Science Meeting, Washington DC, USA on July 3-8, 2005.

[11] P. S. Hall, M. Ricci, T. W. Hee, “Characterization of On-body Communication Channels”. Microwave and Millimetre Wave Technology, 2002. Proceedings. ICMMT 2002. 2002 3rd. Int Conference on, 17-19 Aug. 2002 Pages: 770–772.

[12] W. G. Scanlon and S. L. Cotton, “Understanding On-Body Fading Channels At 2.45 GHz Using Measurements Based On User State And Environment”, Loughborough Antennas & Propagation Conference, 17-18 March 2008, Loughborough, UK.

[13] S. L. Cotton and W. G. Scanlon, “Characterization and Modelling of the Indoor Radio Channel at 868 MHz for a Mobile Body-worn Wireless Personal Area Network”, IEEE Antennas and Wireless Prop Letters, Vol. 6, 2007.

[14] G.F. Pedersen, and M. Pelosi, “‘OTA’ test methods for multi antenna terminals,” in Pervasive Mobile and Ambient Wireless

Communications-COST Action 2100, Roberto Verdone and Alberto Zanella, Eds. London, UK: Springer-Verlag, 2012, ch. 5.

[15] 3GPP, TSG RAN #41 RP-080765, "Verification for OTA performance for MIMO and general multiple receive antenna UEs."

[16] 3GPP, "User equipment (UE) / mobile station (MS) over the air (OTA) antenna performance," 3GPP, TR TS 34.114 V11.1.0, Jun. 2013.

[17] T. Sakata, A. Yamamoto, K. Ogawa, H. Iwai, J. Takada, and K. Sakaguchi, "A Spatial Fading Emulator for Evaluation of MIMO Antennas in a Cluster Environment," IEICE Trans. Commun., vol. E97-B, no. 10, pp. 2127–2135, Oct. 2014.

[18] P. S. Kildal, "Overview of 6 Years R&D on Characterizing Wireless Devices in Rayleigh Fading Using Reverberation Chambers," International Workshop on Antenna Technology (iWAT2007), Cambridge, UK, pp. 162–165, (2007).

[19] Y. Jing, Z. Wen, H. Kong, S. Duffy, and M. Rumney, "Two-stage Over the Air (OTA) Test Method for MIMO Device Performance Evaluation," International Journal of Antennas and Propagation, vol. 2012, 2012.

[20] W. Fan, X. Carreño, F. Sun, J. Ø. Nielsen, M. B. Knudsen, G. F. Pedersen, "Emulating Spatial Characteristics of MIMO Channels for OTA Testing," IEEE Trans. Antennas and Propagation, Vol. 61, No. 8, pp. 4306 - 4314, Aug. 2013.

[21] W. Fan, J. Ø. Nielsen, O. Franek, X. Carreño, J. S. Ashta, M. B. Knudsen, and G. F. Pedersen, "Antenna Pattern Impact on MIMO OTA Testing," IEEE Trans. Antennas and Propagation, Vol. 61, No. 11, pp. 5714 - 5723, Nov. 2013.

[22] W. Fan, F. Sun, J. Ø. Nielsen, X. Carreño, J. S. Ashta, M. B. Knudsen, and G. F. Pedersen, "Probe Selection in Multi-probe OTA Setups," IEEE Trans. Antennas and Propagation, Vol. 62, No. 4, pp. 2109-2120, Jan. 2014.

[23] W. Fan, F. Sun, P. Kyosti, J. Ø. Nielsen, X. Carreño, M. B. Knudsen, and G. F. Pedersen, "Probe Selection in Multi-probe OTA Setups," Electronics Letters, Vol. 49, No. 9, pp. 623-625, Apr. 2013.

[24] W. Fan, X. Carreño, J. S. Ashta, J. Ø. Nielsen, G. F. Pedersen, and M. B. Knudsen, "Channel Verification Results for the SCME models in a Multi-Probe Based MIMO OTA Setup," IEEE 78th Vehicular Technology Conference (VTC Fall), Las Vegas,

USA, 2013.

[25] T. Ohira, and K. Gyoda, “Electronically Steerable Passive Array Radiator Antennas for Low-Cost Analog Adaptive Beamforming,” IEEE International Conference on Phased Array Systems and Techniques Digest, pp. 101-104, May. 2000.

[26] W. C. Y. Lee, “Effects on Correlation between Two Mobile Radio Base Station Antennas,” IEEE Transactions on Communications, vol. 21, no. 11, pp. 1214-1224, Nov. 1973.

[27] C. Park, J. Takada, K. Sakaguchi, and T. Ohira, “Spatial Fading Emulator for Base Station using Cavity-Excited Circular Array based on ESPAR Antenna,” 2004 Fall IEEE Vehicular Technology Conference, Sep. 2004.

[28] T. Sakata, A. Yamamoto, K. Ogawa, and J. Takada, “MIMO Channel Capacity Measurement in the Presence of Spatial Clusters Using a Fading Emulator,” PIMRC2009 Intl. Symp. Digest (Tokyo, Japan), Session D1, No. 2, Sept. 2009.

[29] A. Yamamoto, T. Sakata, T. Hayashi, K. Ogawa, J Ø Nielsen, G. F. Pedersen, J. Takada and K. Sakaduchi: “Effectiveness in MIMO Performance Evaluation of a Spatial Fading Emulator in Comparison With a Radio Propagation Test,” The European Conference on Antennas and Propagation (EuCAP 2010, Barcelona), Intl. Symp. Digest, Apr. 2010.

[30] A. Yamamoto, T. Sakata, T. Hayashi, K. Ogawa, K. Sakaguchi, and J. Takada: “Spatial Fading Emulator Applicable to a Handset MIMO Array Evaluation,” 2010 Asia-Pacific Radio Science Conference Digest, Sep. 2010.

[31] Vodafone, Panasonic, Tokyo Institute of Technology, “MIMO OTA Testing using RF-controlled Spatial Fading Emulator,” 3GPP TSG RAN WG4 #50bis, R4-091390, Mar. 2009.

[32] Panasonic, Tokyo Institute of Technology, “RF performance evaluation of a handset MIMO antenna using an RF-controlled Spatial Fading Emulator,” 3GPP TSG RAN WG4 #52, R4-093157, Aug. 2009.

[33] Panasonic Corporation, Panasonic Mobile Communications Corporation, NTT DOCOMO INC., Aalborg University, Tokyo Institute of Technology, “Handset MIMO antenna measurement using a Spatial Fading Emulator,” 3GPP TSG RAN WG4 Informal MIMO OTA Meeting #1, R4M090006, Oct. 2009.

[34] Panasonic, Aalborg University, Tokyo Institute of Technology, “MIMO performance evaluation of a handset MIMO antenna

using an RF-controlled Spatial Fading Emulator," 3GPP TSG RAN WG4 #52 bis, R4-093891, Oct. 2009.

[35] Panasonic, Tokyo Institute of Technology, "Procedure of determining the dimension of a spatial fading emulator," 3GPP TSG RAN WG4 #53, R4-094317, Nov. 2009.

[36] Panasonic, Tokyo Institute of Technology, "Calibration procedure of an RF-controlled spatial fading emulator," 3GPP TSG RAN WG4 #53, R4-094318, Nov. 2009.

[37] Panasonic, Tokyo Institute of Technology, "MIMO performance evaluation of Handset arrays on WLAN IEEE802.11n system using an RF-controlled Spatial Fading Emulator," 3GPP TSG RAN WG4 #53, R4-094319, Nov. 2009.

[38] N. Yamamoto, N. Shirakata, D. Kobayashi, K. Honda, and K. Ogawa, "BAN radio link characterization using an arm-swinging dynamic phantom replicating human walking motion," IEEE Trans. Antennas and Propagation, Vol. 61, No. 8, pp. 4315–4326, Aug. 2013.

[39] A. Alomainy, Y. Hao, A. Owadally, C. G. Parini, Y. Nechayev, C. C. Constantinou, and P. S. Hall, "Statistical Analysis and Performance Evaluation for On-Body Radio Propagation With Microstrip Patch Antennas," IEEE Trans. Antennas and Propagat., Vol. 55, No. 1, pp.245–248, Jan. 2007.

[40] K. Honda, K. Li, and K. Ogawa, "Weighted-Polarization Wearable MIMO Antenna with Three Orthogonally Arranged Dipoles Based on RF Signal Processing," IEICE Trans. Commn., Vol. E99-B, No.01, pp. 58–68, Jan. 2016.

[41] T. Uusitupa, T. Aoyagi, "Analysis of Dynamic On-Body Communication Channels for Various Movements and Polarization Schemes at 2.45 GHz," IEEE Trans. Antennas and Propagat., Vol. 61, No. 12, pp. 6168–6179, Dec. 2013.

[42] L. Akhoondzadeh-Asl, P. S. Hall, Y. Nechayev, and I. Khan, "Depolarization in On-Body Communication Channels at 2.45 GHz," IEEE Trans. Antennas and Propagat., Vol. 61, No. 2, pp. 882–889, Feb. 2013.

[43] K. Li, K. Honda, and K. Ogawa: "Analysis of the Body Proximity Cross-Polarization Power Ratio in a Human Walking Motion," Asia-Pacific Microwave Conference Digest, pp. 780–782, Nanjing, Dec. 2015.

[44] T. Taga, "Analysis for Mean Effective Gain of Mobile Antennas in Land Mobile Radio Environment," IEEE Transactions on

Vehicular Technology, Vol. 39, No. 2, pp. 117–131, May 1990.
[45] [Altair HyperWorks FEKO] https://www.feko.info/
[46] [SMITHMICRO Poser] http://poser.smithmicro.com/
[47] [Federal Communications Commission] http://www.fcc.gov/fcc-bin/dielec.sh
[48] K. Omote, K. Honda, and K. Ogawa: "Motion Capture Modeling of a Human Walking for Wearable MIMO Antennas," AWAP2014, Kanazawa, Japan, pp.99–100, May 2014.
[49] K. Ogawa, T. Matsuyoshi, K. Monma, "A Study of Effects of a Shoulder on the Effective Gain Characteristics in a Multiple Radio Wave Environment of a Dipole Antenna close to a Human Head," Trans. IEICE, vol. J82-B, no. 10, pp. 1847–1856, Oct. 1999. (in Japanese)
[50] S. R. Saunders and A. Aragon-Zavala, Antennas and Propagation for Wireless Communication Systems, John Wiley & Sons, 2007.
[51] L. Vuokko, P. Vainikainen, and J. Takada, "Clusters extracted from measured propagation channels in macrocellular environments," IEEE Trans. Antennas and Propagation, vol. 53, no. 12, pp. 4089-4098, Dec. 2005.
[52] T. Imai, T. Okano, K. Koshiro, K. Saito, and S. Miura, "Theoretical analysis of adequate number of probe antennas in spatial channel emulator for MIMO performance evaluation of mobile terminals," EuCAP2010, p.131, Apr. 2010.
[53] H. Iwai, A. Yamamoto, T. Sakata, K. Ogawa, K. Sakaguchi, and K. Araki, "Spatial fading emulator for handset antennas," IEEE AP-S Conference, vol. 1A, pp. 218-221, Jul. 2005.
[54] H. Iwai, K. Sakaguchi, T. Sakata, and A. Yamamoto, "Pefromance evaluation of spatial correlation characteristics for handset antennas using spatial fading emulator based on Clarke's model," IEICE Trans. Commun., vol. E93-B, no. 10, pp. 2514-2522, Oct. 2010.
[55] Y. Okano and T. Imai, "Development of spatial channel emulator for MIMO OTA and accuracy evaluation," IEICE Trans. (B), Vol. J93-B, No. 9, pp. 1267–1275, Sept. 2010.
[56] K. Honda, K. Li, and K. Ogawa, "Shadowing-Fading BER Characterization of a BAN Diversity Antenna Based on Statistical Measurements of the Human Walking Motion," IEICE Trans. Commun., Vol. E96-B, No. 10, pp. 2530–2541, Oct. 2013.
[57] R. D' Errico and L. Ouvry, "A Statistical Model for On-Body Dynamic Channels," Int. J. Wireless Inf. Networks, vol. 17, no. 3,

pp. 92–104, Dec. 2010.

[58] R. D' Errico and L. Ouvry, “Time-variant BAN Channel Characterization,” Proceedings of IEEE 20th International Symposium on Personal, Indoor, and Mobile Radio Communications (PIMRC 2009), Tokyo, Japan, pp. 3000–3004, Sept. 2009.

[59] K. Minseok, J. Takada, B. Zhen, L. Materum, T. Kan, Y. Terao, Y. Konishi, K. Nakai, T. Aoyagi, and K. Ryuji, “Statistical Property of Dynamic BAN Channel Gain at 4.5 GHz,” IEEE P802.15-08-0489-02-0006, June 2010.

[60] Z. H. Hu, Y. I. Nechayev, P. S. Hall, C. C. Constantinou, and Y. Hao, “Measurement and Statistical Analysis of On-Body Channel Fading at 2.45 GHz,” IEEE Antennas and Wireless Propagation Letters, Vol. 6, pp. 612–615, 2007.

[61] K. Minseok and J. Takada, “Experimental investigation and modeling of shadow fading by human movement on body surface propagation channel,” IEEE AP-S Intl. Symp., June 2009.

[62] M. Gallo, P. S. Hall, Y. I. Nechayev, and M. Bozzetti, “Use of Animation Software in Simulation of On-body Communications Channels at 2.45 GHz,” IEEE Antennas and Wireless Propagation Letters, Vol. 7, pp. 321–324, 2008.

[63] N. Katayama, K. Takizawa, T. Aoyagi, J. Takada, H. B. Li, and R. Kohno, “Channel Model on Various Frequency Bands for Wearable Body Area Network,” IEICE Trans. Commn., Vol. E92-B, No. 2, pp. 418–424, Feb. 2009.

[64] S. L. Cotton and W. G. Scanlon, “A Statistical Analysis of Indoor Multipath Fading for a Narrowband Wireless Body Area Network,” IEEE 17th International Symposium on Personal, Indoor, and Mobile Radio Communications (PIMRC 2009), Helsinki, Finland, Sept. 2006.

[65] T. Aoyagi, J. Takada, K. Takizawa, H. Sawada, N. Katayama, K. T. Yazadandoost, T. Kobayashi, H. B. Li, and R. Kohno, “Channel Models for WBANs – NICT,” IEEE 802.15 Working Group Document, IEEE 802. 15-08-0416-03-0006, Sept. 2008.

[66] M. Kim, J. Takada, L. Materum, T. Kan, Y. Terao, Y. Konishi, K. Nakai, and T. Aoyagi, “Statistical Property of Dynamic BAN Channel Gain at 4.5GHz,” IEEE 802.15 Working Group Document, IEEE 802. 15-08-0489-00-0006, July. 2008.

[67] H. Sawada, T. Aoyagi, J. Takada, K. Y. Yazdandoost, and R. Kohno, “Channel Models between Body Surface and Wireless

Access Point for UWB Band," IEEE 802.15 Working Group Document, IEEE 802. 15-08-0576-00-0006, Aug. 2008.

[68] Alomainy, A., Y. Hao, A. Owadally, C. G. Parini, Y. Nechayev, C. C Constantinou, and P. S. Hall., "Statistical Analysis and Performance Evaluation for On-Body Radio Propagation with Microstrip Patch Antennas" IEEE Trans. Antennas and Propagat, Vol. 55, No. 1, pp. 245–248, Jan. 2007.

[69] Y. I. Nechayev, P. S. Hall, and Z. H. Hu, "Characterization of Narrowband Communication Channels on the Human Body at 2.45 GHz," IET Microwaves, Antennas and Propagation, Vol.4, No. 6, pp.722–732, Jun. 2010.

[70] K. Ogawa and K. Honda, "BAN shadowing properties of an arm-waving dynamic phantom," The European Conference on Antenna and Propagation (EuCAP 2012, Prague), Int. Symp. Digest, CP08.1, Mar. 2012.

[71] K. Ogawa, A. Yamamoto, and J. Takada, "Multipath Performance of Handset Adaptive Array Antennas in the Vicinity of a Human Operator," IEEE Trans. Antennas Propagat. AP-53, No. 8, pp. 2422–2436, Aug. 2005.

[72] K. Ogawa and K. Honda, "Effects of Received Power Imbalance on the Diversity Gain of a Digital TV MRC Array Antenna," IEICE Trans. Commun., Vol. E96-B, No. 3, pp. 811–819, Mar. 2013.

[73] K. Li, K. Honda, and K. Ogawa: "K-factor Dependent Multipath Characterization for BAN-OTA Testing Using a Fading Emulator," Antennas & Propagation (ISAP), 2013 Proceedings of the International Symposium on, vol. 1, pp. 580–583, Nanjing, China, Oct. 2013.

[74] (#) R4-091995, "Figure of Merits for MIMO OTA Measurements," 3GPP TSG RAN WG4 #51, San Francisco, USA, May 2009.

[75] M. D. Foegelle, "Over-the-air performance testing of wireless devices with multiple antenna," RF Design, pp. 44–52, February 2006.

[76] User Equipment (UE) / Mobile Station (MS) over the air (OTA) antenna performance; Conformance testing (Release 8), 3GPP TS 34.114, Rev. 8.0.0, Dec. 2008.

[77] Test Plan for Mobile Station Over the Air Performance Rev 3.1, CTIA—The Wireless Association Std., Jan. 2011.

[78] Measurement of radiated performance of MIMO and multi-antenna reception for HSPA and LTE terminals (Release 10),

3GPP TR 37.976, Rev. 1.5.0, May 2011.

[79] W. L. Schroeder and Y. Feng, “A critical review of MIMO OTA test concepts—lessons learned from actual measurements,” in XXXth URSI General Assembly and Scientific Symposium (URSI-GASS ’11), Istanbul, Turkey, pp. 1–4, Aug. 2011.

[80] Y. Karasawa, I. Oshima, F. Tamrin, Y. Sakamoto, R. Arif, and K. Sasaki, “Fundamental Propagation Characteristics of Stirrer-less Reverberation Chamber for MIMO-OTA Measurements,” IEICE Trans. Commun., vol. E97-B, no. 10, pp. 2083–2092, Oct. 2014.

[81] K. Rosengren, P. S. Kildal, J. Carlsson, and O. Lunden, “A new method to measure radiation efficiency of terminal antennas,” 2000 IEEE-APS Conf. pp. 5–8, Nov. 2000.

[82] P. S. Kildal, X.Chen, C. Orlenius, M. Franzen, and C. L Patane, “Characterization of reverberation chambers for OTA measurements of wireless devices: Physical formulations of channel matrix and new uncertainty formula,” IEEE Trans. Antennas Propagat., vol. 60, no. 8, pp. 3875–3891, Aug. 2012.

[83] C. L. Holloway, D. A. Hill, J. M. Ladbury, P. F. Wilson, G. Koepke, and J. Coder, “On the Use of Reverberation Chambers to Simulate a Rician Radio Environment for the Testing of Wireless Device,” IEEE Trans. Antenna Propagat., vol. 54, no. 11, pp. 3167–3177, Nov. 2006.

[84] E. Genender, C. L. Holloway, K. A. Remley, J. Ladbury, G. Koepke and H. Garbe, “Use of Reverberation Chamber to Simulate the Power Delay Profile of a Wireless Environment,” EMC Europe Intl. Symp., Hamburg, Germany, pp. 1–6, Sep. 2008.

[85] T. Imai, Y. Okano, K. Kitao, K. Saito, and J. Hagiwara, “Spatial Channel Emulator for MIMO performance Evaluation of Mobile Terminals,” APMC2009, Singapore, pp. 461–464, Dec. 2009.

[86] Y. Okano and T. Imai, “Development of Spatial Emulator for MIMO OTA and Accuracy Evaluation,” IEICE Trans. Commun. Vol. J93B, No. 9 pp. 1237–1275, 2010 (in Japanese).

[87] K. Honda, K. Li, and K. Ogawa, “An 8 × 8 MIMO 3-axis Weighted Polarization Active Antenna for Wearable Radio Applications,” in XXXth URSI General Assembly and Scientific Symposium (URSI-GASS ’14), Beijing, China, Aug. 2014.

[88] Jung-Hwan Choi, Yong-Sun Shin, Ki-Bok Kong, and Seong-Ook Park, “3D Spherical Antenna Measurement System for CTIA OTA Testing and Characterizing of Mobile MIMO Terminals,” ISAPE ’06, pp. 1–4, Oct. 2006.

[89] T. A. Laitinen, J. Ollikainen, C. Icheln, and P. Vainikainen, “Rapid Spherical 3-D Field Measurement System for Mobile Terminal Antennas,” IMTC ’03, vol. 2, pp. 968–972, May 2003.

[90] T. Imai, “Performance Evaluation of Three-dimensional Spatial Channel Emulator for MIMO-OTA Testing,” International Symposium on Antennas and Propagation (ISAP2011), Session WeE1-3, Oct. 2011.

[91] K. Li, K. Honda, and K. Ogawa, “Over-The-Air Assessment for 2-dimensional Arrangement MIMO Array Antenna,” in XXXth URSI General Assembly and Scientific Symposium (URSI-GASS ’14), Beijing, China, Aug. 2014.

[92] K. Ogawa, H. Iwai, A. Yamamoto, and J. Takada, “Channel Capacity of a Handset MIMO Antenna Influenced by the Effects of 3D Angular Spectrum, Polarization, and Operator,” IEEE AP-S Intl. Symp. Digest, pp. 153–156, July 2006.

[93] K. Ogawa, A. Yamamoto, and J. Takada, “Multipath Performance of Handset Adaptive Array Antennas in the Vicinity of a Human Operator,” IEEE Trans. Antennas Propagat. AP-53, No. 8, pp. 2422–2436, Aug. 2005.

[94] K. Li, K. Honda, and K. Ogawa: “Three-dimensional OTA Design Considerations Based on MIMO Antenna Radiation and Multipath Interactions,” Electromagnetics (iWEM), 2014 IEEE International Workshop on, pp. 215-216, Sapporo, Japan, Aug. 2014.

[95] K. Honda and K. Li, “Three-dimensional MIMO-OTA calibration to achieve the Gaussian angular power spectra in elevation,” IEICE Communications Express, Vol. 5, No. 10, pp. 394–400, Oct. 2016.

[96] K. Ogawa and J. Takada, “An analysis of the effective performance of a handset diversity antenna influenced by head, hand and shoulder effects: A proposal for the diversity antenna gain based on a signal bit-error rate and the analytical results for the PDC system,” Trans. IEICE, vol. J83-B, no. 6, pp. 852–865, Jun. 2000. (This paper was translated into English for Electronics and Communications in Japan, Part 2, vol. 84, no. 6, pp. 10–23, 2001.)

[97] Y. Ogawa and T. Ohgane, “Advances in adaptive antenna technologies in Japan,” IEICE Trans. Commun., vol. E84-B, no. 7, pp. 1704–1712, Jul. 2001.

[98] K. Li, K. Honda, and K. Ogawa, “Shadowing-fading BER

characterization of BAN antennas based on realistic walking models," 7th Int. Sym. Medical Inf. Commun. Technol. (ISMICT2013), pp. 183–187, Tokyo, Japan, Mar. 2013.

[99] S. L. Cotton, "A statistical model for shadowed body-centric communications channels: Theory and validation," IEEE Trans. Antennas and Propaga., vol. 61, no. 8, pp. 4315–4326, Aug. 2013.

[100] K. Li, K. Honda, and K. Ogawa, "Rice channel realization for BAN over-the-air testing using a fading emulator with an arm-swinging dynamic phantom," IEICE Trans. Commn., vol. E98-B, no. 4, pp. 543–553, Apr. 2015.

[101] A. Yamamoto, T. Sakata, H. Iwai, K. Ogawa, J. Takada, K. Sakaguchi, and K. Araki, "BER measurements on a handset adaptive antenna array in the presence of cochannel interference generated using a spatial fading emulator," in Proc. IEEE Antennas Propag. Soc. Int. Symp., vol. 4A, pp. 26–29, Washington, USA, Jul. 2005.

[102] R. Fu, Y. Ye, N. Yang, and K. Pahlavan, "Doppler spread analysis of human motions for body area network applications," in Proc. IEEE 22th Int. Symp. Personal, Indoor, Mobile Radio Commun. (PIMRC 2011), pp. 2209–2213, Toronto, Canada, Sep. 2011.

[103] F. Adachi and J. D. Parsons, "Error rate performance of digital FM mobile radio with postdetection diversity," IEEE Trans. Commun., vol. 37, no. 3, pp. 200–210, Mar. 1989.

[104] K. Li, K. Murata, K. Honda, and K. Ogawa, "Bit-error-rate OTA testing of BAN antennas based on shadowing-fading hybrid effects," 10th Int. Sym. Medical Inf. Commun. Technol. (ISMICT2016), pp. 1–5, Worcester, USA, Mar. 2016.

Appendix A. Matlab Program for Rice Channel BAN-OTA Testing

```
% *****************************************************************************
%              Measurement Program of BAN-OTA Testing using Fading Emulator
%                   Based on Network Analyzer HP8753E and DA Converter
%                            made in 2013/02/07
%                                    K.Li
% *****************************************************************************
clear all
clc
adrs=15;
point=5001;
dt=50;
M=5000;
lk=2;
% -------------------------------------------
%           Parameters of Rice theory
% -------------------------------------------
rc=1;
kd=-50;
k=0;
imed=1;
dl2=-40;
dh2=10;
jdiv=100;
for ib=1:1:23
    kca(ib)=-50;
end

id=0;
 while id>-1
    clc
    disp(' ')
    disp(' -----------------------------------------------------')
    disp('                     Menu Selection                   ')
    disp(' -----------------------------------------------------')
    disp('  Graph window open/close/close all          <1><2><3>')
    disp('  Measure                                          <4>')
    disp('  Data dump                                        <5>')
    disp('  Data load                                        <6>')
    disp('  Data list                                        <7>')
    disp('  Graph of phase                                   <8>')
    disp('  Graph of instantaneous response                  <9>')
    disp('  Graph of CDF                                    <10>')
    disp('  Coherent value of instantaneous response        <11>')
    disp('  Graph of instantaneous response(no mean)        <12>')
    disp('  Rice CDF Theory                                 <13>')
    disp('  Plot real and imaginary parts                   <14>')
    disp('  Multi-value of CDF                              <15>')
    disp(' -----------------------------------------------------')
    disp('  END                                             <99>')
    id=READX(id);

    if id==99
        break
    end
```

```
% **********************************************************************
%                            window open
% **********************************************************************
if id==1
    figure;
    id=0;
end

% **********************************************************************
%                            window close
% **********************************************************************
if id==2
    close;
    id=0;
end

% **********************************************************************
%                            all windows close
% **********************************************************************
if id==3
    close all;
    id=0;
end


% **********************************************************************
%                                Measure
% **********************************************************************
if id==4
    [s21j,point,dt,M]=MEASURE(adrs,point,dt,M);
    id=0;
end

% **********************************************************************
%                                Data dump
% **********************************************************************
if id==5
    DUMP(s21j,point,dt,M);
    id=0;
end

% **********************************************************************
%                               Data load
% **********************************************************************
if id==6
    [s21j,point,dt,M]=LOAD;
    id=0;
end

% **********************************************************************
%                              Data list
% **********************************************************************
if id==7
    LIST(s21j,point,dt,M);
    id=0;
end

% **********************************************************************
%                         Graph of phase
% **********************************************************************
if id==8
   PHASE(s21j,point,dt,M);
    id=0;
```

```
    end

    % ********************************************************************
    %                       Graph of instantaneous response
    % ********************************************************************
    if id==9
        IR(s21j,point,dt,M);
        id=0;
    end

    % ********************************************************************
    %                       Graph of CDF
    % ********************************************************************
    if id==10
        CDF(s21j,point,dt,M);
        id=0;
    end   '

    % ********************************************************************
    %                       Coherent value of instantaneous response
    % ********************************************************************
    if id==11
        Coherent;
        id=0;
    end

    % ********************************************************************
    %                       Graph of instantaneous response(no mean)
    % ********************************************************************
    if id==12
        IRmean(s21j,point,dt,M);
        id=0;
    end

    % ********************************************************************
    %                       Rice CDF Theory
    % ********************************************************************
    if id==13
        [rc,kd,k,imed,dl2,dh2,jdiv]=RICE_CDF(rc,kd,k,imed,dl2,dh2,jdiv);
        id=0;
    end

    % ********************************************************************
    %                       Plot real and imaginary parts
    % ********************************************************************
    if id==14
        Realimaginary(s21j,point);
        id=0;
    end
end
```

Sub-Program: MEASURE.m

```
% ********************************************************************
%          Measurement program of Fading Emulator
%                 HP8753E Network Analyzer
%                     made in 2013/02/07
%                           K.Li
% ********************************************************************
function [s21j,point,dt,M,v]=MEASURE(adrs,point,dt,M,v);

clc
```

```
disp(' ')
N=7;
% Number of Scatterers Fading Emulator
disp(' -----------------------------------------')
disp('  Number of Scatterers in Fading Emulator ')
disp(' -----------------------------------------')
N=READX(N);

ofs=0;
% Offset Angle of Scatterers in degree
disp(' --------------------------------------')
disp('  Offset Angle of Scatterers in degree ')
disp('     (plus sign for the CCW rotation)  ')
disp(' --------------------------------------')
ofs=READX(ofs);


% Mobile Moving Distance in Wavelength
disp(' --------------------------------------')
disp('  Mobile Moving Distance in Wavelength ')
disp(' --------------------------------------')
dt=READX(dt);

% Number of Samples during Movement
disp(' -----------------------------------')
disp('  Number of Samples during Movement ')
disp(' -----------------------------------')
M=READX(M);
point=M+1;

NA=1;
% Set up network analyzer HP8753E
disp(' --------------------------------------------------')
disp('    Set up the frequency of network analyzer       ')
disp(' --------------------------------------------------')
disp('                    950MHz                     <1>')
disp('                    600MHz                     <2>')
disp(' --------------------------------------------------')
NA=READX(NA);

% -------------------------------------------
%                Start or Escape
% -------------------------------------------
esc=0;
clc
disp(' ')
disp(' --------------------------')
disp('    If Start, Hit Return   ')
disp('      (999 for Escape)     ')
disp(' --------------------------')
esc=READX(esc);
if esc==999
    return
end

% ---------------------------------------------------------------
%               Set up the network analyzer HP8753E
% ---------------------------------------------------------------
gna=gpib('ni',0,adrs);
set(gna,'InputBufferSize',100240);
set(gna,'OutputBufferSize',50120);
set(gna,'EOSMode','read&write');
set(gna,'CompareBits',8);
```

```
set(gna,'EOSCharCode','CR');
fopen(gna);

fprintf(gna,'S21;')
fprintf(gna,'POLA')
fprintf(gna,'CWFREQ 950MHZ')
if NA==1
    fprintf(gna,'MARK1 950MHZ')
elseif NA==2
    fprintf(gna,'MARK1 600MHZ')
end

% --------------------------------------------------------------
%            Set up the DA converter
% --------------------------------------------------------------
ao0=0;
ao1=0;
ao2=0;
ao3=0;
ao4=0;
ao5=0;
ao6=0;

daqhwinfo('contec')
ao=analogoutput('contec','AIO001')
addchannel(ao,0)
addchannel(ao,1)
addchannel(ao,2)
addchannel(ao,3)
addchannel(ao,4)
addchannel(ao,5)
addchannel(ao,6)
pause(1);

for in=1:1:7
    v(in)=0;
end
% --------------------------------------------------------------
%              Measurement by Fading Emulator
% --------------------------------------------------------------
n=1;
for d=0:dt/M:dt;   % Mobile Moving Distance in Wavelength
    phi=[0.6020,0.2630,0.6541,0.6892,0.7482,0.4505,0.0838];
    for in=1:1:N;
        theta_n=(in-1)*2*pi./N;
        r=exp(j*(2*pi*d*cos(theta_n-ofs)+2*pi*phi(in)));        %amplitude of i-th antenna
        pha=angle(r)+0.5620;       %phase of i-th phaser
        v(in)=0.0623*(pha.^3)-0.1886*(pha.^2)+1.1502*pha+5.3510; % calculation of output voltage of i-th
DA converter
    end
    % --------------------------------------------------------------
    %            control the output voltage of DA converter
    % --------------------------------------------------------------
    ao0=v(1);
    ao1=v(2);
    ao2=v(3);
    ao3=v(4);
    ao4=v(5);
    ao5=v(6);
    ao6=v(7);
    putdata(ao,[ao0,ao1,ao2,ao3,ao4,ao5,ao6]);
    start(ao);
    pause(0.04);
```

```
    % ----------------------------------------------------------------
    %             Reading Data from NA
    % ----------------------------------------------------------------
    fprintf(gna,'OUTPMARK');
    out=fscanf(gna);
    s21=str2num(out);

    re=s21(1)*cos(s21(2)*pi/180);
    im=s21(1)*sin(s21(2)*pi/180);
    s21j(n)=re+j*im;
    n=n+1;
end %for d=0:dt/M:dt;
    ao0=0;     %DA converter stop
    ao1=0;
    ao2=0;
    ao3=0;
    ao4=0;
    ao5=0;
    ao6=0;
    putdata(ao,[ao0,ao1,ao2,ao3,ao4,ao5,ao6]);
    start(ao)
fclose(gna)
```

Appendix B. Matlab Program for BER-OTA Testing

```
% ******************************************************************************
%             Measurement Program of BER-OTA Testing using Fading Emulator
%                  Based on Signal Generator MG3710A (Anritsu)
%                           made in 2016/08/02
%                                  K.Li
% ******************************************************************************
clear all
clc
whitebg('white')
close

id=0;              % menu select
N=14;             % number of sources
id1=1;             % menu select 1-TX/1-RX
id2=1;             % menu select 1-TX/1-RX
id3=1;             % menu select 1-TX/1-RX
id4=1;             % menu select 1-TX/1-RX
adrs=15;
freqset=0.926;      % Center frequency in GHz
myadrs=0;         % computer
spadrs=8;          % spectrum analyzer
myadrs2=1;        % computer
sgadrs=3;          % spectrum analyzer
% --------------------------------------------------------------------------
%          Initial Phase <4>, <5>
% --------------------------------------------------------------------------
filew=1;
filepd=1;
filepu=1;
fnamep='pha1.dat';
dkp1=zeros(1,N);
dkp2=zeros(1,N);
dkp3=zeros(1,N);
dkp4=zeros(1,N);
dkp5=zeros(1,N);
dkp6=zeros(1,N);
dkp7=zeros(1,N);
dkp8=zeros(1,N);
ukp1=zeros(1,N);
ukp2=zeros(1,N);
ukp3=zeros(1,N);
ukp4=zeros(1,N);
ukp5=zeros(1,N);
ukp6=zeros(1,N);
ukp7=zeros(1,N);
ukp8=zeros(1,N);
% --------------------------------------------------------------------------
%          Polarization Initial Phase <6>,<7>
% --------------------------------------------------------------------------
fileq=1;
fnameq='phq1.dat';
kq1=0;
kq2=0;
kq3=0;
kq4=0;
kq5=0;
kq6=0;
```

```
kq7=0;
kq8=0;
% -------------------------------------------------------------------------
%      Parameters  <9>-<1>
% -------------------------------------------------------------------------
L=7;
level=-63.2;
md=21;
mfreq=1;
xpre=0;
M=500;
zend=10;
mdire=270;
ofs=5;
psel=2;
iniph=2;
qsel=2;
vhran=1;
ien=1;
azdis=1;
ksel=2;
y1=-80;
y2=0;
K=1;
pl5=-100;
ph5=-40;
eig=2;
pwr1=0;
ber=0;
M1=12;
M2=18;

while id>-1
    clc
    disp(' ')
    disp(' ----------------------------------------------')
    disp('       PROGRAM of BER_2D_FADING_EMULATOR       ')
    disp(' ----------------------------------------------')
    disp(' ----------------------------------------------')
    disp('  Open/Close/Close All               <1><2><3> ')
    disp(' ----------------------------------------------')
    disp('  Initial Phase File Dump                  <4> ')
    disp('  Initial Phase File Load                  <5> ')
    disp('  Polarization Phase File Dump             <6> ')
    disp('  Polarization Phase File Load             <7> ')
    disp(' ----------------------------------------------')
    disp('  Set-up the SA (R3132)                    <8> ')
    disp('  Measure the Fading by SA_Fix             <9> ')
    disp('  Measure the Fading by SA_Continuous     <10> ')
    disp(' ----------------------------------------------')
    disp('  Measure the BER by SG_Fix               <11> ')
    disp('  Measure the BER by SG_Continuous        <12> ')
    disp(' ----------------------------------------------')
    disp('  Measure the Fading by SA_Fix_Div.       <13> ')
    disp('  Measure the Fading by SA_Conti_Div.     <14> ')
    disp(' ----------------------------------------------')
    disp('  Measure the BER by SG_Fix_Div.          <15> ')
    disp('  Measure the BER by SG_Conti_Div.        <16> ')
    disp('  END                                     <99> ')
    id=READX(id);

    if id==99              % program stop
        break
```

```
end

if id==99
    break
end

% **********************************************************************
%                          Open
% **********************************************************************
if id==1
    figure;
end   % end of 'if id==1'

% **********************************************************************
%                          Close
% **********************************************************************
if id==2
    close
end   % end of 'if id==2'

% **********************************************************************
%                        Close all
% **********************************************************************
if id==3
    close all
end   % end of 'if id==3'

% **********************************************************************
%                        Initial Phase Dump
% **********************************************************************
if id==4
    clc
    disp(' ')
    disp(' -------------------------------------')
    disp('     The Number of Incident Waves    ')
    disp(' -------------------------------------')
    disp('  2-TX                           <1> ')
    disp('  4-TX                           <2> ')
    disp('  8-TX                           <3> ')
    disp('  escape                        <99> ')
    disp(' -------------------------------------')
    filew=READX(filew);

    if (filew>=1)&&(filew<=3)
        [filepd,filepu,filew,fnamep,dkp1,dkp2,dkp3,dkp4,dkp5,dkp6,dkp7,dkp8,...
            ukp1,ukp2,ukp3,ukp4,ukp5,ukp6,ukp7,ukp8,N]=...
            FDUMP_PHASE(filepd,filepu,filew,fnamep,dkp1,dkp2,dkp3,dkp4,dkp5,dkp6,dkp7,dkp8,...
            ukp1,ukp2,ukp3,ukp4,ukp5,ukp6,ukp7,ukp8,N);
    end
end   % end of 'if id==4'

% **********************************************************************
%                       Initial Phase Load
% **********************************************************************
if id==5
    clc
    disp(' ')
    disp(' -------------------------------------')
    disp('     The Number of Incident Waves    ')
    disp(' -------------------------------------')
    disp('  2-TX                           <1> ')
    disp('  4-TX                           <2> ')
    disp('  8-TX                           <3> ')
```

```
    disp('  escape                        <99> ')
    disp(' -----------------------------------')
    filew=READX(filew);

    if (filew>=1)&&(filew<=3)
        [filepd,filepu,filew,fnamep,dkp1,dkp2,dkp3,dkp4,dkp5,dkp6,dkp7,dkp8,...
            ukp1,ukp2,ukp3,ukp4,ukp5,ukp6,ukp7,ukp8,N]=...
            FLOAD_PHASE(filepd,filepu,filew,fnamep,dkp1,dkp2,dkp3,dkp4,dkp5,dkp6,dkp7,dkp8,...
            ukp1,ukp2,ukp3,ukp4,ukp5,ukp6,ukp7,ukp8,N);
    end
end   % end of 'if id==5'

% ********************************************************************
%                      Polarization Initial Phase Dump
% ********************************************************************
if id==6
    clc
    disp(' ')
    disp(' -----------------------------------')
    disp('     The Number of Incident Waves    ')
    disp(' -----------------------------------')
    disp('  2-TX                           <1> ')
    disp('  4-TX                           <2> ')
    disp('  8-TX                           <3> ')
    disp('  escape                        <99> ')
    disp(' -----------------------------------')
    filew=READX(filew);

    if (filew>=1)&&(filew<=3)
        [fileq,filew,fnameq,kq1,kq2,kq3,kq4,kq5,kq6,kq7,kq8,N]=...
            FDUMP_POLPHASE(fileq,filew,fnameq,kq1,kq2,kq3,kq4,kq5,kq6,kq7,kq8,N);
    end
end   % end of 'if id==6'

% ********************************************************************
%                      Polarization Initial Phase Load
% ********************************************************************
if id==7
    clc
    disp(' ')
    disp(' -----------------------------------')
    disp('     The Number of Incident Waves    ')
    disp(' -----------------------------------')
    disp('  2-TX                           <1> ')
    disp('  4-TX                           <2> ')
    disp('  8-TX                            <> ')
    disp('  escape                        <99> ')
    disp(' -----------------------------------')
    filew=READX(filew);

    if (filew>=1)&&(filew<=3)
        [fileq,filew,fnameq,kq1,kq2,kq3,kq4,kq5,kq6,kq7,kq8,N]=...
            FLOAD_POLPHASE(fileq,filew,fnameq,kq1,kq2,kq3,kq4,kq5,kq6,kq7,kq8,N);
    end
end   % end of 'if id==7'

% *******************************************************************
%                     Set-up the SA (R3132)
% *******************************************************************
if id==8
    [freqset]=STUPHP(freqset);
    id=0;
end   % end of 'if id==4'
```

```
    % ******************************************************************
    %         Measure the Fading by SA (Fixed Arm) (R3132)
    % ******************************************************************
    if id==9
        clc
        disp(' ')
        disp(' ------------------------------')
        disp('        Measurement by SA      ')
        disp(' ------------------------------')
        disp('  Measurement              <1> ')
        disp('  Data File Dump           <2> ')
        disp('  Data File Load           <3> ')
        disp('  Drawing the Graph        <4> ')
        disp('  Selection Diversity      <5> ')
        disp('  escape                  <99> ')
        id1=READX(id1);

        if id1==1
            [md,xpre,M,zend,mdire,N,ofs,...
                psel,iniph,qsel,vhran,ien,dkp1,ukp1,azdis,ksel,y1,y2,K,cx,sx,gx,px,...

pl5,ph5,eig,fnamep,kq1,fnameq,myadrs,spadrs,pwr1,freqset,mfreq]=MEASURE_SA_FIXED(md,xpre,M,zend,mdire,N,o
fs,...

psel,iniph,qsel,vhran,ien,azdis,ksel,y1,y2,K,cx,sx,gx,px,pl5,ph5,eig,dkp1,ukp1,fnamep,kq1,fnameq,myadrs,s
padrs,pwr1,freqset,mfreq);
        elseif id1==2
            DUMP_1TX_1RX(pwr1,ien,M,zend);
        elseif id1==3
            [pwr1,ien,M,zend]=LOAD_1TX_1RX;
        elseif id1==4
            [xpre,M,zend,mdire,N,ofs,...
                psel,iniph,qsel,vhran,ien,azdis,ksel,y1,y2,K,cx,sx,gx,px,...
                pl5,ph5,eig,dkp1,ukp1,fnamep,kq1,fnameq,myadrs,spadrs,pwr1]=...
                EIGEN_1TX_1RX_2D_POL(xpre,M,zend,mdire,N,ofs,...
                psel,iniph,qsel,vhran,ien,azdis,ksel,y1,y2,K,cx,sx,gx,px,...
                pl5,ph5,eig,dkp1,ukp1,fnamep,kq1,fnameq,myadrs,spadrs,pwr1);
        elseif id1==5

DUMP_1TX_1RX_Div12(md,xpre,mdire,N,ofs,psel,iniph,qsel,vhran,dkp1,ukp1,azdis,ksel,y1,y2,K,cx,sx,gx,px,...
                pl5,ph5,eig,fnamep,kq1,fnameq,myadrs,spadrs,freqset,mfreq,pwr1,ien,M,zend);
        end
        id1=0;
    end   % end of 'if id==4'

    % ******************************************************************
    %          Measure the Fading by SA (Continuous Swing) (R3132)
    % ******************************************************************
    if id==10
        clc
        disp(' ')
        disp(' ------------------------------')
        disp('        Measurement by SA      ')
        disp(' ------------------------------')
        disp('  Measurement              <1> ')
        disp('  Data File Dump           <2> ')
        disp('  Data File Load           <3> ')
        disp('  Drawing the Graph        <4> ')
        disp('  Selection Diversity      <5> ')
        disp('  escape                  <99> ')
        id2=READX(id2);
```

```
        if id2==1
            [md,xpre,M,zend,mdire,N,ofs,...
                psel,iniph,qsel,vhran,ien,dkp1,ukp1,azdis,ksel,y1,y2,K,cx,sx,gx,px,...

pl5,ph5,eig,fnamep,kq1,fnameq,myadrs,spadrs,pwr1,freqset,mfreq]=MEASURE_SA_CONTINUOUS(md,xpre,M,zend,mdir
e,N,ofs,...

psel,iniph,qsel,vhran,ien,azdis,ksel,y1,y2,K,cx,sx,gx,px,pl5,ph5,eig,dkp1,ukp1,fnamep,kq1,fnameq,myadrs,s
padrs,pwr1,freqset,mfreq);
        elseif id2==2
            DUMP_1TX_1RX(pwr1,ien,M,zend);
        elseif id2==3
            [pwr1,ien,M,zend]=LOAD_1TX_1RX;
        elseif id2==4
            [xpre,M,zend,mdire,N,ofs,...
                psel,iniph,qsel,vhran,ien,azdis,ksel,y1,y2,K,cx,sx,gx,px,...
                pl5,ph5,eig,dkp1,ukp1,fnamep,kq1,fnameq,myadrs,spadrs,pwr1]=...
                EIGEN_1TX_1RX_2D_POL(xpre,M,zend,mdire,N,ofs,...
                psel,iniph,qsel,vhran,ien,azdis,ksel,y1,y2,K,cx,sx,gx,px,...
                pl5,ph5,eig,dkp1,ukp1,fnamep,kq1,fnameq,myadrs,spadrs,pwr1);
        elseif id2==5

DUMP_1TX_1RX_Div12(md,xpre,mdire,N,ofs,psel,iniph,qsel,vhran,dkp1,ukp1,azdis,ksel,y1,y2,K,cx,sx,gx,px,...
                pl5,ph5,eig,fnamep,kq1,fnameq,myadrs,spadrs,freqset,mfreq,pwr1,ien,M,zend);
        end
        id2=0;
    end   % end of 'if id==4'

    % ********************************************************************
    %     Measure the BER by SG (Fixed Arm) (MG3710A)
    % ********************************************************************
    if id==11
        clc
        disp(' ')
        disp(' ------------------------------')
        disp('  Measurement of BER (Fixed Arm)')
        disp(' ------------------------------')
        disp('  Measurement by SG        <1> ')
        disp('  Data File Dump           <2> ')
        disp('  Data File Load           <3> ')
        disp('  Drawing the Graph        <4> ')
        disp('  Selection Diversity      <5> ')
        disp('  escape                  <99> ')
        id3=READX(id3);

        if id3==1
            [L,level,md,xpre,M,zend,mdire,N,ofs,...
                psel,iniph,qsel,vhran,ien,dkp1,ukp1,azdis,ksel,y1,y2,K,cx,sx,gx,px,...

pl5,ph5,eig,fnamep,kq1,fnameq,myadrs2,sgadrs,ber,freqset,mfreq]=MEASURE_SG_FIXED(L,level,md,xpre,M,zend,m
dire,N,ofs,...

psel,iniph,qsel,vhran,ien,azdis,ksel,y1,y2,K,cx,sx,gx,px,pl5,ph5,eig,dkp1,ukp1,fnamep,kq1,fnameq,myadrs2,
sgadrs,ber,freqset,mfreq);
        elseif id3==2
            DUMP_1TX_1RX_BER(ber,ien,M,zend);
        elseif id3==3
            [ber,ien,M,zend]=LOAD_1TX_1RX_BER;
        elseif id3==4
            [xpre,M,zend,mdire,N,ofs,...
                psel,iniph,qsel,vhran,ien,azdis,ksel,y1,y2,K,cx,sx,gx,px,...
                pl5,ph5,eig,dkp1,ukp1,fnamep,kq1,fnameq,myadrs2,sgadrs,ber]=...
                EIGEN_1TX_1RX_2D_POL_BER(xpre,M,zend,mdire,N,ofs,...
```

```
                psel,iniph,qsel,vhran,ien,azdis,ksel,y1,y2,K,cx,sx,gx,px,...
                pl5,ph5,eig,dkp1,ukp1,fnamep,kq1,fnameq,myadrs2,sgadrs,ber);
        elseif id3==5
            DUMP_1TX_1RX_BER_Div12(xpre,M,zend,mdire,N,ofs,...
                psel,iniph,qsel,vhran,ien,azdis,ksel,y1,y2,K,cx,sx,gx,px,...
                pl5,ph5,eig,dkp1,ukp1,fnamep,kq1,fnameq,myadrs2,sgadrs,ber,level);
        end
        id3=0;
    end   % end of 'if id==4'

    % *********************************************************************
    %     Measure the BER by SG (Continuous Swing) (MG3710A)
    % *********************************************************************
    if id==12
        clc
        disp(' ')
        disp(' ---------------------------------')
        disp('  Measurement of BER (Continuous) ')
        disp(' ---------------------------------')
        disp('  Measurement by SG          <1> ')
        disp('  Data File Dump             <2> ')
        disp('  Data File Load             <3> ')
        disp('  Drawing the Graph          <4> ')
        disp('  Selection Diversity        <5> ')
        disp('  escape                    <99> ')
        id4=READX(id4);

        if id4==1
            [md,xpre,M1,M2,zend,mdire,N,ofs,...
                psel,iniph,qsel,vhran,ien,dkp1,ukp1,azdis,ksel,y1,y2,K,cx,sx,gx,px,...

pl5,ph5,eig,fnamep,kq1,fnameq,myadrs2,sgadrs,ber,freqset,mfreq]=MEASURE_SG_CONTINUOUS(md,xpre,M1,M2,zend,
mdire,N,ofs,...

psel,iniph,qsel,vhran,ien,azdis,ksel,y1,y2,K,cx,sx,gx,px,pl5,ph5,eig,dkp1,ukp1,fnamep,kq1,fnameq,myadrs2,
sgadrs,ber,freqset,mfreq);
        elseif id4==2
            DUMP_1TX_1RX_BER(ber,ien,M,zend);
        elseif id4==3
            [ber,ien,M,zend]=LOAD_1TX_1RX_BER;
        elseif id4==4
            [xpre,M,zend,mdire,N,ofs,...
                psel,iniph,qsel,vhran,ien,azdis,ksel,y1,y2,K,cx,sx,gx,px,...
                pl5,ph5,eig,dkp1,ukp1,fnamep,kq1,fnameq,myadrs2,sgadrs,ber]=...
                EIGEN_1TX_1RX_2D_POL_BER(xpre,M,zend,mdire,N,ofs,...
                psel,iniph,qsel,vhran,ien,azdis,ksel,y1,y2,K,cx,sx,gx,px,...
                pl5,ph5,eig,dkp1,ukp1,fnamep,kq1,fnameq,myadrs2,sgadrs,ber);
        elseif id4==5
            DUMP_1TX_1RX_BER_Div12(xpre,M,zend,mdire,N,ofs,...
                psel,iniph,qsel,vhran,ien,azdis,ksel,y1,y2,K,cx,sx,gx,px,...
                pl5,ph5,eig,dkp1,ukp1,fnamep,kq1,fnameq,myadrs2,sgadrs,ber,level);
        end
        id4=0;
    end   % end of 'if id==4'

    % *********************************************************************
    %          Measure the Fading by SA (Fixed Arm) Diver city (R3132)
    % *********************************************************************
    if id==13
        clc
        disp(' ')
        disp(' ------------------------------')
        disp('        Measurement by SA      ')
```

```
        disp(' ------------------------------')
        disp('  Measurement             <1> ')
        disp('  Drawing the Graph       <2> ')
        disp('  escape                 <99> ')
        id1=READX(id1);

        if id1==1
            [md,xpre,M,zend,mdire,N,ofs,...
                psel,iniph,qsel,vhran,ien,dkp1,ukp1,azdis,ksel,y1,y2,K,cx,sx,gx,px,...

pl5,ph5,eig,fnamep,kq1,fnameq,myadrs,spadrs,pwr1,freqset,mfreq]=MEASURE_SA_FIXED_Div(md,xpre,M,zend,mdire
,N,ofs,...

psel,iniph,qsel,vhran,ien,azdis,ksel,y1,y2,K,cx,sx,gx,px,pl5,ph5,eig,dkp1,ukp1,fnamep,kq1,fnameq,myadrs,s
padrs,pwr1,freqset,mfreq);
        elseif id1==2

DUMP_1TX_1RX_Div(md,xpre,mdire,N,ofs,psel,iniph,qsel,vhran,dkp1,ukp1,azdis,ksel,y1,y2,K,cx,sx,gx,px,...
                pl5,ph5,eig,fnamep,kq1,fnameq,myadrs,spadrs,freqset,mfreq,pwr1,ien,M,zend);

        end
        id1=0;
    end   % end of 'if id==4'

    % ************************************************************************
    %          Measure the Fading by SA (Continuous Swing) Diver city (R3132)
    % ************************************************************************
    if id==14
        clc
        disp(' ')
        disp(' ------------------------------')
        disp('       Measurement by SA      ')
        disp(' ------------------------------')
        disp('  Measurement            <1> ')
        disp('  Data File Dump         <2> ')
        disp('  Data File Load         <3> ')
        disp('  Drawing the Graph      <4> ')
        disp('  Selection Diversity    <5> ')
        disp('  escape                <99> ')
        id1=READX(id1);

        if id1==1
            [md,xpre,M,zend,mdire,N,ofs,...
                psel,iniph,qsel,vhran,ien,dkp1,ukp1,azdis,ksel,y1,y2,K,cx,sx,gx,px,...

pl5,ph5,eig,fnamep,kq1,fnameq,myadrs,spadrs,pwr1,freqset,mfreq]=MEASURE_SA_CONTINUOUS_Div(md,xpre,M,zend,
mdire,N,ofs,...

psel,iniph,qsel,vhran,ien,azdis,ksel,y1,y2,K,cx,sx,gx,px,pl5,ph5,eig,dkp1,ukp1,fnamep,kq1,fnameq,myadrs,s
padrs,pwr1,freqset,mfreq);
        elseif id1==2

DUMP_1TX_1RX_Div(md,xpre,mdire,N,ofs,psel,iniph,qsel,vhran,dkp1,ukp1,azdis,ksel,y1,y2,K,cx,sx,gx,px,...
                pl5,ph5,eig,fnamep,kq1,fnameq,myadrs,spadrs,freqset,mfreq,pwr1,ien,M,zend);
        elseif id1==3
            [pwr1,ien,M,zend]=LOAD_1TX_1RX;
        elseif id1==4
            [xpre,M,zend,mdire,N,ofs,...
                psel,iniph,qsel,vhran,ien,azdis,ksel,y1,y2,K,cx,sx,gx,px,...
                pl5,ph5,eig,dkp1,ukp1,fnamep,kq1,fnameq,myadrs,spadrs,pwr1]=...
                EIGEN_1TX_1RX_2D_POL(xpre,M,zend,mdire,N,ofs,...
                psel,iniph,qsel,vhran,ien,azdis,ksel,y1,y2,K,cx,sx,gx,px,...
                pl5,ph5,eig,dkp1,ukp1,fnamep,kq1,fnameq,myadrs,spadrs,pwr1);
```

```
        elseif id1==5

DUMP_1TX_1RX_Div(md,xpre,mdire,N,ofs,psel,iniph,qsel,vhran,dkp1,ukp1,azdis,ksel,y1,y2,K,cx,sx,gx,px,...
                pl5,ph5,eig,fnamep,kq1,fnameq,myadrs,spadrs,freqset,mfreq,pwr1,ien,M,zend);

        end
        id1=0;
    end   % end of 'if id==4'

    % ******************************************************************
    %     Measure the BER by SG (Fixed Arm)  Diver city(MG3710A)
    % ******************************************************************
    if id==15
        clc
        disp(' ')
        disp(' -------------------------------')
        disp('  Measurement of BER (Fixed Arm)')
        disp(' -------------------------------')
        disp('  Measurement by SG         <1> ')
        disp('  Data File Dump            <2> ')
        disp('  Data File Load            <3> ')
        disp('  Drawing the Graph         <4> ')
        disp('  escape                   <99> ')
        id3=READX(id3);

        if id3==1
            [L,level,md,xpre,M,zend,mdire,N,ofs,...
                psel,iniph,qsel,vhran,ien,dkp1,ukp1,azdis,ksel,y1,y2,K,cx,sx,gx,px,...

pl5,ph5,eig,fnamep,kq1,fnameq,myadrs2,sgadrs,ber,freqset,mfreq]=MEASURE_SG_FIXED_Div(L,level,md,xpre,M,ze
nd,mdire,N,ofs,...

psel,iniph,qsel,vhran,ien,azdis,ksel,y1,y2,K,cx,sx,gx,px,pl5,ph5,eig,dkp1,ukp1,fnamep,kq1,fnameq,myadrs2,
sgadrs,ber,freqset,mfreq);
        elseif id3==2
            DUMP_1TX_1RX_BER_Div(xpre,M,zend,mdire,N,ofs,...
                psel,iniph,qsel,vhran,ien,azdis,ksel,y1,y2,K,cx,sx,gx,px,...
                pl5,ph5,eig,dkp1,ukp1,fnamep,kq1,fnameq,myadrs2,sgadrs,ber,level);
        elseif id3==3
            [ber,ien,M,zend]=LOAD_1TX_1RX_BER;
        elseif id3==4
            [xpre,M,zend,mdire,N,ofs,...
                psel,iniph,qsel,vhran,ien,azdis,ksel,y1,y2,K,cx,sx,gx,px,...
                pl5,ph5,eig,dkp1,ukp1,fnamep,kq1,fnameq,myadrs2,sgadrs,ber]=...
                EIGEN_1TX_1RX_2D_POL_BER(xpre,M,zend,mdire,N,ofs,...
                psel,iniph,qsel,vhran,ien,azdis,ksel,y1,y2,K,cx,sx,gx,px,...
                pl5,ph5,eig,dkp1,ukp1,fnamep,kq1,fnameq,myadrs2,sgadrs,ber);
        end
        id3=0;
    end   % end of 'if id==4'

    % ******************************************************************
    %     Measure the BER by SA (Continuous Swing) Diver city (R3132)) (MG3710A)
    % ******************************************************************
    if id==16
        clc
        disp(' ')
        disp(' ---------------------------------')
        disp('  Measurement of BER (Continuous) ')
        disp(' ---------------------------------')
        disp('  Measurement by SG           <1> ')
        disp('  Data File Dump              <2> ')
        disp('  Data File Load              <3> ')
```

```
        disp('   Drawing the Graph           <4> ')
        disp('   escape                     <99> ')
        id4=READX(id4);

        if id4==1
            [md,xpre,zend,mdire,N,ofs,...
                psel,iniph,qsel,vhran,ien,dkp1,ukp1,azdis,ksel,y1,y2,K,cx,sx,gx,px,...

pl5,ph5,eig,fnamep,kq1,fnameq,myadrs2,sgadrs,ber,freqset,mfreq,level]=MEASURE_SG_CONTINUOUS_Div(md,xpre,z
end,mdire,N,ofs,...

psel,iniph,qsel,vhran,ien,azdis,ksel,y1,y2,K,cx,sx,gx,px,pl5,ph5,eig,dkp1,ukp1,fnamep,kq1,fnameq,myadrs2,
sgadrs,ber,freqset,mfreq,level);
        elseif id4==2
            [xpre,M,zend,mdire,N,ofs,...
                psel,iniph,qsel,vhran,ien,azdis,ksel,y1,y2,K,cx,sx,gx,px,...
                pl5,ph5,eig,dkp1,ukp1,fnamep,kq1,fnameq,myadrs2,sgadrs,ber,level]=...
                DUMP_1TX_1RX_BER_Div(xpre,M,zend,mdire,N,ofs,...
                psel,iniph,qsel,vhran,ien,azdis,ksel,y1,y2,K,cx,sx,gx,px,...
                pl5,ph5,eig,dkp1,ukp1,fnamep,kq1,fnameq,myadrs2,sgadrs,ber,level);
        elseif id4==3
            [ber,ien,M,zend]=LOAD_1TX_1RX_BER;
        elseif id4==4
            [xpre,M,zend,mdire,N,ofs,...
                psel,iniph,qsel,vhran,ien,azdis,ksel,y1,y2,K,cx,sx,gx,px,...
                pl5,ph5,eig,dkp1,ukp1,fnamep,kq1,fnameq,myadrs2,sgadrs,ber]=...
                EIGEN_1TX_1RX_2D_POL_BER(xpre,M,zend,mdire,N,ofs,...
                psel,iniph,qsel,vhran,ien,azdis,ksel,y1,y2,K,cx,sx,gx,px,...
                pl5,ph5,eig,dkp1,ukp1,fnamep,kq1,fnameq,myadrs2,sgadrs,ber);
        end
        id4=0;
    end   % end of 'if id==4'

end   % while id>0
```

Sub-Program: MEASURE_SA_CONTINUOUS.m

```
% ********************************************************************
%          Measurement program of Fading Emulator
%                 Signal Generator MG3710A Anritsu
%                     made in 2016/08/02
%                            K.Li
% ********************************************************************
function
[md,xpre,M,zend,mdire,N,ofs,psel,iniph,qsel,vhran,ien,dkp1,ukp1,azdis,ksel,y1,y2,K,cx,sx,gx,px,...
    pl5,ph5,eig,fnamep,kq1,fnameq,myadrs,spadrs,pwr1,freqset,mfreq]=...

MEASURE_SA_CONTINUOUS(md,xpre,M,zend,mdire,N,ofs,psel,iniph,qsel,vhran,ien,azdis,ksel,y1,y2,K,cx,sx,gx,px
,...
    pl5,ph5,eig,dkp1,ukp1,fnamep,kq1,fnameq,myadrs,spadrs,pwr1,freqset,mfreq);

myadrs=0;        % computer
spadrs=8;        % spectrum analyzer
clc
disp(' ')
M=216;
zend=4.32;

clc
disp(' ')
% Measured Direction
disp(' ------------------------')
```

```
disp('    Bilateral MIMO OTA   ')
disp('    Measured Direction   ')
disp(' ------------------------')
disp('   downlink         <21> ')
disp('   uplink           <12> ')
disp(' ------------------------')
md=READX(md);

% Measured Frequency
disp(' --------------------------')
disp('     Measured Frequency    ')
disp(' --------------------------')
disp('   926MHz              <1> ')
disp('   950MHz              <2> ')
disp('   2000MHz             <3> ')
disp(' --------------------------')
mfreq=READX(mfreq);

if mfreq==1
    if freqset~=0.926
        disp(' -----------------------------------------')
        disp('  Caution !!!   Setup of VNA is different ')
        disp(' -----------------------------------------')
        pause(3)
        return
    end

end

clc
disp(' ')
% XPR
disp(' ---------------')
disp('    XPR in dB   ')
disp(' ---------------')
xpre=READX(xpre);
xpr=10^(xpre/10);

% Number of Samples during Movement
disp(' -----------------------------------')
disp('  Number of Samples during Movement ')
disp(' -----------------------------------')
M=READX(M);

% Mobile Moving Distance in Wavelength
disp(' --------------------------------------')
disp('  Mobile Moving Distance in Wavelength ')
disp(' --------------------------------------')
zend=READX(zend);

% Mobile Moving Directions
disp(' ------------------------------------')
disp('  Mobile Moving Directions in degree ')
disp(' ------------------------------------')
mdire=READX(mdire);
mdir=mdire*pi/180;

clc
disp(' ')
% Number of Scatterers in Azimuth
disp(' ---------------------------------')
disp('  Number of Scatterers in Azimuth ')
disp(' ---------------------------------')
```

```
N=READX(N);

% Offset Angle of Scatterers in degree
disp(' --------------------------------------')
disp('  Offset Angle of Scatterers in degree ')
disp('     (plus sign for the CCW rotation)  ')
disp(' --------------------------------------')
ofs=READX(ofs);

% -------------------------------------------
%       Initial Phase
% -------------------------------------------
clc
disp(' ')
disp(' -------------------------------------------------------')
disp('  Use of Random Data for Initial Phase of Scatterers <1>')
disp('  Use of File Data for Initial Phase of Scatterers   <2>')
disp(' -------------------------------------------------------')
psel=READX(psel);

if psel==1
    % Initial Phase of Scatterers
    disp(' -----------------------------')
    disp('  Initial Phase of Scatterers ')
    disp(' -----------------------------')
    disp('  Zero                    <1> ')
    disp('  Random                  <2> ')
    iniph=READX(iniph);
end

disp(' ----------------------------------------------')
disp('  Use of Random Data for Polarization Phase <1>')
disp('  Use of File Data for Polarization Phase   <2>')
disp(' ----------------------------------------------')
qsel=READX(qsel);

if qsel==1
    disp(' --------------------')
    disp('  Polarization Phase ')
    disp(' --------------------')
    disp('  Zero           <1> ')
    disp('  Random         <2> ')
    vhran=READX(vhran);
end

% -------------------------------------------
%       Cluster Parameter
% -------------------------------------------
clc
disp(' ')
% # of Radio Environment
disp(' ---------------------------------')
disp('   # of Radio Environment to Move ')
disp(' ---------------------------------')
ien=READX(ien);
% Scatterers Distribution in Azimuth
disp(' ------------------------------------')
disp('  Scatterers Distribution in Azimuth ')
disp(' ------------------------------------')
disp('  Clarke  Model                  <1> ')
disp('  Cluster Model                  <2> ')
azdis=READX(azdis);
```

```
clc
disp(' ')
disp(' --------------------------------')
disp('   pl for Channel Response in dB  ')
disp(' --------------------------------')
pl5=READX(pl5);

disp(' --------------------------------')
disp('   ph for Channel Response in dB  ')
disp(' --------------------------------')
ph5=READX(ph5);

% ------------------------------------------------------------------------
%               Start or Escape
% ------------------------------------------------------------------------
esc=0;
clc
disp(' ')
disp(' -------------------------')
disp('    If Start, Hit Return   ')
disp('      (999 for Escape)     ')
disp(' -------------------------')
esc=READX(esc);
if esc==999
    return
end

tic;
% --------------------------------
%    Spectrum Analyzer
% --------------------------------
% Board index myadrs(0) & Primary adress spadrs(18)
gsp=gpib('ni',myadrs,spadrs);
% Connect to the instrument
fopen(gsp)
% Assert the EOI line
set(gsp,'EOSMode','read&write')
set(gsp,'EOSCharCode','LF')

if md==21
    fprintf(gsp,'MN');
elseif md==12
    fprintf(gsp,'MN');
end

% --------------------------------------------------------------
%             Set up the DA converter
% --------------------------------------------------------------
ao0=0;
ao1=0;
ao2=0;
ao3=0;
ao4=0;
ao5=0;
ao6=0;
ao7=0;
ao8=0;
ao9=0;
ao10=0;
ao11=0;
ao12=0;
ao13=0;
daqhwinfo('contec')
```

```
ao=analogoutput('contec','AIO001');
addchannel(ao,0)
addchannel(ao,1)
addchannel(ao,2)
addchannel(ao,3)
addchannel(ao,4)
addchannel(ao,5)
addchannel(ao,6)
addchannel(ao,7)
addchannel(ao,8)
addchannel(ao,9)
addchannel(ao,10)
addchannel(ao,11)
addchannel(ao,12)
addchannel(ao,13)
pause(1);

for in=1:1:14
    v(in)=0;
end

z=0:zend/(M-1):zend;  % mobile locations from 0 to zend in wavelength
% --------------------------------------------------------------------------
%              Measurement Start
% --------------------------------------------------------------------------
for ie=1:ien
    c1=round(ofs:360/N:360-360/N+ofs);
    for i=1:N
        if c1(i)<0
            c1(i)=c1(i)+360;
        end
        if c1(i)>360
            c1(i)=c1(i)-360;
        end
    end

     if md==21   %downlink
        if psel==1   % (Random Data)
            if iniph==1                     % zero initial phase distribution
                dkp1=ones(1,N);
                A1s=dkp1;
            elseif iniph==2                 % random initial phase distribution
                dkp1=rand(1,N);
                A1s=exp(j*2*pi*dkp1);
            end
        elseif psel==2   %  (File Data)
            A1s=exp(j*2*pi*dkp1);
        end

    end

    if qsel==1
        if vhran==1                     % zero phase
            kq1=ones(1,N);
            phrr1=kq1;
        else                            % random phase
            kq1=rand(1,N);
            phrr1=exp(j*2*pi*kq1);
        end
    elseif qsel==2           phrr1=exp(j*2*pi*kq1);
    end

    if azdis==1        % uniform source distribution in azimuth (Clarke model)
```

```
        A1=A1s;

    end

    hbar=waitbar(0,'Now Mobile is Moving to...');
    for ir=1:M
        waitbar(((ie-1)*M+ir)/(M*ien));

        for i=1:1:N;
            r=A1*exp(j*(2*pi*z(ir)*cos((c1(i)-zend)*pi/180)));         % amplitude of i-th antenna
            pha=angle(r)+pi;                                            % phase of i-th phaser

            v(i)=0.0659*(pha(i).^3)-0.8360*(pha(i).^2)+4.4370*pha(i)-2.2930;
            if v(i)<0
                v(i)=0;
            elseif v(i)>10
                v(i)=10;
            end

        end

        % ---------------------------------------------------------------
        %             control the output voltage of DA converter
        % ---------------------------------------------------------------
        ao0=v(1);
        ao1=v(2);
        ao2=v(3);
        ao3=v(4);
        ao4=v(5);
        ao5=v(6);
        ao6=v(7);
        ao7=v(8);
        ao8=v(9);
        ao9=v(10);
        ao10=v(11);
        ao11=v(12);
        ao12=v(13);
        ao13=v(14);

        putdata(ao,[ao0,ao1,ao2,ao3,ao4,ao5,ao6,ao7,ao8,ao9,ao10,ao11,ao12,ao13]);
        start(ao);
        pause(0.04);

        % ---------------------------------------------------------------
        %             Reading Data from SA
        % ---------------------------------------------------------------
        fprintf(gsp,'ML?');
        pause(0.001);
        out=fscanf(gsp);
        pwr1(ir)=eval(out);
        R=rem(ir,18)
        if R==0
            clc
            disp(' Change Arm Angle')

            pause;
        else
        end
            end  % for ir=1:M
        close(hbar);
end  % for ie=1:ien
%DA converter stop
ao0=0;
```

```
ao1=0;
ao2=0;
ao3=0;
ao4=0;
ao5=0;
ao6=0;
ao7=0;
ao8=0;
ao9=0;
ao10=0;
ao11=0;
ao12=0;
ao13=0;
putdata(ao,[ao0,ao1,ao2,ao3,ao4,ao5,ao6,ao7,ao8,ao9,ao10,ao11,ao12,ao13]);
start(ao);
fclose(gsp);
clear gsp
% --------------------------------------------------------------------------
%     Measurement Stop
% --------------------------------------------------------------------------

for ie=1:ien
    for ir=1:M
        x((ie-1)*M+ir)=(ie-1)*M+ir;
    end
end

% --------------------------------------------------------------------------
%     Instantaneous Response
% --------------------------------------------------------------------------
scrsz = get(0,'ScreenSize');
h1=figure('Position',[10 scrsz(4)/2.4 scrsz(3)/2.05 scrsz(4)/2.05]);

% H((ie-1)*M+ir,i1,j1)
% h11med=10*log10(median(abs(pwr1)));
% plot(x,10*log10(abs(pwr1))-h11med,'k','LineWidth',2);   % h11
h11med=10*log10(median(10.^(pwr1/10)));
plot(x,pwr1,'k','LineWidth',2);   % h11

title('Instantaneous Response','FontSize',16,'FontName','Times New Roman','Color','k')
xlabel('Traveling Distance [Wavelength]','FontSize',14,'FontName','Times New Roman','Color','k')
ylabel('Received Power [dB]','FontSize',14,'FontName','Times New Roman','Color','k')
% h=legend('h11','Location','SouthEast');
% set(h, 'FontSize', 12)
grid off
xt=[0; ien*M/10; ien*M/10*2; ien*M/10*3; ien*M/10*4; ien*M/10*5; ien*M/10*6; ien*M/10*7;...
    ien*M/10*8; ien*M/10*9; ien*M/10*10];
set(gca, 'Xtick', xt)
xtl=[0; zend/10; zend/10*2; zend/10*3; zend/10*4; zend/10*5; zend/10*6; zend/10*7;...
    zend/10*8; zend/10*9; zend/10*10];
set(gca, 'XtickLabel', xtl)
set(gca, 'FontSize', 12,'FontName','Times New Roman')

ymin=pl5;
ymax=ph5;
xpos=0.05*M*ien;
ypos=ymin+0.26*(ymax-ymin);
fsize=12;
A=sprintf('%6.2f',h11med);
hm=num2str(A);
tx=strcat('Po =',hm,'dBm');
text(xpos,ypos,tx,'FontSize',fsize,'FontName','Times New Roman');
axis([0 ien*M -100 -40]);
```

```
% ------------------------------
%       CDF
% ------------------------------
scrsz = get(0,'ScreenSize');
h2=figure('Position',[scrsz(3)/2 scrsz(4)/2.4 scrsz(3)/2.05 scrsz(4)/2.05]);

xmin=-30;
xmax=10;
ymin=0.1;
ymax=100;

div=100;
for i=1:div+1
    xt(i)=xmin+(xmax-xmin)/div*(i-1);        % x-axis value referenced to tyuou-ti
    xr=10^(xt(i)/20);                         % natural value for x
    yt(i)=((1-exp(-log(2)*(xr^2))))*100;     % Rayleigh characteristics
end

semilogy(xt,yt,'--g','LineWidth',2)           % drawing Rayleigh characteristics

% H((ie-1)*M+ir,i1,j1)
yy=[1:M*ien]/(M*ien)*100;
% xx1=sort(10*log10(abs(pwr1)));   % h11
xx1=sort(pwr1);   % h11
xxm1=xx1(round(M*ien/2));
xx1=xx1-xxm1;
hold on
semilogy(xx1,yy,'k','LineWidth',2)   % h11
axis([xmin xmax ymin ymax]);
set(gca, 'FontSize', 12,'FontName','Times New Roman')
title('CDF of Channel Response','FontSize',16,'FontName','Times New Roman','Color','k')
xlabel('Normalized Received Power [dB]','FontSize',14,'FontName','Times New Roman','Color','k')
ylabel('Cumulative Percentage [%]','FontSize',14,'FontName','Times New Roman','Color','k')
% h=legend('Rayleigh','h11','Location','SouthEast');
% set(h, 'FontSize', 12)
grid off
toc
pause
```

Sub-Program: MEASURE_SG_CONTINUOUS.m

```
% ****************************************************************
%          Measurement program of Fading Emulator
%                 Signal Generator MG3710A Anritsu
%                     made in 2016/08/02
%                            K.Li
% ****************************************************************
function
[md,xpre,M1,M2,zend,mdire,N,ofs,psel,iniph,qsel,vhran,ien,dkp1,ukp1,azdis,ksel,y1,y2,K,cx,sx,gx,px,...
    pl5,ph5,eig,fnamep,kq1,fnameq,myadrs2,sgadrs,ber,freqset,mfreq]=...

MEASURE_SG_CONTINUOUS(md,xpre,M1,M2,zend,mdire,N,ofs,psel,iniph,qsel,vhran,ien,azdis,ksel,y1,y2,K,cx,sx,g
x,px,...
    pl5,ph5,eig,dkp1,ukp1,fnamep,kq1,fnameq,myadrs2,sgadrs,ber,freqset,mfreq);

myadrs2=1;                    % computer
sgadrs=3;                     % signal generator (MG3710A)
clc
disp(' ')
M=216;
zend=4.32;
```

```
level=-63.2;

% Measured Direction
disp(' ------------------------')
disp('    Bilateral MIMO OTA   ')
disp('    Measured Direction   ')
disp(' ------------------------')
disp('   downlink         <21> ')
disp('   uplink           <12> ')
disp(' ------------------------')
md=READX(md);

% Measured Frequency
disp(' --------------------------')
disp('     Measured Frequency    ')
disp(' --------------------------')
disp('   926MHz              <1> ')
disp('   950MHz              <2> ')
disp('   2000MHz             <3> ')
disp(' --------------------------')
mfreq=READX(mfreq);

if mfreq==1
    if freqset~=0.926
        disp(' -----------------------------------------')
        disp('  Caution !!!   Setup of VNA is different ')
        disp(' -----------------------------------------')
        pause(3)
        return
    end
    end

clc
disp(' ')
% XPR
disp(' ---------------')
disp('    XPR in dB   ')
disp(' ---------------')
xpre=READX(xpre);
xpr=10^(xpre/10);

% Number of Samples during Movement
disp(' -----------------------------------')
disp('  Number of Samples during Movement ')
disp(' -----------------------------------')
M=READX(M);


% Mobile Moving Distance in Wavelength
disp(' --------------------------------------')
disp('  Mobile Moving Distance in Wavelength ')
disp(' --------------------------------------')
zend=READX(zend);

% Tx power start
disp(' --------------------------------------')
disp(' --------------------------------------')
disp('        Tx power start                 ')
disp(' --------------------------------------')
level=READX(level);

% Mobile Moving Directions
disp(' ------------------------------------')
```

```
disp('  Mobile Moving Directions in degree ')
disp(' ----------------------------------')
mdire=READX(mdire);
mdir=mdire*pi/180;

clc
disp(' ')
% Number of Scatterers in Azimuth
disp(' --------------------------------')
disp('  Number of Scatterers in Azimuth ')
disp(' --------------------------------')
N=READX(N);

% Offset Angle of Scatterers in degree
disp(' --------------------------------------')
disp('  Offset Angle of Scatterers in degree ')
disp('     (plus sign for the CCW rotation)  ')
disp(' --------------------------------------')
ofs=READX(ofs);



% -------------------------------------------
%       Initial Phase
% -------------------------------------------
clc
disp(' ')
disp(' -------------------------------------------------------')
disp('  Use of Random Data for Initial Phase of Scatterers <1>')
disp('  Use of File Data for Initial Phase of Scatterers   <2>')
disp(' -------------------------------------------------------')
psel=READX(psel);

if psel==1
    % Initial Phase of Scatterers
    disp(' ----------------------------')
    disp('  Initial Phase of Scatterers ')
    disp(' ----------------------------')
    disp('  Zero                  <1> ')
    disp('  Random                <2> ')
    iniph=READX(iniph);
end

disp(' ---------------------------------------------')
disp('  Use of Random Data for Polarization Phase <1>')
disp('  Use of File Data for Polarization Phase   <2>')
disp(' ---------------------------------------------')
qsel=READX(qsel);

if qsel==1
    disp(' -------------------')
    disp('  Polarization Phase ')
    disp(' -------------------')
    disp('  Zero          <1> ')
    disp('  Random        <2> ')
    vhran=READX(vhran);
end

%-------------------------------------------------------------------------
%                Start or Escape
% -------------------------------------------------------------------------
esc=0;
clc
```

```
disp(' ')
disp(' ------------------------')
disp('    If Start, Hit Return   ')
disp('      (999 for Escape)     ')
disp(' ------------------------')
esc=READX(esc);
if esc==999
    return
end
tic;

% -----------------------
%    SG(MG3710A)
% -----------------------
gsg=gpib('ni',myadrs2,sgadrs);   % Board index myadrs(0) & Primary adress spadrs(8)
fopen(gsg)                      % Connect to the instrument
set(gsg,'EOSMode','read&write') % Assert the EOI line
set(gsg,'EOSCharCode','CR')
fprintf(gsg,'SOUR:POW %g',level)

for M1=1:1:1;
    % ----------------------------------------------------------
    %             Set up the DA converter
    % ----------------------------------------------------------
    ao0=0;
    ao1=0;
    ao2=0;
    ao3=0;
    ao4=0;
    ao5=0;
    ao6=0;
    ao7=0;
    ao8=0;
    ao9=0;
    ao10=0;
    ao11=0;
    ao12=0;
    ao13=0;


    daqhwinfo('contec')
    ao=analogoutput('contec','AIO001');
    addchannel(ao,0)
    addchannel(ao,1)
    addchannel(ao,2)
    addchannel(ao,3)
    addchannel(ao,4)
    addchannel(ao,5)
    addchannel(ao,6)
    addchannel(ao,7)
    addchannel(ao,8)
    addchannel(ao,9)
    addchannel(ao,10)
    addchannel(ao,11)
    addchannel(ao,12)
    addchannel(ao,13)

    pause(1);
    for in=1:1:14
        v(in)=0;
    end

    z=0:zend/(M-1):zend;  % mobile locations from 0 to zend in wavelength
```

```
    % ------------------------------------------------------------------------
    %             Measurement Start
    % ------------------------------------------------------------------------
    for ie=1:ien
        c1=round(ofs:360/N:360-360/N+ofs);
        for i=1:N
            if c1(i)<0
                c1(i)=c1(i)+360;
            end
            if c1(i)>360
                c1(i)=c1(i)-360;
            end
        end

        if md==21   %downlink
            if psel==1   % (Random Data)
                if iniph==1                    % zero initial phase distribution
                    dkp1=ones(1,N);
                    A1s=dkp1;
                elseif iniph==2                % random initial phase distribution
                    dkp1=rand(1,N);
                    A1s=exp(j*2*pi*dkp1);
                end
            elseif psel==2   % (File Data)
                A1s=exp(j*2*pi*dkp1);
            end

        end

        if qsel==1   % (Random Data)
            if vhran==1                    % zero phase
                kq1=ones(1,N);
                phrr1=kq1;
            else                           % random phase
                kq1=rand(1,N);
                phrr1=exp(j*2*pi*kq1);
            end
        elseif qsel==2   % (File Data)
            phrr1=exp(j*2*pi*kq1);
        end


        if azdis==1        % uniform source distribution in azimuth (Clarke model)
            A1=A1s;
        end
        hbar=waitbar(0,'Now Mobile is Moving to...');
        fprintf(gsg,'BERT:LOG:CLEar')
        fprintf(gsg,'BERT:TBIT 200000')
        fprintf(gsg,'BERT:RSYNc:COUN:ACT KEEP')
        for ir=1:M
            waitbar(((ie-1)*M+ir)/(M*ien));
            for i=1:1:N;
                r=A1*exp(j*(2*pi*z(ir)*cos((c1(i)-zend)*pi/180)));            % amplitude of i-th
antenna
                pha=angle(r)+pi;                                         % phase of i-th phaser
                v(i)=0.0659*(pha(i).^3)-0.8360*(pha(i).^2)+4.4370*pha(i)-2.2930;
                if v(i)<0
                    v(i)=0;
                elseif v(i)>10
                    v(i)=10;
                end
            end
```

```
            % --------------------------------------------------------------
            %             control the output voltage of DA converter
            % --------------------------------------------------------------
            ao0=v(1);
            ao1=v(2);
            ao2=v(3);
            ao3=v(4);
            ao4=v(5);
            ao5=v(6);
            ao6=v(7);
            ao7=v(8);
            ao8=v(9);
            ao9=v(10);
            ao10=v(11);
            ao11=v(12);
            ao12=v(13);
            ao13=v(14);
            putdata(ao,[ao0,ao1,ao2,ao3,ao4,ao5,ao6,ao7,ao8,ao9,ao10,ao11,ao12,ao13]);
            start(ao);
            pause(0.04);
            % --------------------------------------------------------------
            %             Reading Data from SG
            % --------------------------------------------------------------
            fprintf(gsg,'INIT:BERT');
            pause(6)
            fprintf(gsg,'FETC:BERT:ERR:RATE? EP')
            out=fscanf(gsg);
            fprintf(gsg,'ABOR:BERT');
            ber(ir)=eval(out)
            R=rem(ir,18)
            if R==0
                clc
                disp('Change Arm Angle')
                pause;
            else
            end
        end  % for ir=1:M
        close(hbar);
    end  % for ie=1:ien
    DUMP_1TX_1RX_BER_Continuous(ber,ien,M,zend,level);
end
%DA converter stop
ao0=0;
ao1=0;
ao2=0;
ao3=0;
ao4=0;
ao5=0;
ao6=0;
ao7=0;
ao8=0;
ao9=0;
ao10=0;
ao11=0;
ao12=0;
ao13=0;
putdata(ao,[ao0,ao1,ao2,ao3,ao4,ao5,ao6,ao7,ao8,ao9,ao10,ao11,ao12,ao13]);
start(ao);
fclose(gsg);
clear gsg
```

```
% -------------------------------------------------------------------------
%     Measurement Stop
% -------------------------------------------------------------------------
for ie=1:ien
    for ir=1:M
        x((ie-1)*M+ir)=(ie-1)*M+ir;
    end
end
pause(0.2)
toc
% -------------------------------------------------------------------------
%     Instantaneous Response
% -------------------------------------------------------------------------
scrsz = get(0,'ScreenSize');
h1=figure('Position',[10 scrsz(4)/2.4 scrsz(3)/2.05 scrsz(4)/2.05]);
ber1=0.01*(ber);
tber=mean(ber);
semilogy(x,ber1,'k','LineWidth',2.5);   % h11
title('BER Characteristic','FontSize',16,'FontName','Times New Roman','Color','k')
xlabel('Traveling Distance [Wavelength]','FontSize',14,'FontName','Times New Roman','Color','k')
ylabel('Instantaneous Bit Error Rate','FontSize',14,'FontName','Times New Roman','Color','k')
% h=legend('h11','Location','SouthEast');
% set(h, 'FontSize', 12)
grid off
xt=[0; ien*M/10; ien*M/10*2; ien*M/10*3; ien*M/10*4; ien*M/10*5; ien*M/10*6; ien*M/10*7;...
    ien*M/10*8; ien*M/10*9; ien*M/10*10];
set(gca, 'Xtick', xt)
xtl=[0; zend/10; zend/10*2; zend/10*3; zend/10*4; zend/10*5; zend/10*6; zend/10*7;...
    zend/10*8; zend/10*9; zend/10*10];
set(gca, 'XtickLabel', xtl)
set(gca, 'FontSize', 12,'FontName','Times New Roman')
ymin=10^-4;
ymax=1;
xpos=0.05*M*ien;
ypos=ymin+0.26*(ymax-ymin);
fsize=12;
A=sprintf('%6.1f',tber);
hm=num2str(A);
tx=strcat('BER_m =',hm,'%');
text(xpos,ypos,tx,'FontSize',fsize,'FontName','Times New Roman');

axis([0 ien*M 10^-6 1]);
```

Appendix C. Setup of BER Detection

C.1. BER Measurement Devices

Fig. C.1 shows the configuration of BER measurement devices. The transmitting and receiving side is connect using a coaxial cable, indicating a simple case of wired measurement. When the BER-OTA testing is carried, the Tx side will be connected to the surrounding scatterers while the Rx side will be connected to the DUT antenna, as the setup shown in Fig. 6.2. The setup of FSK module and signal generator is shown as below.

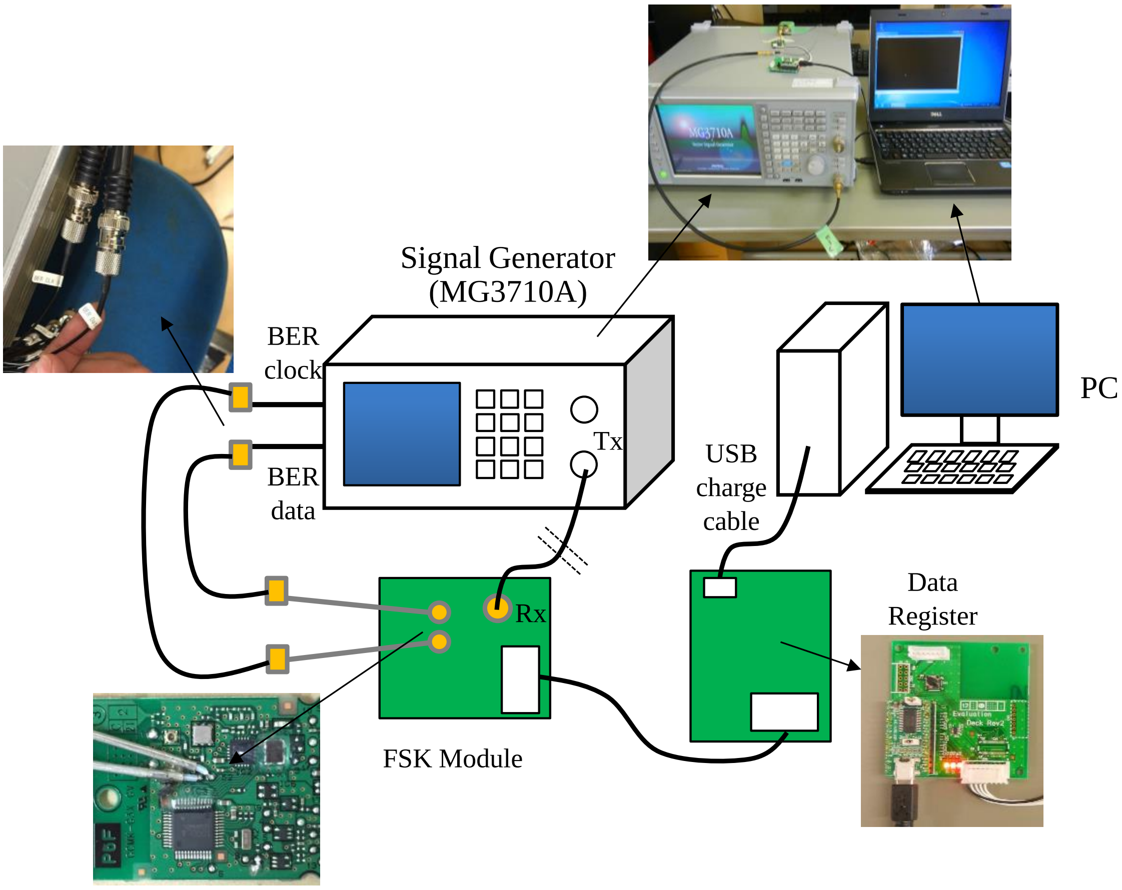

Fig. C.1 Configuration of BER measurement without using fading emulator

C.2. Setup of FSK Wireless Module

- Start Tera Term and select the serial port
- Read the configuration file (UART 3)
- Enter the password (AP0743563127SDBU)
- When “DOK!” or “? 000” is displayed, shift to inspection mode
- Enter the following characters without using back space

```
TC11=01AA
T121=02000A640147AE0291FF18BC0A000C0404100295E5720000000
00000000000FFFFFFFF0A3D0C3320764B00
TD31=3404
TD31=3510
TD31=3304
TD31=3602
TD31=3795
TD31=38E5
```

C.3. Setup Procedure of Signal Generator

- Copy the data file: Press the button as following procedure
  - Mode: Copy (F6): Drive: D
  - Focus Pattern (F6): Copy Pattern
- Read the data file
  - Load: Update Info (F3): Focus Pattern (F2)
  - Load Pattern (F6): Confirm overwriting
  - Select: Focus Package (F2): Select

C.4. Setup Procedure for BER Measurement

- Press the button as following procedure
  - Aux Pctn: BER
  - Count Mode: Data: Enter the number of measurement bits
  - Measure Mode (F4): Endless
  - Data Type: PN9

C.5. BER Measurement

- Press the button as following procedure
  - Level: Change the output power
  - Aux Pctn: BER: Start BER test
  - Stop BER test
  - Make a note of the BER numbers and return

Note that C.5 is the situation of manual measurement of BER. When the BER-OTA testing using the combined devices of FSK module, signal generator and fading emulator is conducted, the measurement is automatically controlled by using the measurement program in [Apx. B].

Thesis for Degree Application

[1] Kun LI, Kazuhiro HONDA, and Koichi OGAWA, "Rice Channel Realization for BAN Over-The-Air Testing Using a Fading Emulator with an Arm-Swinging Dynamic Phantom," IEICE Trans. Commun., Vol. E98-B, No. 4, pp. 543–553, Apr. 2015.

[2] Kun LI, Kazuhiro HONDA, and Koichi OGAWA, "Three-Dimensional Over-The-Air Assessment for Vertically Arranged MIMO Array Antennas," IEICE Trans. Commun., Vol. E99-B, No.1, pp. 167–176, Jan. 2016.

[3] Kun Li, Kazuhiro Honda, and Koichi Ogawa, "Dual-Discrete Processing for Bit-Error-Rate OTA Testing in Shadowing-Fading BAN Channel," IEEE Antennas and Wireless Propaga. Lett., vol., pp. ***–***, 2017. (accepted)

[4] Kun Li, Kazuhiro Honda, and Koichi Ogawa, "Weighted-polarization wearable antenna for on-body dynamic channels," IEICE Communications Express, Vol. 5, No. 6, pp. 189–194, Jun. 2016.

[5] Kun Li, Kazuhiro Honda, and Koichi Ogawa, "An Analysis of the Body Proximity Cross-Polarization Power Ratio in a Human Walking Motion," IEICE, Vol. J99-B, No. 7, pp. 544–547, Jul. 2016. (in Japanese)

Publication

Journal Paper

[1] K. Honda, **K. Li**, and K. Ogawa, “Shadowing-Fading BER Characterization of a BAN Diversity Antenna Based on Statistical Measurements of the Human Walking Motion,” IEICE Trans. Commun., Vol. E96-B, No. 10, pp. 2530–2541, Oct. 2013.

[2] **K. Li**, K. Honda, and K. Ogawa, “Rice Channel Realization for BAN Over-The-Air Testing Using a Fading Emulator with an Arm-Swinging Dynamic Phantom,” IEICE Trans. Commun., Vol. E98-B, No. 4, pp. 543–553 , Apr. 2015.

[3] K. Honda, K. Kaga, **K. Li**, and K. Ogawa, “A simultaneous conjugate-matching algorithm for N-element array antennas,” IEICE Communications Express, Vol. 4, No. 11, 327–332, Dec. 2015.

[4] **K. Li**, K. Honda, and K. Ogawa, “Three-Dimensional Over-The-Air Assessment for Vertically Arranged MIMO Array Antennas,” IEICE Trans. Commun., Vol. E99-B, No.1, pp. 167–176, Jan. 2016.

[5] K. Honda, **K. Li**, and K. Ogawa, “Weighted-Polarization Wearable MIMO Antenna with Three Orthogonally Arranged Dipoles Based on RF Signal Processing,” IEICE Trans. Commun., Vol. E99-B, No.1, pp. 58–68, Jan. 2016.

[6] **K. Li**, K. Honda, and K. Ogawa, “Weighted-polarization wearable antenna for on-body dynamic channels,” IEICE Communications Express, Vol. 5, No. 6, pp. 189–194, Jun. 2016.

[7] K. Honda, T. Yamashita, and **K. Li**, “High efficiency mw-band dielectric resonator rectenna using distributed capacitors,” IEICE Communications Express, Vol. 5, No. 8, pp. 254–259, Aug. 2016.

[8] K. Honda, and **K. Li**, “Optimum phase shift applied to weighted-polarization MIMO antenna in various use scenarios,” IEICE Communications Express, Vol. 5, No. 8, pp. 266–271, Aug. 2016.

[9] K. Honda and **K. Li**, “A method of controlling the base station correlation for MIMO-OTA based on Jakes model,” IEICE Communications Express, Vol. 5, No. 9, pp. 297–302, Jun. 2016.

[10] **K. Li**, K. Honda, and K. Ogawa, “An Analysis of the Body Proximity Cross-Polarization Power Ratio in a Human Walking Motion,” IEICE, Vol. J99-B, No. 7, pp. 544–547, Jul. 2016. (in Japanese)

[11] K. Honda and **K. Li**, "Three-dimensional MIMO-OTA calibration to achieve the Gaussian angular power spectra in elevation," IEICE Communications Express, Vol. 5, No. 10, pp. 394–400, Oct. 2016.

[12] **K. Li**, K. Honda, and K. Ogawa, "Dual-Discrete Processing for Bit-Error-Rate OTA Testing in Shadowing-Fading BAN Channel," IEEE Antennas and Wireless Propaga. Lett., vol., pp. ***–***, 2017. (accepted)

[13] H. Kirino, K. Honda, **K. Li**, and Koichi Ogawa, "Simplified Equations for Calculating Wavelengths in a Fast and Slow Wave Waffle-iron Ridge Guide and their Application to the Design of Array Antennas," IEICE Trans. Commun., Vol. E100-B., No. 2, pp. 219–226, Feb. 2017.

[14] K. Honda, T. Kitamura, **K. Li**, and K. Ogawa, "Regression-Based Channel Capacity for the Evaluation of 2 x 2 MIMO Antennas," IEICE Trans. Commun., Vol. E100-B, No. 2, pp. 323–335, Feb. 2017.

[15] K. Omote, K. Honda and **K. Li**, "Decoupling stub-loaded parallel dipole array with orthogonal polarization," IEICE Communications Express, Vol. 6, No. 2, pp. 97–102, Feb. 2017.

[16] H. Kirino, K. Honda, **K. Li** and K. Ogawa, "A Phase Shifter using Waffle-iron Ridge Guides and its Application to a Beam Steering Antenna," IEICE Communications Express, Vol. **, No. **, pp. ***–***, ***. 2017. (accepted)

[17] T. Maekawa, K. Honda, **K. Li**, and K. Ogawa: "A Method of Reducing the Internal Interference Noise in Intra-EMC using Decoupling Techniques", IEICE Vol. J**-B, No. **, pp. ***–***, ***. 2017. (submitted, in Japanese)

[18] K. Honda, **K. Li**, and K. Ogawa: "An Optimum Impedance Matching Circuit for Maximizing the Bandwidth Averaged Channel Capacity of a MIMO Dipole Array", IEICE Vol. J**-B, No. **, pp. ***–***, ***. 2017. (submitted, in Japanese)

[19] K. Honda, **K. Li**, K. Ogawa, Y. Koyanagi, H. Sato, and R. Miura: "A Method of 2×2 MIMO Throughput OTA Testing Using a Commercial LTE Mobile Terminal under the Cluster Propagation Environment", IEICE Vol. J**-B, No. **, pp. ***–***, ***. 2017. (submitted, in Japanese)

[20] H. Kirino, K. Honda, **K. Li**, and Koichi Ogawa, "A Fast and Slow-wave Combined Mode Waffle-iron Ridge Guide for Array Antenna Applications," IEICE Trans. Commun., Vol. E***-B., No. **, pp.

–, ***. 2017. (submitted)

[21] **K. Li**, K. Honda, and Koichi Ogawa, "Human Body - Incident Wave Mutual Interactions of a Browsing Handset MIMO Antenna in Street Microcell Environments," IEICE Trans. Commun., Vol. E***-B., No. **, pp. ***–***, ***. 2017. (submitted)

International Conference

[1] **K. Li**, K. Honda, and K. Ogawa: "Shadowing-Fading BER Characterization of BAN Antennas Based on Realistic Walking Models," Medical Information and Communication Technology (ISMICT), 2013 7th International Symposium on, pp. 183–187, Tokyo, Japan, Mar. 2013.

[2] K. Honda, **K. Li**, and K. Ogawa: "Impact of the Human Walking Motion on BAN Diversity Effects," Electromagnetic Theory (EMTS), Proceedings of 2013 URSI International Symposium on, pp. 1136–1139, Hiroshima, Japan, May 2013.

[3] K. Ogawa, **K. Li**, and K. Honda: "BAN-OTA Testing Using a Fading Emulator with an Arm-Swinging Dynamic Phantom," 2013 IEEE Antennas and Propagation Society International Symposium (APSURSI), pp. 2187–2188, Orlando, USA, July 2013.

[4] **K. Li**, K. Honda, and K. Ogawa: "K-factor Dependent Multipath Characterization for BAN-OTA Testing Using a Fading Emulator," Antennas & Propagation (ISAP), 2013 Proceedings of the International Symposium on, vol. 1, pp. 580–583, Nanjing, China, Oct. 2013.

[5] K. Ogawa, **K. Li**, and K. Honda: "BAN-OTA Testing Using an Arm-Swinging Dynamic Phantom," IEEE MTT-S International Microwave Workshop Series on RF and Wireless Technologies for Biomedical and Healthcare Applications (IMWS-Bio 2013, Singapore) Symp. Digest, TP2-1, pp. 1–2, Dec. 2013. **(Invited Paper)**

[6] K. Kaga, **K. Li**, K. Honda, and K. Ogawa: "A Sequential Automatic Impedance-Matching Algorithm to Achieve Simultaneous Complex-Conjugate Condition in Multi-element Antennas," Electromagnetics (iWEM), 2014 IEEE International Workshop on, pp. 24-25, Sapporo, Japan, Aug. 2014. **(Finalist Student Paper Contest)**

[7] **K. Li**, K. Honda, and K. Ogawa: "Three-dimensional OTA Design Considerations Based on MIMO Antenna Radiation and Multipath Interactions," Electromagnetics (iWEM), 2014 IEEE International Workshop on, pp. 215–216, Sapporo, Japan, Aug. 2014.

[8] **K. Li**, K. Honda, and K. Ogawa: "Over-The-Air Assessment for 2-dimensional Arrangement MIMO Array Antennas," General Assembly and Scientific Symposium (URSI GASS), 2014 XXXIth URSI, Beijing, China, Aug. 2014.

[9] K. Honda, **K. Li**, and K. Ogawa: "An 8×8 MIMO 3-axis Weighted Polarization Active Antenna for Wearable Radio Applications," General Assembly and Scientific Symposium (URSI GASS), 2014 XXXIth URSI, Beijing, China, Aug. 2014.

[10] **K. Li**, K. Honda, and K. Ogawa: "Channel Capacity Experiment of a Polarization Controlled MIMO Antenna for Wearable Applications," IEEE Progress in Electromagnetic Research Symposium (PIERS 2014), PIERS Proceedings, pp. 2170–2174, Guangzhou, China, Aug. 2014.

[11] **K. Li**, K. Honda, and K. Ogawa: "On-body Polarization-controlled Active Antenna to Enhance Signal Power in Human Dynamic Channels," Antennas and Propagation (ISAP), 2014 International Symposium on, pp. 93–94, Kaohsiung, Taiwan, Dec. 2014. **(Finalist Student Paper Contest)**

[12] **K. Li**, K. Honda, and K. Ogawa: "Experiments of a Polarization-controlled Active Antenna to Enhance BAN On-body Link in Human Dynamic Channels," 2015 9th International Symposium on Medical Information and Communication Technology (ISMICT), pp. 117–120, Kamakura, Japan, Mar. 2015.

[13] K. Honda, T. Kabeya, K. Karitani, **K. Li**, K. Ogawa, Y. Koyanagi, H. Sato, and R. Miura: "A Base Station Correlation-Controlled Bilateral Emulator for MIMO-OTA," 2015 IEEE International Symposium on Antennas and Propagation & USNC/URSI National Radio Science Meeting, pp. 294–295, Vancouver, Canada, July 2015.

[14] **K. Li**, Y. Ishisaka, K. Honda, and K. Ogawa: "Dual-Polarized Turn-Style Patch Antenna for Wearable Applications," 2015 IEEE International Symposium on Antennas and Propagation & USNC/URSI National Radio Science Meeting, pp. 641–642, Vancouver, Canada, July 2015.

[15] K. Omote, H. Sato, **K. Li**, K. Honda, Y. Koyanagi, and K. Ogawa:

"Disk-Loaded Monopole Stacked with Patch Antenna," 2015 IEEE International Symposium on Antennas and Propagation & USNC/URSI National Radio Science Meeting, pp. 709–710, Vancouver, Canada, July 2015.

[16] K. Honda, T. Kabeya, K. Karitani, **K. Li**, K. Ogawa, Y. Koyanagi, H. Sato, and R. Miura: "A Polarization-Controlled MIMO Antenna with an Optimum Phase Shift in Accordance with Various Use Scenarios," 2015 IEEE International Symposium on Antennas and Propagation & USNC/URSI National Radio Science Meeting, pp. 1234–1235, Vancouver, Canada, July 2015.

[17] **K. Li**, K. Honda, and K. Ogawa: "Analysis of the Body Proximity Cross-Polarization Power Ratio in a Human Walking Motion," Electromagnetics: Applications and Student Innovation Competition (iWEM), 2015 International Workshop on, Hsinchu, Taiwan, Nov. 2015.

[18] K. Omote, H. Sato, **K. Li**, K. Honda, Y. Koyanagi and K. Ogawa: "Three-Axis Decoupling Stub-Loaded Parallel Dipole Array with Tri-Orthogonal Polarization Directivity," Electromagnetics: Applications and Student Innovation Competition (iWEM), 2015 International Workshop on, Hsinchu, Taiwan, Nov. 2015.

[19] H. Sato, K. Omote, **K. Li**, K. Honda, Y. Koyanagi, and K. Ogawa: "The 3-axis polarization antenna using Disk-Loaded Monopole stacked with Patch Antenna in PCB," 2015 Asia-Pacific Microwave Conference (APMC), vol. 1, pp. 490–492, Nanjing, China, Dec. 2015.

[20] **K. Li**, K. Honda, and K. Ogawa: "Analysis of the Body Proximity Cross-Polarization Power Ratio in a Human Walking Motion," 2015 Asia-Pacific Microwave Conference (APMC), vol. 2, pp. 780–782, Nanjing, China, Dec. 2015.

[21] K. Honda, K. Murata, **K. Li**, K. Ogawa, Y. Koyanagi, H. Sato, and R. Miura: "Bit-Error-Rate Over-The-Air Testing of Weighted-Polarization BAN Antenna Using an Arm-Swinging Dynamic Phantom," The 55.th Annual Conference of Japanese Society for Medical and Biological Engineering (JSMBE55), 1OS4-3-5, Toyama, Japan, Apr. 2016. **(Invited paper)**

[22] T. Maekawa, **K. Li**, K. Honda, and K. Ogawa: "Proposal of decoupling technique for intra-EMC," 2016 Asia-Pacific International Symposium on Electromagnetic Compatibility (APEMC), Shenzhen, May. 2016.

Meeting, Technical Reports

[1] K. Honda, **K. Li**, and K. Ogawa: "Shadowing-Multipath Analysis of a BAN Diversity Antenna Based on Statistical Dynamic Measurements of the Human Walking Motion", IEICE Technical Report, AP2012-155, pp. 177–182, Jan. 2013. (in Japanese)

[2] K. Ogawa, **K. Li**, and K. Honda: "Over-The-Air Testing of BAN antennas using Dynamic Phantom and Fading Emulator," MICT2013-1, pp. 1–21, May 2013. **(Invited paper)**

[3] **K. Li**, K. Honda, and K. Ogawa: "BAN-OTA Testing Using a Fading Emulator Considering the Variation of K-factor Due to the Dynamic Characteristics of Human Motion", IEICE Technical Report, AP2013-90, pp. 19–24, Oct. 2013.

[4] K. Honda, **K. Li**, and K. Ogawa: "An Analysis of the Channel Capacity for an 8×8 MIMO 3-Axis Weighted-Polarization Active Antenna Mounted on the Wrist", IEICE Technical Report, AP2013-173, pp. 39–44, Feb. 2014. (in Japanese)

[5] K. Ogawa, K. Honda, and **K. Li**: "OTA Assessment for 2-Dimensional Arrangement MIMO Array Antennas", IEICE Technical Report, AP2013-196, pp. 63–68, Mar. 2014. (in Japanese)

[6] K. Honda, **K. Li**, and K. Ogawa: "A Calibration Method for the OTA Testing of Active MIMO Antennas", IEICE Technical Report, AP2014-60, pp. 67–72, Jul. 2014. (in Japanese)

[7] K. Honda, T. Kabeya, K. Karitani, **K. Li**, K. Ogawa, Y. Koyanagi, H. Sato, and R. Miura: "A Bilateral MIMO-OTA System for the Combined Antenna Evaluation Considering Uplink and Downlink Channels", IEICE Technical Report, AP2014–74, pp. 13-18, Aug. 2014. (in Japanese)

[8] **K. Li**, K. Honda, and K. Ogawa: "Experiments of a Polarization-controlled Antenna to Enhance BAN On-body Link in Human Dynamic Channels", IEICE Technical Report, MICT2014-46, pp. 1–6, Oct. 2014.

[9] K. Honda, T. Kabeya, K. Karitani, **K. Li**, K. Ogawa, Y. Koyanagi, H. Sato, and R. Miura: "A Base Station Correlation-Controlled Bilateral Emulator for MIMO-OTA", IEICE Technical Report, AP2014-190, pp. 21–26, Feb. 2015. (in Japanese)

[10] K. Omote, H. Sato, **K. Li**, K. Honda, Y. Koyanagi, and K. Ogawa: "Disk-Loaded Monopole Stacked with Patch Antenna", IEICE Technical Report, AP2014-212, pp. 7–12, Mar. 2015. (in Japanese)

[11] K. Honda, K. Karitani, **K. Li**, K. Ogawa, Y. Koyanagi, H. Sato, and R. Miura: “4×4 MIMO Channel Capacity Experiment Using Bilateral Emulator for MIMO-OTA”, IEEJ Technical Report, IM-15-022, pp. 19–24, Jul. 2015. (in Japanese)

[12] **K. Li**, K. Honda, K. Ogawa: “An Analysis of the Body Proximity Cross-Polarization Power Ratio in a Human Walking Motion”, IEICE Technical Report, AP2015-69, pp.49–54, Aug. 2015.

[13] K. Omote, H. Sato, **K. Li**, K. Honda, Y. Koyanagi, and K. Ogawa: “Decoupling Stub-Loaded Parallel Dipole Array with Orthogonal Polarization Directivity”, IEICE Technical Report, AP2015-71, pp. 61–66, Aug. 2015. (in Japanese)

[14] **K. Li**, K. Honda, K. Ogawa: “Bit-Error-Rate OTA Testing of BAN Antennas Based on Shadowing-Fading Hybrid Effects”, IEICE Technical Report, MICT2015-49, pp. 45–50, Jan. 2016.

[15] K. Honda, T. Kabeya, K. Karitani, **K. Li**, K. Ogawa, Y. Koyanagi, H. Sato, and R. Miura: “A Method of Realizing Gaussian Angular Power Spectra in Elevation Using a Three-Dimensional Fading Emulator”, IEICE Technical Report, AP2015-197, pp. 37–42, Feb. 2016. (in Japanese)

[16] K. Honda, T. Kabeya, K. Karitani, **K. Li**, K. Ogawa, Y. Koyanagi, H. Sato, and R. Miura: “A Calibration Method for Measuring the MIMO Channel Capacity using the Three-Dimensional MIMO-OTA Evaluation Apparatus”, IEICE Technical Report, AP2015-215, pp. 63–68, Mar. 2016. (in Japanese)

[17] T. Maekawa, **K. Li**, K. Honda, and K. Ogawa: “A Method of Reducing the Internal Interference Noise in Intra-EMC using Decoupling Techniques,” IEICE Technical Report, EMCJ2016-45, pp. 7–12, July. 2016. (in Japanese)

[18] **K. Li**, K. Honda, K. Ogawa: “OTA Assessment for BAN Diversity Antennas in Human Dynamic Channel”, IEICE Technical Report, MICT2016-14, pp. 13–18, July. 2016.

[19] **K. Li**, K. Honda, K. Ogawa: “OTA Assessment of BAN Diversity Antenna Using a Bias Switch”, IEICE Technical Report, AP2016-79, pp. 63–68, Aug. 2016.

[20] K. Honda, R. Takebayashi, **K. Li**, K. Ogawa: “Analysis of Received Signal Power in On-Body Dynamic Channel using Statistics Data of Human Walking Motion”, IEICE Technical Report, MICT2016-71, pp. 35–40, Jan. 2017. (in Japanese)

[21] K. Honda, **K. Li**, K. Ogawa: “An Implementation Method of 4×4 Correlation Matrix of Base Station MIMO Antenna for Bilateral

OTA", IEICE Technical Report, AP2016-164, pp. 43–48, Feb. 2017. (in Japanese)

[22] D. Iwamoto, K. Honda, **K. Li**, K. Ogawa: "XPR Measurement Accuracy Improvement of the 3D-OTA Device Using the Slot Antenna", IEICE Technical Report, AP2017-**, pp. ***–***, Apr. 2017. (in Japanese)

General Conference in Japan

[1] K. Honda, **K. Li**, and K. Ogawa: "BER Analysis of BAN Diversity Antennas Based on Statistical Measurements of the Human Walking Motion", IEICE Society Conference, No. BS-7-6, Sep. 2012. (in Japanese)

[2] **K. Li**, K. Honda, K. Ogawa: "BER Degradation of QPSK Signals for BAN Antennas due to the Arm Swinging", IEICE Society Conference, No. B-1-128, Sep. 2012.

[3] K. Honda, **K. Li**, and K. Ogawa: "Measurements of the K-factor in Indoor Propagation Environments Using BAN Phantoms", IEICE General Conference, No. B-1-40, Mar. 2013. (in Japanese)

[4] **K. Li**, K. Honda, and K. Ogawa: "BAN-OTA Testing Using a Fading Emulator with a Dynamic Phantom", IEICE General Conference, No. BS-8-8, Mar. 2013.

[5] K. Honda, **K. Li**, and K. Ogawa: "Effects of Floor on the Radiation Pattern Characteristics of BAN antennas", IEICE Society Conference, No. B-1-40, Mar. 2013. (in Japanese)

[6] **K. Li**, K. Honda, K. Ogawa: "K-factor Dependent Multipath Characterization for BAN-OTA Testing Using a Fading Emulator", IEEE Nagoya Chapter, Midland Student Express 2013 Spring, S3-2, Apr. 2013.

[7] K. Honda, **K. Li**, and K. Ogawa: "BER Analysis of a BAN Antenna Mounted on the Wrist", IEICE Society Conference, No. BS-9-21, Sep. 2013. (in Japanese)

[8] **K. Li**, K. Honda, K. Ogawa: "K-factor Dependent Multipath Characterization for BAN-OTA Testing Using a Fading Emulator", IEICE Society Conference, No. BS-9-14, Sep. 2013.

[9] **K. Li**, K. Honda, K. Ogawa: "Enhancement of the Channel Capacity Degradation by a Handset Holding Angle Variation Using a 3-axis Weighted-Polarization MIMO Antenna", IEICE General Conference, No. B-1-65, Mar. 2014. (in Japanese)

[10] K. Honda, **K. Li**, and K. Ogawa: "A 3-Axis Weighted-Polarization

8×8 MIMO Antenna for Realizing Ultra High-Capacity Mobile Communications", IEICE General Conference, No. ABS-1-7, Mar. 2014. (in Japanese)

[11] K. Ogawa, K. Honda, and **K. Li**: "OTA Assessment for Two-Dimensional Arrangement MIMO Array Antennas", IEICE General Conference, No. B-1-237, Mar. 2014. (in Japanese)

[12] K. Honda, **K. Li**, and K. Ogawa: "A Calibration Method for the OTA Testing of Active MIMO Antennas", IEICE Society Conference, No. B-1-141, Sep. 2014. (in Japanese)

[13] K. Honda, T. Kabeya, K. Karitani, **K. Li**, K. Ogawa, Y. Koyanagi, H. Sato, and R. Miura: "A Figure-of-Merit for Designing MIMO Antennas Considering Uplink and Downlink Channels", IEICE Society Conference, No. B-1-138, Sep. 2014. (in Japanese)

[14] **K. Li**, K. Honda, and K. Ogawa: "On-body Polarization-controlled Active Antenna to Enhance Signal Power in Human Dynamic Channels", IEICE Society Conference, No. B-20-1, Sep. 2014.

[15] **K. Li**, K. Honda, and K. Ogawa: "Three-dimensional OTA Design Considerations Based on MIMO Antenna Radiation and Multipath Interactions", IEICE Society Conference, No. BS-1-9, Sep. 2014.

[16] K. Honda, T. Kabeya, K. Karitani, **K. Li**, K. Ogawa, Y. Koyanagi, H. Sato, and R. Miura: "A Polarization-Controlled MIMO Antenna Realizing an Optimum State in Accordance with Various Use Scenes", IEICE General Conference, No. B-1-214, Mar. 2015. (in Japanese)

[17] K. Honda, T. Kabeya, K. Karitani, **K. Li**, K. Ogawa, Y. Koyanagi, H. Sato, and R. Miura: "A Method of Controlling the Base Station Correlation for MIMO-OTA", IEICE General Conference, No. B-1-213, Mar. 2015. (in Japanese)

[18] K. Karitani, **K. Li**, K. Honda, and K. Ogawa: "Channel Capacity Experiment of Polarization-controlled MIMO Antenna Using Arm-swinging Dynamic Phantom", IEICE General Conference, No. B-1-133, Mar. 2015. (in Japanese)

[19] T. Kabeya, K. Karitani, **K. Li**, K. Honda, K. Ogawa, Y. Koyanagi, H. Sato, and R. Miura: "An Evaluation of the Mechanism of Throughput Reduction Using a Base Station Simulator", IEICE General Conference, No. B-1-179, Mar. 2015. (in Japanese)

[20] K. Omote, H. Sato, **K. Li**, K. Honda, Y. Koyanagi, and K. Ogawa: "Disk-Loaded Monopole Stacked with Patch Antenna", IEICE General Conference, No. B-1-152, Mar. 2015. (in Japanese)

[21] **K. Li**, Y. Ishisaka, K. Honda, and K. Ogawa: "Dual-Polarized Turn-style Patch Antenna for Wearable Applications", IEICE General Conference, No. B-20-13, Mar. 2015.

[22] K. Omote, H. Sato, **K. Li**, K. Honda, Y. Koyanagi, and K. Ogawa: "Decoupling Stub-Loaded Parallel Dipole Array with Orthogonal Polarization Directivity", IEICE Society Conference, No. B-1-30, Sep. 2015. (in Japanese)

[23] H. Sato, K. Omote, **K. Li**, K. Honda, Y. Koyanagi, and K. Ogawa: "A Three-axis Polarization Disk-Loaded Monopole Stacked with Patch Antenna Comprised of PCB", IEICE Society Conference, No. B-1-119, Sep. 2015. (in Japanese)

[24] K. Honda, K. Karitani, **K. Li**, K. Ogawa, Y. Koyanagi, H. Sato, and R. Miura: "A Method of Controlling 4×4 MIMO Base Station Correlations for MIMO-OTA", IEICE Society Conference, No. B-1-137, Sep. 2015. (in Japanese)

[25] K. Honda, K. Karitani, **K. Li**, K. Ogawa, Y. Koyanagi, H. Sato, and R. Miura: "Channel Capacity OTA Experiment of Polarization-controlled MIMO Antenna Based on the Optimum Phase Shift in Accordance with Various Use Scenes", IEICE Society Conference, No. B-1-138, Sep. 2015. (in Japanese)

[26] **K. Li**, K. Honda, and K. Ogawa: "Analysis of the Body Proximity Cross-Polarization Power Ratio in a Human Walking Motion", IEICE Society Conference, No. B-20-5, Sep. 2015.

[27] K. Karitani, **K. Li**, K. Honda, K. Ogawa, Y. Koyanagi, H. Sato, and R. Miura: "Throughput Variation Mechanism of Commercial LTE Smartphone 2 × 2 MIMO Antenna using OTA Measurement", IEEJ Hokuriku Branch General Conference, No. C-15, Sep. 2015. (in Japanese) **(Best Student Paper)**

[28] K. Omote, H. Sato, **K. Li**, K. Honda, Y. Koyanagi, and K. Ogawa: "Stub-loaded parallel dipole array for decoupling and orthogonal polarization", IEEJ Hokuriku Branch General Conference, No. C-14, Sep. 2015. (in Japanese)

[29] K. Honda, **K. Li**, K. Murata, and K. Ogawa: "A Method of BER-OTA Testing of Weighted-Polarization BAN Antenna Using an Arm-Swinging Dynamic Phantom", IEICE General Conference, No. B-20-1, Mar. 2016. (in Japanese)

[30] T. Maekawa, **K. Li**, K. Honda, and K. Ogawa: "Decoupling Technique for Reducing Internal Interference Noise for Intra-EMC," IEICE General Conference, No. B-4-49, Mar. 2016. (in Japanese)

[31] K. Omote, H. Sato, **K. Li**, K. Honda, Y. Koyanagi, and K. Ogawa: "MIMO Channel Capacity Measurement of Disk-Loaded Monopole Stacked with Patch Antenna", IEICE General Conference, No. B-1-221, Mar. 2016. (in Japanese)

[32] K. Honda, T. Kabeya, K. Karitani, **K. Li**, K. Ogawa, Y. Koyanagi, H. Sato, and R. Miura: "A Calibration Method for the Three-Dimensional MIMO-OTA Testing", IEICE General Conference, No. B-1-170, Mar. 2016. (in Japanese)

[33] K. Karitani, T. Kabeya, **K. Li**, K. Honda, K. Ogawa, Y. Koyanagi, H. Sato, and R. Miura: "A Throughput OTA Testing Using Weighted-Polarization MIMO Antenna", IEICE General Conference, No. B-1-169, Mar. 2016. (in Japanese)

[34] **K. Li**, T. Kabeya, K. Karitani, K. Honda, K. Ogawa, Y. Koyanagi, H. Sato, and R. Miura: "A Method of Realizing Gaussian Elevation Distribution for 3D-OTA", IEICE General Conference, No. B-1-180, Mar. 2016.

[35] **K. Li**, K. Murata, K. Honda, and K. Ogawa: "Bit-Error-Rate OTA Testing of BAN Antennas Based on Shadowing-Fading Hybrid Effects", IEICE General Conference, No. BS-1-15, Mar. 2016.

[36] **K. Li**, K. Murata, K. Honda, and K. Ogawa: "Bit-Error-Rate OTA Testing of BAN Antennas Based on Shadowing-Fading Hybrid Effects," 2016 10th International Symposium on Medical Information and Communication Technology (ISMICT), pp. 1-5, Worcester, USA, Mar. 2016. **(Invited paper)**

[37] K. Omote, **K. Li**, K. Honda, Y. Koyanagi, and K. Ogawa: "Measurement of Two-Element Stub-Loaded Parallel Dipole Array Antenna", IEEJ Hokuriku Branch General Conference, No. C-11, Sep. 2016. (in Japanese)

[38] Y. Tsuneyoshi, K. Omote, **K. Li**, K. Honda, Y. Koyanagi, and K. Ogawa: "Optimization of Phase Shift Value of DLMP Weighted-Polarization Antenna", IEEJ Hokuriku Branch General Conference, No. C-20, Sep. 2016. (in Japanese)

[39] K. Murata, **K. Li**, K. Honda, Y. Koyanagi, and K. Ogawa: "BER performance evaluation by OTA measurement of BAN diversity antenna", IEEJ Hokuriku Branch General Conference, No. C-22, Sep. 2016. (in Japanese)

[40] R. Takebayashi, K. Honda, **K. Li**, K. Ogawa: "Analysis of Received Signal Power in On-Body Dynamic Channel Considering Floor Reflection Effects", IEICE General Conference, No. B-20-4, Mar. 2017. (in Japanese)

[41] **K. Li**, K. Honda, K. Ogawa: "Analysis of Wearable MIMO Antenna with Random-Directional Human Movement in Street Microcell Environment", IEICE General Conference, No. B-1-132, Mar. 2017. (in Japanese)

[42] K. Honda, **K. Li**, K. Ogawa: "An Implementation Method of 4×4 Correlation Matrix of Base Station Antenna for Bilateral OTA", IEICE General Conference, No. B-1-174, Mar. 2017. (in Japanese)

[43] D. Iwamoto, **K. Li**, K. Honda, K. Ogawa: "Alleviation of the Scatterers Reflected Wave in 3D-OTA Device using Slot Antenna", IEICE General Conference, No. B-1-175, Mar. 2017. (in Japanese)

Others

[1] **K. Li**: "A Study on Wearable Antenna and 3D-OTA Assessment Methodology for High Reliable Medical Data Communication Realization", Young Researchers Academic Exchange and Presentation of Toyama University, Sep. 2015.

[2] **K. Li**: "A Study on OTA Performance Evaluation of Bio-Wireless Sensor Considering the Interactions of Human Body / Radio Wave Propagation", Toyama Science GALA 2016, Sep. 2016.

[3] **K. Li**: "A Study on Performance Evaluation of Bio-Wireless Sensor Considering Human Body / Radio Propagation Effect for Medical ICT Applications", Toyama University of Industry, Academy, Government and Finance Exchange Conference 2016, Nov. 2016.

[4] **K. Li**: "High Reliable Wireless Biosensor for Advanced Medical ICT in Aging Society", The 13th IEEE Transdisciplinary-Oriented Workshop for Emerging Researchers, Dec. 2016.

Funding

Name of project	**JSPS KAKENHI (C)**
Research Title	A Study on the Development of a Fading Emulator for BAN Antenna Assessment
Project / Area Number	25420363
Research Field	Communication/Network engineering
Research Institution	Toyama University
Research Category	Grant-in-Aid for Scientific Research (C)
Principal Investigator	Koichi Ogawa
Collaborators	Kazuhiro Honda, **Kun Li**
Project Fiscal Year	2013-04-01 – 2016-03-31
Budget Amount	¥ 4,000,000 JPY

Name of project	**SCOPE2013 PHASE I**
Research Title	Wrist-Mounted MIMO Array Antenna and OTA Assessment for Gigabit Channel Capacity by Adaptive Signal Processing Considering Human and Propagation Effects
Grant Number	135005102
Research Institution	Toyama University
Principal Investigator	Koichi Ogawa
Collaborators	Kazuhiro Honda
Project Fiscal Year	2013 – 2014
Budget Amount	¥ 4,070,000 JPY

Name of project	**SCOPE2014-2015 PHASE II**
Research Title	Wearable Antenna and OTA Assessment Considering Human Motion and Propagation Effects for MICT Network Establishment with Cooperation of Human and Social Infrastructure
Grant Number	145005101
Research Institution	Toyama University
Principal Investigator	Koichi Ogawa
Collaborators	Kazuhiro Honda, Yoshio Koyanagi, Hiroshi Sato, Ritsu Miura
Project Fiscal Year	2014 – 2016
Budget Amount	¥ 35,760,000 JPY

Award

Year	Title	Organization	Location
2013	International Exchange Scholarship	ASAHI International Education Foundation	Toyama, Japan
2013	Student Overseas Travel Assistance Project	Gofuku Campus, Toyama University	Toyama, Japan
2014	International Student Scholarship	Gofuku Campus, Toyama University	Toyama, Japan
2014	Finalist of the Student Paper Contest	IEEE International Workshop on Electromagnetics (iWEM2014)	Sapporo, Japan
2014	Finalist of the Student Paper Contest	International Symposium on Antennas and Propagation (ISAP2013)	Taiwan
2015	Scholarship of Rotary Yoneyama	Rotary Yoneyama Memorial Foundation	Toyama, Japan
2015	Outstanding Young Researcher Award	Toyama University	Toyama, Japan
2015	Best Student Paper	IEEJ Hokuriku Branch	Kanazawa, Japan
2015	IEEE AP-S Japan Student Award (SPA)	IEEE Antennas and Propagation Society Tokyo Chapter	Tokyo, Japan
2016	Student Research and Travel Assistance Award	International Symposium on Medical Information and Communication Technology (ISMICT2016)	Worcester, USA
2016	IEEE Nagoya Section Conference Presentation Awards	IEEE Nagoya Section	Nagoya, Japan
2016	Outstanding Young Researcher Award	Toyama Science GALA2016	Toyama, Japan.

Biography

り　こん
李　鯤
Li　Kun

Education

2014-2017	PhD, Communication System, Toyama University, Japan
2012-2014	Master, Communication System, Toyama University, Japan
2007-2011	Bachelor, Communication Engineering, Nanjing University of Posts and Telecommunications, China

Research

Since 2012, the author is engaged in research and development work on an over-the-air testing methodology for body-area-networks and MIMO systems. His research interests include evaluation technologies for mobile communication systems, low-profile wearable antenna, diversity / adaptive / MIMO array antennas for body-area-network systems, electromagnetic interaction between antennas and a human body, and human vicinity radio propagation behaviors. He is a student member of the IEEE and IEICE.